Precision determination of the strong coupling constant

ARCHIVES

MASSACHUSETTS INSTITUTE OF TECHNOLOGY
AUG 01 2012
LIBRARIES

by

Riccardo Abbate

Submitted to the Department of Physics
in partial fulfillment of the requirements for the degree of

Doctor of Philosophy

at the

MASSACHUSETTS INSTITUTE OF TECHNOLOGY

June 2012

© Massachusetts Institute of Technology 2012. All rights reserved.

Author .....
Department of Physics
May 18, 2012

Certified by .....
Iain W. Stewart
Associate Professor of Physics
Thesis Supervisor

Accepted by .....
Krishna Rajagopal
Associate Department Head for Education

Precision determination of the strong coupling constant

by

Riccardo Abbate

Submitted to the Department of Physics
on May 18, 2012, in partial fulfillment of the
requirements for the degree of
Doctor of Philosophy

Abstract

In this thesis we study the event shapes variable thrust. Event shape variables are observables that characterize the shape of the distribution of the final state particles of a reaction. We take advantage of the formalism of Soft Collinear Effective Theory (SCET), an effective theory of the strong interactions appropriate for describing energetic jets. We give a factorization theorem for the process e^+e^- to hadrons, valid in the whole range of thrust values. This factorization theorem resums large logarithms at the N^{3}LL accuracy and contains the full $\mathcal{O}(\alpha_s^3)$ result for the fixed order cross section. In order to be able to describe the whole range of thrust values, we define the profile functions, which are thrust-dependent factorization scales which smoothly interpolate between regions where resummation of large logarithms is important and where it is not. To determine non perturbative effects, we fit renormalon-free non-perturbative matrix elements of operators defined in field theory, Ω_1. We perform a global analysis to all available thrust data in the tail region, where a two parameter fit to $\alpha_s(m_Z)$ and the first power correction Ω_1 suffices. We find $\alpha_s(m_Z) = 0.1135 \pm (0.0002)_{expt} \pm (0.0005)_{hadr} \pm (0.0009)_{pert}$, with $\chi^2/\mathrm{dof}(= 485) = 0.91$, where the displayed 1-sigma errors are the total experimental error, the hadronization uncertainty, and the perturbative theory uncertainty, respectively. Furthermore, we perform a global analysis to all available data on the first moment of the thrust distribution. This analysis is a partially independent check of the tail fit, in fact it probes different regions of the thrust distribution and the analysis of experimental systematic uncertainties was conducted independently with respect to the data for the distribution. We find $\alpha_s(m_Z) = 0.1141 \pm (0.0004)_{\mathrm{exp}} \pm (0.0014)_{\mathrm{hadr}} \pm (0.0007)_{\mathrm{pert}}$ with $\chi^2/\mathrm{dof}(= 45) = 1.33$. We also consider pp collisions, in particular the Drell-Yan process. Here we calculate analytically the beam thrust logarithms of the relevant beam functions and of the coefficient function at $\mathcal{O}(\alpha_s^2)$. This is a necessary ingredient for the calculation of the nonsingular terms in resummed predictions.

Thesis Supervisor: Iain W. Stewart
Title: Associate Professor of Physics

Acknowledgments

I would like to thank first my advisor Prof. Iain Stewart, who followed me, assisted me and taught me innumerable things in these 5 years at MIT. Many thanks go to the members of my committee, Jesse Thaler and Bolek Wyslouch for comments on the manuscript. The work in this thesis has been done in collaboration with Prof. Andre Hoang (University of Vienna), Dr. Vicent Mateu, Dr. Michael Fickinger (University of Arizona), Dr. Frank Tackmann and Dr. Teppo Jouttenus. It has been a pleasure to work with such passionate physicists. A special thanks go to Scott Morley, Joyce Berggren and Charles Suggs for the exceptional job they do in making everything in the CTP going smoothly.

I want to extend my thanks to all the friends I met during these years in Cambridge, at MIT and doing Judo, who contributed to make me feel at home.

Finally, I want to thank my family and Gaia for their constant support, help and patience.

Contents

List of Figures

List of Tables

Chapter 1

Introduction

1.1 Strong Interaction and Phenomenology

In the era of the Large Hadron Collider (LHC), it is impossible to overestimate the relevance of the theory of the Strong Interactions, also known as Quantum Chromodynamics (QCD). QCD is, among Gravity, Electricity and Magnetism, and the Weak Interactions, one of the four fundamental forces known in Nature, and it is responsible for binding quarks and gluons into observable mesons and hadrons. QCD is one of the building blocks of the Standard Model of Particle Physics, and it has been extensively tested in the last fifty years of experiments. A great variety of experiments have been set up to test the predictions of the Standard Model (SM). A set of experiments, which will be relevant for this thesis, have been conducted at the Large Electron-Positron Collider (LEP), at CERN, where the detector was in operation from 1989 to 2000. In a first stage (LEP1), it collected precision electroweak measurements at the Z resonance, $m_Z = 91.2$ GeV, and in a second stage (LEP2) the center of mass energy was increased first to the W-pair production threshold and then to the limit of the machine, $Q = 210$ GeV. These experiment were able to test the predictions of the Standard Model showing a remarkable agreement. An important prediction of the SM, which still lacks experimental verification is the presence of the Higgs boson, a scalar particle which, in the Model, plays a crucial role in giving the observed mass to the fundamental particles.

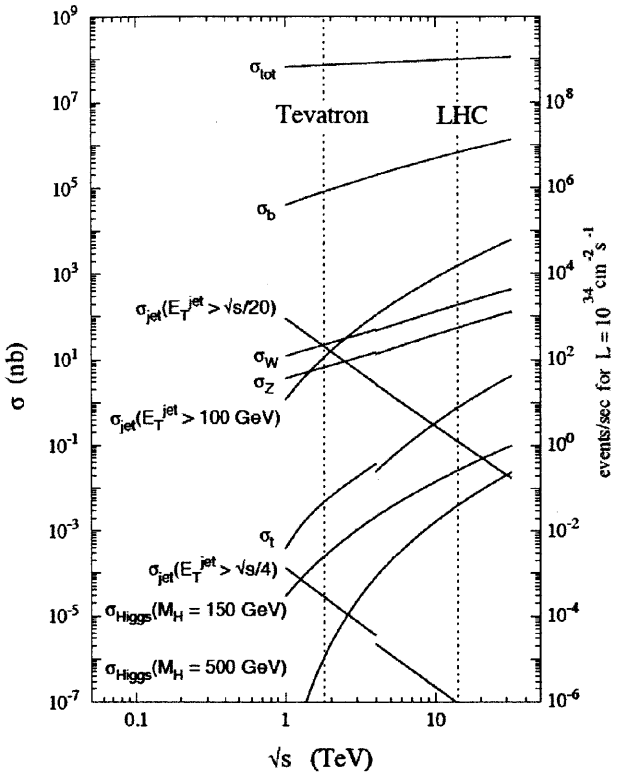

Figure 1-1: Cross Sections for Specific Physics Processes from the ATLAS TDR (2003), [101]. The dotted lines show the energies of two hadron collider (The Tevatron at 1.96 TeV, and The LHC at 14 TeV). The discontinuities are due to the difference in parton content between $p\bar{p}$ and pp collisions.

Evidence for a signal compatible with the Higgs boson has been looked for in recent experiments conducted by the Tevatron at Fermilab, but without significant results. The LHC has been built with the aim to find the Higgs boson and to test different scenarios of physics behind the Standard Model. The LHC is currently colliding protons at a center of mass energy of 7 TeV, and it is designed to reach a center of mass energy of 14 TeV. However, as shown in Fig. 1.1, the cross section to produce the Higgs boson is 10 orders of magnitude smaller than the total cross section. This means that in order to isolate the signal, it is necessary to separate it from the background. Since the background is mainly due to QCD, now more than ever it is crucial to have the best possible predictions from the theory of strong interactions. QCD is an asymptotically free theory, meaning that the strong coupling constant is small.

at very high energies, and is very large at small energies, where the theory exhibits confinement. This in turns implies that the degrees of freedom of the theory are not physically observable and in fact particles charged under QCD, referred to as colored particles, have never been directly observed in experiments. For this reason, QCD is a very complicated theory and different approaches have been developed in order to perform calculations of experimentally observable quantities.

The main object of this thesis is a precision determination of the strong coupling constant at the scale of the mass of the Z boson, $\alpha_s(m_Z)$. In order to accomplish that, we will consider only e^+ e^- annihilation events. The reason for this choice is that, in these collisions, QCD is involved only in the final state of the reaction, therefore they provide a very clean environment to study QCD itself. The reaction can be described as follows: the electron and positron collision happens at the center of mass energy Q of these initial state particles and colored particles are formed in the interaction. A characteristic of QCD is that colored particles evolve by branching into additional colored particles, ending up in collimated beams of hadrons, called jets, whose energy scale is the jet energy scale. Jets must be formed by color neutral objects, and there will be an exchange of soft radiation between different jets in order to change the color structure of these objects and make them color neutral. We see therefore that e^+e^- annihilation processes are characterized by the presence of three different scales, the center of mass energy, called the hard scale μ_H, the jet energy scale, μ_J, and the scale of the soft radiation, the soft scale μ_S. A convenient approach to face a problem where different scales are involved is the Effective Field Theory Approach.

In the next sections, we will give a brief overview of Effective Field Theories in general, and in particular, of Soft Collinear Effective Theory, the tool we use in this thesis. We will then introduce event shape variables and in particular thrust, which is the observable under study in this thesis.

1.2 Effective Field Theory

A very important concept in Physics is the concept of Effective Field Theory, EFT. Its importance relies on the fact that even though the world is incredibly rich with interesting phenomena at every scale we look at, from the age of the universe, about 10^{18} seconds, to the lifetime of the W or Z boson, about 10^{-25} seconds, it is often possible to isolate a set of phenomena from the rest, so that we can describe them without having to understand everything. In the words of Georgi, [88], *we can divide up the parameter space of the world into different regions, in each of which there is a different appropriate description of the important physics.* EFTs are the tools we use to describe the appropriate description of the important physics in a given region of the parameter space. A very simple example of this concept is Newtonian Mechanics, which is an EFT of Special Relativity valid in a region of parameter space in which all velocities are small as compared to the speed of light. This example illustrates that it is not always necessary to use EFT, because in some cases the more fundamental theory may be known. However, even in such cases, sometimes it is very convenient to follow an approach based on EFTs. In Particle Physics the relevant parameters are the distance scales. The EFT strategy is to take features of the physics that are small compared to the relevant scales of the problem and shrink them to zero size. The finite size effects that have been ignored in this way, are small and can be included as perturbations. The process of shrinking to zero size small distance physics is referred to as *integrating out* the corresponding modes, and the procedure of including these effects as perturbations is referred to as *matching* the EFT onto the fundamental theory.

Several EFTs have been developed to study QCD in different regions of the parameter space, in this thesis we will make use of the Soft Collinear Effective Field Theory.

1.3 Soft Collinear Effective Theory

Soft Collinear Effective Theory (SCET) [20, 22, 27, 26, 21] is an EFT for QCD appropriate for describing energetic jets (SCET_I), and and energetic hadrons (SCET_II), and in general for describing the interaction of soft and collinear particles. In this thesis we will work within the context of SCET_I and we will refer to it as SCET. As mentioned before, the EFT approach to a problem consists in first identifying the physics we want to describe and the scale at which it happens, then shrinking to zero size the physics associated with distances small in comparison to it, and find the minimal set of degrees of freedom to appropriately describe the physics. In this thesis we study the process of annihilation of electrons and positrons and the subsequent creation of jets. In particular we study an observable which depends on the distribution of the particles in the final state. The important physics happens at the scale μ_J, and therefore it is convenient to integrate out the physics associated with the hard scale μ_H and take it into consideration as perturbations. In SCET we integrate out modes corresponding to virtualities of the order $p^2 \geq \lambda^2 \mu_H^2 \sim \lambda^2 Q^2$, ($\lambda \ll 1$ is a dimensionless parameter that will be discussed in more detail later) allowing us to give a description which is appropriate for this task and is extremely convenient because it does so taking advantage of the underlying structure of collinear and soft singularities of QCD. In this subsection we will briefly describe the formalism of SCET, introducing light-cone coordinates and the degrees of freedom of SCET, the factorization of soft and collinear degrees of freedom and the resummation of large logarithms. All these aspects play a fundamental role in the results described in this thesis.

It is convenient to work with light cone coordinates, where every four-vector p is decomposed as

$$p^\mu = n \cdot p \frac{\bar{n}^\mu}{2} + \bar{n} \cdot p \frac{n^\mu}{2} + p_\perp^\mu, \tag{1.1}$$

where n and $\bar{n}$ are two light cone vectors such that $n^2 = \bar{n}^2 = 0$ and $n \cdot \bar{n} = 2$, and $p_\perp^\mu$ is expressed in the Minkowskian notation so that $p_\perp^2 = -\vec{p}_\perp{}^2$. It is conventional to define $p^+ = n \cdot p$ and $p^- = \bar{n} \cdot p$ so that the particle's invariant mass is $p^2 = p^+ p^- + p_\perp^2$.

	$p^\mu(p^+, p^-, p_\perp)$
n-collinear	$(\lambda^2, 1, \lambda)\, Q$
$\bar{n}$-collinear	$(1, \lambda^2, \lambda)\, Q$
soft	$(\lambda^2, \lambda^2, \lambda^2)\, Q$

Table 1.1: Degrees of freedom in SCET_I and associated scaling. In the literature, the modes referred here to as soft are sometimes called ultrasoft, the term soft being reserved for momenta scaling as $(\lambda, \lambda, \lambda)Q$. Since we do not need soft modes, we will refer to the ultrasoft modes as soft for brevity.

This is convenient because in these coordinates a boost corresponds to a multiplicative factor for the $p^\pm$ components, such that $p^+\, p^-$ is invariant. Highly energetic particles collinear to the direction n have momentum that scales as

$$(p^+, p^-, p_\perp) \sim (\lambda^2, 1, \lambda)\, p^-, \tag{1.2}$$

where $p^- \sim \mu_H$, $\lambda \ll 1$ is the SCET power counting parameter, and corresponds parametrically to $p_\perp / p^-$. This scaling results from taking a particle with homogeneous scaling $(\lambda, \lambda, \lambda)\mu_H$ in its rest frame and boosting it in the n-direction, so that $p^+ \to \lambda p^+$ and $p^- \to \lambda^{-1} p^-$. The minimal set of degrees of freedom that describes the relevant physics and does not spoil the power counting is summarized in Table 1.1

The momentum $p \sim (\lambda^2, 1, \lambda)Q$ of the generic QCD field ψ after integrating out modes with virtualities larger than $p^2 = \lambda^2 Q^2$ is split as

$$p^\mu = p_\ell^\mu + p_r^\mu \tag{1.3}$$

where $p_\ell = (0, 1, \lambda)\, Q$ is called *label* momentum and represents a discrete n-collinear momentum and $p_r \sim (\lambda^2, \lambda^2, \lambda^2)Q$ is called *residual* momentum.

We split the generic quark field ψ in QCD, into an n-collinear field $\hat{\xi}_n$ and a subleading field $\hat{\varphi}_{\bar{n}}$

$$\psi = \hat{\xi}_n + \hat{\varphi}_{\bar{n}} \tag{1.4}$$

with

$$\hat{\xi}_n \equiv \frac{\not{n}\bar{\not{n}}}{4}\psi \qquad \hat{\varphi}_{\bar{n}} \equiv \frac{\bar{\not{n}}\not{n}}{4}\psi. \tag{1.5}$$

The subleading field $\hat{\varphi}_{\bar{n}}$ is integrated out via its equation of motion, and the n-collinear field is written

$$\hat{\xi}_n(x) = \sum_{p_\ell \neq 0} e^{-ip_\ell x}\, \xi_{n,p_\ell}(x), \tag{1.6}$$

separating the large collinear component from the soft residual one, $i\,\partial\, \xi_{n,p_\ell} \sim \lambda^2\, \xi_{n,p_\ell}$. Observe that the value of the label momentum p_ℓ must be different from 0 for the field to be considered collinear. Defining an operator $\mathcal{P}$ such that

$$\mathcal{P}^\mu\, \xi_{n,p_\ell} \equiv p_\ell^\mu\, \xi_{n,p_\ell}, \tag{1.7}$$

we can write the n-collinear field $\hat{\xi}_n$ as

$$\hat{\xi}_n(x) = e^{-i\mathcal{P}x} \sum_{p_\ell \neq 0} \xi_{n,p_\ell}(x) \equiv e^{-i\mathcal{P}x}\, \xi_n(x). \tag{1.8}$$

The gluon field A^μ is split into a collinear field A_n with collinear scaling, and an ultrasoft A_{us} field with ultrasoft scaling. Integrating out hard offshell fluctuations and constructing gauge invariant structures in SCET, it is necessary to include collinear Wilson lines W_n, defined as

$$W_n(y) = P \exp\left(ig \int_{-\infty}^{0} ds\, \bar{n} \cdot A_n(s\bar{n} + y) \right), \tag{1.9}$$

where the P stands for path ordering. At the leading order in the power counting parameter λ, it turns out that the soft degrees of freedom can be decoupled from the collinear degrees of freedom using the BPS field redefinition, [26],

$$\xi_{n,p}(x) \to Y_n(x)\, \xi_{n,p}(x) \qquad A_{n,p} \to Y_n(x)\, A_{n,p}(x)\, Y_n^\dagger(x), \tag{1.10}$$

with

$$Y_n(x) = P \exp\left(ig \int_{-\infty}^{0} ds\, n \cdot A_{us}(sn + x) \right). \tag{1.11}$$

A very important consequence of this decoupling is that, within SCET, it is possible to derive factorization theorems. These consist in equations where the contribution of each scale involved in the process is represented by a factor which is independent from the physics coming from different scales. A simplified version of the factorization theorem we use in this thesis is

$$\frac{\mathrm{d}\sigma}{\mathrm{d}\tau}(\tau) = Q\, \sigma_0\, H_Q(Q, \mu) \int \mathrm{d}s\, J_\tau(s, \mu)\, S_\tau\left(Q\tau - \frac{s}{Q}, \mu\right). \tag{1.12}$$

Here we have a hard function H_Q, a jet function J_τ and a soft function S_τ. Each of these factors have simple expressions only if evaluated at their natural scales, μ_H, μ_J and μ_S respectively. However, in the factorization theorems as Eq.(1.12) they appear at a common factorization scale, μ. It turns out that this implies that the cross section contains logarithms of the form $\log \frac{\mu}{\mu_H}$, $\log \frac{\mu}{\mu_J}$ and $\log \frac{\mu}{\mu_S}$. In the case of the thrust observable, Eq. (1.12), the jet and soft scales are proportional to the thrust itself, as explained in detail in Chapter 2, and these logarithms are of the form $\log \tau$. Indicating with L any of these logarithms, the general structure of the cross section is

$$\begin{aligned} \frac{\sigma}{\sigma_0} \sim \exp\Bigg\{ &\left[L \sum_{k=1}^{\infty} (\alpha_s L)^k \right]_{\mathrm{LL}} + \left[\sum_{k=1}^{\infty} (\alpha_s L)^k \right]_{\mathrm{NLL}} \\ &+ \left[\alpha_s \sum_{k=0}^{\infty} (\alpha_s L)^k \right]_{\mathrm{NNLL}} + \left[\alpha_s^2 \sum_{k=0}^{\infty} (\alpha_s L)^k \right]_{\mathrm{N^3LL}} + \cdots \Bigg\}. \end{aligned} \tag{1.13}$$

Whenever the scales which enter in the logarithms are such that $\alpha_s L \sim 1$, the perturbative expansion breaks down, and in order to be able to give reliable predictions, we need to resum a whole tower of logarithms. Resummation of the first bracket in Eq. 1.13 is called leading log resummation (LL), resummation of the second bracket is called next-to-leading log resummation (NLL), and resummation of the k-th bracket

is called next-to-next-$\cdots$-leading log resummation ($\mathrm{N^kLL}$). These resummations are obtained using the renormalization group equations (RGE) to derive evolution factors which contain the logarithmic dependence at the required logarithmic accuracy. The factorization theorem after having performed resummation is

$$\begin{aligned}\frac{\mathrm{d}\sigma}{\mathrm{d}\tau}(\tau) =& Q\sigma_0\, H_Q(Q,\mu_H)\, U_H(Q,\mu_H,\mu)\int \mathrm{d}s\, \mathrm{d}s'\, J_\tau(s',\mu_J)\, U_J^\tau(s-s',\mu,\mu_J) \\ &\times \int \mathrm{d}k'\, U_S^\tau(k',\mu,\mu_S) S_\tau\Big(Q\tau - \frac{s}{Q} - k',\mu_S\Big),\end{aligned} \tag{1.14}$$

where the evolution factors $U(\mu_a,\mu_b)$ perform the resummation of the logarithms of the form $\log\frac{\mu_a}{\mu_b}$ up to the specified logarithmic accuracy, and the hard, jet and soft function are evaluated at their natural scales, where they don't have large logarithms and can be calculated in perturbation theory.

1.4 Event Shape Observables: Thrust Distribution

The aim of an Event Shape Observable [133] is to define a quantity which characterizes the shape of an event, for example whether the distribution of hadrons is pencil-like, planar, spherical etc. The procedure is to define a quantity e which measures some particular aspect of the shape of the hadronic final states. The distribution $d\sigma/de$ can be measured and compared with the theoretical calculation. For the latter to be calculable in perturbation theory, the variable should be Infra-Red (IR) safe, *i.e.* insensitive to the emission of soft or collinear gluons. In particular, if $\vec{p}_i$ is any momentum occurring in the definition of e, the latter must be invariant under the branching

$$\vec{p}_i \to \vec{p}_i + \vec{p}_k \tag{1.15}$$

whenever $\vec{p}_i$ and $\vec{p}_k$ are parallel or one of them is small. Quantities made out of linear sums of momenta meet this requirement. In this thesis we analyze the thrust [77] for

hadronic final state in e^+e^- annihilation. It is an event shapes observable defined as

$$T = \max_{\hat{t}} \left(\frac{\sum_i |\hat{t} \cdot \vec{p}_i|}{\sum_i |\vec{p}_i|} \right) \equiv 1 - \tau \tag{1.16}$$

where $\vec{p}_i$ denotes the three momentum of particle i, with the sum running over all particles. The unit vector $\hat{t}$ is varied to find the thrust direction $\hat{t}_T$ that maximizes the expression in parenthesis. Algorithms to calculate numerically the thrust in an efficient way can be found in [148]. The range of values that τ, to which we will refer to as thrust in this thesis, changes depending on the number of particles in the final state[1]:

- a two-particle final state has $\tau = 0$ and a thrust axis equal to one of the two particles' direction.

- a three-particles final state has $0 \leq \tau \leq 1/3$. The maximum thrust is reached when the particle 3-momenta point towards the vertices of an equilateral triangle, and the thrust axis is one of the direction of the particles.

- a four-particle final state has $0 \leq \tau \leq 1 - 1/\sqrt{3}$. The maximum thrust is reached in a configuration where the particles point toward the vertices of a regular tetrahedron, and the thrust axis is obtained summing the directions of any two particles.

- a five-particle final state has $0 \leq \tau \leq 1 - 2\sqrt{2}/5$. The maximum thrust is reached when all the particles have the same momentum, three particles point to the vertices of an equilateral triangle and the other two are perpendicular to the plane defined by the triangle and opposite to each other. The thrust axis in this case is the sum of the directions of the particle moving perpendicular to the triangle and of one of the particles in the plane where the triangle lies.

- for a final state with infinitely many particles uniformly distributed on the sphere, spherical symmetry tells us that any direction can be taken as thrust

[1]These ranges are strictly true for massless particles.

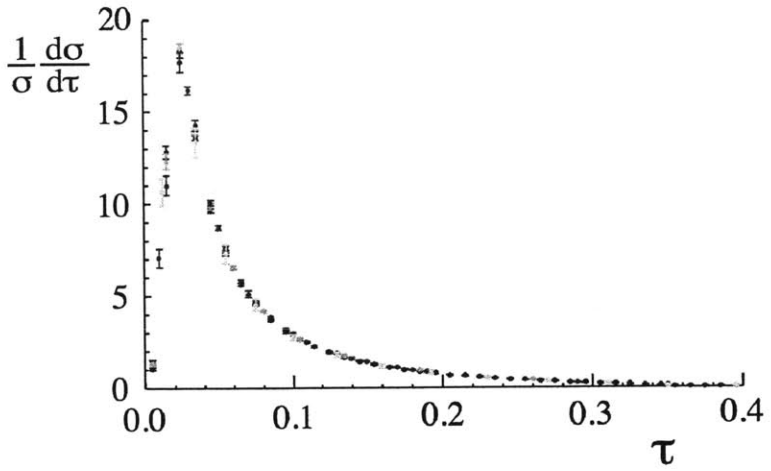

Figure 1-2: Experimental data on e^+e^- colliders at the center of mass energy equal to the mass of the Z boson, $Q = m_Z$. In the picture is shown data from ALEPH(blue), DELPHI(red), L3(cyan), OPAL(green) and SLD(grey).

axis, so taking $\hat{t} = (0, 0, 1)$ and $\vec{p}_i = (\sin\theta\ \cos\phi, \sin\theta \sin\phi, \cos\theta)$ we have

$$T = \frac{\sum_{i=1}^{\infty} |\vec{p}_i \cdot \hat{t}|}{\sum_{i=1}^{\infty} |\vec{p}_i|} = \frac{2\int_0^1 d\cos\theta \int_0^{2\pi} d\phi \cos\theta}{\int_{-1}^1 d\cos\theta \int_0^{2\pi} d\phi} = \frac{1}{2} \tag{1.17}$$

In the limit in which $\tau \to 0$, it is possible to express thrust as

$$\tau \sim \frac{M_1^2 + M_2^2}{Q^2}, \qquad \tau \to 0 \tag{1.18}$$

where $M_{1,2}^2$ are called hemisphere invariant masses, and are defined as

$$M_a^2 = \Big(\sum_{i \in a} p_i\Big)^2, \tag{1.19}$$

where the sum is carried over the four momenta of all particles that belong to hemisphere a. The two hemispheres are separated by the plane passing through the origin and perpendicular to the thrust axis.

The thrust distribution collected at electron-positron colliders at center-of-mass energy $Q = m_Z$ is shown in Figure 1.4. The range of the thrust distribution is typically split in three regions: the peak, the tail and the multijet or far tail. The peak region is

characterized by the presence, in the final state, of two jets and soft radiation. Here, denoting with Q the center of mass energy, we have that $Q^2 \gg Q^2\tau \gg (Q\tau)^2 \sim \Lambda^2_{\rm QCD}$. We will see later on in the factorization theorem in Chapter 2 that the scale $Q^2\tau$ is associated with the jet scale μ_J^2, the scale $Q^2\tau^2$ with the soft scale μ_S^2, and $Q^2 = \mu_H^2$. In the tail region there are events with two or three jets and soft radiation, and $Q^2 \gg Q^2\tau \gg (Q\tau)^2 \gg \Lambda^2_{\rm QCD}$. The multijet region is composed by events with more than three jets in the final state. Here $Q^2 \sim Q^2\tau \sim (Q\tau)^2 \gg \Lambda^2_{\rm QCD}$. Since in the peak region $\tau \sim \Lambda_{\rm QCD}/Q$, we observe that the position of the peak is a Q dependent quantity and therefore so is the splitting between peak and tail region. The splitting between the tail and the multijet region instead, is well defined by the value of $\tau = 1/3$, which is the maximum thrust a three particle final state can have. Since the scales in the problem have different relations between each other in different thrust regions, the best way to theoretical describe the data has to change accordingly. In the peak region, the scales are widely separated, meaning that in order to avoid large logarithms of these scales, resummation has to be performed. Moreover, the soft scale $\mu_S = Q\tau \sim \Lambda_{\rm QCD}$, and therefore this region is sensitive to non perturbative physics. In the tail region, the scales are much larger than $\Lambda_{\rm QCD}$ and are widely separated, so again resummation is a necessary ingredient to an appropriate description of this region. In order to describe the effects of the soft radiation, it is necessary to correctly include the first $1/Q$ power correction. Finally, in the multijet region, the scales are of the same order and the data can be described with fixed order perturbation theory with power corrections. Because of this complex structure, the appropriate theoretical description of the thrust distribution changes depending on which region we want to focus on. A great amount of data have been collected about event shapes in e^+e^- collisions in experiments conducted at LEP1 and LEP2 (collaborations: ALEPH, DELPHI, OPAL, L3), SLAC (SLD collaboration), DESY (TASSO, JADE collaborations) and KEK (AMY collaboration). At these colliders, the different collaborations provided binned values for the thrust distributions at various center of mass energies. In Figure 1.4 we show the experimental data at $Q = m_Z$. However, due to the theoretical limitations we mentioned above, all these data

have previously not been subjected to a global analysis. Typical analyses focused on the tail region of a subset of the whole experimental data. The state of the art before the work described in this thesis was published in Ref. [1] was that the full set of $\mathcal{O}(\alpha_s^3)$ to the 2-,3-,and 4-jet final states was determined and made available in the program package EERAD3[86], resummation of large logarithms at N^{3}LL accuracy in SCET for thrust was performed in Ref. [31] and at NLL following the classic exponentiation techniques of Ref. [51]. In this thesis, we resolve the theoretical problems mentioned above, giving a theoretical description of the thrust distribution which is appropriate in the peak, tail and multijet region. Our factorization theorem provides also a field theoretical description of the non perturbative parameter Ω_1 which determines the first power correction, giving a contribution of the order of $\mathcal{O}(\Omega_1/Q)$ to the cross section. Our analysis allows us to define a global dataset which includes all experimental data. For ease of comparison to previous analyses, we consider, in Chapter 3, the thrust distribution in the tail region and we perform a 2 parameter fit for $\alpha_s(m_Z)$ and Ω_1.

The JADE, OPAL, ALEPH, DELPHI and L3 collaborations provided also experimental data for moments of event shapes. This set of data is analyzed independently from the binned distributions, and has been used to perform separate determinations of $\alpha_s(m_Z)$. In Chapter 4, we apply our formalism to perform a global analysis of the moments of the thrust distribution, determining a value for $\alpha_s(m_Z)$ and Ω_1 compatible with the analysis in Chapter 3.

In the next section we will describe the main ingredients of our analysis, highlighting the improvements with respect to previous analyses.

1.5 Precision measurement of $\alpha_s(m_Z)$

In this thesis we extend the event shape formalism in the SCET framework. The formula we derive has a N^{3}LL order summation of logarithms for the partonic singular $\alpha_s^j \ln^k(\tau)/\tau$ terms, and $\mathcal{O}(\alpha_s^3)$ fixed-order contributions for the partonic nonsingular terms. Our theoretical improvements beyond earlier work include:

- A factorization formula that can be simultaneously applied to data in the peak and the tail regions of the thrust distribution and for multiple c.m. energies Q, as well as being consistent with the multijet thresholds in the far-tail region.

- In the factorization formula a nonperturbative soft function defined from field theory is implemented using the method of Ref. [95] to incorporate hadronization effects.

- In the tail region the leading power correction to $\mathrm{d}\sigma/\mathrm{d}\tau$ is determined by a nonperturbative parameter Ω_1 that appears through a factorization theorem for the singular distribution. Ω_1 is a field theory matrix element of an operator, and is also related to the first moment of the nonperturbative soft function.

- Defining the matrix element $\bar{\Omega}_1$ in $\overline{\mathrm{MS}}$, the perturbative cross section suffer from an $\mathcal{O}(\Lambda_{\mathrm{QCD}})$ renormalon. In our analysis this renormalon is removed by using an R-gap scheme for the definition of Ω_1 [95]. This scheme choice induces subtractions on the leading power $\overline{\mathrm{MS}}$ cross section which simultaneously remove the renormalon there. Large logarithms in the subtractions are summed to all orders in α_s using R-evolution equations given in Refs. [92, 93].

- Finite bottom quark mass corrections are included using a factorization theorem for event shapes involving massive quarks, derived in Refs. [79, 80].

- QED corrections at NNLL order are incorporated, counting $\alpha_{\mathrm{em}} \sim \alpha_s^2$. This includes QED Sudakov effects, final state radiation, and QED/QCD renormalization group interference.

- The 3-loop finite term h_3 of the quark form factor in $\overline{\mathrm{MS}}$ is extracted using the results of Ref. [18], and is included in our analysis.

- The most important corrections from the axial anomaly are included. The anomaly modifies the axial-vector current contributions at $\mathcal{O}(\alpha_s^2)$ by terms involving the top quark mass.

For the numerical analyses carried out in this work we have created within our collaboration two completely independent codes. One code within Mathematica [147] implements the theoretical expressions exactly as given in this thesis, and one code is based on theoretical formulae in Fourier space and realized as a fast Fortran code suitable for parallelized runs on computer clusters. These two codes agree for the thrust distribution at the level of 10^{-6}.

While the resulting theoretical code can be used for all values of τ, in Chapter 3 of this thesis we focus our numerical analysis on a global fit of e^+e^- thrust data in the tail region, for c.m. energies Q between 35 and 207 GeV, to determine $\alpha_s(m_Z)$,[2] and we show the predictions of the results of this fit for the peak and far-tail regions.

Our global fit exhibits consistency across all available data sets, and reduces the overall experimental uncertainty. For a single Q we find a strong correlation between the effect of $\alpha_s(m_Z)$ and Ω_1 on the cross section. This degeneracy is broken by fitting data at multiple Qs. The hadronization uncertainty is significantly decreased by our simultaneous global fit to $\alpha_s(m_Z)$ and Ω_1. To estimate the perturbative uncertainty in the fit we use a random scan in a 12-dimensional theory parameter space. This space includes 6 parameters for μ-variation, 3 parameters for theory uncertainties related to the finite statistics of the numerical fixed-order results, one parameter for the unknown 4-loop cusp anomalous dimension, and two parameters for unknown constants in the perturbative 3-loop jet and 3-loop soft functions. We also analyze in detail the dependence of the fit results on the range in τ used in the fit.

In Chapter 4 we use our code to perform a global fit of e^+e^- thrust moment data to determine $\alpha_s(m_Z)$. Moments M_n,

$$M_n = \frac{1}{\sigma}\int_0^{\tau_{\max}=1/2} \mathrm{d}\tau\, \tau^n \frac{\mathrm{d}\sigma}{\mathrm{d}\tau}, \tag{1.20}$$

probe different regions of the distribution than the tail fit and it is therefore important that our code is predictive in the whole thrust range. Experimental results are available for many center-of-mass energies Q, and the analysis of systematic uncer-

[2]Throughout this thesis we use the $\overline{\mathrm{MS}}$ scheme for α_s with five light flavors.

tainties is to a large extent independent from that for the binned distribution. Thus, the outcome for a fit of data for the first moment M_1 to $\alpha_s(m_Z)$ and Ω_1 serves as an important cross check of the results obtained in Chapter 3. The M_n moments are not sensitive to large logarithms, and so provide also a non-trivial check on whether the N^{3}LL+$\mathcal{O}(\alpha_s^3)$ full spectrum results, which contains the resummation of logarithms can reproduce this property. In this chapter we also discuss the structure of higher order power corrections in moments.

1.6 Outline

The outline of this thesis is the following: In Chapter 2 we will describe in detail the theoretical ingredients of the factorization theorem for thrust. In Chapter 3 we will discuss the numerical analysis we performed to determine the value of $\alpha_s(m_Z)$ and Ω_1.

In Chapter 4 we will analyze the moments of the thrust distribution and provide a determination of $\alpha_s(m_Z)$ and Ω_1.

In Chapter 5 we will discuss pp collision. In particular, we will consider the Initial State Radiation (ISR) in the Drell-Yan process with 0-jets and calculate the contributions of order α_s^2 to the coefficient functions.

Chapter 2

Factorization Theorem for Thrust

2.1 Introduction

In this Chapter we present the factorization theorem for thrust explaining in detail all the elements that have been highlighted in Chapter 1.5. This work has been published in [1].

2.2 Formalism

2.2.1 Overview

The factorization formula we use for the fits to the experimental thrust data is

$$\frac{\mathrm{d}\sigma}{\mathrm{d}\tau} = \int \mathrm{d}k \left(\frac{\mathrm{d}\hat{\sigma}_{\mathrm{s}}}{\mathrm{d}\tau} + \frac{\mathrm{d}\hat{\sigma}_{\mathrm{ns}}}{\mathrm{d}\tau} + \frac{\Delta \mathrm{d}\hat{\sigma}_b}{\mathrm{d}\tau} \right) \left(\tau - \frac{k}{Q} \right) \times S_\tau^{\mathrm{mod}} \left(k - 2\bar{\Delta}(R, \mu_S) \right) + \mathcal{O}\left(\sigma_0 \, \alpha_s \frac{\Lambda_{\mathrm{QCD}}}{Q} \right) . \tag{2.1}$$

Here $\mathrm{d}\hat{\sigma}_{\mathrm{s}}/\mathrm{d}\tau$ contains the singular partonic QCD corrections $\alpha_s^j \, [\ln^k(\tau)/\tau]_+$ and $\alpha_s^j \, \delta(\tau)$ with the standard plus-functions as defined in Eq. (A.22). It also contains the singular partonic QED corrections depending on α_{em} which are discussed in Sec. 2.2.8. This $\mathrm{d}\hat{\sigma}_{\mathrm{s}}/\mathrm{d}\tau$ term accounts for matrix element corrections and the resummation of $\ln \tau$ terms within the SCET formalism up to $\mathrm{N^3LL}$ order, which we discuss in Sec. 2.2.3.

Our definition of N^{3}LL, N^{3}LL$'$, and other orders is discussed in detail in Sec. 2.2.2 (see also Tab. 2.1).

The term $\mathrm{d}\hat{\sigma}_{\mathrm{ns}}/\mathrm{d}\tau$, which we call the nonsingular partonic distribution, contains the thrust distribution in strict fixed-order expansion with the singular terms $\propto \alpha_s^j \ln^k(\tau)/\tau$ subtracted to avoid double counting. The most singular terms in $\mathrm{d}\hat{\sigma}_{\mathrm{ns}}/\mathrm{d}\tau$ scale as $\ln^k \tau$ for $\tau \to 0$.[1] Our implementation of nonsingular terms is discussed in detail in Sec. 2.2.5.

Finally, $\Delta\mathrm{d}\hat{\sigma}_b/\mathrm{d}\tau$ contains corrections to the singular and nonsingular cross sections due to the finite mass of the bottom quark. The b-mass corrections are implemented as a difference of the massive and massless cross sections computed at NNLL order as discussed in Sec. 2.2.7.

The function S_τ^{mod} that is convoluted with these partonic cross sections in Eq. (2.1) describes the nonperturbative effects from soft gluons including large angle soft radiation [107, 37]. The definition of S_τ^{mod} also depends on the hemisphere prescription inherent to the thrust variable. This is a hadronic function that enters in a universal way for both massless and massive cross sections, and is independent of the value of Q. The universality of S_τ^{mod} in Eq. (2.1) follows from the leading power thrust factorization theorem [107, 79, 136], and the thrust factorization theorem for massive quarks in Refs. [79, 80]. Our treatment of the convolution of S_τ^{mod} with $\mathrm{d}\hat{\sigma}_{\mathrm{ns}}/\mathrm{d}\tau$ yields a consistent treatment of multijet thresholds and the leading power correction to the operator expansion for the first moment of thrust. Details of our implementation of power corrections and nonperturbative corrections are discussed in Sec. 2.2.4 and Sec 2.4. The function S_τ^{mod} is normalized to unity and can be determined from experimental data. Its form depends on a gap parameter $\bar{\Delta}$ and additional moment parameters Ω_i which are discussed below.

The factorization formula given in Eq. (2.1) can be applied simultaneously in the peak, tail, and the far-tail regions, i.e. for all τ values. In the peak region $\mathrm{d}\hat{\sigma}_{\mathrm{ns}}/\mathrm{d}\tau$ is significantly smaller than $\mathrm{d}\hat{\sigma}_{\mathrm{s}}/\mathrm{d}\tau$, and the full analytic form of the soft nonpertur-

[1] For $\mathrm{d}\hat{\sigma}_{\mathrm{ns}}/\mathrm{d}\tau$ the resummation of $\ln\tau$ terms is currently unknown. These terms could be determined with subleading factorization theorems in SCET.

bative function $S_\tau^{\rm mod}(k)$ is relevant to determine the τ-distribution since $\mu_S \simeq \Lambda_{\rm QCD}$. Because $\mu_H \gg \mu_J \gg \mu_S$, the summation of logarithms of τ is also crucial to achieve an accurate theoretical description.

For much of the tail region the summation of $\ln\tau$ terms remains important, although this is no longer the case when we reach $\tau \simeq 1/3$. Likewise, the dominance of the singular partonic contributions remains as long as $\tau < 1/3$, but the nonsingular terms become more important for increasing τ (see Fig. 2-4 below). Near $\tau \simeq 1/3$ the nonsingular terms become equal in size to the singular terms with opposite sign. Since $\mu_S \gg \Lambda_{\rm QCD}$ in the tail region the effects of $S_\tau^{\rm mod}$ can be parameterized in terms of the moments

$$\Omega_i = \int \mathrm{d}k \left(\frac{k}{2}\right)^i S_\tau^{\rm mod}(k - 2\bar{\Delta}), \tag{2.2}$$

where $\Omega_0 = 1$ since $S_\tau^{\rm mod}$ is normalized. Their importance is determined by $\Omega_i/(Q\tau)^i$ as discussed in Sec. 2.2.4, so the first moment Ω_1 parameterizes the dominant power correction and higher moments provide increasingly smaller corrections. The first moment is defined by

$$\Omega_1 \equiv \bar{\Delta} + \frac{1}{2N_c}\langle 0|\mathrm{tr}\ \overline{Y}_{\bar{n}}^T(0) Y_n(0)\, i\widehat{\partial}\, Y_n^\dagger(0)\overline{Y}_{\bar{n}}^*(0)|0\rangle, \tag{2.3}$$

where $Y_n^\dagger(0) = \mathrm{P}\exp\left(ig\int_0^\infty ds\, n\cdot A(ns)\right)$, $\overline{Y}_{\bar{n}}^\dagger$ is similar but in the $\overline{3}$ representation, and we trace over color. Here

$$i\widehat{\partial} \equiv \theta(i\bar{n}\cdot\partial - in\cdot\partial)\, in\cdot\partial + \theta(in\cdot\partial - i\bar{n}\cdot\partial)\, i\bar{n}\cdot\partial, \tag{2.4}$$

is a derivative operator[2] involving light-like vectors $n = (1, \hat{\mathbf{t}})$ and $\bar{n} = (1, -\hat{\mathbf{t}})$. Ω_1 is the field theory analog of the parameter α_0 employed in the low-scale effective coupling approach to power corrections. Since the renormalon subtractions depend on a cutoff scale R and the renormalization scale μ_S, all moments $\Omega_i(R, \mu_S)$ as well

[2]Note that $i\widehat{\partial}$ is defined in the c.m. frame of the colliding e^+e^-. One may also write $i\hat{\partial} = \int \mathrm{d}\eta\, e^{-|\eta|}\hat{\mathcal{E}}_T(\eta)$ where $\hat{\mathcal{E}}_T(\eta)$ measures the sum of absolute transverse momenta at a given rapidity η with respect to the thrust axis $\hat{t}$ [107, 32].

as $\bar{\Delta}(R, \mu_S)$ are scale and scheme dependent quantities. The scheme we use to define $\Omega_1(R, \mu_S)$ is described in Sec. 2.2.6. In our fit to experimental data we use the R-gap scheme, and extract the first moment at a reference scale $R_\Delta = \mu_\Delta = 2$ GeV, i.e. we use $\bar{\Delta}(R_\Delta, \mu_\Delta)$ and hence $\Omega_1 = \Omega_1(R_\Delta, \mu_\Delta)$. In the factorization theorem the gap appears evaluated at $\bar{\Delta}(R, \mu_S)$ and the scales (R, μ_S) are connected to the reference scales (R_Δ, μ_Δ) using renormalization group equations.

Finally, in the far-tail region $\tau \simeq 0.3$ the singular and the nonsingular partonic contributions $\mathrm{d}\hat{\sigma}_\mathrm{s}/\mathrm{d}\tau$ and $\mathrm{d}\hat{\sigma}_\mathrm{ns}/\mathrm{d}\tau$ become nearly equal with opposite signs, exhibiting a strong cancellation. This is due to the strong suppression of the fixed-order distribution in the three- and four-jet endpoint regions at $\tau \gtrsim 1/3$ in fixed-order perturbation theory. In this region the summation of logarithms of τ must be switched off to avoid messing up this cancellation. Here our Eq. (2.1) reduces to the pure fixed-order partonic thrust distribution supplemented with power corrections coming from the convolution with the soft function. All three regions are smoothly joined together in Eq. (2.1). The proper summation (or non-summation) of logarithms is achieved through τ-dependent renormalization scales, $\mu_J(\tau)$, $\mu_S(\tau)$, and $R(\tau)$ which we call *profile functions*. They are discussed in detail in Sec. 2.3.

In the following subsections various ingredients of the factorization formula of Eq. (2.1) are presented in more detail. Compact results for the corresponding analytic expressions for massless quarks in QCD are given in App. A. In Secs. 2.2.7 and 2.2.8 we describe how finite bottom mass and QED corrections are included in our analysis. The full formulae for these corrections will be presented in a future publication.

2.2.2 Order Counting

In the classic order counting used for fits to event shape distributions it is common to separately quote orders for the summation of logarithms and the fixed-order matching contributions. For fixed-order contributions the $\mathcal{O}(\alpha_s)$ contributions are called LO, the $\mathcal{O}(\alpha_s^2)$ contributions are called NLO, etc. This counting is motivated from the fact that at tree level the fixed-order thrust distribution vanishes for $\tau > 0$. For the summation one refers to LL (leading-log) summation if the one-loop cusp anomalous

	cusp	non-cusp	matching	$\beta[\alpha_s]$	nonsingular	$\gamma_\Delta^{\mu,R}$	δ
LL	1	-	tree	1	-	-	-
NLL	2	1	tree	2	-	-	-
NNLL	3	2	1	3	1	1	1
N^{3}LL	4^{pade}	3	2	4	2	2	2
NLL$'$	2	1	1	2	1	1	1
NNLL$'$	3	2	2	3	2	2	2
N^{3}LL$'$	4^{pade}	3	3	4	3	3	3

Table 2.1: Loop orders j for perturbative corrections of $\mathcal{O}(\alpha_s^j)$. Here cusp, non-cusp, and $\gamma_\Delta^{\mu,R}$ refer to anomalous dimensions, while matching, nonsingular, and the gap subtraction δ refer to fixed-order series. For convenience in our numerical analysis we use the four-loop beta function for the α_s running in all orders displayed.

	peak (any k)	tail and far-tail ($k = 0, 1, 2$)
$\frac{\mathrm{d}\hat{\sigma}_s}{\mathrm{d}\tau}$	$\alpha_s^i \frac{\ln^j\tau}{\tau} \frac{\Omega_k}{(Q\tau)^k}$	$\alpha_s^i \frac{\ln^j\tau}{\tau} \frac{\Omega_k}{(Q\tau)^k}$
$\frac{\mathrm{d}\hat{\sigma}_{ns}}{\mathrm{d}\tau}$	$\alpha_s^i f_{ik}(\tau) \frac{\Omega_k}{(Q\tau)^k}$	$\alpha_s^i f_{ik}(\tau) \frac{\Omega_k}{(Q\tau)^k}$
$\frac{\mathrm{d}\hat{\sigma}_b}{\mathrm{d}\tau}$	$\alpha_s^i g_{ik}\big(\tau, \frac{m_b}{Q}\big) \frac{\Omega_k}{(Q\tau)^k}$	$\alpha_s^i g_{ik}\big(\tau, \frac{m_b}{Q}\big) \frac{\Omega_k}{(Q\tau)^k}$
p.c.	$\alpha_s \frac{\Lambda_{\text{QCD}}}{Q}$	$\alpha_s \frac{\Lambda_{\text{QCD}}}{Q}$

Table 2.2: Nonperturbative corrections included in $\mathrm{d}\sigma/\mathrm{d}\tau$ with implicit sums over i and k. All powers $\Omega_k/(Q\tau)^k$ can be included in the peak region with the function S_τ^{mod}, while only a fixed set of power correction parameters are included in the tail and far-tail regions. The row labeled p.c. shows the scaling of the the first power correction that is not entirely determined by the earlier rows and hence yield corrections to Eq. (2.1).

dimension is used to sum the double Sudakov logs, and NLL (next-to-leading-log) if the two-loop cusp and the one-loop non-cusp anomalous dimension terms are also included.

In our analysis the summation orders (LL, NLL, ...) match the classical language. For the fixed-order contributions we account for the tree level $\delta(\tau)$ in LL and NLL, and we include $\mathcal{O}(\alpha_s)$ corrections at NLL$'$ and NNLL, etc, as shown in Tab. 2.1. In SCET the summation can be carried out at both NNLL and N^{3}LL [31]. The corresponding loop orders for the anomalous dimensions are also shown in Tab. 2.1. Within SCET the summation of logarithms is achieved by renormalization group evolution and the fixed-order corrections enter as series evaluated at each of the transition scales μ_H,

μ_J, and μ_S which we refer to as matching or matrix element corrections. The logs in the singular thrust cross section exponentiate to all orders if we use y, the Fourier-transformed variable to τ. The orders we consider correspond to summing the terms

$$\ln\left[\frac{\mathrm{d}\tilde{\sigma}_s}{\mathrm{d}y}\right] \sim \left[L\sum_{k=1}^{\infty}(\alpha_s L)^k\right]_{\mathrm{LL}} + \left[\sum_{k=1}^{\infty}(\alpha_s L)^k\right]_{\mathrm{NLL}} + \left[\alpha_s\sum_{k=0}^{\infty}(\alpha_s L)^k\right]_{\mathrm{NNLL}} + \left[\alpha_s^2\sum_{k=0}^{\infty}(\alpha_s L)^k\right]_{\mathrm{N^3LL}}, \tag{2.5}$$

where $L = \ln(iy)$, and the series in the exponent makes clear the structure of the large logs that are summed at each order.

The nonsingular counting in Tab. 2.1 for the fixed-order series in $\mathrm{d}\hat{\sigma}_{\mathrm{ns}}/\mathrm{d}\tau$ must be the same as for the matching and matrix element corrections to ensure that we exactly reproduce the fixed-order cross section when the resummed result is expanded. Since the relative importance of the log resummation and the nonsingular terms varies depending on the τ-region, we also consider an alternative "primed" counting scheme. In the primed counting all series for fixed-order quantities are included to one higher order in α_s. In this counting scheme the $\mathcal{O}(\alpha_s^3)$ fixed-order results occur in N^{3}LL$'$, which is the order we use for our final analysis.

Also shown in Tab. 2.1 are columns for the fixed-order gap subtractions $\delta = \delta(R,\mu)$, and the gap anomalous dimensions $\gamma_\Delta^{\mu,R}$. These terms are required to remove the leading $\mathcal{O}(\Lambda_{\mathrm{QCD}})$ renormalon from the perturbative corrections, while still maintaining the same level of log resummation for terms in the cross section. The resummation of these large logarithms is missing in the recent analysis of Ref. [64] and is discussed further in Sec. 2.2.6.

A crucial aspect of our analysis is the inclusion of power corrections in a rigorous manner through field theoretic techniques. In the effective theory there are several types of power corrections which arise from the possible ratios of the scales μ_H, μ_J, μ_S, and Λ_{QCD}:

$$1)\ \frac{\Lambda_{\mathrm{QCD}}}{\mu_S} = \frac{\Lambda_{\mathrm{QCD}}}{Q\tau}, \qquad 2)\ \frac{\mu_S^2}{\mu_J^2} = \tau, \qquad 3)\ \frac{\Lambda_{\mathrm{QCD}}}{\mu_H} = \frac{\Lambda_{\mathrm{QCD}}}{Q}. \tag{2.6}$$

Any $\Lambda_{\rm QCD}/\mu_J$ power correction can be taken as a cross-term between types 1) and 2) for the purpose of enumeration. The type 1 power corrections are enhanced by the presence of the soft scale and are encoded by the moments $\Omega_k \sim \Lambda_{\rm QCD}^k$ of the soft function. Type 2 are kinematic power corrections that occur because of the expansion about small τ, and can be computed with perturbation theory. The importance of these first two types depends on the region considered in 1.4, with all terms in type 2 becoming leading order for the far-tail region. Type 3 are non-enhanced power correction that are of the same size in any region. There are also cross-terms between the three types.

In our analysis we keep all power corrections of types 1 and 2, and the dominant terms of type 3. Our treatment of the nonsingular cross section also includes cross-terms between 1 and 2 in a manner that is discussed in Sec. 2.2.4. For the different thrust regions we display the relevant terms kept in our analysis in Tab. 2.2. The nonsingular cross section corrections fully account for the power corrections of type 2. The factor $[\Lambda_{\rm QCD}/(Q\tau)]^k$ in the peak region denotes the fact that we sum over all type 1 power corrections from the leading soft function. In the tail and multijet regions we only consider the first three orders: k=0 (partonic result), k=1 (power correction involving Ω_1) and , k=2 (power correction involving Ω_2). Here $k = 2$ terms are used in our error analysis for our simultaneous fit to $\alpha_s(m_Z)$ and Ω_1. The leading power correction that is not fully captured in all regions is of type 3, and are of $\mathcal{O}(\alpha_s\Lambda_{\rm QCD}/Q)$. Since our analysis is dominated by $Q = m_Z$ or larger, parametrically this gives an uncertainty of

$$\left[\frac{\delta\alpha_s}{\alpha_s}\right]_{\rm p.c.} \sim \frac{\Lambda_{\rm QCD}}{Q} \simeq 0.3\% \tag{2.7}$$

in our final fit (taking $\Lambda_{\rm QCD} = 0.3\,{\rm GeV}$ to obtain the number here). This estimate has been validated by running our fits in the presence of an additional $\alpha_s\Lambda_{\rm QCD}/Q$ power correction.[3]

[3]To perform this test we include an $\alpha_s(\mu_{\rm ns})\Lambda_1/Q$ correction in the normalized thrust cross section, vary $\Lambda_1 = \pm 1.0\,{\rm GeV}$, and perform our default fit to $\alpha_s(m_Z)$ and Ω_1 as described in Sec. 3.1. This variation causes only a $\pm 0.1\%$ change to these fit parameters, which is smaller than the estimate in Eq. (2.7).

2.2.3 Singular Partonic Distribution

The singular partonic thrust distribution $\mathrm{d}\hat{\sigma}_s/\mathrm{d}\tau$ contains the most singular terms $\propto \alpha_s^j \ln^k(\tau)/\tau$ and $\alpha_s^j \delta(\tau)$ that arise from perturbation theory. Using SCET one can derive a factorization theorem for these terms which allows for the resummation of the logarithmic terms to all orders in perturbation theory. In massless QCD the factorization formula for the perturbative corrections involving α_s reads

$$\begin{aligned}\frac{\mathrm{d}\hat{\sigma}_s^{\mathrm{QCD}}}{\mathrm{d}\tau}(\tau) =& Q \sum_I \sigma_0^I \, H_Q^I(Q,\mu_H)\, U_H(Q,\mu_H,\mu) \int \mathrm{d}s\, \mathrm{d}s' \\ & \times J_\tau(s',\mu_J)\, U_J^\tau(s-s',\mu,\mu_J) \int \mathrm{d}k'\, U_S^\tau(k',\mu,\mu_S) \\ & \times e^{-2\frac{\delta(R,\mu_S)}{Q}\frac{\partial}{\partial\tau}}\, S_\tau^{\mathrm{part}}\Big(Q\tau - \frac{s}{Q} - k', \mu_S\Big). \end{aligned} \tag{2.8}$$

Here σ_0^I is the total partonic e^+e^- cross section for quark pair production at tree level from a current of type $I = \{uv, dv, bv, ua, da, ba\}$ as explained below. Large logs are summed by the renormalization group factors U_H between the hard scale and μ, U_J^τ between the jet scale and μ, and U_S^τ between the soft scale and μ. The choice of μ is arbitrary and the dependence on μ cancels out exactly when working at any particular order in the resummed expansion. Short distance virtual corrections are contained in the hard function H_Q^I. The term J_τ is the thrust jet function. The term S_τ^{part} is the partonic soft function and the $\delta(R,\mu_S)$-dependent exponential implements the perturbative renormalon subtractions. There are four renormalization scales governing the factorization formula, the hard scale $\mu_H \sim Q$, the jet scale μ_J, the soft scale μ_S, and the renormalon subtraction scale R. We have $R \sim \mu_S$ to properly sum logarithms related to the renormalon subtractions, and there is also a renormalization group evolution in R. The typical values for μ_J, μ_S, and R depend on τ as discussed in Sec. 2.3.

The total tree level partonic e^+e^- cross section $\sigma_0^I = \sigma_0^I(Q, m_Z, \Gamma_Z)$ depends on the c.m. energy Q, the Z-mass, and Z-width, and has six types of components, σ_0^{uv}, σ_0^{ua}, σ_0^{dv}, σ_0^{da}, σ_0^{bv}, σ_0^{ba}, where the first index denotes flavor, u = up + charm, d = down+strange, and b = bottom, and the other index denotes production through

the vector (v) and axial-vector (a) currents. For QCD corrections we have the hard functions $H_Q^v \equiv H_Q^{uv} = H_Q^{dv} = H_Q^{bv}$, H_Q^{ua}, H_Q^{da}, and H_Q^{ba}, where the vector current terms do not depend on the flavor of the quark. For massless quark production the axial-vector hard functions differ from the vector due to flavor singlet contributions. All six σ_0^I's and H_Q^I's are relevant for the implementation of the b-mass and QED corrections. Since we use data taken for energies close to the Z pole we adopt $i/(q^2 - m_Z^2 + i\,Q^2\Gamma_z/m_Z)$ as the Z-boson propagator which is the form of the width term used for thrust data analyses. The modifications of Eq. (2.8) required to include QED effects are discussed in Sec. 2.2.8. The hard factor H_Q contains the hard QCD effects that arise from the matching of the two-jet current in SCET to full QCD. For $\mu_H = Q$ we have $H_Q^v(Q,Q) = 1 + \sum_{j=1}^3 h_j[\alpha_s(Q)/4\pi]^j$, and the full hard function with $\ln(\mu_H/Q)$ dependence is given in Eq. (A.8). For the flavor nonsinglet contributions where the final-state quarks are directly produced by the current one can obtain the matching coefficient from the on-shell quark vector current form factor, which is known to $\mathcal{O}(\alpha_s^3)$ [120, 119, 83, 122, 113, 18]. Converting the bare result in Ref. [113] (see also Refs. [18, 90]) to the $\overline{\rm MS}$ scheme and subtracting $1/\epsilon_{\rm IR}^k$ divergences present in SCET graphs, the three-loop non-singlet constant, which is one of the new ingredients in our analysis, is

$$
\begin{aligned}
h_3 &= C_F^3\bigg[-460\zeta(3) - \frac{140\pi^2\zeta(3)}{3} + 32\zeta(3)^2 + 1328\zeta(5) - \frac{5599}{6} + \frac{4339\pi^2}{36} - \frac{346\pi^4}{15} \\
&\quad + \frac{27403\pi^6}{17010}\bigg] + C_A C_F^2\bigg[-\frac{52564\zeta(3)}{27} + \frac{1690\pi^2\zeta(3)}{9} + \frac{592\zeta(3)^2}{3} - \frac{5512\zeta(5)}{9} + \frac{824281}{324} \\
&\quad - \frac{406507\pi^2}{972} + \frac{92237\pi^4}{2430} - \frac{1478\pi^6}{1701}\bigg] + C_A^2 C_F\bigg[\frac{505087\zeta(3)}{243} - \frac{1168\pi^2\zeta(3)}{9} - \frac{2272\zeta(3)^2}{9} \\
&\quad - \frac{868\zeta(5)}{9} - \frac{51082685}{26244} + \frac{596513\pi^2}{2187} - \frac{4303\pi^4}{4860} + \frac{4784\pi^6}{25515}\bigg] + C_F^2 n_f\bigg[\frac{26080\zeta(3)}{81} - \frac{148\pi^2\zeta(3)}{9} \\
&\quad - \frac{832\zeta(5)}{9} - \frac{56963}{486} + \frac{13705\pi^2}{243} - \frac{1463\pi^4}{243}\bigg] + C_A C_F n_f\bigg[-\frac{8576\zeta(3)}{27} + \frac{148\pi^2\zeta(3)}{9} - \frac{8\zeta(5)}{3} \\
&\quad + \frac{3400342}{6561} - \frac{201749\pi^2}{2187} - \frac{35\pi^4}{243}\bigg] + C_F n_f^2\bigg[-\frac{832\zeta(3)}{243} - \frac{190931}{6561} + \frac{1612\pi^2}{243} + \frac{86\pi^4}{1215}\bigg] \\
&= 20060.0840 - 2473.4051 n_f + 52.2009 n_f^2 \,. \qquad (2.9)
\end{aligned}
$$

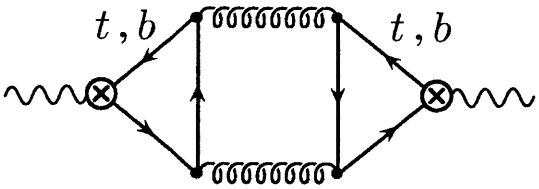

Figure 2-1: Two-loop singlet correction to the axial current. Its cuts contribute to the hard coefficient and nonsingular terms.

For $n_f = 5$ we have $h_3 = 8998.080$, which is the value used for our analysis.[4]

The axial-vector hard functions H_Q^{ua} and H_Q^{da} are equal to H_Q^v up to additional singlet corrections that enter at $\mathcal{O}(\alpha_s^2)$ and $\mathcal{O}(\alpha_s^3)$. The fact that the SCET hard functions have these singlet corrections was discussed in Ref. [138]. At $\mathcal{O}(\alpha_s^2)$ only the axial-vector current gets a singlet correction. It arises from the axial-vector anomaly, from suitable cuts of the graph shown in Fig. 2-1 where each axial current is connected to a triangle. Summing over the light quarks u, d, s, c gives a vanishing contribution from this graph, but it does not vanish for heavy quarks due to the large bottom-top mass splitting [104]. Since for the Qs we consider top-pairs are never produced, the required terms can be obtained in the limit $m_b/m_t \to 0$. For the axial current the hard correction arises from the $b\bar{b}$ cut and gives $H_Q^{ua} = H_Q^{da} = H_Q^v$, and $H_Q^{ba} = H_Q^v + H_Q^{\text{singlet}}$, where

$$H_Q^{\text{singlet}}(Q, r_t, \mu_H) = \frac{1}{3}\left(\frac{\alpha_s(\mu_H)}{\pi}\right)^2 I_2(r_t)\,. \tag{2.10}$$

Here $r_t = Q^2/(4m_t^2)$ and the function $I_2(r_t)$ from Ref. [104] is given in Eq. (A.9). Throughout our analysis we use $m_t = 172\,\text{GeV}$. H_Q^{singlet} is a percent level correction to the cross section at the Z peak and hence is non-negligible at the level of precision of our analysis. (The uncertainty in the top mass is numerically irrelevant.) At $\mathcal{O}(\alpha_s^3)$ the singlet corrections for vector currents are known [18], but they are numerically tiny. We therefore neglect the $\mathcal{O}(\alpha_s^3)$ vector current singlet corrections together with the unknown $\mathcal{O}(\alpha_s^3)$ singlet corrections for the axial-vector current. Likewise we do not account for $\mathcal{O}(\alpha_s^3)$ singlet corrections to the nonsingular distributions discussed

[4]The analytic expression for h_3 in Eq. (2.9) is consistent with Eq. (7.3) given in Ref. [82].

in Sec. 2.2.5.

The full anomalous dimension of H_Q^I is known at three-loops, $\mathcal{O}(\alpha_s^3)$ [140, 119, 122]. It contains the cusp anomalous dimension, responsible for the resummation of the Sudakov double logarithms, and the non-cusp anomalous dimension. To determine the corresponding hard renormalization group factor U_H at the orders N^{3}LL$'$ and N^{3}LL we need the $\mathcal{O}(\alpha_s^4)$ cusp anomalous dimension $\Gamma_3^{\rm cusp}$ which is still unknown and thus represents a source of theory error in our analysis. We estimate the size of $\Gamma_3^{\rm cusp}$ from the order [1/1] Padé approximant in α_s built from the known lower order coefficients, which is within 13% of the two other possible Padé approximants, [0/2] and [0/1]. For our theory error analysis we assign 200% uncertainty to this estimate and hence scan over values in the range $\Gamma_3^{\rm cusp} = 1553.06 \pm 3016.12$.

The thrust jet function J_τ is the convolution of the two hemisphere jet functions that describe collinear radiation in the $\hat{\rm t}$ and $-\hat{\rm t}$ directions,

$$J_\tau(s,\mu) = \int {\rm d}s'\, J(s',\mu)\, J(s-s',\mu) = \frac{1}{\mu^2} \sum_{n=-1}^{\infty} J_n[\alpha_s(\mu)] \mathcal{L}_n(s/\mu^2)\,. \tag{2.11}$$

Here the coefficients J_n are multiplied by the functions

$$\mathcal{L}_{-1}(x) = \delta(x)\,, \qquad\qquad \mathcal{L}_n(x) = \Big[\frac{\ln^n x}{x}\Big]_+\,, \tag{2.12}$$

where $n \geq 0$. Here $\mathcal{L}_{n\geq 0}(x)$ are the standard plus-functions, see Eq. (A.22). At $\mathcal{O}(\alpha_s^3)$ only $J_{-1}(\alpha_s)$ through $J_5(\alpha_s)$ are nonzero. The results are summarized in Eq. (A.21). In SCET the inclusive jet function is defined as

$$J(Qr^+,\mu) = \frac{-1}{4\pi N_c Q}\, {\rm Im}\Big[i \int d^4x\, e^{ir\cdot x}\, \langle 0|{\rm T}\{\bar\chi_n(0) \frac{\bar{n}\!\!\!/}{2} \chi_n(x)\}|0\rangle \Big], \tag{2.13}$$

where the χ_n are quark fields multiplied by collinear Wilson lines. The hemisphere jet function has been computed at $\mathcal{O}(\alpha_s)$ [117, 25] and $\mathcal{O}(\alpha_s^2)$ [29]. Its anomalous dimension is known at three loops, and can be obtained from Ref. [121]. At the order N^{3}LL$'$ we need the $\mathcal{O}(\alpha_s^3)$ corrections to the jet function. From the anomalous dimension we know the logarithmic terms, J_0 to J_{-5} in Eq. (2.11), at three loops.

In the non-logarithmic term J_{-1} at $\mathcal{O}(\alpha_s^3)$ there is an unknown coefficient j_3 (which we define as the constant non-logarithmic 3-loop coefficient in the position space hemisphere jet function). We estimate a range for j_3 from the largest value obtained from the three Padé approximations for the position space hemisphere jet function that one can construct from the available results. This gives $j_3 = 0 \pm 3000$ for the range of variation in our theory error analysis. We note that for the $\mathcal{O}(\alpha_s^3)$ coefficient h_3 the corresponding Padé estimate $h_3 = 0 \pm 10000$ covers the exact value given in Eq. (2.9).

The renormalization group factors of the thrust jet function U_J^τ and thrust soft function U_S^τ sum up large logs involving the jet and the soft scales. The required cusp and non-cusp anomalous dimensions are fully known at three-loops, but again there is dependence on the four-loop cusp anomalous dimension $\Gamma_3^{\rm cusp}$. This dependence is included when we scan this parameter as described above in our description of the hard evolution.

The hadronic thrust soft function S_τ describes soft radiation between the two jets. It is defined by

$$S_\tau(k,\mu) = \frac{1}{N_c}\langle 0|\mathrm{tr}\,\overline{Y}_{\bar n}^T Y_n\,\delta(k - i\widehat{\partial}) Y_n^\dagger \overline{Y}_{\bar n}^*|0\rangle\,, \tag{2.14}$$

where $Y_n = Y_n(0)$ and $\overline{Y}_{\bar n} = \overline{Y}_{\bar n}(0)$ are defined below Eq. (2.3). The soft function factorizes into a partonic perturbative part $S_\tau^{\rm part}$ and a nonperturbative part $S_\tau^{\rm mod}$, $S_\tau = S_\tau^{\rm part} \otimes S_\tau^{\rm mod}$, as discussed in detail in Sec. 2.2.4. This factorization has already been used above in Eqs. (2.1) and (2.8).

At the partonic level the soft function is

$$S_\tau^{\rm part}(k,\mu) = \frac{1}{\mu}\sum_{n=-1}^{\infty} S_n[\alpha_s(\mu)]\mathcal{L}_n(k/\mu)\,, \tag{2.15}$$

where S_{-1} to S_5 are the only nonzero coefficients at $\mathcal{O}(\alpha_s^3)$, and $\mathcal{L}_n(x)$ is defined in Eq. (2.12). Results for these $S_k(\alpha_s)$ are summarized in Eq. (A.16). $S_\tau^{\rm pert}$ was calculated at $\mathcal{O}(\alpha_s)$ in Ref. [136, 79]. At $\mathcal{O}(\alpha_s^2)$ the non-logarithmic correction was

determined in Refs. [31, 94] using numerical output from EVENT2 [49, 50]. The numerical constant that appears in the non-logarithmic $\mathcal{O}(\alpha_s^2)$ term S_{-1} is referred to as s_2 (which is defined as the constant 2-loop coefficient in the logarithm of the position space soft function). We use $s_2 = -39.1 \pm 2.5$ [94], and this uncertainty is taken into account in our theory error analysis.[5] The anomalous dimension of the soft function is a linear combination of the anomalous dimensions of the hard and jet functions which can be obtained from the consistency conditions [80, 31]. As for the jet function we need the $\mathcal{O}(\alpha_s^3)$ corrections to S_τ^{part}. From its anomalous dimension we know the logarithmic terms at three loops, namely S_0 to S_5 in Eq. (2.15). The only unknown is the $\mathcal{O}(\alpha_s^3)$ non-logarithmic correction in S_{-1}, referred to as s_3 (which is defined as the constant non-logarithmic term in the logarithm of the position space hemisphere soft function). Just like for the constant j_3 we estimate a value for s_3 from the largest value obtained from the three possible Padé approximations to the position space soft function that one can construct from the available results. This yields the range $s_3 = 0 \pm 500$, which we scan over in our theory error analysis.

As already mentioned, in Ref. [31] an analytic expression for the resummed singular thrust distribution was presented. Their derivation relies on the Laplace transform of the jet and soft functions. In our analysis we have derived the resummed cross section using two independent procedures, performing all convolutions either in momentum space (as presented in App. A), or in Fourier space. These two approaches have been implemented in two independent codes and we have checked that they give exactly the same results. We note that the Fourier transform method is equivalent to the Laplace procedure used by Becher and Schwartz in Ref. [31] through a contour deformation, and we find agreement with their quoted N^{3}LL formula including matrix elements and anomalous dimensions. Furthermore, we also agree with their result for the fixed-order singular terms up to $\mathcal{O}(\alpha_s^3)$.

In summary, the singular terms in the thrust factorization theorem are known at N^{3}LL order, up to the unknown constant Γ_3^{cusp}. The effect of the cusp anomalous dimension at 4-loops is much smaller than one might estimate, so for numerical pur-

[5]Note that in Ref. [94] our s_2 was called s_1.

poses the cross section is known at this order. The constants s_3 and j_3 only enter for our N^{3}LL$'$ order. For the singular terms they predominantly affect the peak region with spread into the tail region only due to RG evolution. Thus in the tail region the numerically dominant N^{3}LL$'$ terms are all known. The uncertainties from $\Gamma_3^{\rm cusp}$, s_3, and j_3 are discussed more explicitly in Sec. 3.2

2.2.4 Ω_1 and Nonperturbative Corrections

In this section we discuss nonperturbative corrections to the thrust distribution included in our analysis, as shown in Tab. 2.2. We focus in particular on those associated to the first moment parameter Ω_1. Our analysis includes the operator product expansion (OPE) for the soft function in the tail region, and combining perturbative and nonperturbative information to smoothly connect the peak and tail analyses. We also discuss our treatment of nonperturbative corrections in the far-tail region, and for the nonsingular terms in the cross section.

In the tail region where $k \sim Q\tau \gg \Lambda_{\rm QCD}$ we can perform an operator product expansion of the soft function in Eq. (2.14). At tree level this gives [110, 111]

$$S_\tau(k,\mu) = \delta(k) - \delta'(k)\, 2\bar\Omega_1 + \dots\,. \tag{2.16}$$

where the nonperturbative matrix element $\bar\Omega_1$ is defined in the $\overline{\rm MS}$ scheme as

$$\bar\Omega_1 = \frac{1}{2N_c}\langle 0|{\rm tr}\, \overline{Y}^T_{\bar n}(0) Y_n(0)\, i\widehat\partial\, Y_n^\dagger(0)\overline{Y}^*_{\bar n}(0)|0\rangle\,. \tag{2.17}$$

Dimensional analysis indicates that $\bar\Omega_1 \sim \Lambda_{\rm QCD}$. When the OPE is performed beyond tree level we must add perturbative corrections at a scale $\mu \simeq k$ to Eq. (2.16). The first operator in the OPE is the identity, and its Wilson coefficient is the partonic soft function. Thus $\delta(k) \to S_\tau^{\rm part}(k,\mu)$ when the matching of the leading power operator is performed at any fixed order in perturbation theory. Here we derive the analog for

the Wilson coefficient of the $\bar{\Omega}_1$ matrix element and prove that

$$S_\tau(k,\mu) = S_\tau^{\rm part}(k) - \frac{{\rm d}S_\tau^{\rm part}(k)}{{\rm d}k}\, 2\bar{\Omega}_1 + \dots\,. \tag{2.18}$$

This result implies that the leading perturbative corrections that multiply the power correction are determined by the partonic soft function to all orders in perturbation theory. The proof of Eq. (2.18) is given in App. A.1. The uniqueness of the leading power correction $\bar{\Omega}_1$ to all orders in the perturbative matching can be derived following Ref. [110], and we carry out an all orders matching computation to demonstrate that the Wilson coefficient is ${\rm d}S_\tau^{\rm part}(k)/{\rm d}k$. At first order in $\bar{\Omega}_1/k \ll 1$ Eq. (2.18) shows that the perturbative corrections in the OPE are consistent with a simple shift to $S_\tau(k-2\bar{\Omega}_1,\mu)$. This type of shift was first observed in the effective coupling model [73].

To smoothly connect the peak and tail regions we use a factorized soft function [95, 106, 116]

$$S_\tau(k,\mu) = \int\!{\rm d}k'\; S_\tau^{\rm part}(k-k',\mu)\; S_\tau^{\rm mod}(k')\,, \tag{2.19}$$

where $S_\tau^{\rm part}$ is a fixed-order perturbative $\overline{\rm MS}$ expression for the partonic soft function, and $S_\tau^{\rm mod}$ contains the nonperturbative ingredients. In the tail region this expression can be expanded for $k' \ll k$ and reduces to precisely the OPE in Eq. (2.18) with the identification

$$2\bar{\Omega}_1 = \int {\rm d}k'\; k'\, S_\tau^{\rm mod}(k')\,, \tag{2.20}$$

and normalization condition $\int {\rm d}k'\, S_\tau^{\rm mod}(k') = 1$ [95]. All moments of $S_\tau^{\rm mod}(k')$ exist so it has an exponential tail, whereas the tail for $S_\tau^{\rm part}(k)$ is a power law. In the peak region the full nonperturbative function $S_\tau^{\rm mod}(k)$ becomes relevant, and Eq. (2.19) provides a nonperturbative function whose μ dependence satisfies the $\overline{\rm MS}$ renormalization group equation for the soft function. In position space the convolution in Eq. (2.19) is a simple product, making it obvious that Eq. (2.19) provides a completely general parametrization of the nonperturbative corrections. The complete

basis of functions used to parameterize $S_\tau^{\rm mod}(k)$ in the peak region is discussed in Sec. 2.4.

The expression in Eq. (2.19) also encodes higher order power corrections of type 1 from Eq. (2.6) through the moments $2^i\,\bar\Omega_i = \int \mathrm{d}k\; k^i\, S_\tau^{\rm mod}(k)$, which for tree level matching in the OPE can be identified as the matrix elements $\langle 0|\mathrm{tr}\,\overline{Y}_{\bar n}^T(0) Y_n(0)\,(i\widehat{\partial})^i\, Y_n^\dagger(0)\overline{Y}_{\bar n}^*(0)|0\rangle/N_c$. For $i \geq 2$ perturbative α_s corrections to the soft function OPE would have to be treated in a manner similar to App. A.1 to determine the proper Wilson coefficients, and whether additional operators beyond the powers $(i\widehat{\partial})^i$ start contributing. The treatment of perturbative corrections to these higher order nonperturbative corrections is beyond the level required for our analysis.

Using Eq. (2.19) the hadronic version of the singular factorization theorem which involves S_τ immediately yields Eq. (2.8) and the first term in Eq. (2.1). The conversion of $S_\tau^{\rm part}(k)$ and $\bar\Omega_1$ from $\overline{\rm MS}$ to a renormalon-free scheme is discussed in Sec. 2.2.6.

Next we turn to the effect of $\Lambda_{\rm QCD}$ power corrections on the nonsingular terms in the cross section in Eq. (2.1). The form of these power corrections can be constrained by factorization theorems for subleading power corrections when $\tau \ll 1$, and by carrying out an OPE analysis for power corrections to the moments of the thrust distribution. In the following we consider both of these.

Based on the similarity of the analysis of power corrections to thrust with those in $B \to X_s\gamma$ [112, 132], the factorization theorems for the nonsingular corrections involves subleading hard functions, jet functions and soft functions. They have the generic structure $H_Q^{(a,b)}(Q,\tau,x_i) \otimes J_\tau^{(a)}(s_j,x_i) \otimes S_\tau^{(b)}(Q\tau, s_j/Q)$, where the x_i and s_j are various convolution variables. Here $S_\tau^{(b)}$ includes the leading order soft function in Eq. (2.14) as well as power suppressed soft functions. Neglecting nonperturbative corrections the nonsingular cross section yields terms we refer to as kinematic power corrections of type 2 in Eq. (2.6). If we do not wish to sum large logs in the nonsingular partonic terms, they can be treated in fixed-order perturbation theory and determined from the full fixed-order computations. In the tail region these τ-suppressed terms grow and become much more important than the $\Lambda_{\rm QCD}/Q$ power

corrections of type 3 from subleading soft functions. In the transition to the far-tail region, near $\tau = 1/3$, they become just as important as the leading perturbative singular terms. In this region there are large cancellations between the singular and nonsingular terms (shown below in Fig. 2-4), and one must be careful with the treatment of the nonsingular terms not to spoil this.

We require the nonsingular cross section terms to yield perturbative corrections at leading power in $\Lambda_{\rm QCD}$ that are consistent with the fixed-order results and with multijet thresholds. Our treatment of power corrections in the nonsingular terms is done in a manner consistent with these goals and with the OPE for the first moment of the thrust distribution. To achieve this we use

$$\int \mathrm{d}k' \, \frac{\mathrm{d}\hat{\sigma}_{\rm ns}}{\mathrm{d}\tau}\Big(\tau - \frac{k'}{Q}, \frac{\mu_{\rm ns}}{Q}\Big) S_\tau^{\rm mod}(k'), \tag{2.21}$$

where $\mathrm{d}\hat{\sigma}_{\rm ns}/\mathrm{d}\tau$ is the partonic nonsingular cross section in fixed-order perturbation theory, whose determination we discuss in Sec. 2.2.5. Eq. (2.21) is independent of the renormalization scale $\mu_{\rm ns}$ order by order in its series expansion in $\alpha_s(\mu_{\rm ns})$. The convolution with the same $S_\tau^{\rm mod}(k')$ as the singular terms allows the perturbative corrections in $\mathrm{d}\hat{\sigma}_s/\mathrm{d}\tau + \mathrm{d}\hat{\sigma}_{\rm ns}/\mathrm{d}\tau$ to smoothly recombine into the fixed-order result in the far-tail region as required by the multijet thresholds. Eq. (2.21) yields the second term in Eq. (2.1). We will treat the conversion of $\bar{\Omega}_1$ and $S_\tau^{\rm mod}$ to a renormalon-free scheme in the same manner as for the singular cross section, which again for consistency requires a perturbative subtraction for the partonic $\mathrm{d}\hat{\sigma}_{\rm ns}/\mathrm{d}\tau$ that we treat in Sec. 2.2.6.

Note that Eq. (2.21) neglects the fact that not all of the τ dependence in $\mathrm{d}\hat{\sigma}_{\rm ns}/\mathrm{d}\tau$ must necessarily be convoluted with $S_\tau^{\rm mod}$. This causes a deviation which is $\sim \alpha_s \tau \Lambda_{\rm QCD}/(Q\tau)$ and hence is at the same level as other power corrections that we neglect. The largest uncertainty from our treatment of $\mathrm{d}\hat{\sigma}_{\rm ns}/\mathrm{d}\tau$ arises from the fact that we do not sum $\ln\tau$ terms, which would require anomalous dimensions for the subleading soft and hard functions for these nonsingular terms. These logs are most important in the peak region, and less relevant in the tail region. The size of miss-

ing higher order nonsingular terms such as log enhanced terms will be estimated by varying the scale $\mu_{\rm ns}$.

Our setup is also consistent with the OPE for the first moment of the thrust distribution. Eq. (2.1) yields

$$\int \mathrm{d}\tau\, \tau \frac{\mathrm{d}\sigma}{\mathrm{d}\tau} = \int \mathrm{d}\tau\, \tau \Big[\frac{\mathrm{d}\hat{\sigma}_s}{\mathrm{d}\hat{\tau}} + \frac{\mathrm{d}\hat{\sigma}_{\rm ns}}{\mathrm{d}\hat{\tau}}\Big] + \sum_I \sigma_0^I \, \frac{2\bar{\Omega}_1}{Q} + \dots \,, \tag{2.22}$$

where the ellipses denote $\mathcal{O}(\alpha_s \Lambda_{\rm QCD}/Q)$ and $\mathcal{O}(\Lambda_{\rm QCD}^2/Q^2)$ power corrections. In App. A.1.1 we demonstrate that a direct OPE computation for the thrust moment also gives the same result, and in particular involves precisely the same matrix element $\bar{\Omega}_1$ at this order. The theoretical expression in Eq. (2.1) simultaneously includes the proper matrix elements that encode power corrections in the peak region, tail region, and for moments of the thrust distribution. This implies a similar level of precision for the multijet region. Although Eq. (2.1) does not encode all $\alpha_s \Lambda_{\rm QCD}/Q$ corrections, it turns out that the ones it does encode, involving Ω_1, numerically give an accurate description of the multijet cross section. (This is visible in Fig. 3-9 and will be discussed further in Sec. 3.2.) This agreement provides additional support for our treatment of nonperturbative corrections in the nonsingular cross section in Eq. (2.21).

2.2.5 Nonsingular Distribution

The nonsingular partonic thrust distribution $\mathrm{d}\hat{\sigma}_{\rm ns}/\mathrm{d}\tau$ accounts for contributions in the thrust distribution that are kinematically power suppressed. We write

$$\frac{\mathrm{d}\hat{\sigma}_{\rm ns}}{\mathrm{d}\tau}(\tau) = \sum_I \sigma_0^I \, e^{-2\frac{\delta(R,\mu_S)}{Q}\frac{\partial}{\partial\tau}} f^I\Big(\tau, \frac{\mu_{\rm ns}}{Q}\Big) \,, \tag{2.23}$$

with the same superscript I notation for different currents as in Eq. (2.8). The presence of the $\delta(R,\mu_S)$-dependent exponent arises because $S_\tau^{\rm mod}$ depends on Ω_1 and we use the same renormalon-free definition for Ω_1 as for the singular terms. In our numerical evaluation we integrate by parts so that the $\partial/\partial\tau$ derivative acts on $S_\tau^{\rm mod}$

in Eq. (2.1). This exponent is discussed in detail in Sec. 2.2.6.

In this section we discuss our determination of the functions f^I in pure QCD with massless quarks, while the generalization to include m_b effects is discussed in Sec. 2.2.7 and to include QED effects in Sec. 2.2.8. For pure QCD there is one function $f^v_{\rm qcd} = f^{uv}_{\rm qcd} = f^{dv}_{\rm qcd} = f^{bv}_{\rm qcd}$ for the vector current, and functions $f^{ua}_{\rm qcd} = f^{da}_{\rm qcd}$, and $f^{ba}_{\rm qcd}$ for the axial-vector currents. In general f^I is the partonic fixed-order distribution where the singular terms which are already contained in $\mathrm{d}\hat{\sigma}_{\rm s}/\mathrm{d}\tau$ are subtracted to avoid double counting. Setting the renormalization scale $\mu_{ns} = Q$ they have the form

$$\begin{aligned}
f^v_{\rm qcd}(\tau,1) &= \frac{\alpha_s}{2\pi}\, f_1(\tau) + \frac{\alpha_s^2}{(2\pi)^2}\, f_2(\tau) + \frac{\alpha_s^3}{(2\pi)^3}\, f_3(\tau) + \ldots\,, \\
f^{ua}_{\rm qcd}(\tau,1) &= f^{da}_{\rm qcd}(\tau,1) = f^v_{\rm qcd}(\tau,1)\,, \\
f^{ba}_{\rm qcd}(\tau,1) &= f^v_{\rm qcd}(\tau,1) + \frac{\alpha_s^2}{(2\pi)^2} f_{\rm singlet}(\tau,r_t)\,,
\end{aligned} \tag{2.24}$$

where here $\alpha_s = \alpha_s(Q)$ and $r_t = Q^2/(4m_t^2)$. The required results for $f^I(\tau,\mu_{\rm ns}/Q)$ can be obtained by shifting $\alpha_s(Q)$ to $\alpha_s(\mu_{\rm ns})$ using the fixed-order relation between these couplings at $\mathcal{O}(\alpha_s^2)$.

The full $\mathcal{O}(\alpha_s)$ partonic thrust distribution has been known analytically for a long time [76]. For the one-loop nonsingular distribution it gives

$$\begin{aligned}
f_1(\tau) =& \frac{4}{3\tau(\tau-1)}\Bigg[\left(-6\tau^2+6\tau-4\right)\log\left(\frac{1}{\tau}-2\right) \\
&+ 9\tau^3 - 3\tau^2 - 9\tau + 3\Bigg]\theta\left(\frac{1}{3}-\tau\right) + \frac{4}{3\tau}\left[3+4\log(\tau)\right].
\end{aligned} \tag{2.25}$$

This result is plotted in Fig. 2-2(a). The kink at $\tau = 1/3$ appears because the full one-loop distribution vanishes at this value with a nonzero slope, and there is an exact cancellation between the fixed-order singular and nonsingular one-loop expressions. For $\tau > 1/3$ the one-loop nonsingular distribution is precisely the negative of the one-loop fixed-order singular distribution.

The $\mathcal{O}(\alpha_s^2)$ and $\mathcal{O}(\alpha_s^3)$ QCD distributions are available in numeric form from the Fortran programs EVENT2 [49, 50] and EERAD3 [86] (see also Ref. [85, 143,

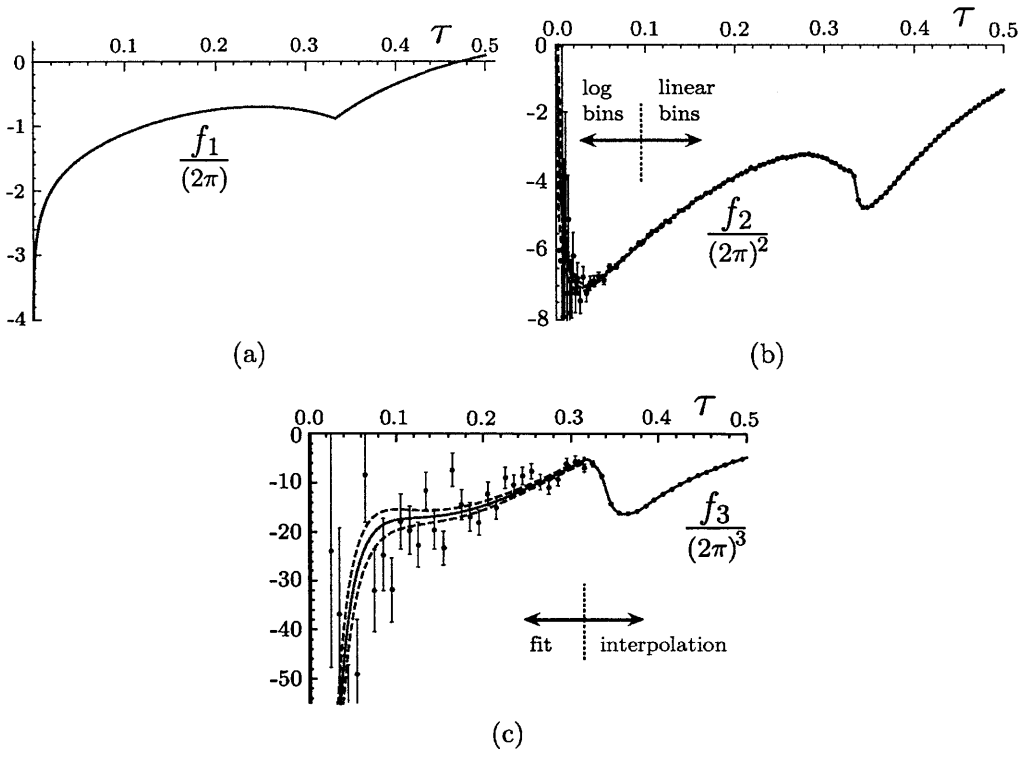

Figure 2-2: Nonsingular Thrust Distribution. (a) $\mathcal{O}(\alpha_s)$ nonsingular thrust distribution. (b) $\mathcal{O}(\alpha_s^2)$ nonsingular thrust distribution. (c) $\mathcal{O}(\alpha_s^3)$ nonsingular thrust distribution. For simplicity we only show the data binned with 0.01 bin size.

144]), respectively. These programs are used to derive results for our $f_2(\tau)$ and $f_3(\tau)$ nonsingular distributions in a manner discussed below. At $\mathcal{O}(\alpha_s^2)$ there is also the singlet correction $f_{\text{singlet}}(\tau, r)$ for the axial-vector contribution arising from the large bottom-top mass splitting. The three-parton quark-antiquark-gluon cut from Fig. 2-1 contributes to the nonsingular distribution, and we have included this contribution analytically [89]. The formula for $f_{\text{singlet}}(\tau, r)$ is given in Eq. (A.46). There is also a contribution from the four-parton cut. Its contribution to $f_{\text{singlet}}(\tau, r)$ is unknown, but it is tiny for the total cross section [104] and can therefore be safely neglected.

At $\mathcal{O}(\alpha_s^2)$ we use linear binned EVENT2 results for $\tau > 0.095$ and log-binning results for $\tau < 0.095$ each obtained from runs with 10^{10} events and infrared cutoff $y_0 = 10^{-8}$. For $\tau > 0.095$ (using a 0.005 bin size) the resulting statistical uncertainties in the nonsingular distribution are always below the percent level and neg-

ligible and we can use an interpolation of numerical tables for $f_2(\tau)$. For $\tau < 0.095$ the singular terms dominate the distribution which leads to large cancellations and an enhancement of the statistical uncertainties. Here we use the ansatz $f_2(\tau) = \sum_{i=0}^{3} a_i \ln^i \tau + \tau \sum_{i=2}^{3} b_i \ln^i \tau$ and fit the coefficients a_i and b_i to the EVENT2 output, including the constraint that the integral over the full distribution reproduces the known $\mathcal{O}(\alpha_s^2)$ coefficient for the total cross section. The result has the form $f_2(\tau) + \epsilon_2 \delta_2(\tau)$, where f_2 represents the best fit and δ_2 is the 1-sigma error function with all correlations included. The term ϵ_2 is a parameter which we vary during our α_s-Ω_1 fit procedure to account for the error. Here f_2 and δ_2 also depend on the coefficient s_2 in the partonic soft function S_τ which is known only numerically. In Fig. 2-2(b) we plot the EVENT2 data we used, along with our $f_2(\tau)$ with $s_2 = -39.1$. The dashed curves show the result for $\epsilon_2 = \pm 1$, with the region inbetween corresponding to the 1-sigma error band.

For the determination of f_3 at $\mathcal{O}(\alpha_s^3)$ we implement a similar approach as for f_2, using results from EERAD3 [86] computed with 6×10^7 events for the three leading color structures and 10^7 events for the three subleading ones, using an infrared cutoff $y_0 = 10^{-5}$. We employ linearly binned results with 0.01 bin size for $\tau > 0.315$ (keeping the statistical error below the percent level) and with 0.005 bin size for $\tau < 0.315$. For the fit for $\tau < 0.315$ our ansatz function has the form $f_3(\tau) = \sum_{i=1}^{5} c_i \ln^i \tau$ and the result has the form $f_3(\tau) + \epsilon_3 \delta_3(\tau)$, with f_3 being the best fit and δ_3 the 1-sigma error function. The constant ϵ_3 is the analog of ϵ_2 and is varied in the error analysis. We note that f_3 and δ_3 depend on the constant s_2 and on the constants s_3 and j_3 that account for the unknown non-logarithmic terms in the $\mathcal{O}(\alpha_s^3)$ soft and jet functions. This dependence is included in our error analysis. In Fig. 2-2(c) we plot the EERAD3 data with bin size 0.01, along with our $f_3(\tau)$ with $s_2 = -39.1$, $h_3 = 8998.08$, $j_3 = s_3 = 0$. The dashed curves show the result for $\epsilon_3 = \pm 1$, with the region inbetween corresponding to the 1-sigma error band.

In our analysis we use the values $-1, 0, 1$ for ϵ_2 and ϵ_3 to account for the numerical uncertainties of our fit functions in the small τ region. The nonsingular partonic distribution depends on one common renormalization scale $\mu_{\rm ns}$ which is varied in our

theory error analysis as given in Sec. 2.3.

2.2.6 Gap Formalism

The partonic soft function $S_\tau^{\rm part}(k)$ computed perturbatively in $\overline{\rm MS}$ has an $\mathcal{O}(\Lambda_{\rm QCD})$ renormalon ambiguity. The same renormalon is present in the partonic $\overline{\rm MS}$ thrust cross section with or without resummation. This is associated with the fact that the partonic threshold at $k = 0$ in $S_\tau^{\rm part}(k)$ is not the same as the physical hadronic threshold for the distribution of soft radiation that occurs in $S_\tau(k)$. One can see this explicitly in the large-β_0 approximation, where it is associated to a pole at $u = 1/2$ in the Borel transform [95]

$$B\Big[S_\tau^{\rm part}(k,\mu)\Big]\Big(u \approx \frac{1}{2}\Big) = \mu \frac{16 C_F e^{-5/6}}{\pi\beta_0\,(u-\frac{1}{2})}\,\frac{\partial}{\partial k} S_\tau^{\rm part}(k,\mu)\,. \tag{2.26}$$

This result shows that $S_\tau^{\rm part}(k)$ in the $\overline{\rm MS}$ scheme suffers from the renormalon ambiguity for all $k \geq 0$. The $\overline{\rm MS}$ matrix element $\bar\Omega_1$ defined in Eq. (2.17) also has an $\mathcal{O}(\Lambda_{\rm QCD})$ renormalon ambiguity. Together, the renormalon in this power correction and in the perturbative series for $S_\tau^{\rm part}(k)$ combine to give a soft function $S_\tau(k)$ that is free from this $\mathcal{O}(\Lambda_{\rm QCD})$ renormalon. If left unsubtracted this renormalon ambiguity leads to numerical instabilities in perturbative results for the thrust distribution and in the large order dependence for the determination of the soft nonperturbative function $S_\tau^{\rm mod}$. In this section we resolve this problem by switching to a new scheme for Ω_1. This scheme change induces subtractions on $\mathrm{d}\sigma^{\rm part}/\mathrm{d}\tau$ that render it free of this renormalon. We start by reviewing results from Ref. [95].

Consider a class of soft nonperturbative functions with a gap parameter Δ, which only have support for $k \geq \Delta$, so $S_\tau^{\rm mod}(k) \to S_\tau^{\rm mod}(k - 2\Delta)$. Here the $\overline{\rm MS}$ moment relation in Eq. (2.20) becomes

$$2\Delta + \int \mathrm{d}k\, k\, S_\tau^{\rm mod}(k) = 2\bar\Omega_1\,, \tag{2.27}$$

where Δ accounts for the complete renormalon ambiguity contained in $\bar\Omega_1$. We can

now obtain a renormalon-free definition for Ω_1 by splitting Δ into a nonperturbative component $\bar{\Delta}(R,\mu_S)$ that is free of the $\mathcal{O}(\Lambda_{\rm QCD})$ renormalon, and a suitably defined perturbative series $\delta(R,\mu_S)$ that has the same renormalon ambiguity as $\bar{\Omega}_1$. The parameter Δ is scheme and renormalization group invariant, while $\bar{\Delta}$ and δ individually depend on the subtraction scale R and in general also on the soft scale μ_S. Writing

$$\Delta = \bar{\Delta}(R,\mu_S) + \delta(R,\mu_S)\,, \tag{2.28}$$

the factorization of perturbative and nonperturbative components in Eq. (2.19) becomes

$$\begin{aligned} S_\tau(k,\mu_S) &= \int \mathrm{d}k'\; S_\tau^{\rm part}(k-k'-2\delta,\mu_S)\; S_\tau^{\rm mod}(k'-2\bar{\Delta}) \\ &= \int \mathrm{d}k' \left[e^{-2\delta\frac{\partial}{\partial k}} S_\tau^{\rm part}(k-k',\mu_S)\right] S_\tau^{\rm mod}(k'-2\bar{\Delta})\,. \end{aligned} \tag{2.29}$$

Here the exponential operator induces perturbative subtractions (in powers of $\alpha_s(\mu_S)$) on the $\overline{\rm MS}$ series in $S_\tau^{\rm part}(k)$ that render it free of the renormalon. This exponential modifies perturbative results for the cross section in the manner we have shown earlier in Eqs. (2.8) and (2.23). The convolution of the nonsingular cross-section with $S_\tau^{\rm mod}$ in Eq. (2.21) now becomes

$$\int \mathrm{d}k' \,\frac{\mathrm{d}\hat{\sigma}_{\rm ns}}{\mathrm{d}\tau}\Big(\tau - \frac{k'}{Q}, \frac{\mu_{\rm ns}}{Q}\Big) S_\tau^{\rm mod}(k'-2\bar{\Delta})\,. \tag{2.30}$$

Furthermore, with Eq. (2.29) the result in Eq. (2.27) becomes

$$2\bar{\Delta}(R,\mu_S) + \int \mathrm{d}k\; k\, S_\tau^{\rm mod}(k) = 2\Omega_1(R,\mu_S)\,, \tag{2.31}$$

where here $\Omega_1(R,\mu_S)$ is renormalon-free. Combining Eqs. (2.31) and (2.27) we see that the scheme conversion formula from $\overline{\rm MS}$ to the new scheme is

$$\Omega_1(R,\mu_S) = \bar{\Omega}_1 - \delta(R,\mu_S)\,. \tag{2.32}$$

Thus, the precise scheme for $\Omega_1(R,\mu_S)$ is specified by the choice of the subtraction series $\delta(R,\mu_S)$. Note that in general the gap parameter $\bar{\Delta}$ is an additional non-perturbative parameter that can be determined together with other parameters in the function $S_\tau^{\rm mod}$ from fits to experimental data. However, in the tail region the power corrections are dominated by a single parameter, $\Omega_1(R,\mu_S)$, which encodes the dependence on $\bar{\Delta}$.

In Ref. [94] a convenient scheme for $\delta(R,\mu_S)$ was derived (based on a scheme proposed in Ref. [100]) where

$$\delta(R,\mu) = \frac{R}{2}\, e^{\gamma_E}\, \tfrac{d}{d\ln(ix)} \Big[\ln S_\tau(x,\mu) \Big] \Big|_{x=(iRe^{\gamma_E})^{-1}} . \tag{2.33}$$

Here $S_\tau(x,\mu)$ is the position space partonic soft function, and the fact that we write this result for S_τ rather than for the hemisphere soft function explains the extra factor of $1/2$ relative to the formula in Ref. [94]. The cutoff parameter R, having mass dimension 1, is a scale associated with the removal of the infrared renormalon. To achieve the proper cancellation of the renormalon in Eq. (2.29) one has to expand $\delta(R,\mu_S)$ together with $S_\tau^{\rm part}(k,\mu_S)$ order by order in $\alpha_s(\mu_S)$. The perturbative series for the subtraction is

$$\delta(R,\mu_S) = e^{\gamma_E} R \sum_{i=1}^{\infty} \alpha_s^i(\mu_S)\, \delta_i(R,\mu_S)\,, \tag{2.34}$$

where the $\delta_{i\geq 2}$ depend on both the adjoint Casmir $C_A = 3$ and the number of light flavors in combinations that are unrelated to the QCD beta function. For five light flavors the one, two, and three-loop coefficients are [94]

$$\begin{aligned}
\delta_1(R,\mu_S) &= -0.848826 L_R\,,\\
\delta_2(R,\mu_S) &= -0.156279 - 0.46663 L_R - 0.517864 L_R^2\,,\\
\delta_3(R,\mu_S) &= 0.0756831 + 0.01545386\, s_2 - 0.622467 L_R\\
&\quad - 0.777219 L_R^2 - 0.421261 L_R^3\,,
\end{aligned} \tag{2.35}$$

with $L_R = \ln(\mu_S/R)$. We will refer to the scheme defined by Eq. (2.33) as the R-gap scheme for Ω_1.

From the power counting $\bar{\Omega}_1 \sim \Lambda_{\rm QCD}$ one expects that a cutoff $R \sim 1\,\text{GeV}$ should be used, such that $\Omega_1 \sim \Lambda_{\rm QCD}$ and perturbation theory in $\alpha_s(R)$ remains applicable. We refer to this as the power counting criterion for R. Since in the tail region $\mu_S \sim Q\tau \gg 1$ GeV the factors of L_R in Eq. (2.35) are then large logs. To avoid large logarithms in the subtractions $\delta_i(R, \mu_S)$ it is essential to choose $R \sim \mu_S$, so that the subtraction scale R is dependent on τ much like the soft scale μ_S. We refer to this as the large-log criterion for R. To resolve the conflict between these two criteria, and sum the large logs while keeping $\bar{\Delta}(R, \mu_S \sim R)$ renormalon-free, we make use of R-evolution [92, 93]. Formulas for the gap case were given in Ref. [94] and are reviewed here. In this scheme $\bar{\Delta}(R,\mu)$ satisfies an R-RGE and μ-RGE

$$\begin{aligned} R\frac{d}{dR}\bar{\Delta}(R,R) &= -R\sum_{n=0}^{\infty}\gamma_n^R\Big(\frac{\alpha_s(R)}{4\pi}\Big)^{n+1}, \\ \mu\frac{d}{d\mu}\bar{\Delta}(R,\mu) &= 2Re^{\gamma_E}\sum_{n=0}^{\infty}\Gamma_n^{\rm cusp}\Big(\frac{\alpha_s(\mu)}{4\pi}\Big)^{n+1}, \end{aligned} \tag{2.36}$$

so that $\gamma_\Delta^\mu = -2e^{\gamma_E}\Gamma^{\rm cusp}[\alpha_s]$. For five flavors the anomalous dimension coefficients up to three loops are

$$\gamma_0^R = 0\,, \qquad \gamma_1^R = -43.954260\,, \qquad \gamma_2^R = 1615.42228 + 54.6195541\,s_2\,, \tag{2.37}$$

while the coefficients $\Gamma_n^{\rm cusp}$ are given in Eq. (A.36). The solution of Eq. (2.36) at N^{k}LL is

$$\begin{aligned} \bar{\Delta}(R,\mu) =& \bar{\Delta}(R_\Delta,\mu_\Delta) + Re^{\gamma_E}\omega[\Gamma^{\rm cusp},\mu,R] + R_\Delta e^{\gamma_E}\omega[\Gamma^{\rm cusp},R_\Delta,\mu_\Delta] \\ &+ \Lambda_{\rm QCD}^{(k)}\,D^{(k)}\big[\alpha_s(R),\alpha_s(R_\Delta)\big], \end{aligned} \tag{2.38}$$

where the resummed $\omega[\Gamma^{\rm cusp},\mu,\mu_0]$ is given in Eq. (A.28) and the resummed $D^{(k)}[\alpha_s(R),\alpha_s(R_\Delta)]$ is given in Eq. (A.47). Both the gap subtraction and R-evolution equations at $\mathcal{O}(\alpha_s^3)$ depend on the constant s_2 which we vary within its errors in our theory error scan. In

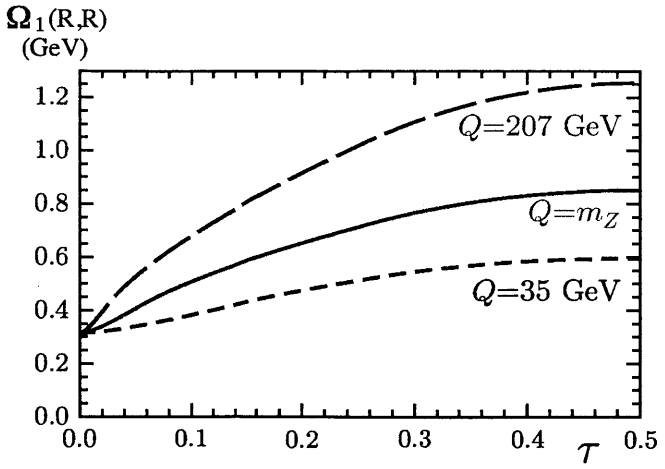

Figure 2-3: The running of $\Omega_1(R,R)$ with $R = R(\tau)$, plotted as a function of τ for $Q = 35, 91.2, 207\,\text{GeV}$.

our analysis, when quoting numerical results, we always use the parameter $\bar{\Delta}(R_\Delta, \mu_\Delta)$ at the reference scales $R_\Delta = \mu_\Delta = 2\,\text{GeV}$ to satisfy the power counting criterion for R. We then use Eq. (2.38) to run up to the scale $R \sim \mu_S$ in order to satisfy the large-log criterion. The precise R value is a function of τ, $R = R(\tau)$, and given in Sec. 2.3 with our discussion of the profile functions. The RGE solution for $\bar{\Delta}(R, \mu_S)$ in Eq. (2.38) yields a similar solution for a running $\Omega_1(R, \mu_S)$ using Eq. (2.31). In Fig. 2-3 we show the result for the running $\Omega_1(R,R)$ with the boundary value $\Omega_1(R_\Delta, \mu_\Delta) = 0.323\,\text{GeV}$. The anomalous dimension and $R(\tau)$ profile function cause an increase in the size of the power correction for increasing τ and for increasing Q.

Note that our R-gap subtraction scheme differs from the subtractions in the low-scale effective coupling model of Ref. [73], which is not based on the factorization of the soft large angle radiation but on the assumption that the $\mathcal{O}(\Lambda_{\text{QCD}})$ renormalon ambiguity is related entirely to the low-energy behavior of the strong coupling α_s. In the effective coupling model the subtractions involve logarithms, $\ln(\mu/\mu_I)$, where μ is the usual renormalization scale of perturbation theory and μ_I is the low-momentum subtraction scale, which is set to $\mu_I = 2\,\text{GeV}$. The scale μ_I plays a role very similar to the scale R in the R-gap scheme. These logarithms are the analogs of L_R in Eq. (2.35) and, since $\mu \propto Q$ these logarithms also become large. In the effective coupling model an appropriate resummation formalism for large logs in the subtractions remains an

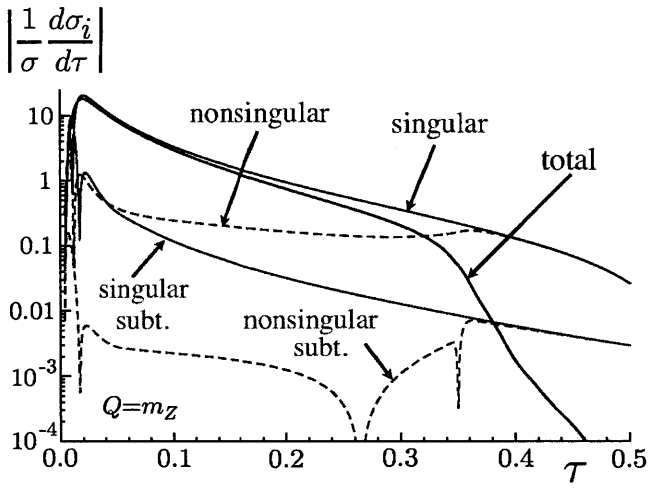

Figure 2-4: Components of the pure QCD cross section. Here $\Omega_1 = 0.35$ GeV and $\alpha_s(m_Z) = 0.114$.

open question.

In Fig. 2-4 we plot the absolute value of four components of our cross section for our complete QCD result at N^{3}LL$'$ order in the R-gap scheme at $Q = m_Z$. The cross section components include the singular terms (solid blue), nonsingular terms (dashed blue), and separately the contributions from terms that involve the subtraction coefficients δ_i, for both singular subtractions (solid red) and nonsingular subtractions (dashed red). The sum of these four components gives the total cross section (solid black line). The subtraction components are a small part of the cross section in the tail region, but have an impact at the level of precision obtained in our computation. In the peak region at very small τ the solid red singular subtraction grows to be the same size as the solid blue singular term, and is responsible for yielding a smooth positive definite total cross section. In both the peak and tail regions the singular cross section dominates over the nonsingular cross section. But as we approach the threshold $\tau \sim 1/3$ for the far-tail region they appear with opposite signs and largely cancel. This is clear from the figure where individually the singular and nonsingular lines are larger than the total cross section in this region. The same cancellation occurs for the singular subtraction and nonsingular subtraction terms.

2.2.7 Bottom Mass Effects

In this work we implement bottom mass effects using the SCET factorization framework for massive quarks [79, 80]. We include m_b-dependence in the kinematics, which starts at tree level, and in the $\mathcal{O}(\alpha_s)$ corrections in the partonic singular and nonsingular distributions. We also account for the resummation of large logs and for hadronization effects in the m_b-dependent terms. The mass dependent factorization theorem implies that the renormalization group summation of logarithms is identical to the one for massless quarks, and that all power corrections of type 1 from Eq. (2.6) are described by the nonperturbative soft function S_τ^{mod} already defined for the massless case [79, 80]. We have already indicated this with the convolution $\Delta \mathrm{d}\hat{\sigma}_b/\mathrm{d}\tau \otimes S_\tau^{\text{mod}}$ shown in Eq. (2.1). Since for the numerical analysis in this work we fit to data in the tail region, where $Q\tau > 6$ GeV, and since the massive quark thrust factorization theorem implies for the soft scale $\mu_S \sim Q\tau > 6$ GeV, we do not have to account for any flavor threshold in the renormalization group evolution and can always use $n_f = 5$. The mass dependent factorization theorem further implies that the only nontrivial m_b-dependence in the singular distribution arises in the thrust jet function. Thus the jet scale $\mu_J \sim Q\sqrt{\tau} \gg m_b$ for the region of our fit and we use the $\overline{\text{MS}}$ bottom mass $\overline{m}_b(\mu_J)$ to parameterize the m_b corrections with $\bar{m}_b(\bar{m}_b) = 4.2\,\text{GeV}$ as our input value. Using the $\overline{\text{MS}}$ mass rather than the pole mass avoids the appearance of large higher order effects related to the $\mathcal{O}(\Lambda_{\text{QCD}})$ pole mass renormalon.

We implement the partonic bottom mass corrections as an additive term to the massless partonic N^{3}LL$'$ cross section. These corrections come from the production of bottom quarks by the virtual γ or Z,

$$\frac{\Delta \mathrm{d}\hat{\sigma}_b}{\mathrm{d}\tau} = \frac{\mathrm{d}\hat{\sigma}_b}{\mathrm{d}\tau} - \frac{\mathrm{d}\hat{\sigma}_b^{\bar{m}_b=0}}{\mathrm{d}\tau}\,, \tag{2.39}$$

where both $\mathrm{d}\hat{\sigma}_b/\mathrm{d}\tau$ and $\mathrm{d}\hat{\sigma}_b^{\bar{m}_b=0}/\mathrm{d}\tau$ are computed at NNLL. Because the effect of $\bar{m}_b \neq 0$ in $\Delta \mathrm{d}\hat{\sigma}_b/\mathrm{d}\tau$ is expected to be a percent level correction to the tail cross section, we anticipate that the NNLL level of precision suffices. (This is also justified a posteriori by the relatively small effect of the m_b corrections on our fit results.)

An important aspect in the discussion of the finite quark mass effects is in which way hadron and heavy quark masses need to be accounted for in the definition of thrust in Eq. (1.16). In the experimental analyses Monte Carlo generators are used to convert the actual measurements to the momentum variables needed to compute τ, and this conversion depends on hadron masses. Since the final state stable hadrons are light, these effects are related to nonperturbative physics. Theoretically they are therefore implicitly encoded within our fit of the nonperturbative corrections. In the partonic theoretical computation light hadron masses are neglected in the computation of the τ distribution, and it is consistent to set $\sum_i |\vec{p}_i| = Q$ in the denominator of Eq. (1.16).

To understand how the heavy quark masses affect the definition of thrust in Eq. (1.16) we recall that the partonic computation relies on the inclusive nature of the measurements and that, experimentally, only light and long-lived hadrons reach the detectors and are accounted for in the $\vec{p}_i$ momenta that enter in computing τ. Thus for heavy hadrons containing bottom (or charm) quarks, it is their light and long-lived hadronic decay products that enter the particle sum $\sum_i$. Due to energy conservation it is therefore necessary to set $\sum_i |\vec{p}_i| = Q$ in the denominator of the thrust definition of Eq. (1.16) for the leading power partonic computations involving heavy quarks. On the other hand, due to three-momentum conservation, it is consistent to use the heavy quark three-momentum in the numerator of Eq. (1.16) for the partonic computations. This makes the partonic thrust computations involving heavy quarks simple because we do not need to explicitly account for the heavy quark decay in the calculations. Together with the relation $\sum_i |\vec{p}_i| = Q$ in the denominator of Eq. (1.16) this induces a shift of the observed thrust distribution for b quarks to larger τ values. Comparing to the massless quark situation, the small-τ endpoint is moved from 0 to

$$\tau_b^{\min} = 1 - \sqrt{1 - 4\bar{m}_b^2/Q^2}\,, \tag{2.40}$$

where here $\bar{m}_b = \bar{m}_b(\mu_J)$. At tree level this shifts $\delta(\tau) \to \delta(\tau - \tau_b^{\min})$. For the

fixed-order result at $\mathcal{O}(\alpha_s)$ the three-jet endpoint is moved from $1/3$ to $\tau_b^{\text{3jet}} = 5/3 - 4/3\sqrt{1-3\bar{m}_b^2/Q^2}$. At leading order in $\bar{m}_b^2/Q^2 \ll 1$ we have $\tau_b^{\min} = 2\bar{m}_b^2/Q^2 + \mathcal{O}(\bar{m}_b^4/Q^4)$ and $\tau_b^{\text{3jet}} = 1/3 + 2\bar{m}_b^2/Q^2 + \mathcal{O}(\bar{m}_b^4/Q^4)$, so the shift is the same for both endpoints. Numerically, for $\bar{m}_b = 4.2\,\text{GeV}$ and $Q = (35, 91.2, 207)\,\text{GeV}$, τ is shifted by $(0.029, 0.004, 0.0008)$. This shift is also observed experimentally in flavor tagged thrust analyses [12, 48, 3].

In the following we outline the method used to compute the partonic $\mathrm{d}\hat{\sigma}_b/\mathrm{d}\tau$. Like for the massless case the distribution is divided into singular and nonsingular parts

$$\frac{\mathrm{d}\hat{\sigma}_b}{\mathrm{d}\tau} = \frac{\mathrm{d}\hat{\sigma}_b^{\text{s}}}{\mathrm{d}\tau} + \frac{\mathrm{d}\hat{\sigma}_b^{\text{ns}}}{\mathrm{d}\tau}\,. \tag{2.41}$$

The implementation of the bottom mass effects into the singular distribution $\mathrm{d}\hat{\sigma}_b^{\text{s}}/\mathrm{d}\tau$ follows the NLL′ analysis in Ref. [80], except that the evolution in the present work is incorporated fully at NNLL order and that the exact partonic threshold at $\tau = \tau_b^{\min}$ is accounted for,

$$\begin{aligned}\frac{\mathrm{d}\hat{\sigma}_b^{\text{s}}}{\mathrm{d}\tau} =& Q\,\sigma_0^b\Big(\frac{\bar{m}_b}{Q}\Big)\,H_Q^v(Q,\mu_H)\,U_H(Q,\mu_H,\mu)\int \mathrm{d}s\,\mathrm{d}s'\,J_{\tau b}(s',\bar{m}_b,\mu_J)\,U_J^\tau(s-s',\mu,\mu_J)\\ &\times\int \mathrm{d}k\,U_S^\tau(k,\mu,\mu_S)e^{-2\frac{\delta(R,\mu_S)}{Q}\frac{\partial}{\partial\tau}}\;S_\tau^{\text{part}}\Big(Q\tau - Q\tau_b^{\min} - \frac{s}{Q} - k,\mu_S\Big)\\ &+ (\overline{\text{MS}}\text{-pole mass scheme change terms})\,,\end{aligned} \tag{2.42}$$

where $\sigma_0^b(x) = \sigma_0^{bv}\sqrt{1-4x^2}(1+2x^2) + \sigma_0^{ba}(1-4x^2)^{3/2}$. Perturbative bottom mass effects in the soft function start at two loops, so at $\mathcal{O}(\alpha_s)$ S_τ^{part} remains unchanged. Since we have $\bar{m}_b/Q \ll 1$, only the thrust jet function for bottom quark production, $J_{\tau b}(s,\bar{m}_b,\mu)$ [43], receives modifications from the finite m_b. These modifications lead to a shift of the partonic threshold of the thrust jet function from invariant mass $p^2 = 0$ to $p^2 = \bar{m}_b^2$. In $J_{\tau b}(s,\bar{m}_b,\mu)$ the variable $s = p^2 - \bar{m}_b^2$, and the presence of the mass leads to $\tau_b^{\min}$ in Eq. (2.42). It also gives a more complicated form for $\mathcal{O}(\alpha_s)$ corrections in $J_{\tau b}$ involving regular functions of m_b^2/s in addition to singular terms $\propto \delta(s)$ and $[\ln^k(s/\mu^2)/(s/\mu^2)]_+$ familiar from the massless quark jet function. More details and explicit formulae can be found in Refs. [79, 80].

The bottom quark mass effects in the nonsingular partonic distribution $\mathrm{d}\hat{\sigma}_b^{\mathrm{ns}}/\mathrm{d}\tau$ are more complicated since finite mass effects at $\mathcal{O}(\alpha_s)$ differ for vector and axial-vector current induced jet production,

$$\begin{aligned}\frac{\mathrm{d}\hat{\sigma}_b^{\mathrm{ns}}}{\mathrm{d}\tau} =& e^{-2\frac{\delta(R,\mu_s)}{Q}\frac{\partial}{\partial\tau}}\left[\sigma_0^{bv} f_b^v\Big(\tau,\frac{\bar{m}_b}{Q},\frac{\mu_{\mathrm{ns}}}{Q}\Big)+\sigma_0^{ba} f_b^a\Big(\tau,\frac{\bar{m}_b}{Q},\frac{\mu_{\mathrm{ns}}}{Q}\Big)\right] \\ &+ (\overline{\mathrm{MS}}\text{-pole mass scheme change terms})\,. \end{aligned} \tag{2.43}$$

In our analysis we implement analytic expressions for the nonsingular functions f_b^v and f_b^a. The full $\mathcal{O}(\alpha_s)$ distributions for $\tau > 0$ can be obtained from integrating the known double differential $b\bar{b}$ energy distribution for vector-induced and axial-vector-induced production, respectively, see e.g. Refs. [99, 128].[6] The corresponding $\mathcal{O}(\alpha_s)$ coefficient of the $\delta(\tau - \tau_b^{\min})$ term is obtained using the one-loop correction to the total $b\bar{b}$ cross section as a constraint. To determine the nonsingular distributions $f_b^{v,a}$ we proceed much like for the massless case and subtract the singular contributions expanded to $\mathcal{O}(\alpha_s)$ from the full $\mathcal{O}(\alpha_s)$ distribution. Further details and explicit formulas for $f_b^{v,a}$ will be given in a future publication.

2.2.8 QED Corrections

For the electroweak corrections to the thrust distribution we can distinguish purely weak contributions and QED effects. The dominant effects to jet production from the purely weak interactions are given by virtual one-loop corrections to the hard Wilson coefficient H_Q. Since the contribution of the singular thrust distribution $\mathrm{d}\hat{\sigma}_{\mathrm{s}}/\mathrm{d}\tau$ dominates in the τ ranges we use for our fits as well as in the total cross section $\sigma_{\mathrm{tot}} = \int \mathrm{d}\tau\, \mathrm{d}\sigma/\mathrm{d}\tau$ (see Fig. 2-4), the purely weak corrections largely drop out when the distribution is normalized to the total cross section. This is consistent with the explicit computations carried out in Refs. [66, 67], where purely weak corrections were found to be tiny. In our analysis we therefore neglect purely weak effects.

For QED corrections the situation is more complicated because, apart from virtual

[6] Results for bottom mass corrections at $\mathcal{O}(\alpha_s^2)$ were determined in Refs. [46, 125, 134], but are not used in our analysis due to the small effect the bottom mass corrections have in our fits.

effects which again largely cancel in the normalized distribution, one also has corrections due to initial state and final state radiation. In addition, one has to account for the fact that the treatment of QED effects in the thrust measurements depends on the experiment. In general, using Monte Carlo simulations, all experimental data were corrected to eliminate the effects from initial state radiation. However, they differ concerning the treatment of final state photon corrections, which were either eliminated or included in the corrected data sets. In Sec. 3.1 we review information on the approach followed by the various experimental collaborations. Since many experiments did not remove final state radiation, we have configured a version of our code that adds final state photons and QED Sudakov effects, and does so on an experiment by experiment basis. A parametric estimate of the potential impact of these QED effects on the measurement of $\alpha_s(m_Z)$ is $\sim -0.244\,\alpha_{\rm em}/(C_F\alpha_s) \sim -1\%$, where 0.244 is the average of the square of the electromagnetic charges for the five lightest flavors.

We implement the leading set of QED corrections to all components that go into the main factorization formula of Eq. (2.1) in the massless quark limit counting $\alpha_{\rm em} \sim \alpha_s^2$ to make a correspondence with Tab. 2.1 and remembering to include cross terms such as terms of $\mathcal{O}(\alpha_{\rm em}\alpha_s)$. Exceptions where QED corrections are not included are the gap subtraction $\delta(R,\mu_S)$ and the R-evolution equation for the gap parameter $\bar{\Delta}$. This is because QED effects do not lead to $\mathcal{O}(\Lambda_{\rm QCD})$ infrared renormalon ambiguities. Most of the required QED results can be obtained in a straightforward manner from modifications of the known QCD corrections.

Our implementation of QED effects is briefly described as follows: For the evolution of the strong coupling we included the $\mathcal{O}(\alpha_s^2\alpha_{\rm ew})$ corrections to the QCD beta function. There are also effects from the evolution of the QED coupling $\alpha_{\rm em}(\mu)$ which we define in the $\overline{\rm MS}$ scheme. In the beta function for the QED coupling $\alpha_{\rm em}$ we account for the dominant $\mathcal{O}(\alpha_{\rm em}^2)$ and the next-to-leading $\mathcal{O}(\alpha_{\rm em}^2\alpha_s)$ contributions. For the full singular partonic distribution which includes both QCD and QED effects

we have

$$\frac{\mathrm{d}\hat{\sigma}_{\mathrm{s}}}{\mathrm{d}\tau} = Q \sum_I \sigma_0^I \, H_Q^I(Q,\mu_H)\, U_H^I(Q,\mu_H,\mu) \int \mathrm{d}s\, \mathrm{d}s' \times J_\tau^I(s',\mu_J)\, U_J^{\tau I}(s-s',\mu,\mu_J) \times \int \mathrm{d}k\, U_S^{\tau I}(k,\mu,\mu_S) e^{-2\frac{\delta(R,\mu_S)}{Q}\frac{\partial}{\partial\tau}} \, S_\tau^{\mathrm{part}I}\Big(Q\,\tau - \frac{s}{Q} - k, \mu_S\Big), \tag{2.44}$$

where all factors now depend on the index I due to their dependence on the electromagnetic charges $q^{I=uv,ua} = +2/3$ and $q^{I=dv,da,bv,ba} = -1/3$. We implement one-loop QED corrections in the hard factor H_Q^I, the jet function J_τ^I and the soft functions $S_\tau^{\mathrm{part}I}$. In the renormalization group evolution factors U_H^I, $U_J^{\tau I}$, $U_S^{\tau I}$ we account for the one-loop QED corrections to the cusp and the non-cusp anomalous dimensions. In the nonsingular partonic distribution $\mathrm{d}\hat{\sigma}_{\mathrm{ns}}/\mathrm{d}\tau$ the same approach is employed. Here the $\mathcal{O}(\alpha_{\mathrm{em}})$ contributions that are analogous to the $\mathcal{O}(\alpha_s)$ terms are included by writing the full functions f^I to be used in Eq. (2.23) as

$$f^I\Big(\tau, \frac{\mu_{\mathrm{ns}}}{Q}\Big) = f_{\mathrm{qcd}}^I\Big(\tau, \frac{\mu_{\mathrm{ns}}}{Q}\Big) + \frac{3\,\alpha(\mu)\,(q^I)^2}{8\pi} f_1(\tau)\,. \tag{2.45}$$

The 1% parametric estimate and the moderate size of the QED effects we observe from the results of our fits justifies the neglect of higher order QED effects. A more precise treatment of QED effects is also not warranted given the level of accuracy of the Monte Carlo generators used to correct the experimental data. More details and explicit formulae for the QED corrections discussed here will be given in a future publication.

2.3 Profile functions

The factorization formula for the singular partonic distribution $\mathrm{d}\hat{\sigma}_{\mathrm{s}}/\mathrm{d}\tau$ in Eq. (2.8) is governed by three renormalization scales, the hard scale μ_H, the jet scale μ_J, and the soft scale μ_S. To avoid large logarithms appearing in the corrections to the hard coefficient H_Q, the jet function J_τ and the soft function S_τ, the corresponding scales

must satisfy the following theoretical constraints in the three τ regions:

$$\begin{aligned}
&\text{1) peak:} && \mu_H \sim Q\,, \quad \mu_J \sim \sqrt{\Lambda_{\rm QCD} Q}\,, && \mu_S \gtrsim \Lambda_{\rm QCD}\,,\\
&\text{2) tail:} && \mu_H \sim Q\,, \quad \mu_J \sim Q\sqrt{\tau}\,, && \mu_S \sim Q\tau\,,\\
&\text{3) far-tail:} && \mu_H = \mu_J = \mu_S \sim Q\,. && \qquad (2.46)
\end{aligned}$$

In the peak region, where the full nonperturbative function $S_\tau^{\rm mod}$ is relevant we have $\mu_H \gg \mu_J \gg \mu_S \sim \Lambda_{\rm QCD}$. In the tail region, where the nonperturbative effects are described by a series of moments of the soft function we have $\mu_H \gg \mu_J \gg \mu_S \gg \Lambda_{\rm QCD}$. To achieve an accurate theoretical description, we resum logarithms of τ in the peak and tail region where μ_H, μ_J, and μ_S are separated. Finally, in the far-tail region the partonic contributions are described by usual fixed-order perturbation theory, and a proper treatment of fixed order multijet thresholds requires that the three μ parameters merge close together in the far-tail region and become equal at $\tau = 0.5$, with $\mu_H = \mu_J = \mu_S \sim Q \gg \Lambda_{\rm QCD}$. Thus in the far-tail region logarithms of τ are not summed. The merging of μ_H, μ_J, and μ_S in the far-tail region is of key importance for the cancellations between singular and nonsingular cross sections shown in Fig. 2-4. To obtain a continuous factorization formula that is applicable in all three regions we use τ-dependent renormalization scales, which we call *profile functions*. These are smooth functions of τ which satisfy the theoretical constraints listed in Eq. (2.46).

In addition to the three renormalization scales of the singular partonic distribution there are two more scales, $\mu_{\rm ns}$ and R. The renormalization scale $\mu_{\rm ns}$ governs the perturbative series for the function f^I contained in the nonsingular partonic distribution $\mathrm{d}\hat{\sigma}_{\rm ns}/\mathrm{d}\tau$. The subtraction scale R arises when we implement the gap subtractions in the R-gap scheme for Ω_1 that remove the $\mathcal{O}(\Lambda_{\rm QCD})$ renormalon contained in the $\overline{\rm MS}$ soft function. This R also corresponds to the endpoint of the R-evolution for $\bar{\Delta}(R, \mu_S)$ given in Eq. (2.38). To avoid large logarithms in the subtraction $\delta(R, \mu_S)$, the value of R needs to be chosen of order μ_S and is therefore also a function of τ.

The factorization formula (2.1) is formally invariant under $\mathcal{O}(1)$ changes of the profile function scales, that is, changes that do not modify the hierarchies. The

residual dependence on the choice of profile functions constitutes one part of the theoretical uncertainties and provides a method to estimate higher order perturbative corrections. We adopt a set of six parameters that can be varied in our theory error analysis which encode this residual freedom while still satisfying the constraints in Eq. (2.46).

For the profile function at the hard scale, we adopt

$$\mu_H = e_H\, Q, \tag{2.47}$$

where e_H is a free parameter which we vary from 1/2 to 2 in our theory error analysis.

For the soft profile function we use the form

$$\mu_S(\tau) = \begin{cases} \mu_0 + \frac{b}{2t_1}\tau^2, & 0 \le \tau \le t_1, \\ b\tau + d, & t_1 \le \tau \le t_2, \\ \mu_H - \frac{b}{1-2t_2}(\frac{1}{2} - \tau)^2, & t_2 \le \tau \le \frac{1}{2}. \end{cases} \tag{2.48}$$

Here, t_1 and t_2 represent the borders between the peak, tail and far-tail regions. μ_0 is the value of μ_S at $\tau = 0$. Since the thrust value where the peak region ends and the tail region begins is Q dependent, we define the Q-independent parameter $n_1 = t_1\,(Q/1\,\mathrm{GeV})$. To ensure that $\mu_S(\tau)$ is a smooth function, the quadratic and linear forms are joined by demanding continuity of the function and its first derivative at $\tau = t_1$ and $\tau = t_2$, which fixes $b = 2\,(\mu_H - \mu_0)/(t_2 - t_1 + \frac{1}{2})$ and $d = [\mu_0(t_2 + \frac{1}{2}) - \mu_H\, t_1]/(t_2 - t_1 + \frac{1}{2})$. In our theory error analysis we vary the free parameters n_1, t_2 and μ_0.

The profile function for the jet scale is determined by the natural relation between the hard, jet, and soft scales

$$\mu_J(\tau) = \left(1 + e_J\left(\frac{1}{2} - \tau\right)^2\right)\sqrt{\mu_H\,\mu_S(\tau)}. \tag{2.49}$$

The term involving the free $\mathcal{O}(1)$-parameter e_J implements a modification to this relation and vanishes in the multijet region where $\tau = 1/2$. We use a variation of

e_J to include the effect of such modifications in our estimation of the theoretical uncertainties.

For the subtraction scale R the choice $R = \mu_S(\tau)$ ensures that we avoid large logarithms in the $\delta_i(R, \mu_S)$ subtractions for the soft function. In the peak region, however, it is convenient to deviate from this choice so that the $\mathcal{O}(\alpha_s)$ subtraction term $\delta_1(R, \mu_S) = -0.848826 \ln(\mu_S/R)$ is nonzero (see Eq. (2.35)). We therefore use the form

$$R(\tau) = \begin{cases} R_0 + \mu_1 \tau + \mu_2 \tau^2, & 0 \le \tau \le t_1, \\ \mu_S(\tau), & t_1 \le \tau \le 0.5\,. \end{cases} \tag{2.50}$$

Imposing continuity of $R(\tau)$ and its first derivative at $\tau = t_1$ requires $\mu_1 = (2d - 2R_0 + b\,t_1)/t_1$ and $\mu_2 = (-d + R_0)/t_1^2$. The only free parameter is R_0 which sets the value of R at $\tau = 0$. We take $R_0 = 0.85\mu_0$ to give the one loop subtraction $\delta_1(R, \mu_S)$ the appropriate sign to cancel the renormalon in the peak region. Since our focus here is not the peak region, we leave further discussion of the appropriate choice of R_0 to a future publication.

In our theory error analysis we vary $\mu_{\rm ns}$ to account for our ignorance on the resummation of logarithms of τ in the nonsingular corrections. We account for the possibilities

$$\mu_{\rm ns}(\tau) = \begin{cases} \mu_H, & n_s = 1, \\ \mu_J(\tau), & n_s = 0, \\ \frac{1}{2}(\mu_J(\tau) + \mu_S(\tau)), & n_s = -1. \end{cases} \tag{2.51}$$

We do not include the choice $\mu_{\rm ns} = \mu_S$ since we find that the choice of this small scale enhances the nonsingular contributions in an unnatural way.

In total, we have introduced six free parameters which we vary to account for renormalization scale uncertainties. In our analysis we use the following central values and variations: $\mu_0 = 2^{+0.5}_{-0.5}$ GeV, $n_1 = 5^{+3}_{-3}$, $t_2 = 0.25^{+0.05}_{-0.05}$, $e_J = 0^{+1}_{-1}$, $e_H = 2^h$ with $h = 0^{+1}_{-1}$ and $n_s = (-1, 0, 1)$. In Fig. 2-5 we show the form of the profile functions for

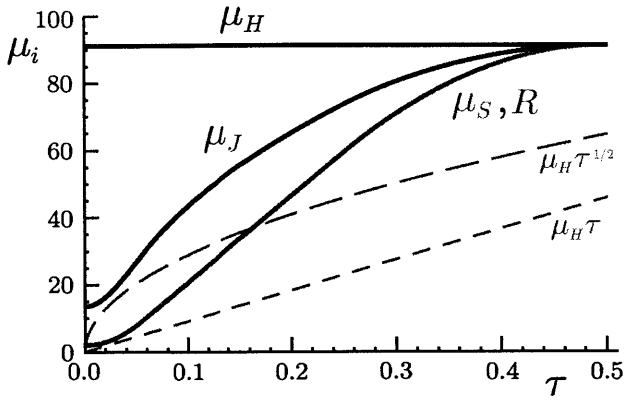

Figure 2-5: Profile functions for the renormalization scales $\mu_J(\tau)$, $\mu_S(\tau)$, and subtraction scale $R(\tau)$ that appear in the factorization theorem. Shown are results for the central parameter values at $Q = m_Z$.

$Q = m_Z = 91.2$ GeV and all profile parameters at their central values. The dashed lines represent the functions $Q\sqrt{\tau}$ and $Q\tau$ which were the central choices for $\mu_J(\tau)$ and $\mu_S(\tau)$ used in Ref. [31], but which do not meet in the multijet region. In order for our profile for $\mu_S(\tau)$ to join smoothly onto μ_H and $\mu_J(\tau)$ it is necessary for $\mu_S(\tau)$ to have a slope $\sim 2Q\tau$ in the tail region. Since $\ln 2$ is not large our profiles sum the same $\ln\tau$'s as with the choice in Ref. [31], but satisfy the criteria necessary to treat the multijet thresholds.[7]

2.4 Nonperturbative Model Function

The soft nonperturbative function $S_\tau^{\rm mod}(k)$ parameterizes the dominant nonperturbative hadronic effects in the thrust distribution. It describes the hadronization contributions that arise from how soft hadrons that are radiated in between the jets enter the thrust variable in Eq. (1.16). It is normalized, has the property $S_\tau(0) = 0$, is positive definite and has support for $k \geq 0$. To keep the representation of $S_\tau^{\rm mod}$ as much as possible independent of a particular analytic parametrization we adopt the approach of Ref. [116] and write the soft nonperturbative function as a linear

[7]In Ref. [64] where NLL resummation is achieved by exponentiation, the log resummation is turned off at a predefined threshold $\tau_{\rm max}$ with the log-R method [51]. In this approach the transition to fixed order results in the multijet region differs from ours.

combination of an infinite set of basis functions which can in principle describe any function with the properties mentioned above. The model function we use has the form

$$S_\tau^{\rm mod}(k,\lambda,\{c_i\}) = \frac{1}{\lambda}\left[\sum_{n=0}^{N} c_n\, f_n\!\left(\frac{k}{\lambda}\right)\right]^2, \tag{2.52}$$

where the basis functions are [116]

$$\begin{aligned} f_n(z) &= 8\sqrt{\frac{2z^3(2n+1)}{3}}\, e^{-2z}\, P_n\Big(g(z)\Big), \\ g(z) &= \frac{2}{3}\Big(3 - e^{-4z}\,(3+12z+24z^2+32z^3)\Big) - 1, \end{aligned} \tag{2.53}$$

and P_n are Legendre polynomials. For $\sum_i c_i^2 = 1$ the norm of $S_\tau^{\rm mod}(k)$ is unity, $\Omega_0 = 1$. The choice of basis in Eqs. (2.52) and (2.53) depends on specifying one dimensionful parameter λ which is characteristic of the width of the soft function. With $N = \infty$ the parameter λ would be redundant, but in practice we truncate the sum in Eq. (2.52) at a finite N, and then λ is effectively an additional parameter of the model function.

In this work we fit to experimental thrust data in the tail region where the predominant effects of the soft model function are described by its first moment $\Omega_1(\lambda,\bar{\Delta},\{c_i\})$. As explained below, we use the second moment $\Omega_2(\lambda,\bar{\delta},\{c_i\})$ to validate our error analysis and confirm the validity of neglecting this parameter in the fit. Since in the tail region the exact form of the soft model function is not relevant, we take $N = 2$ setting $c_{n>2} = 0$. Variations of the parameter c_1 are highly correlated with variations of λ and are hence not necessary for our purposes, so we set $c_1 = 0$. For this case

$$\begin{aligned} \Omega_1 =& \bar{\Delta} + \frac{\lambda}{2}\left[c_0^2 + 0.201354 c_0 c_2 + 1.10031 c_2^2\right], \\ \Omega_2 =& \bar{\Delta}^2 + \bar{\Delta}\lambda\left[c_0^2 + 0.201354 c_0 c_2 + 1.10031 c_2^2\right] \\ &+ \frac{\lambda^2}{4}\left[1.25 c_0^2 + 1.03621 c_0 c_2 + 1.78859 c_2^2\right], \end{aligned} \tag{2.54}$$

and the normalization condition $c_0^2 + c_2^2 = 1$ can be used to eliminate $c_0 > 0$. Recall that in the soft model function in the factorization theorem we must use $S_\tau^{\rm mod}\big(k -$

$2\bar{\Delta}(R,\mu_S),\lambda,\{c_i\})$ where $R = R(\tau)$ and $\mu_S = \mu_S(\tau)$ are determined by the profile functions. When we quote numbers for parameters we use $\bar{\Delta} = \bar{\Delta}(R_\Delta,\mu_\Delta)$ and hence $\Omega_{1,2} = \Omega_{1,2}(R_\Delta,\mu_\Delta)$ with reference scales $\mu_\Delta = R_\Delta = 2\,\text{GeV}$. The running between the scales (R,μ_S) and (R_Δ,μ_Δ) is determined by Eq. (2.38).

For our default fit in the tail region only the parameter Ω_1 is numerically relevant so without loss of generality we can take $c_0 = 1$, $c_2 = 0$, and set $\bar{\Delta}(R_\Delta,\mu_\Delta) = 0.05$ GeV. In this case all higher moments $\Omega_{n>1}$ are determined as a function of Ω_1 and $\bar{\Delta}$. For example we have $\Omega_2 = (\bar{\Delta}^2 - 2\bar{\Delta}\Omega_1 + 5\Omega_1^2)/4$ for the second moment.

In Sec. 3.2 we analyze the dependence of our fit results on changes of Ω_2. Because c_2 has a rather strong correlation to Ω_2, we implement these Ω_2 variations by using Eq. (2.54) and setting c_2 to nonzero values. In this case we can hold Ω_1 fixed by a suitable choice of λ for a given c_2.

To obtain results from our code that do not include nonperturbative corrections we can simply turn them off by setting $S_\tau^{\text{mod}}(k) = \delta(k)$ and $\bar{\Delta} = \delta = 0$.

2.5 Normalization and Convergence

The experimental data is normalized to the total number of events. In our prediction we therefore need to normalize the distribution to the total cross section, i.e. we have to calculate $(1/\sigma)\mathrm{d}\sigma/\mathrm{d}\tau$. Since the factorization formula in Eq. (2.1) is valid for all thrust values we have the option to use either the integral of our $\mathrm{d}\sigma/\mathrm{d}\tau$ distribution for the norm, or the available fixed-order result for the total hadronic cross section.

The fixed-order total cross section is

$$\begin{aligned}
&\sigma_{\text{tot}}^{\text{FO}} = \sum \sigma_0^I R^I\,, \quad R^{uv} = R^{dv} = R^{ua} = R^{da} = R_{\text{Had}}\,,\\
&R^{ba} = R_{\text{Had}} + R_A + \frac{\alpha_s^2}{3\pi^2} I(r_t)\,, \quad R^{bv} = R_{\text{Had}} + R_V.
\end{aligned} \tag{2.55}$$

Here R_{Had} is the pure QCD cross section for massless quarks, $R_{A,V}$ are mass corrections depending on m_b/Q, and $I(r_t)$ is the isosinglet correction from the axial anomaly and large top-bottom mass splitting [104]. Setting $\mu = Q$ the QCD cross sections for

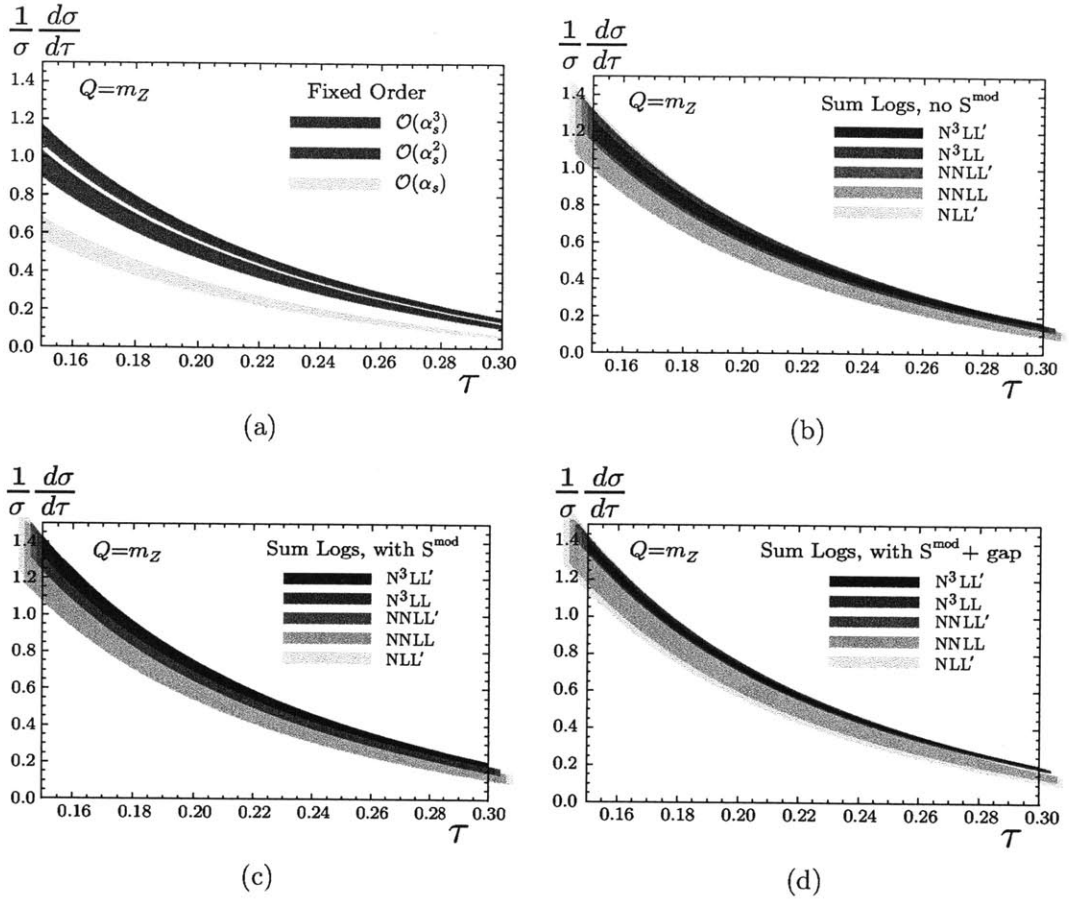

Figure 2-6: Theory scan for errors in pure QCD with massless quarks. The panels are a) fixed-order, b) resummation with no nonperturbative function, c) resummation with a nonperturbative function using the $\overline{\rm MS}$ scheme for $\bar{\Omega}_1$ without renormalon subtraction, d) resummation with a nonperturbative function using the R-gap scheme for Ω_1 with renormalon subtraction.

massless quarks at three loops is

$$R_{\rm Had} \;=\; 1 + 0.3183099\,\alpha_s(Q) + 0.1427849\,\alpha_s^2(Q) - \;0.411757\,\alpha_s^3(Q)\,. \qquad (2.56)$$

We refer to the review in Ref. [55] for a discussion of the fixed-order hadronic cross section. We note that the α_s series for the fixed-order hadronic cross section exhibits an excellent and fast convergence. At $\mathcal{O}(\alpha_s^3)$ the perturbative uncertainty is much below the permille level and hence entirely negligible for the purpose of our analysis.

In the R-gap scheme in pure QCD, from a numerical analysis at $Q = m_Z$, we

find at N^{3}LL$'$ order that the integrated norm of the thrust distribution for the default setting of all theory parameters (see Tab. 3.1) gives about $0.99\,\sigma_{\rm tot}^{\rm FO}$ at $\mathcal{O}(\alpha_s^3)$. However we also find that the perturbative uncertainty of the integrated norm (determined by the theory scan as described in Sec. 3.1) is about $\pm 2.5\%$, which is substantially larger than for the fixed-order cross section. This larger uncertainty is due to the perturbative errors of the thrust distribution in the peak region. At N^{3}LL$'$ order we therefore employ the fixed order cross section to normalize the thrust distribution we use for the fits.

At the lower orders in the R-gap scheme (N^{3}LL, NNLL$'$, NNLL, NLL$'$) we find that the integrated norm for central theory parameters is more appropriate since the order-by-order convergence to $\sigma_{\rm tot}^{\rm FO}$ is substantially slower than that of the rapid converging fixed-order QCD result in Eq. (2.56). Again we find that the large perturbative uncertainties in the peak region render the perturbative errors of the integrated norm larger than those of the fixed-order norm. We therefore evaluate the integrated norms at the lower orders with the theory parameters fixed at their default values (see Tab. 3.1). This means that to estimate the theoretical errors in our fits to experimental data at orders below N^{3}LL$'$ in the R-gap scheme, we vary the theory parameters only for the distribution and not for the norm computation. In the $\overline{\rm MS}$ scheme for $\bar{\Omega}_1$ we also adopt the integrated norm at all orders. When we evaluate the thrust distribution with log-resummation but without nonperturbative effects we use the same normalization choices as for the R-gap scheme, which makes comparison to earlier work in Sec. 3.4 easier. For the situation where the cross-section is evaluated at fixed-order, without resummation or nonperturbative effects, we use the appropriate fixed order normalization at each order.

As discussed in Sec. 3.1, to compare with the binned experimental data we integrate our theoretical expression for the distribution $(1/\sigma)(\mathrm{d}\sigma/\mathrm{d}\tau)$ over each bin $[\tau_1, \tau_2]$. A potential alternative is to use theoretical results for the cumulant

$$\Sigma(\tau) = \int_0^\tau \mathrm{d}\tau' \, \frac{1}{\sigma} \frac{\mathrm{d}\sigma}{\mathrm{d}\tau}(\tau') \,. \tag{2.57}$$

Here one sums large logs of τ rather than τ', and the SCET based cumulant has τ dependent profiles, $\Sigma(\tau, \mu_i(\tau))$. The presence of $\mu_i(\tau)$ implies that the derivative of the cumulant is not precisely equal to the distribution,

$$\frac{\mathrm{d}}{\mathrm{d}\tau}\Sigma\big(\tau, \mu_i(\tau)\big) = \frac{1}{\sigma}\frac{\mathrm{d}\sigma}{\mathrm{d}\tau}\big(\tau, \mu_i(\tau)\big) + \frac{d\mu_i(\tau)}{d\tau}\frac{\partial}{\partial\mu_i}\int_0^\tau d\tau' \frac{d\sigma}{d\tau'}\big(\tau', \mu_i(\tau)\big)\,. \tag{2.58}$$

The difference coming from the second term in Eq. (2.58) can be numerically important for certain observables. To test this we consider using for the cross-section integrated over the bin $[\tau_1, \tau_2]$ the theoretical expression

$$\Sigma(\tau_2, \mu_i(\tilde{\tau}_2)) - \Sigma(\tau_1, \mu_i(\tilde{\tau}_1))\,, \tag{2.59}$$

and will examine several choices for $\tilde{\tau}_{1,2}$.

One simple possibility is to use $\tilde{\tau}_1 = \tau_1$ and $\tilde{\tau}_2 = \tau_2$, so that $\Sigma(\tau_2, \mu_i(\tau_2)) - \Sigma(\tau_1, \mu_i(\tau_1))$ is used. In this case there is a spurious contribution from outside the $[\tau_1, \tau_2]$ bin associated to the second term in Eq. (2.58),

$$\Sigma(\tau_1, \mu_i(\tau_2)) - \Sigma(\tau_1, \mu_i(\tau_1)) \simeq (\tau_2 - \tau_1)\frac{d\mu_i(\tau_1)}{d\tau}\frac{\partial}{\partial\mu_i}\int_0^{\tau_1} d\tau' \frac{d\sigma}{d\tau'}\big(\tau', \mu_i(\tau_1)\big)\,, \tag{2.60}$$

where the $\simeq$ holds under the approximation that the derivative do not change very much across the bin. With our default setup the deviation of this simple choice for the cumulants from our integrated result for the distribution is 2% to 8% for $\tau \in [0.1, 0.3]$, bin-size $\tau_2 - \tau_1 = 0.01$, and $Q = 91.2\,\mathrm{GeV}$.[8] In the far-tail region $\tau_1 \in [0.3, 0.45]$, where the cross-section becomes small, the deviation grows from 8% to 1000%. The size of the spurious contribution is not reduced by increasing the bin-size to $\tau_2 - \tau_1 = 0.05$, and is only mildly dependent on Q. Any choice in Eq. (2.59) where $\tilde{\tau}_1 \neq \tilde{\tau}_2$ leads to a spurious contribution from $\tau \in [0, \tau_1]$.

If we instead use $\tilde{\tau}_1 = \tilde{\tau}_2 = (\tau_1 + \tau_2)/2$ then the spurious contribution is identically zero. In this case the difference between Eq. (2.59) and our integrated thrust distri-

[8]For the profile functions used by Becher and Schwartz [31], discussed in section 3.4, this deviation has similar size but opposite sign.

bution is reduced to 0.5% for $\tau_1 \in [0.1, 0.3]$ and for $\tau_1 \in [0.3, 0.45]$ grows from 0.5% to only 20%. Although dramatically reduced, the difference to the integrated distribution in the far-tail region is still quite sizeable. This discrepancy occurs because only for the distribution $(1/\sigma)(\mathrm{d}\sigma/\mathrm{d}\tau)$ can the $\mu_i(\tau)$ profile functions be constructed such that they satisfy exactly the criteria discussed in Sec. 2.3. Due to the above issues, and since the binned datasets are intended as representations of the thrust distribution, we have determined that our approach of integrating the thrust distribution is conceptually the best.

In the rest of this section we discuss the perturbative behavior of the thrust distribution in the tail region. The values of the physical parameters used in our numerical analysis are collected in Eq. (A.4). For our lower order fits we always use the four-loop beta function in the running of the strong coupling constant, as mentioned in the caption of Tab. 2.1. Furthermore, we always consider five active flavors in the running and do not implement bottom threshold corrections, since our lowest scale in the profile functions (the soft scale μ_S) is never smaller than 6 GeV in the tail where we perform our fit.

In Fig. 2-6 we display the normalized thrust distribution in the tail thrust range $0.15 < \tau < 0.30$ at the different orders taking $\alpha_s(m_Z) = 0.114$ and $\Omega_1(R_\Delta, \mu_\Delta) = 0.35$ GeV as reference values, and neglecting m_b and QED corrections. We display the case $Q = m_Z$ where the experimental measurements from LEP-I have the smallest statistical uncertainties. The qualitative behavior of the results agrees with other c.m. energies. The colored bands represent the theoretical errors of the predictions at the respective orders, which have been determined by the scan method described in Sec. 3.1.

In Fig. 2-6a we show the $\mathcal{O}(\alpha_s)$ (light/yellow), $\mathcal{O}(\alpha_s^2)$ (medium/purple) and $\mathcal{O}(\alpha_s^3)$ (dark/red) fixed-order thrust distributions without summation of large logarithms. The common renormalization scale is chosen to be the hard scale μ_H. In the fixed-order results the higher order corrections are quite large and our error estimation obviously underestimates the theoretical uncertainty of the fixed-order predictions. This panel including the error bands is very similar to the analogous figures in Refs. [85]

and [144]. This emphasizes the importance of summing large logarithms.

In Fig. 2-6b the fully resummed thrust distributions at NLL′ (yellow), NNLL (green), NNLL′ (purple), N^{3}LL (blue) and N^{3}LL′ (red) order are shown, but without implementing the soft nonperturbative function $S_\tau^{\rm mod}$ or the renormalon subtractions related to the R-gap scheme. The yellow NLL′ error band is mostly covered by the green NNLL order band, and similarly the purple NNLL′ band is covered by the blue N^{3}LL one. Moreover the blue N^{3}LL band is within the purple NNLL band. Compared to the fixed-order results, the improvement coming from the systematic summation of large logarithms is obvious. In particular we see that our way of estimating theoretical uncertainties is appropriate once the logarithms are properly summed. At N^{3}LL and at N^{3}LL′ order the relative uncertainties of these resummed thrust distributions in the tail region $\tau \in [0.1, 0.3]$ are about $\pm 7.8\%$ and $\pm 4.6\%$, respectively.

The results shown in Fig. 2-6c are very similar to panel b but now include also the soft nonperturbative function $S_\tau^{\rm mod}$ without renormalon subtractions, where $\bar{\Omega}_1$ is defined in the $\overline{\rm MS}$ scheme. In the tail region the soft nonperturbative function leads to a horizontal shift of the distribution towards larger thrust values by an amount $\delta\tau \propto 2\bar{\Omega}_1/Q$. This is clearly visible by comparing the values at $\tau = 0.15$ where the curves intersect the y-axis. Concerning the uncertainty bands and the behavior of predictions at the different orders the results are very similar to those in panel b.

Finally, in Fig. 2-6d we show the results with summation of large logarithms including the soft model function with renormalon subtractions, where Ω_1 is defined in the R-gap scheme. In the R-gap scheme the convergence of perturbation theory is improved, and correspondingly the size of the uncertainties from the same variation of the theory parameters is decreased. The decrease of the uncertainties is clearly visible comparing the blue N^{3}LL and the red N^{3}LL′ uncertainty bands with panel c. The relative uncertainties of the thrust distribution at N^{3}LL and at N^{3}LL′ order in the tail region $\tau \in [0.1, 0.3]$ are now about $\pm 3.4\%$ and $\pm 1.7\%$, respectively. This improvement illustrates the numerical impact of the $\mathcal{O}(\Lambda_{\rm QCD})$ renormalon contained in the partonic soft function and shows the importance of eliminating the $\mathcal{O}(\Lambda_{\rm QCD})$ renormalon.

Chapter 3

Analysis of Thrust Distribution: Tail fit

3.1 Experimental data and fit procedure

Experimental data for thrust are available for various c.m. energies Q between 14 and 207 GeV. In our analysis we fit the factorization formula (2.1) in the tail region to extract α_s and Ω_1. As our default data set we use the thrust range $6/Q \leq \tau \leq 0.33$, and we only employ data from $Q \geq 35$ GeV. The lower boundary $6/Q$ removes data in the peak where higher order moments become important, while the upper boundary of 0.33 removes data in the far-tail region where the $\alpha_s\Lambda_{\rm QCD}/Q$ power corrections become more important. We take $Q \geq 35\,\mathrm{GeV}$ since a more sophisticated treatment of b quark effects is required at lower energies. The data we use are from TASSO with $Q = \{35, 44\}$ GeV [47], AMY with $Q = 55.2$ GeV [115], JADE with $Q = \{35, 44\}$ GeV [124], SLC with $Q = 91.2$ GeV [8], L3 with $Q = \{41.4,$ 55.3, 65.4, 75.7, 82.3, 85.1, 91.2, 130.1, 136.1, 161.3, 172.3, 182.8, 188.6, 194.4, 200.0, 206.2$\}$ GeV [12, 14], DELPHI with $Q = \{45,$ 66, 76, 89.5, 91.2, 93, 133, 161, 172, 183, 189, 192, 196, 200, 202, 205, 207$\}$ GeV [6, 10, 146, 9], OPAL with $Q = \{91,$ 133, 161, 172, 177, 183, 189, 197$\}$ GeV [5, 13, 4] and ALEPH with $Q = \{91.2,$ 133, 161, 172, 183, 189, 200, 206$\}$ GeV [91]. (For TASSO and AMY we have separated statistical and systematic errors using information from the experimental papers.) All data is

given in binned form, and we therefore integrate Eq. (2.1) over the same set of bins to obtain appropriate theory results for the fit to the experimental numbers. For the case that either $\tau = 6/Q$ or $\tau = 0.33$ are located within an experimental bin, that bin is excluded from the data set if more than half of it lies outside the chosen interval. For the $Q > m_Z$ data we removed five bins with downward fluctuations that were incompatible at the $>$ 10-sigma level with the cross section implied by neighboring data points and other experimental data in the same region. The list of these bins is: L3 (136.1 GeV): $[0.25, 0.275]$, DELPHI (161 GeV): $[0.32, 0.40]$, DELPHI (183 GeV): $[0.08, 0.09]$, DELPHI (196 GeV): $[0.16, 0.18]$, ALEPH (200 GeV): $[0.16, 0.20]$.[1] Our default global data set contains a total of 487 bins. In the numerical analysis performed in Sec. 3.2 we also examine alternative global data sets with different τ-ranges.

The data sets were corrected by the experiments to eliminate the QED effects from initial state radiation using bin-by-bin correction factors determined from Monte Carlo simulations. The primary aim of these corrections was to eliminate the effective reduction of the c.m. energy available for the production of the hadronic final state. In addition, in the data sets from the TASSO, L3 and ALEPH collaborations the effects from final state radiation of photons were eliminated, while they have been fully included in the data sets from the AMY, JADE, SLC, DELPHI and OPAL collaborations. It should also be noted that the approaches used by the experiments to treat photon radiation were dependent on the c.m. energy Q. For the $Q = m_Z$ data any radiation of initial state photons is naturally suppressed as the effective c.m. energy for the hadronic final state gets shifted away from the Z pole. Therefore no specific photon cuts were applied for the $Q = m_Z$ data prior to the application of the bin-by-bin correction factors. For the data taken off the Z pole for either $Q < m_Z$ or $Q > m_Z$ the effects of initial state radiation are substantial and explicit hard photon cuts were applied in the data taking prior to the application of the bin-by-bin correction procedure. We therefore consider the $Q = m_Z$ data sets as more reliable concerning the treatment of QED effects.

[1] Four out of these bins lie in our $\tau \in [6/Q, 0.33]$ default fit range. If they are included in the default dataset then for our final fit in Eq. (3.5) the $\chi^2 = 439$ increases by $+81$ and the central fit values show a slight decrease to $\alpha_s(m_Z) = 0.1132$ and a slight increase to $\Omega_1 = 0.336\,\mathrm{GeV}$.

Since the size of the QED effects we find in the measurements of α_s and the soft function moment Ω_1 is comparable to the experimental uncertainties (see the results and discussions in Sec. 3.2), a less Monte Carlo dependent treatment of QED radiation would be certainly warranted. (See Ref. [67] for a recent discussion of QED radiation based on full one-loop matrix elements.) However, given that the impact of QED corrections we find for α_s and Ω_1 is still smaller than the current theoretical uncertainties from QCD, we use for our default numerical analysis the theory code with QED effects switched on, as described in Sec. 2.2.8. In Sec. 3.2 we also present results when QED corrections are neglected for all data sets, and for the case when they are neglected only for the TASSO, L3 and ALEPH data sets.

For the fitting procedure we use a χ^2-analysis, where we combine the statistical and the systematic experimental errors into the correlation matrix. We treat the statistical errors of all bins as independent. The systematic errors of the bins are correlated, but - unfortunately - practically no information on the correlation is given in the experimental publications. We therefore have to rely on a correlation model. For our analysis we assume as the default that within one thrust data set, i.e. for the set of thrust bins obtained by one experiment at one Q value, the systematic experimental errors are correlated in the minimal overlap model used by the LEP QCD working group [91, 5]. In the minimal overlap model the off-diagonal entries of the experimental covariance matrix for the bins i and j within one data set are equal to $[\min(\Delta_i^{\rm sys}, \Delta_j^{\rm sys})]^2$, where $\Delta_{i,j}^{\rm sys}$ are the systematic errors of the bins i and j. This model implies a positive correlation of systematic uncertainties within each thrust data set. As a cross check that our default correlation model does not introduce a strong bias we also carry out fits were the experimental systematic errors are assumed to be uncorrelated. Details are given in Sec. 3.2.

To estimate the theoretical errors in the α_s-Ω_1 plane at any order and for any approximation used for the factorization formula (2.1), we carry out independent fits for 500 different sets of theory parameters which are randomly chosen in the ranges discussed in the previous sections and summarized in Tab. 3.1. We take the area covered by the points of the best fits in the α_s-Ω_1 plane as the theory uncertainty

parameter	default value	range of values
μ_0	2 GeV	1.5 to 2.5 GeV
n_1	5	2 to 8
t_2	0.25	0.20 to 0.30
e_J	0	-1,0,1
e_H	1	0.5 to 2.0
n_s	0	-1,0,1
s_2	-39.1	-36.6 to -41.6
$\Gamma_3^{\rm cusp}$	1553.06	-1553.06 to $+4569.18$
j_3	0	-3000 to $+3000$
s_3	0	-500 to $+500$
ϵ_2	0	-1,0,1
ϵ_3	0	-1,0,1

Table 3.1: Theory parameters relevant for estimating the theory uncertainty, their default values and range of values used for the theory scan during the fit procedure.

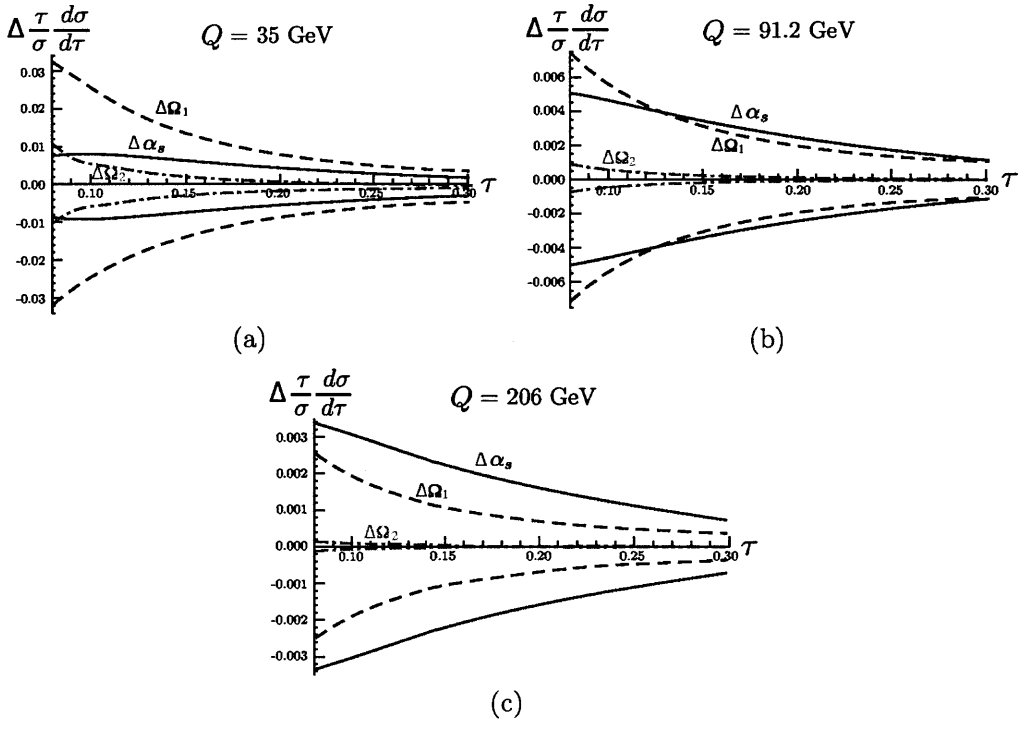

Figure 3-1: Difference between default cross section and the cross section varying only one parameter as a function of τ. We vary $\alpha_s(m_Z)$ by ± 0.001 (solid red curves), $2\Omega_1$ by ± 0.1 (dashed blue curves) and c_2 by ± 0.5 (dash dotted green curves). The plot is shown for three different values of the center of mass energy: (a) $Q = 35$ GeV, (b) $Q = 91.2$ GeV, (c) $Q = 206$ GeV.

treated like 1-sigma.[2] We emphasize that this method to estimate theoretical errors is more conservative than the error band method [102] employed for example in Refs. [31, 68]. However, our method required considerably more computer power and it was necessary to use the Tier-2 centers at Garching and MIT, as well as clusters at the MPI and the University of Arizona. In Sec. 3.2 we also present the outcome of other ways to estimate the theoretical error.

It is an important element of our analysis that we carry out global fits to the data from all values of $Q \geq 35$ (and all experiments). This is motivated by the strong degeneracy between α_s and Ω_1 in the tail region which can only be lifted when data from different Q values are simultaneously included in the fits.[3] In Fig. 3-1 the difference $\mathrm{d}\sigma/\mathrm{d}\tau - (\mathrm{d}\sigma/\mathrm{d}\tau)_{\mathrm{default}}$ is displayed for $0.08 \leq \tau \leq 0.30$ and $Q = 35$, 91.2 and 206 GeV. Here $(\mathrm{d}\sigma/\mathrm{d}\tau)_{\mathrm{default}}$ is the cross section for the default setting of the theory parameters with $\alpha_s(m_Z) = 0.114$ and $\Omega_1 = 0.35\,\mathrm{GeV}$ and for $\mathrm{d}\sigma/\mathrm{d}\tau$ we vary either $\alpha_s(m_Z)$ by ± 0.001 (solid red curves) or $2\Omega_1$ by $\pm 0.1\,\mathrm{GeV}$ (dashed blue curves) from their default values. The figures show that in the tail region changes in α_s can be compensated by changes in Ω_1. This degeneracy makes it impossible to determine α_s and Ω_1 simultaneously with small uncertainties from tail fits that use data from one Q value (or from a narrow range of Q values). On the other hand, we see that the correlation is Q dependent when considering a large enough range of Q values. In our fits it is particularly important to include, apart from the data from $Q = m_Z$, the low-energy data from JADE, TASSO, and AMY, and the high energy data from the LEP-II experiments. Although the errors in these analyses are larger than from the high-statistics $Q = m_Z$ run at LEP-I these data sets are essential for breaking the degeneracy and simultaneously extracting α_s and Ω_1.

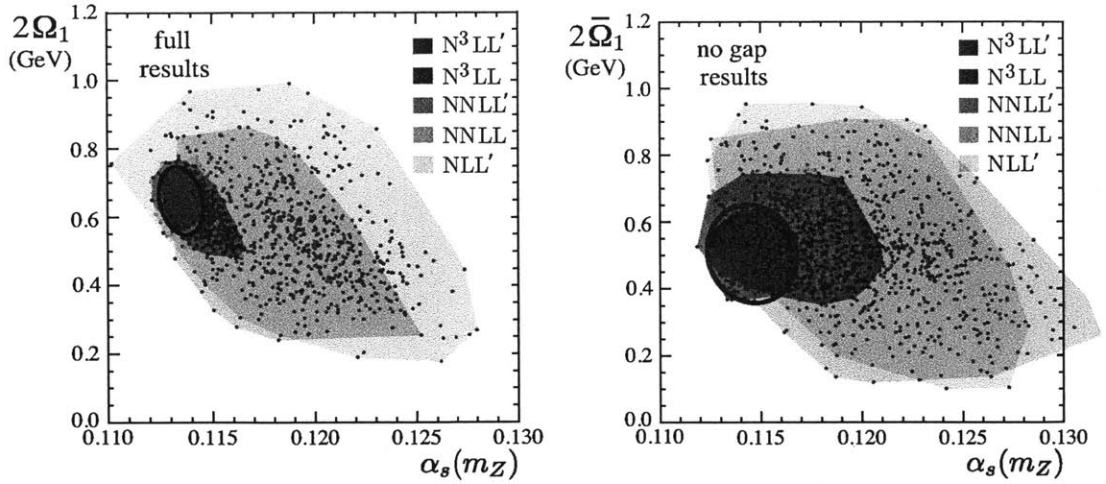

Figure 3-2: Distribution of best fit points in the $\alpha_s(m_Z)$-$2\Omega_1$ and $\alpha_s(m_Z)$-$2\bar{\Omega}_1$ planes. Panel (a) shows results including perturbation theory, resummation of the logs, the soft nonperturbative function and Ω_1 defined in the R-gap scheme with renormalon subtractions. Panel (b) shows the results as in panel a, but with $\bar{\Omega}_1$ defined in the $\overline{\rm MS}$ scheme without renormalon subtractions. In both panels the respective total (experimental+theoretical) 39% CL standard error ellipses are displayed (thick dark red lines), which correspond to 1-sigma (68% CL) for either one-dimensional projection.

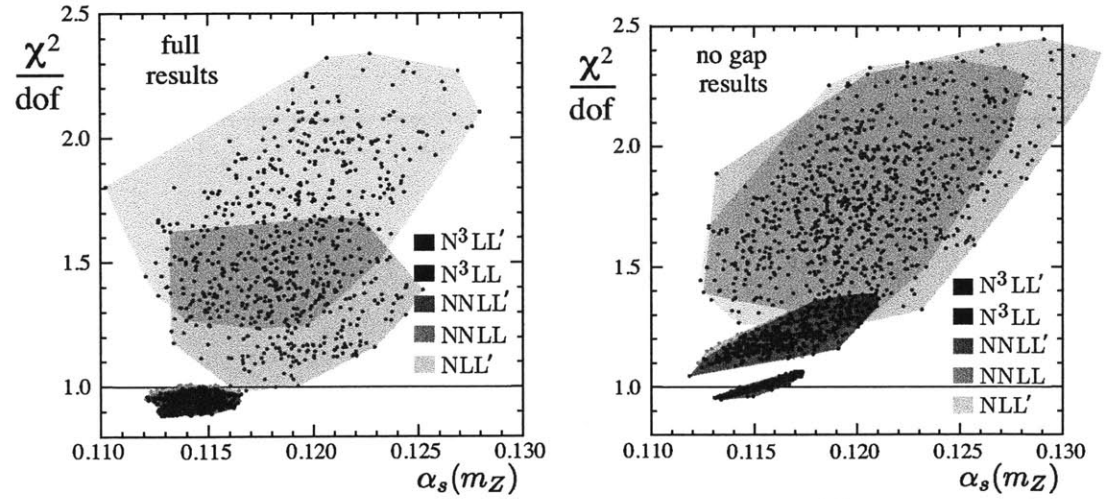

Figure 3-3: Distribution of best fit points in the $\alpha_s(m_Z)$-χ^2/dof plane. Panel (a) shows the χ^2/dof values of the points given in Fig. 3-2a. Panel (b) shows the χ^2/dof values of the points given in Fig. 3-2b.

3.2 Numerical Analysis

Having explained all ingredients of the factorization formula (2.1) and the fit procedure we are now in the position to discuss the numerical results of our analysis based on a global fit to the experimental data for $Q \geq 35$ GeV in the tail region. In the tail region the dominant power corrections are encoded in the first moment Ω_1, see Eq. (2.3), so we can determine $\alpha_s(m_Z)$ and Ω_1 from a simultaneous fit. In this section we examine in detail the numerical results of our fits concerning the treatment of the perturbative, hadronization and experimental errors, QED and bottom mass corrections and their dependence on the choice of the data set. We note that the values quoted for Ω_1 in the R-gap scheme are given for reference scales $R_\Delta = \mu_\Delta = 2$ GeV, see Sec. 2.2.6.

Theory Scan

In Fig. 3-2 the best fit points of the theory parameters scan in the α_s-$2\Omega_1$ plane are displayed at NLL′ (brown), NNLL (magenta), NNLL′ (green), N^{3}LL (blue) and N^{3}LL′ (red) order. The fit results at N^{3}LL′ order include bottom mass and QED corrections. In Fig. 3-2a the results in the R-gap scheme with renormalon subtractions are shown, and in Fig. 3-2b the results in the $\overline{\text{MS}}$ scheme without gap subtractions are given.

At each order 500 fits were carried out with the theory parameters randomly chosen in the ranges given in Tab. 3.1. As described in Sec. 3.1, we take the size of the area in the α_s-$2\Omega_1$ plane covered by the best fit points as a measure for the theoretical uncertainties. To visualize the theoretical uncertainties we have colored the respective areas according to the orders. The fit results clearly show a substantial reduction of the theoretical uncertainties with increasing orders. Explicit numerical results for the respective central values (determined by the mean of the respective maximal and minimal values) and the theory errors (determined by half of the difference between maximal and minimal values) for α_s and Ω_1 are given in Tabs. 3.2 and 3.3, respectively.

[2]This corresponds to a 1-sigma error (68% CL) in α_s as well as in Ω_1.

[3]The presence of this degeneracy is presumably also related to why Monte Carlos that are tuned to LEP data tend to have smaller hadronization corrections at $Q = m_Z$ than at larger Q values. See Sec. 3.4.

order	$\alpha_s(m_Z)$ (with $\bar{\Omega}_1^{\overline{\rm MS}}$)	$\alpha_s(m_Z)$ (with $\Omega_1^{\rm Rgap}$)
NLL′	0.1203 ± 0.0079	0.1191 ± 0.0089
NNLL	0.1222 ± 0.0097	0.1192 ± 0.0060
NNLL′	0.1161 ± 0.0038	0.1143 ± 0.0022
N^{3}LL	0.1165 ± 0.0046	0.1143 ± 0.0022
N^{3}LL′ (full)	0.1146 ± 0.0021	$\mathbf{0.1135 \pm 0.0009}$
N^{3}LL′$_{(\rm QCD+m_b)}$	0.1153 ± 0.0022	0.1141 ± 0.0009
N^{3}LL′$_{(\rm pure\ QCD)}$	0.1152 ± 0.0021	0.1140 ± 0.0008

Table 3.2: Theory errors from the parameter scan and central values for $\alpha_s(m_Z)$ at various orders. The N^{3}LL′ value above the horizontal line is our final scan result, while the N^{3}LL′ values below the horizontal line show the effect of leaving out the QED corrections, and leaving out both the b-mass and QED respectively. The central values are the average of the maximal and minimal values reached from the scan.

order	$\bar{\Omega}_1$ ($\overline{\rm MS}$)	Ω_1 (R-gap)
NLL′	0.264 ± 0.213	0.293 ± 0.203
NNLL	0.256 ± 0.197	0.276 ± 0.155
NNLL′	0.283 ± 0.097	0.316 ± 0.072
N^{3}LL	0.274 ± 0.098	0.313 ± 0.071
N^{3}LL′ (full)	0.252 ± 0.069	$\mathbf{0.323 \pm 0.045}$
N^{3}LL′$_{(\rm QCD+m_b)}$	0.238 ± 0.070	0.310 ± 0.049
N^{3}LL′$_{(\rm pure\ QCD)}$	0.254 ± 0.070	0.332 ± 0.045

Table 3.3: Theory errors from the parameter scan and central values for Ω_1 defined at the reference scales $R_\Delta = \mu_\Delta = 2$ GeV in units of GeV at various orders. The N^{3}LL′ value above the horizontal line is our final scan result, while the N^{3}LL′ values below the horizontal line show the effect of leaving out the QED corrections, and leaving out both the b-mass and QED respectively. The central values are the average of the maximal and minimal values reached from the scan.

We will consider these theory errors as 1-sigma. At N^{3}LL′ order with Ω_1 in the R-gap scheme the theory error for $\alpha_s(m_Z)$ is ± 0.0009 compared to ± 0.0021 with $\bar{\Omega}_1$ in the $\overline{\rm MS}$ scheme. Also at NNLL′ and N^{3}LL we see that the removal of the $\mathcal{O}(\Lambda_{\rm QCD})$ renormalon leads to a reduction of the theoretical uncertainties by about a factor of two in comparison to the results with $\bar{\Omega}_1$ in the $\overline{\rm MS}$ scheme without renormalon subtraction. The proper treatment of the renormalon subtraction is thus a substantial part of a high-precision analysis for Ω_1 as well as for α_s.

It is instructive to analyze the minimal χ^2 values for the best fit points shown in Fig. 3-2. In Fig. 3-3 the distributions of the best fits in the α_s-$\chi^2_{\rm min}$/dof plane are shown using the color scheme of Fig. 3-2. Figure 3-3a displays the results in R-gap

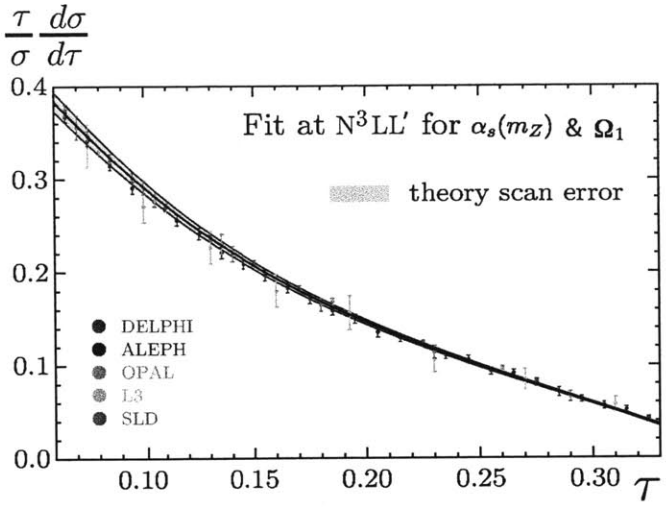

Figure 3-4: Thrust distribution at N^{3}LL$'$ order and $Q = m_Z$ including QED and m_b corrections using the best fit values for $\alpha_s(m_Z)$ and Ω_1 in the R-gap scheme given in Eq. (3.5). The pink band represents the perturbative error determined from the scan method described in Sec. 3.1. Data from DELPHI, ALEPH, OPAL, L3, and SLD are also shown.

scheme, and Fig. 3-3b the ones in the $\overline{\text{MS}}$ scheme. For both schemes we find that the χ^2_{min} values and the size of the covered area in the α_s-χ^2_{min}/dof plane systematically decrease with increasing order. While the analysis in the $\overline{\text{MS}}$ scheme for $\bar{\Omega}_1$ leads to χ^2_{min}/dof values around unity and thus an adequate description of the entire global data set at N^{3}LL$'$ order, we see that accounting for the renormalon subtraction in the R-gap scheme leads to a substantially improved theoretical description having χ^2_{min}/dof values below unity already at NNLL$'$ and N^{3}LL orders, with the N^{3}LL$'$ order result slightly lower at $\chi^2_{\text{min}}/\text{dof} \simeq 0.91$. This demonstrates the excellent description of the experimental data contained in our global data set. It also validates the smaller theoretical uncertainties we obtain for α_s and Ω_1 at N^{3}LL$'$ order in the R-gap scheme.

As an illustration of the accuracy of the fit, in Fig. 3-4 we show the theory thrust distributions at $Q = m_Z$ for the full N^{3}LL$'$ order with the R-gap scheme for Ω_1, for the default theory parameters and the corresponding best fit values shown in bold in Tabs. 3.2 and 3.3. The pink band displays the theoretical uncertainty from the scan method. The fit result is shown in comparison with data from DELPHI, ALEPH, OPAL, L3, and SLD, and agrees very well. (Note that the theory values displayed

	Band method 1	Band method 2	Our scan method
N^{3}LL$'$ with $\Omega_1^{\rm Rgap}$	0.0004	0.0008	0.0009
N^{3}LL$'$ with $\bar{\Omega}_1^{\overline{\rm MS}}$	0.0016	0.0019	0.0021
N^{3}LL$'$ without $S_\tau^{\rm mod}$	0.0018	0.0021	0.0034
$\mathcal{O}(\alpha_s^3)$ fixed-order	0.0018	0.0026	0.0046

Table 3.4: Theoretical uncertainties for $\alpha_s(m_Z)$ obtained at N^{3}LL$'$ order from two versions of the error band method, and from our theory scan method. The uncertainties in the R-gap scheme (first line) include renormalon subtractions, while the ones in the $\overline{\rm MS}$ scheme (second line) do not and are therefore larger. The same uncertainties are obtained in the analysis without nonperturbative function (third line). Larger uncertainties are obtained from a pure $\mathcal{O}(\alpha_s^3)$ fixed-order analysis (lowest line). Our theory scan method is more conservative than the error band method.

are actually binned according to the ALEPH data set and then joined by a smooth interpolation.)

Band Method

It is useful to compare our scan method to determine the perturbative errors with the error band method [102] that was employed in the analyses of Refs. [68, 31, 69]. In the error band method first each theory parameter is varied separately in the respective ranges specified in Tab. 3.1 while the rest are kept fixed at their default values. The resulting envelope of all these separate variations with the fit parameters $\alpha_s(m_Z)$ and Ω_1 held at their best fit values determines the error bands for the thrust distribution at the different Q values. Then, the perturbative error is determined by varying $\alpha_s(m_Z)$ keeping all theory parameters to their default values and the value of the moment Ω_1 to its best fit value. The resulting perturbative errors of $\alpha_s(m_Z)$ for our full N^{3}LL$'$ analysis in the R-gap scheme are given in the first line of Tab. 3.4. In the second line the corresponding errors for $\alpha_s(m_Z)$ in the $\overline{\rm MS}$ scheme for $\bar{\Omega}_1$ are displayed. The left column gives the error when the band method is applied such that the $\alpha_s(m_Z)$ variation leads to curves strictly inside the error bands for all Q values. For this method it turns out that the band for the highest Q value is the most restrictive and sets the size of the error. The resulting error for the N^{3}LL$'$ analysis in the R-gap scheme is more than a factor of two smaller than the error obtained from

our theory scan method, which is shown in the right column. Since the high Q data has a much lower statistical weight than the data from $Q = m_Z$, we do not consider this method to be sufficiently conservative and conclude that it should not be used. The middle column gives the perturbative error when the band method is applied such that the $\alpha_s(m_Z)$ variation minimizes a χ^2 function which puts equal weight to all Q and thrust values. This second band method is more conservative, and for the N^{3}LL$'$ analyses in the R-gap and the $\overline{\text{MS}}$ schemes the resulting errors are only 10% smaller than in the scan method that we have adopted. The advantage of the scan method we use is that the fit takes into account theory uncertainties including correlations.

Effects of QED and the bottom mass

Given the high-precision we can achieve at N^{3}LL$'$ order in the R-gap scheme for Ω_1, it is a useful exercise to examine also the numerical impact of the corrections arising from the nonzero bottom quark mass and the QED corrections. In Fig. 3-5 the distributions of the best fit points in the α_s-$2\Omega_1$ plane at N^{3}LL$'$ in the R-gap scheme is displayed for pure massless QCD (light green points), including the bottom mass corrections (medium blue points) and the bottom mass as well as the QED corrections (dark red points). The distribution of the best fit points with bottom mass and QED corrections (dark red points) was already shown in Fig. 3-2a. The large black dots represent the corresponding central values. The corresponding numerical results are shown at the bottom of Tabs. 3.2 and 3.3.

We see that the QED and bottom quark mass effects are somewhat smaller than the theoretical errors of the N^{3}LL$'$ analysis but not negligible. Moreover we find that the qualitative impact of the QED and the bottom quark mass effects is quite intuitive: The nonzero bottom quark mass primarily causes a horizontal shift of the thrust distribution towards larger τ values, since the small-τ threshold for massive quark production is moved to a finite τ value. Here this is compensated primarily by a reduced value of Ω_1. Concerning QED effects, they cause an effective increase of the coupling strength in the final state interactions leading primarily to a decrease of

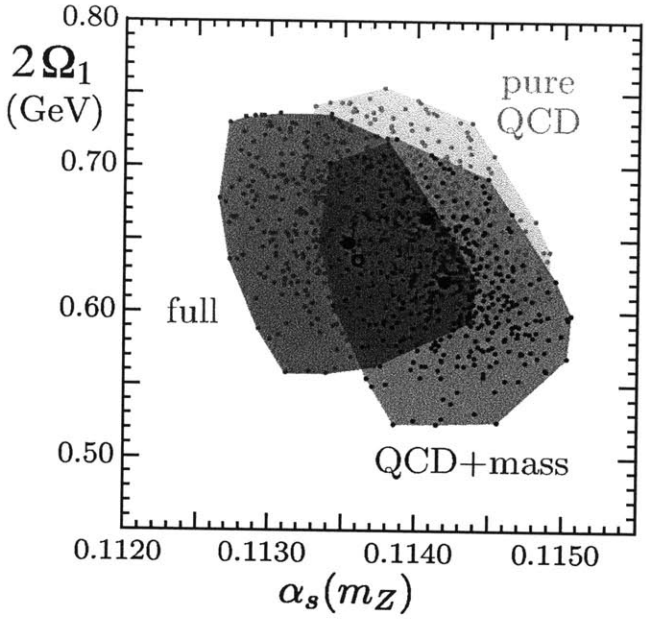

Figure 3-5: Distribution of best fit points at N^{3}LL$'$ order with Ω_1 in the R-gap scheme in pure QCD (light green), including m_b effects (medium blue) and including m_b effects and QED corrections (dark red). Solid circles indicate the central points for these three cases. The hollow circle represents the central point from the global fit with QED corrections neglected for the data from TASSO, L3 and ALEPH, but included for all other data sets.

α_s in the fit.

As explained in Sec. 3.1 the experimental correction procedures applied to the AMY, JADE, SLC, DELPHI and OPAL data sets were designed to eliminate initial state photon radiation, while those of the TASSO, L3 and ALEPH collaborations eliminated initial and final state radiation. It is straightforward to test for the effect of these differences in the fits by using our theory code with QED effects turned on or off depending on the data set. Since our χ^2 procedure treats data from different experiments as uncorrelated it is also easy to implement this technically. Using our N^{3}LL$'$ order code in the R-gap scheme we obtain the central values $\alpha_s(m_Z) = 0.1136$ and $\Omega_1 = 0.318$ GeV, indicated by the hollow circle in Fig. 3-5. Comparing to our default results given in Tabs. 3.2 and 3.3, which are based on the theory code were QED effects are included for all data sets, we see that the central value for α_s is larger by 0.0001 and the one for Ω_1 is smaller by 0.006 GeV. This shift is substantially smaller

than our perturbative error, and justifies our choice to use the theory code with QED effects included as the default code for our analysis.

Hadronization and Experimental Error

An important element in the construction of the χ^2 function used for our fit procedure is the correlation model for the systematic uncertainties given for the experimental thrust bins. The results discussed above rely on the minimal overlap model for the systematic experimental errors explained in Sec. 3.1. The 1-sigma ellipse based on the central values of Eq. (3.1) and centered around $(\alpha_s, 2\Omega_1) = (0.1135, 0.647\ \text{GeV})$ is shown in Fig. 3-6 by the red solid ellipse. This ellipse yields the experimental errors and hadronization uncertainty related to Ω_1 in our analysis. We find that the size and correlation coefficients of the 1-sigma error ellipses at $\text{N}^3\text{LL}'$ order of all fits made in our theory scan are very similar, and hence we can treat the theory error and these hadronization/experimental errors as independent.

The correlation matrix of the red solid error ellipses is $(i, j = \alpha_s, 2\Omega_1)$

$$
\begin{aligned}
V_{ij} &= \begin{pmatrix} \sigma_{\alpha_s}^2 & \sigma_{\alpha_s}\sigma_{2\Omega_1}\rho_{\alpha\Omega} \\ \sigma_{\alpha_s}\sigma_{2\Omega_1}\rho_{\alpha\Omega} & \sigma_{2\Omega_1}^2 \end{pmatrix} \\
&= \begin{pmatrix} 3.29(16)\cdot 10^{-7} & -2.30(12)\cdot 10^{-5}\ \text{GeV} \\ -2.30(12)\cdot 10^{-5}\ \text{GeV} & 1.90(18)\cdot 10^{-3}\ \text{GeV}^2 \end{pmatrix},
\end{aligned}
\tag{3.1}
$$

where the correlation coefficient is significant and reads

$$
\rho_{\alpha\Omega} = -0.9176(60)\,. \tag{3.2}
$$

The numbers in the parentheses represent the variance from the theory scan. From Eq. (3.1) it is straightforward to extract the experimental error for α_s and Ω_1 and

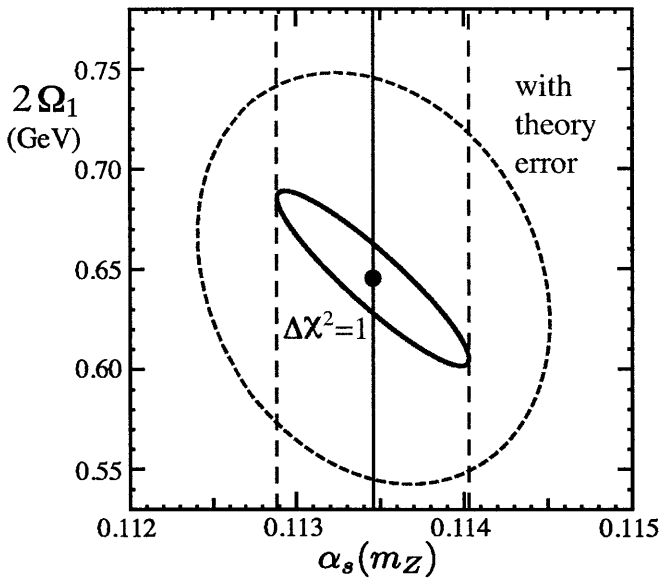

Figure 3-6: Experimental 1-sigma standard error ellipse (red solid) in the α_s-$2\Omega_1$ plane. The larger ellipse shows the total uncertainty including theory errors (blue dashed). The fit is at N^{3}LL$'$ order in the R-gap scheme for Ω_1 using the central values of the correlation matrix given in Eq. (3.1). The center of the ellipse are the central values of our final result given in Eq. (3.5).

the error due to variations of Ω_1 and α_s, respectively:

$$\begin{aligned}
\sigma_{\alpha_s}^{\rm exp} &= \sigma_{\alpha_s}\sqrt{1-\rho_{\alpha\Omega}^2} = 0.0002\,,\\
\sigma_{\Omega_1}^{\rm exp} &= \sigma_{\Omega_1}\sqrt{1-\rho_{\alpha\Omega}^2} = 0.009\ {\rm GeV}\,,\\
\sigma_{\alpha_s}^{\Omega_1} &= \sigma_{\alpha_s}\,|\rho_{\alpha\Omega}| \;=\; 0.0005\,,\\
\sigma_{\Omega_1}^{\alpha_s} &= \sigma_{\Omega_1}\,|\rho_{\alpha\Omega}| \;=\; 0.020\ {\rm GeV}\,.
\end{aligned} \tag{3.3}$$

For α_s, the error due to Ω_1 variations is the dominant part of the hadronization uncertainty. The blue dashed ellipse in Fig. 3-6 shows the total error in our final result quoted in Eq. (3.5) below.

The correlation exhibited by the red solid error ellipse in Fig. 3-6 is indicated by the line describing the semimajor axis

$$\frac{\Omega_1}{41.5\,{\rm GeV}} = 0.1213 - \alpha_s(m_Z)\,. \tag{3.4}$$

Note that extrapolating this correlation to the extreme case where we neglect the nonperturbative corrections ($\Omega_1 = 0$) gives $\alpha_s(m_Z) \to 0.1213$. This value is consistent with the fits in Refs. [68, 69] shown in Tab. 3.6, which are dominated by $Q = m_Z$ where the Monte Carlo hadronization uncertainties are smallest.

Individual Theory Scan Errors

It is a useful exercise to have a closer look at the size of the theory uncertainties caused by the variation of each of the theory parameters we vary in our fit procedure in order to assess the dominant sources of theory errors. In Fig. 3-7 two bar charts are shown for the variation of the best fit values for $\alpha_s(m_Z)$ and $\Omega_1(R_\Delta, \mu_\Delta)$ at N^{3}LL$'$ order in the R-gap scheme with our default theory parameters. The bars show individual up-down variations of each of the theory parameters in the ranges given in Tab. 3.1. The changes of the best fit values related to up variations of the theory parameters are given in dark blue and those related to down variations are given in light green.

We see that the dominant theory uncertainties are related to variations of the profile functions (n_1, t_2, e_J, e_H) and the renormalization scale parameter (n_s) for the nonsingular partonic distribution $\mathrm{d}\hat{\sigma}_{\mathrm{ns}}/\mathrm{d}\tau$. The uncertainties related to the numerical errors of the perturbative constants (s_2, s_3, j_3) as well as the numerical errors in the extraction of the nonsingular distribution for small τ values, (ϵ_2, ϵ_3) are – with the exception of s_2 – much smaller and do not play an important role. The theory error related to the unknown 4-loop contribution to the cusp anomalous dimension is negligible. Adding quadratically the symmetrized individual errors shown in Fig. 3-7 for each parameter, we find 0.0006 for α_s and 0.029 for Ω_1. This is about 2/3 of the theoretical uncertainty we have obtained by the theory parameter scan, and it demonstrates that the theory parameter scan represents a more conservative method to estimate the theory error.

In Fig. 3-7 we have also shown the variation of the best fit values for $\alpha_s(m_Z)$ and $\Omega_1(R_\Delta, \mu_\Delta)$ due to variations of the second soft function moment parameter Ω_2. Our default choice for the parametrization of the soft function S_τ^{mod} uses $c_0 = 1$ and $c_{n>0} = 0$ with $\bar{\Delta}(R_\Delta, \mu_\Delta) = 0.05$ GeV. In this case λ is the only variable parameter of

the soft model function $S_\tau^{\rm mod}$, and Ω_2 is predetermined by Eq. (2.54) with $c_2 = 0$. As explained in Sec. 2.4 we modify Ω_2 by setting c_2 to nonzero values. It is instructive to discuss the Ω_2 values one should consider. From the Cauchy-Schwarz inequality one can show that $\Omega_2/\Omega_1^2 \geq 1$, giving a strict lower bound on Ω_2. This bound can only be reached if $S_\tau^{\rm mod}$ is a delta-function. Moreover, if $S_\tau^{\rm mod}$ is positive definite, vanishing at $k = 0$, has a width of order $\Lambda_{\rm QCD}$, has its maximum at a k value of order $\Lambda_{\rm QCD}$, and has an exponential fall-off for large k, then one finds $\Omega_2/\Omega_1^2 < 1.5$. We therefore adopt the range $1 \leq \Omega_2/\Omega_1^2 \leq 1.5$ as a conservative Ω_2 variation to carry out an error estimate. For our default parametrization we have $\Omega_2/\Omega_1^2 = 1.18$ and changing c_2 between ± 0.5 gives a variation of Ω_2/Ω_1^2 between 1.05 and 1.35. We find that the best fit values for α_s and Ω_1 are smooth linear functions of Ω_2/Ω_1^2 which allows for a straightforward extrapolation to the conservative range between 1.0 and 1.5. The results for the variations of the best fit values for $\alpha_s(m_Z)$ and Ω_1 for $\Omega_2/\Omega_1^2 = 1.18^{+0.32}_{-0.18}$ read $(\delta\alpha_s(m_Z))_{\Omega_2} = ^{+0.00017}_{-0.00013}$ and $(\delta\Omega_1)_{\Omega_2} = ^{+0.011}_{-0.015}$ and are also shown in Fig. 3-7. The symmetrized version of these errors are included in our final results. For our final results for $\alpha_s(m_Z)$ we add the uncertainties from Ω_1 and the one from Ω_2 quadratically giving the total hadronization error. For $\Omega_1(R_\Delta, \mu_\Delta)$ we quote the error due to Ω_2 separately.

Final Results

As our final result for $\alpha_s(m_Z)$ and $\Omega_1(R_\Delta, \mu_\Delta)$, obtained at N^{3}LL$'$ order in the R-gap scheme for Ω_1, including bottom quark mass and QED corrections we obtain

$$\begin{aligned}
\alpha_s(m_Z) &= 0.1135 \pm (0.0002)_{\rm exp} \pm (0.0005)_{\rm hadr} \pm (0.0009)_{\rm pert}, \\
\Omega_1(R_\Delta, \mu_\Delta) &= 0.323 \pm (0.009)_{\rm exp} \pm (0.013)_{\Omega_2} \pm (0.020)_{\alpha_s(m_Z)} \pm (0.045)_{\rm pert}\ {\rm GeV},
\end{aligned} \tag{3.5}$$

where $R_\Delta = \mu_\Delta = 2$ GeV and we quote individual 1-sigma errors for each parameter. Eq. (3.5) is the main result of this work. In Fig. 3-6 (blue dashed line) and Fig. 3-2a (thick dark red line) we have displayed the corresponding combined total (experimen-

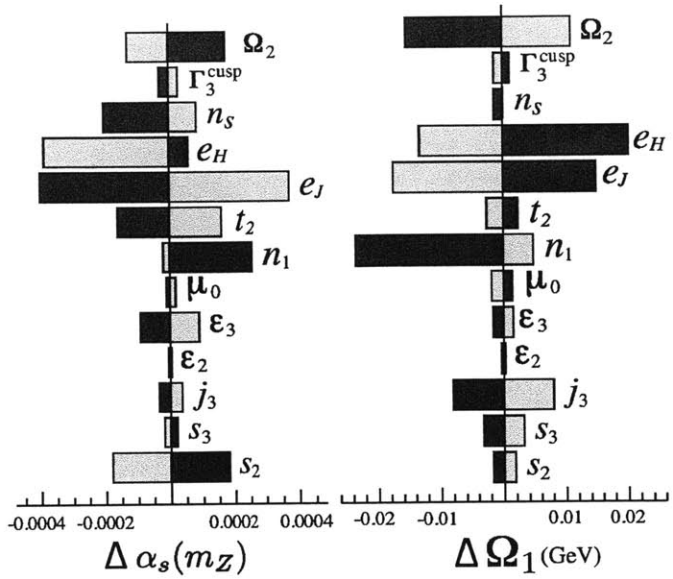

Figure 3-7: Variations of the best fit values for $\alpha(m_Z)$ and Ω_1 from up (dark shaded blue) and down (light shaded green) variations for the theory parameters with respect to the default values and in the ranges given in Tab. 3.1. For the variation of the moment Ω_2 we use $\Omega_2/\Omega_1^2 = 1.18^{+0.32}_{-0.18}$ as explained in the text.

tal+theoretical) standard error ellipse. To obtain the combined ellipse we take the theory uncertainties given in Tabs. 3.2 and 3.3 together with the Ω_2 uncertainties, adding them in quadrature. The central values in Eq. (3.5) are determined by the average of the respective maximal and minimal values of the theory scan, and are very close to the central values obtained when running with our default theory parameters. The fit has $\chi^2/dof = 0.91$ with a variation of ± 0.03 for the displayed scan points. Having added the theory scan and Ω_2 uncertainties reduces the correlation coefficient in Eq. (3.2) to $\rho_{\alpha\Omega}^{\rm total} = -0.212$. As a comparison we have also shown in Fig. 3-2b the combined total (experimental+theoretical) error ellipse at N^{3}LL$'$ in the $\overline{\rm MS}$ scheme for $\bar{\Omega}_1$ where the $\mathcal{O}(\Lambda_{\rm QCD})$ renormalon is not subtracted.

Since our treatment of the correlation of the systematic experimental errors is based on the minimal overlap model, it is instructive to also examine the results treating all the systematic experimental errors as uncorrelated. At N^{3}LL$'$ order in the R-gap scheme the results that are analogous to Eqs. (3.5) read $\alpha_s(m_Z) = 0.1141 \pm (0.0002)_{\rm exp} \pm (0.0005)_{\rm hadr} \pm (0.0010)_{\rm pert}$ and $\Omega_1(R_\Delta, \mu_\Delta) = 0.303 \pm (0.006)_{\rm exp} \pm$

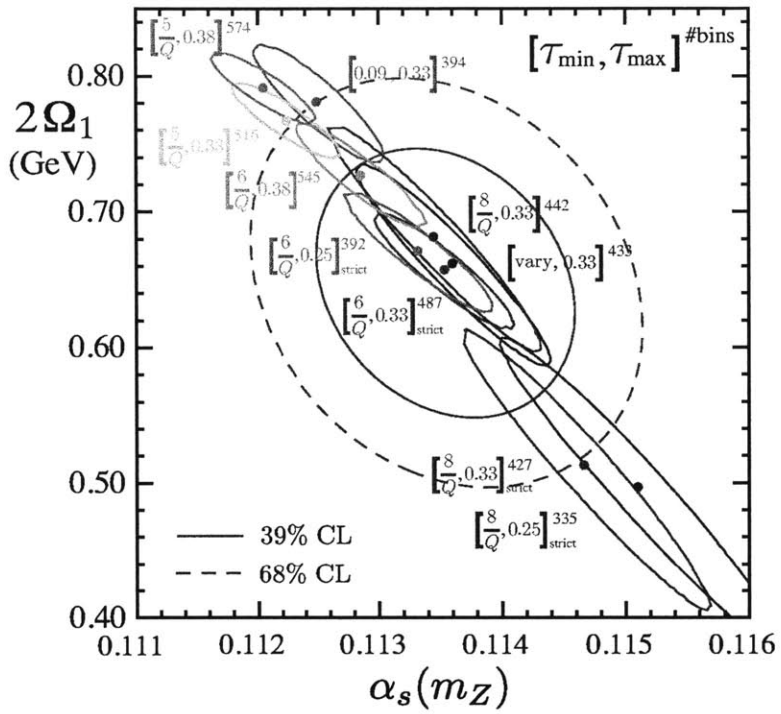

Figure 3-8: The smaller elongated ellipses show the experimental 39% CL error (1-sigma for α_s) and best fit points for different global data sets at N^{3}LL$'$ order in the R-gap scheme and including bottom quark mass and QED effects. The default theory parameters given in Tab. 3.1 are employed. The larger ellipses show the combined theoretical plus experimental error for our default data set with 39% CL (solid, 1-sigma for one dimension) and 68% CL (dashed).

$(0.013)_{\Omega_2} \pm (0.022)_{\alpha_s} \pm (0.055)_{\text{pert}}$ GeV with a combined correlation coefficient of $\rho_{\alpha\Omega}^{\text{total}} = -0.180$. The results are compatible with the results of Eqs. (3.5) and indicate that the ignorance of the exact correlation of the systematic experimental errors does not crucially affect the outcome of the fit.

Data Set Choice

We now address the question to which extent the results of Eqs. (3.5) depend on the thrust ranges contained in the global data set used for the fits. Our default global data set accounts for all experimental thrust bins for $Q \geq 35$ in the intervals $[\tau_{\min}, \tau_{\max}] = [6/Q, 0.33]$. (See Sec. 3.1 for more details.) This default global data set is the outcome of a compromise that (i) keeps the τ interval large to increase statistics, (ii) sets $\tau_{\min}$ sufficiently large such that the impact of the soft function moments Ω_i

with $i \geq 2$ is small and (iii) takes $\tau_{\rm max}$ sufficiently low to exclude the far-tail region where the missing order $\alpha_s \Lambda_{\rm QCD}/Q$ corrections potentially become important.

In Fig. 3-8 the best fits and the respective experimental 39% and 68% CL error ellipses for the default values of the theory parameters given in Tab. 3.1 are shown for global data sets based on different τ intervals. The results for the various τ intervals are each given in different colors. The results for our default global data set is given in red color, and the subscript "strict" for some intervals means that bins are included in the data set if more than half their range is contained within the interval. For intervals without a subscript the criterion for selecting bins close to the boundaries of the τ interval is less strict and generically, if the $\tau_{\rm min}$ and $\tau_{\rm max}$ values fall in such bins, these bins are included. The numbers in superscript for each of the τ intervals given in the figure refers to the total number of bins contained in the global data set. We observe that the main effect on the outcome of the fit is related to the choice of $\tau_{\rm min}$ and to the total number of bins. Interestingly all error ellipses have very similar correlation and are lined up approximately along the line

$$\frac{\Omega_1}{50.2\,\text{GeV}} = 0.1200 - \alpha_s(m_Z)\,. \tag{3.6}$$

Lowering $\tau_{\rm min}$ increases the dependence on Ω_2 and leads to smaller α_s and larger Ω_1 values. On the other hand, increasing $\tau_{\rm min}$ leads to a smaller data set and to larger experimental error ellipses, hence to larger uncertainties.

It is an interesting but expected outcome of the fits that the pure experimental error for α_s (the uncertainty of α_s for fixed central Ω_1) depends fairly weakly on the τ range and the size of the global data sets shown in Fig. 3-8. If we had a perfect theory description then we would expect that the centers and the sizes of the error ellipses would be statistically compatible. Here this is not the case, and one should interpret the spread of the ellipses shown in Fig. 3-8 as being related to the theoretical uncertainty contained in our N^{3}LL$'$ order predictions. In Fig. 3-8 we have also displayed the combined (experimental and theoretical) 39% CL standard error ellipse from our default global data set which was already shown in Fig. 3-2a (and is

	$\alpha_s(m_Z)\pm$(pert. error)	χ^2/(dof)
N^{3}LL$'$ with $\Omega_1^{\rm Rgap}$	0.1135 ± 0.0009	0.91
N^{3}LL$'$ with $\bar{\Omega}_1^{\overline{\rm MS}}$	0.1146 ± 0.0021	1.00
N^{3}LL$'$ without $S_\tau^{\rm mod}$	0.1241 ± 0.0034	1.26
$\mathcal{O}(\alpha_s^3)$ fixed-order without $S_\tau^{\rm mod}$	0.1295 ± 0.0046	1.12

Table 3.5: Comparison of global fit results for our full analysis to a fit where the renormalon is not canceled with $\bar{\Omega}_1$, a fit without $S_\tau^{\rm mod}$ (meaning without power corrections with $S_\tau^{\rm mod}(k) = \delta(k)$), and a fit at fixed order without power corrections and log resummation. All results include bottom mass and QED corrections.

1-sigma, 68% CL, for either one dimensional projection). We also show the 68% CL error ellipse by a dashed red line, which corresponds to 1-sigma knowledge for both parameters. As we have shown above, the error in both the dashed and solid larger ellipses is dominated by the theory scan uncertainties, see Eqs. (3.5). The spread of the error ellipses from the different global data sets is compatible with the 1-sigma interpretation of our theoretical error estimate, and hence is already represented in our final results.

Analysis without Power Corrections

Using the simple assumption that the thrust distribution in the tail region is proportional to α_s and that the main effect of power corrections is a shift of the distribution in τ, we estimatethat a 300 MeV power correction will lead to an extraction of α_s from $Q = m_Z$ data that is $\delta\alpha_s/\alpha_s \simeq (-9 \pm 3)\%$ lower than an analysis without power corrections. In our theory code we can easily eliminate all nonperturbative effects by setting $S_\tau^{\rm mod}(k) = \delta(k)$ and $\bar{\Delta} = \delta = 0$. At N^{3}LL$'$ order and using our scan method to determine the perturbative uncertainty a global fit to our default data set yields $\alpha_s(m_Z) = 0.1241 \pm (0.0034)_{\rm pert}$ which is indeed 9% larger than our main result in Eq. (3.5) which accounts for nonperturbative effects. It is also interesting to do the same fit with a purely fixed-order code, which we can do by setting $\mu_S = \mu_J = \mu_H$ to eliminate the summation of logarithms. The corresponding fit yields $\alpha_s(m_Z) = 0.1295 \pm (0.0046)_{\rm pert}$, where the displayed error has again been determined from the theory scan which in this case accounts for variations of μ_H and

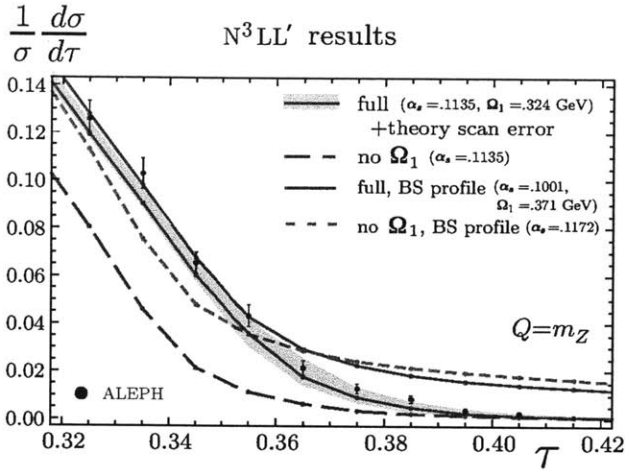

Figure 3-9: Thrust distributions in the far-tail region at N^{3}LL′ order with QED and m_b corrections included at $Q = m_Z$ together with data from ALEPH. The red solid line is the cross section in the R-gap scheme using $\alpha_s(m_Z)$ and Ω_1 obtained from fits using our full code, see Eq. (3.5). The light red band is the perturbative uncertainty obtained from the theory scan method. The red dashed line shows the distribution with the same α_s but without power corrections. The light solid blue line shows the result of a full N^{3}LL′ fit with the BS profile that does not properly treat the multijet thresholds. The short dashed green line shows predictions at N^{3}LL′ with the BS profile, without power corrections, and with the value of $\alpha_s(m_Z)$ obtained from the fit in Ref. [31]. All theory results are binned in the same manner as the experimental data, and then connected by lines.

the numerical uncertainties associated with ϵ_2 and ϵ_3. (A comparison with Ref. [68] is given below in Sec. 3.4.)

These results have been collected in Tab. 3.5 together with the α_s results of our analyses with power corrections in the R-gap and the $\overline{\text{MS}}$ schemes. For completeness we have also displayed the respective χ^2/dof values which were determined by the average of the maximal and the minimum values obtained in the scan.

3.3 Far-tail and Peak Predictions

The factorization formula (2.1) can be simultaneously used in the peak, tail, and far-tail regions. To conclude the discussion of the numerical results of our global analysis in the tail region, we use the results obtained from this tail fit to make predictions in

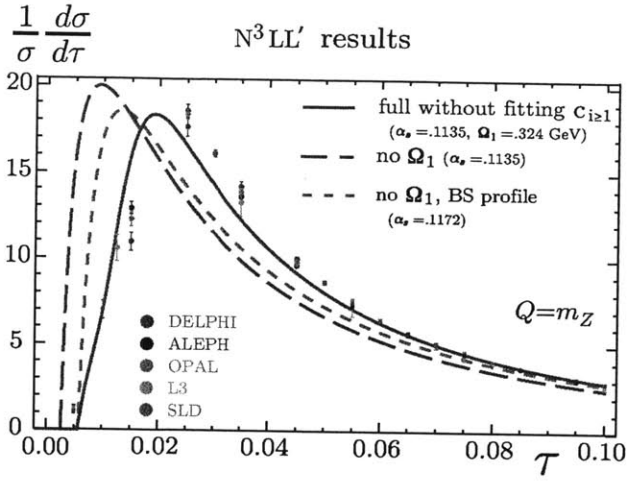

Figure 3-10: Thrust cross section for the result of the N^{3}LL′ fit, with QED and m_b corrections included at $Q = m_Z$. The red solid line is the cross section in the R-gap scheme using $\alpha_s(m_Z)$ and Ω_1 obtained from fits using our full code, see Eq. (3.5). The red dashed line shows the distribution with the same α_s but without power corrections. The short-dashed green line shows predictions at N^{3}LL′ with the BS profile, without power corrections, and with the value of $\alpha_s(m_Z)$ obtained from the fit in Ref. [31]. Data from ALEPH, DELPHI, L3, SLD, and OPAL are also shown.

the peak and the far-tail regions.

In Fig. 3-9 we compare predictions from our full N^{3}LL′ code in the R-gap scheme (solid red line) to the accurate ALEPH data at $Q = m_Z$ in the far-tail region. As input for $\alpha_s(m_Z)$ and Ω_1 we use our main result of Eq. (3.5) and all other theory parameters are set to their default values (see Tab. 3.1). We find excellent agreement within the theoretical uncertainties (pink band). Key features of our theoretical result in Eq. (2.1) that are important in this far-tail region are i) the nonperturbative correction from Ω_1, and ii) the merging of $\mu_S(\tau)$, $\mu_J(\tau)$, and μ_H toward $\mu_S = \mu_J = \mu_H$ at $\tau = 0.5$ in the profile functions, which properly treats the cancellations occurring at multijet thresholds. To illustrate the importance of Ω_1 we show the long-dashed red line in Fig. 3-9 which has the same value of $\alpha_s(m_Z)$, but turns off the nonperturbative corrections. To illustrate the importance of the treatment of multijet thresholds in our profile function, we take the BS profile which does not account for the thresholds (the BS profile is defined and discussed below in Sec. 3.4), and use the smaller $\alpha_s(m_Z)$ and larger Ω_1 that are obtained from the global fit in this case. The result is shown by

the solid light blue line in Fig. 3-9, which begins to deviate from the data for $\tau > 0.36$ and gives a cross section that does not fall to zero at $\tau = 0.5$. The fact that $\alpha_s(m_Z)$ is smaller by 0.0034 for the light blue line, relative to the solid red line, indicates that the proper theoretical description of the cross section in the far-tail region has an important impact on the fit done in the tail region. The final curve shown in Fig. 3-9 is the short-dashed green line, which is the result at the level of precision of the analysis by Becher and Schwartz in Ref. [31]. It uses the BS profile, has no power corrections, and has the value of α_s obtained from the fit in Ref. [31]. It also misses the $Q = m_Z$ data in this region. The results of other $\mathcal{O}(\alpha_s^3)$ thrust analyses, such as Davison and Webber [64] and Dissertori et al. [68, 69], significantly undershoot the data in this far-tail region.[4] To the best of our knowledge, the theoretical cross section presented here is the first to obtain predictions in this far-tail region that agree with the data. Note that our analysis does include some $\mathcal{O}(\alpha_s^k \Lambda_{\rm QCD}/Q)$ power corrections through the use of Eq. (2.21). It does not account for the full set of $\mathcal{O}(\alpha_s \Lambda_{\rm QCD}/Q)$ power corrections as indicated in Eq. (2.1) (see also Tab. 2.2), but the agreement with the experimental data seems to indicate that missing power corrections may be smaller than expected.

Unbinned predictions for the thrust cross section at $Q = m_Z$ in the peak region are shown in Fig. 3-10. The green dashed curve shows the result at the level of precision in Becher and Schwartz, that is N^{3}LL$'$, with the BS profile, without power corrections, and with the value of $\alpha_s(m_Z) = 0.1172$ obtained from their fit. This purely perturbative result peaks to the left of the data. With the smaller value of $\alpha_s(m_Z)$ obtained from our fit, the result with no power corrections peaks even slightly further to the left, as shown by the long-dashed red curve. In contrast, the red solid curve shows the prediction from our full N^{3}LL$'$ code in the R-gap scheme with our central fit values of $\alpha_s(m_Z)$ and Ω_1 given in Eq. (3.5). It clearly indicates that the value of Ω_1 obtained from the fit in the tail region shifts the theory prediction in the peak region much closer to the experimental data. The residual difference between

[4]See the top panel of Fig. 9 in Ref. [64], the top left panel of Fig. 4 in Ref. [68], and the left panel of Fig. 2 in Ref. [69].

the solid red theory curve and the experimental data can be attributed to the fact that the peak is sensitive to power corrections from higher moments, $\Omega_{k\geq 2}$, which have not been fit in our analysis. In our theoretical cross section result this would correspond to fitting $\bar{\Delta}(R_\Delta, \mu_\Delta)$, and a subset of the higher coefficients $c_{i\geq 1}$. The $c_{i\geq 1}$ were all set to zero in the curves shown here, and we leave the presentation of results of this extended fit to a future publication.

3.4 Cross checks and Comparisons

The result for $\alpha_s(m_Z)$ we obtain from our global N^{3}LL$'$ analysis in the R-gap scheme with 487 bins given in Eq. (3.5) is consistent at 1-sigma with the result of Davison and Webber [64] ($\alpha_s(m_Z) = 0.1164 \pm (0.0022)_{\text{hadr+exp}} \pm (0.0017)_{\text{pert}}$). They also carried out a global thrust analysis with a total of 430 experimental bins. In their theory formula, nonperturbative effects were included as a power correction in the effective coupling model which was fit from the experimental data, and their approach also accounts for a renormalon subtraction of the perturbative distribution. In these respects their analysis is similar to ours. However, it differs as their theory formula contains only resummation of logarithms at NLL order, and it also uses a different renormalon subtraction scheme which is based on the running coupling approximation for the subtraction corrections and does not account for the resummation of large logarithms. Moreover the separation of singular and nonsingular perturbative contributions and method to turn off the log resummation at large τ is not equivalent to the one we employ. The difference between their central value and perturbative error and our Eq. (3.5) can be attributed to these items. Their combined hadronization and experimental uncertainty utilizes an error rescaling using the value $\chi^2_{\text{min}}/\text{dof} = 1.09$ obtained for their best fit.

On the other hand, our main result for $\alpha_s(m_Z)$ given in Eq. (3.5) is smaller than the results of Dissertori et al. [68] by 2.9-sigma, of Dissertori et al. [69] by 2.2-sigma, and of Becher and Schwartz [31] by 1.6-sigma. (These results are displayed in Table 3.6.) In these analyses $\alpha_s(m_Z)$ was determined from fits to data for individual Q values and

	sum logs	power corrections	$\alpha_s(m_Z)$
Ref. [68]	no	Monte Carlo (MC)	$0.1240 \pm 0.0034^*$
Ref. [31]	N^{3}LL	uncertainty from MC	$0.1172 \pm 0.0021^*$
Ref. [64]	NLL	effective coupling model	$0.1164 \pm 0.0028^\#$
Ref. [38]	NLL	Monte Carlo	$0.1172 \pm 0.0051^{**}$
Ref. [69]	NLL	Monte Carlo	$0.1224 \pm 0.0039^*$

Table 3.6: Recent thrust analyses which use the $\mathcal{O}(\alpha_s^3)$ fixed-order results. The theoretical component of the errors were determined as indicated, by either: * the error band method, ** variation of the renormalization scale μ, or # by a simultaneous fit to $\alpha_s(m_Z)$ and α_0 (see text for more details). The analyses of Refs. [31, 64] used thrust data only, while Refs.[68, 38, 69] employed six different event shapes.

nonperturbative corrections and their associated uncertainty were taken from Monte Carlo generators in Dissertori et al., or left out from the fit and used to assign the hadronization uncertainty for the final result in Becher and Schwartz. It is possible to turn off pieces of our theoretical code to reproduce the perturbative precision of the codes used in Refs. [68][5] and [31]. It is the main purpose of the remainder of this section to show the outcome of the fits based on these modified theory codes. We show in particular, that the main reason why the above results for $\alpha_s(m_Z)$ are higher than our result of Eq. (3.5) is related to the fact that the nonperturbative corrections extracted from Monte Carlo generators at $Q = m_Z$ are substantially smaller than and incompatible with the ones obtained from our fit of the field theory power correction parameter Ω_1. The use of e^+e^- MC generators to estimate power corrections is problematic since the partonic contributions are based on LL parton showers with at most one-loop matrix elements, complemented by hadronization models below the shower cutoff that are not derived from QCD. The parameters of these models have been tuned to LEP data, and thus unavoidably encode both nonperturbative effects as well as higher order perturbative corrections. Hence, one must worry about double counting, and this makes MC generators unreliable for estimating nonperturbative corrections in higher order LEP analyses.

We start with an examination related to the code used by Becher and Schwartz [31],

[5]We do not attempt to reproduce the NLL/$\mathcal{O}(\alpha_s^3)$ code of Ref. [69] as the final outcome is similar to Ref. [68].

Experiment	Energy	BS results [31]	our BS profile	default profile
ALEPH	91.2 GeV	0.1168(1)	0.1170	0.1223
ALEPH	133 GeV	0.1183(37)	0.1187	0.1235
ALEPH	161 GeV	0.1263(70)	0.1270	0.1328
ALEPH	172 GeV	0.1059(80)	0.1060	0.1088
ALEPH	183 GeV	0.1160(43)	0.1166	0.1205
ALEPH	189 GeV	0.1203(22)	0.1214	0.1260
ALEPH	200 GeV	0.1175(23)	0.1182	0.1224
ALEPH	206 GeV	0.1140(23)	0.1149	0.1185
OPAL	91 GeV	0.1189(1)	0.1198	0.1251
OPAL	133 GeV	0.1165(38)	0.1175	0.1218
OPAL	177 GeV	0.1153(33)	0.1160	0.1200
OPAL	197 GeV	0.1189(14)	0.1197	0.1241
average		0.1172(10)	0.1180	0.1221
global fit (stat)	all Q		0.1188	0.1242
global fit (stat+syst)	all Q		0.1192	0.1245

Table 3.7: Comparison of the results for $\alpha_s(m_Z)$ quoted by Becher and Schwartz in Ref. [31] with results we obtain from our adapted code where power corrections, the m_b and QED corrections, the $\mathcal{O}(\alpha_s^2)$ axial singlet corrections are neglected. The $\mathcal{O}(\alpha_s^3)$ nonlogarithmic constants h_3 and s_3 are set to the values used in Ref. [31] as described in the text. We follow the fit approach of Ref. [31] and employ their profile functions for the nonsingular, hard, jet and soft scales, with results shown in the column labeled "our BS profile". In the last column we show results with this same code, but using our default profile functions. The errors in the third column are the statistical experimental uncertainty.

which has N^{3}LL$'$ accuracy but does not include power corrections or renormalon subtractions. This treatment can be reproduced in our factorization formula by turning off the nonperturbative soft nonperturbative function by setting $S_\tau^{\rm mod}(k) = \delta(k)$ and $\bar{\Delta} = \delta = 0$. Moreover they used the central scale setting $\mu_H = Q$, $\mu_J = Q\sqrt{\tau}$ and $\mu_S = Q\tau$. We can reproduce this from our profile functions for $\mu_0 = n_1 = e_J = 0$, $t_2 = 3/2$ and $e_H = n_s = 1$, which we call the BS profile setting. The BS profile functions for $\mu_J(\tau)$ and $\mu_S(\tau)$ are shown by dashed curves in Fig. 2-5. (Note that the BS profile setting does not cause μ_S, μ_J, and μ_H to merge in the far-tail region and become equal at $\tau = 0.5$, which is needed to switch off the SCET resummation of logarithms in the multijet region to satisfy the constraints from multijet thresholds.)

Becher and Schwartz set the $\mathcal{O}(\alpha_s^3)$ nonlogarithmic correction in the Euclidean hard factor $C(-q^2)$ to zero (with $H_Q = |C(q^2)|^2$ for $q^2 = Q^2 > 0$), which in our notation corresponds to $h_3 = 11771.50$ (somewhat larger than the now known h_3). We also set $s_2 = -40.1$ (see Ref. [94, 31]) and $s_3 = -324.631$ for the non-logarithmic $\mathcal{O}(\alpha_s^2)$ and $\mathcal{O}(\alpha_s^3)$ constants in the soft function (both within our range of uncertainties). The value for s_3 corresponds to setting the $\mathcal{O}(\alpha_s^3)$ nonlogarithmic corrections in the expanded position space soft function to zero. Finally, we also turn off our QED and bottom quark mass corrections and the $\mathcal{O}(\alpha_s^2)$ axial singlet corrections, and use the fixed-order normalization from Eq. (2.56). For the fit procedure we follow Becher and Schwartz and analyze all ALEPH and OPAL data for individual Q values in the τ ranges given in their work and account only for statistical experimental errors in the χ^2 functions. The outcome of the fits for $\alpha_s(m_Z)$ at N^{3}LL$'$ order is given in the fourth column of Tab. 3.7. The third column shows their central values and the respective statistical experimental errors as given in Ref. [31]. The numbers we obtain are 0.0001 to 0.0011 higher than their central values, and we attribute this discrepancy to the nonsingular contributions.[6] (Becher and Schwartz also used a difference of cumulants for their fits, as in Eq. (2.59) with the choice $\tilde{\tau}_1 = \tau_1$ and $\tilde{\tau}_2 = \tau_2$, rather than integrating $\mathrm{d}\sigma/\mathrm{d}\tau$ as we do for the table. The spurious contribution induced by this choice has a significant effect on the χ^2 values, but a small effect on $\alpha_s(m_Z)$, changing the values shown in the table by ≤ 0.0003. For cumulants that use $\tilde{\tau}_1 = \tilde{\tau}_2 = (\tau_1 + \tau_2)/2$ with no spurious contribution, the difference from our integrated distribution results is reduced to ≤ 0.0001 for $\alpha_s(m_Z)$, and χ^2 values are almost unaffected.)

The numbers obtained at N^{3}LL$'$ above are significantly larger than our central fit result $\alpha_s(m_Z) = 0.1135$ shown in Eq. (3.5) obtained from our full code. These differences are mainly related to the nonperturbative power correction and partly due to the BS profile setting. To distinguish these two and other effects we can take the purely perturbative code described above and turn back to our default setting

[6]Becher and Schwartz uncovered a numerical problem with the original EERAD3 code at very small τ, which correspondingly had an impact on the nonsingular function used in their analysis which was extracted from EERAD3. When their nonsingular distribution is updated to results from the new EERAD3 code they become significantly closer to ours, differing by $\lesssim 0.0002$. We thank M. Schwartz for correspondence about this and for providing us with their new fit values.

for the profile functions with the parameters given in Tab. 3.1. The results are shown in the fifth column in Tab. 3.7 using again only statistical experimental errors in the χ^2 functions. The $\alpha_s(m_Z)$ values using our default profile functions are by 0.0028 to 0.0058 larger than for the BS profile setting in the fourth column.[7] (The fifth column results again integrate the distribution over each bin rather than using differences of cumulants, which for our profile is important for the reasons discussed in Sec. 2.5.[8]) A similar difference arises from a global fit to our default data set of Sec. 3.1 using the same fit procedure: For the BS profile setting we obtain $\alpha_s(m_Z) = 0.1189$, while the default profile setting gives $\alpha_s(m_Z) = 0.1242$ (second to last line of Tab. 3.7). Using instead the χ^2-analysis of our main analysis which includes the experimental systematical errors we obtain $\alpha_s(m_Z) = 0.1192$ for the BS profile setting and $\alpha_s(m_Z) = 0.1245$ for the default profile setting (last line of Tab. 3.7). The latter result is by 0.0110 larger than our 0.1135 central fit result in Eq. (3.5). This 10% effect is almost entirely coming from the power correction Ω_1. The difference of 0.3% to the full perturbative result of $\alpha_s(m_Z) = 0.1241$ given in Table 3.5 illustrates the combined effect of the QED, the bottom quark mass and the $\mathcal{O}(\alpha_s^2)$ axial singlet corrections and the $\mathcal{O}(\alpha_s^3)$ hard constant h_3.

Finally, let us examine the results related to the code used by Dissertori et al. in Ref. [68], which uses the fixed-order $\mathcal{O}(\alpha_s^3)$ results without a resummation of logarithms, but accounts for nonperturbative corrections determined from the difference of running Monte Carlo generators in parton and hadron level modes. Since in this work we are not concerned with extracting the parton-hadron level transfer matrix from Monte Carlo generators, we use in the following our code neglecting power corrections by setting $S_\tau^{\rm mod}(k) = \delta(k)$, setting $\bar{\Delta} = \delta = 0$, and setting $\mu_H = \mu_J = \mu_S$. The latter switches off the log resummation factors in Eq. (2.1) such that only the $\mathcal{O}(\alpha_s^3)$ fixed order expression remains. We also include the m_b corrections, but neglect

[7] With our full code, which accounts in particular for power corrections and renormalon subtractions, the shift due to the modified profile functions becomes smaller; shifts in $\alpha_s(m_Z)$ of 0.005 become 0.003.

[8] Using the cumulant method with $\tilde{\tau}_1 = \tau_1$ and $\tilde{\tau}_2 = \tau_2$ in Eq. (2.59), which has a spurious contribution, changes the values in the fifth column of Tab. 3.1 by about -0.003 to -0.005. On the other hand, using the cumulant method without a spurious contribution, $\tilde{\tau}_1 = \tilde{\tau}_2 = (\tau_1 + \tau_2)/2$, changes the values in the fifth column by ≤ 0.0001.

Experiment	Energy	Dissertori et al. results [68]	Our fixed order code
ALEPH	91.2 GeV	0.1274(3)	0.1281
ALEPH	133 GeV	0.1197(35)	0.1289
ALEPH	161 GeV	0.1239(54)	0.1391
ALEPH	172 GeV	0.1101(72)	0.1117
ALEPH	183 GeV	0.1132(32)	0.1247
ALEPH	189 GeV	0.1140(20)	0.1295
ALEPH	200 GeV	0.1094(22)	0.1260
ALEPH	206 GeV	0.1075(21)	0.1214

Table 3.8: Comparison of the thrust results quoted in Ref. [68] with our numerical reproduction. For this numerical exercise we have used their procedure to get the error matrix for the experimental data. This amounts to considering only the statistical errors in an uncorrelated way, with the resulting experimental error shown in the third column. Whereas in the code of Ref. [68] hadronization corrections are included determined from Monte Carlo simulations our numbers are based on a pure partonic code neglecting nonperturbative effects. We use the default value for the scale setting, i.e. $\mu = Q$.

QED effects. Since these modifications give us a code that does not contain nonperturbative corrections, the differences to Ref. [68] we obtain will serve as a quantitative illustration for the size of the hadronization corrections obtained by a transfer matrix from the Monte Carlo generators PYTHIA, HERWIG, and ARIADNE, tuned to global hadronic observables at m_Z.

For the fits for $\alpha_s(m_Z)$ we follow Dissertori et al. [68] analyzing ALEPH data for individual Q values in the τ ranges given in their work and accounting only for statistical experimental errors in the χ^2 functions. The results of Dissertori et al. and the outcome for our best fits are given in the third and fourth column of Tab. 3.8, respectively. We have also quoted the respective statistical errors from Ref. [68]. For the high statistics data at $Q = m_Z$ our $\alpha_s(m_Z)$ result is larger than theirs, but the discrepancy amounts to only 0.0007 which is a 0.5% shift in $\alpha_s(m_Z)$. This illustrates the small size of the nonperturbative hadronization corrections encoded in the Monte Carlo transfer matrix at $Q = m_Z$. This is clearly incompatible with the size of the nonperturbative correction we have obtained from simultaneous fits of α_s and Ω_1, confirming the concerns on Monte Carlo hadronization corrections. Interestingly, with the exception of $Q = 172\,\text{GeV}$, our fixed-order results for all Q are relatively

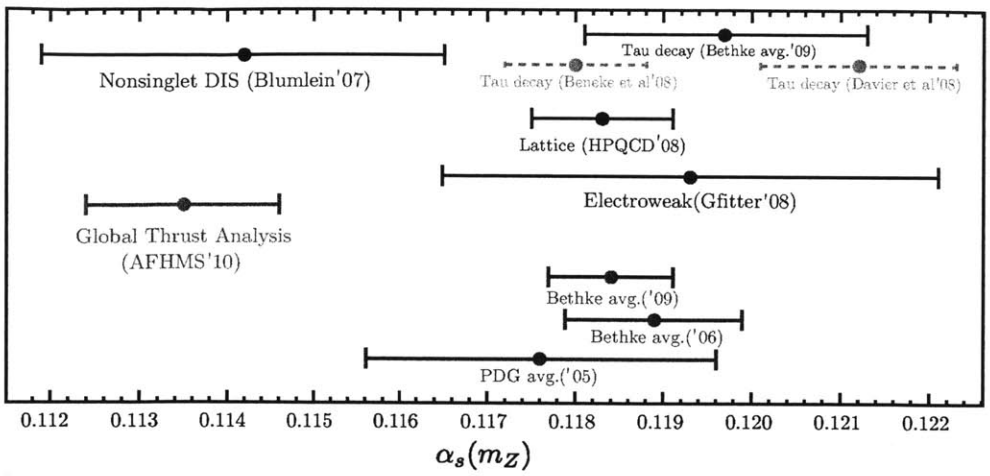

Figure 3-11: Comparison of selected determinations of $\alpha_s(m_Z)$ defined in the $\overline{\text{MS}}$ scheme.

stable and close to the result at $Q = m_Z$, while their $\alpha_s(m_Z)$ values, which use the transfer matrix for nonperturbative effects, are systematically lower for $Q > m_Z$ by 7 to 13%. Thus the nonperturbative effects from the Monte Carlo transfer matrix are substantially larger for $Q > m_Z$.[9] The same behavior is also visible in the results of Ref. [69], which includes NLL resummation of logarithms. Since the transfer matrix is obtained from Monte Carlo tuned to the more accurate $Q = m_Z$ data, we believe that this issue deserves further investigation. To complete the discussion we use the same fixed-order theory code to quote results for a global fit to our default data set. Using the fit procedure as described in Sec. 3.1 we obtain $\alpha_s(m_Z) = 0.1300 \pm (0.0047)_{\text{pert}}$. (The corresponding errors obtained from the error band method are given in the fourth line of Tab. 3.4.)

3.5 Conclusions

In this work we have provided a factorization formula for the thrust distribution in e^+e^- annihilation which incorporates the previously known $\mathcal{O}(\alpha_s^2)$ and $\mathcal{O}(\alpha_s^3)$ per-

[9]Note that the weighted average of the $Q > m_Z$ thrust results of Dissertori et al. is $\alpha_s(m_Z) = 0.1121$ and is consistent with our result in Eq. (3.5) within the larger uncertainties. Also note that the Q dependence of our $\Omega_1(R,R)/Q$ power correction is affected by its anomalous dimension, cf. Fig. 2-3.

turbative QCD corrections and summation of large logarithms at N^3LL order for the singular terms in the dijet limit where the thrust variable $\tau = 1 - T$ is small. The factorization formula used here incorporates a systematic description of nonperturbative effects with a soft function defined in field theory. The soft function describes the dynamics of soft particle radiation at large angles. We have also accounted for bottom mass and QED photon effects for fixed-order contributions as well as for the summation of QED logarithms. With specifically designed τ-dependent profile functions for the renormalization scales the factorization formula can be applied in the peak, tail and far-tail regions of the thrust distribution. It has all nonperturbative effects accounted for up to terms of $\mathcal{O}(\alpha_s \Lambda_{\rm QCD}/Q)$, which is parametrically smaller than the remaining perturbative uncertainty ($< 2\%$ for $Q = m_Z$) of the thrust distribution predictions in the tail region where we carried out the fits to the experimental data.

In the tail region, $2\Lambda_{\rm QCD}/Q \ll \tau \lesssim 1/3$, the dominant effects of the nonperturbative soft function are encoded in its first moment Ω_1, which is a power correction to the cross section. Fitting to tail data at multiple Qs as we did in this work, the strong coupling $\alpha_s(m_Z)$ and the moment Ω_1 can be simultaneously determined. An essential ingredient to reduce the theoretical uncertainties to the level of $< 2\%$ in the thrust distribution is our use of a short-distance scheme for Ω_1, called the R-gap scheme, that induces subtractions related to an $\mathcal{O}(\Lambda_{\rm QCD})$ renormalon contained in the $\overline{\rm MS}$ perturbative thrust cross section from large angle soft gluon radiation. The R-gap scheme introduces an additional scale that leads to large logarithms in the subtractions, and we carry out a summation of these additional logarithms with renormalization group equations in the variable R. The R-gap scheme reduces the perturbative uncertainties in our best highest order theory code by roughly a factor of two compared to the pure $\overline{\rm MS}$ definition, $\bar{\Omega}_1$, where renormalon effects are not treated.

The code we use in this analysis represents the most complete theoretical treat-

ment of thrust existing at this time. As our final result we obtain

$$\alpha_s(m_Z) = 0.1135 \pm 0.0011,$$

$$\Omega_1(R_\Delta, \mu_\Delta) = 0.323 \pm 0.051 \text{ GeV}, \tag{3.7}$$

where α_s is defined in the $\overline{\text{MS}}$ scheme, and Ω_1 in the R-gap scheme at the reference scales $R_\Delta = \mu_\Delta = 2$ GeV. Here the respective total 1-sigma errors are shown. The results with individual 1-sigma errors quoted separately for the different sources of uncertainties are given in Eq. (3.5). Neglecting the nonperturbative effects incorporated in the soft function, and in particular Ω_1, from the fits gives $\alpha_s(m_Z) = 0.1241$ which exceeds the result in Eq. (3.7) by 9%.

Analyses of event shapes with a simultaneous fit of α_s and a power correction have been carried out earlier with the effective coupling model. Davison and Webber [64] analyzed the thrust distribution and determined $\alpha_s(m_Z) = 0.1164 \pm 0.0028$ also using $\mathcal{O}(\alpha_s^3)$ fixed-order input, but implementing the summation of logarithms only at NLL order (for further discussion see Sec. 3.4). Recently Gehrmann et al. [84] analyzed moments of different event shape distributions, also with the effective coupling model, and obtained $\alpha_s(m_Z) = 0.1153 \pm 0.0029$ using fixed-order perturbation theory at $\mathcal{O}(\alpha_s^3)$. Both analyses neglected bottom mass and QED corrections. Our result in Eq. (3.7) is compatible with these analyses at 1-sigma, but has smaller uncertainties.

These results and our result for $\alpha_s(m_Z)$ in Eq. (3.7) are substantially smaller than the results of event shape analyses employing input from Monte Carlo generators to determine nonperturbative effects. We emphasize that using parton-to-hadron level transfer matrices obtained from Monte Carlo generators to incorporate nonperturbative effects is not compatible with a high-order theoretical analysis such as ours, and thus analyses relying on such Monte Carlo input contain systematic errors in the determination of α_s from thrust data. The small effect of hadronization corrections on thrust observed in Monte Carlo generators at $Q = m_Z$ and the corresponding small shift in $\alpha_s(m_Z)$ do not agree with the 9% shift we have obtained from our fits as mentioned above. For the reasons discussed earlier, we believe Monte Carlo should

not be used for hadronization uncertainties in higher order analyses.

Although our theoretical approach represents the most complete treatment of thrust at this time, and all sources of uncertainties known to us have been incorporated in our error budget, there are a number of theoretical issues related to subleading contributions that deserve further investigation. These issues include (i) the summation of logarithms for the nonsingular partonic cross section, (ii) the structure of the $\mathcal{O}(\alpha_s\Lambda_{\rm QCD}/Q)$ power corrections, (iii) analytic perturbative computations of the $\mathcal{O}(\alpha_s^2)$ and $\mathcal{O}(\alpha_s^3)$ nonlogarithmic coefficients s_2 and s_3 in the partonic soft function, the $\mathcal{O}(\alpha_s^3)$ nonlogarithmic coefficient j_3 in the partonic jet function, and the 4-loop QCD cusp anomalous dimension $\Gamma_3^{\rm cusp}$. Concerning issue (i) we have incorporated in our analysis the nonsingular contributions in fixed-order perturbation theory and estimated the uncertainty related to the higher order logarithms through the usual renormalization scale variation. Further theoretical work is needed to derive the renormalization group structure of subleading jet, soft, and hard functions in the nonsingular contributions and to use these results to sum the corresponding logarithms. Concerning issue (ii) we have shown that our theoretical description for the thrust distribution contains a remaining theoretical uncertainty from nonperturbative effects of order $\mathcal{O}(\alpha_s\Lambda_{\rm QCD}/Q)$. Parametrically, this uncertainty is substantially smaller than the perturbative error of about 1.7% for the thrust distribution in the tail region at LEP-I energies that is contained in our best theory code. Furthermore, our predictions in the far-tail region at $Q = m_Z$ appear to indicate that the dominant corrections of this order are already captured in our setup. Nevertheless a systematic analysis of these subleading effects is certainly warranted.

Apart from investigating these theoretical issues, it is also warranted to apply the high-precision approach using soft-collinear effective theory to other event shape distributions in order to validate the result in Eq. (3.7). Event shapes that can be clearly treated with similar techniques are: heavy and light jet masses, the C-parameter, and the angularities [36, 96]. For many of these event shapes it has been proven field theoretically that the same parameter Ω_1 describes the leading power corrections in the tail region [110], although there might be caveats related to the experimental treat-

ment of hadron masses [135, 81]. Thus, one has the potential to extend the analysis done here to include additional data without additional parameters. An analysis for the heavy jet mass accounting for perturbative contributions at $\mathrm{N^3LL}$ in $\overline{\mathrm{MS}}$ with different profile functions and a simple soft function model for power corrections without renormalon subtractions, was recently carried out in Ref. [56], providing a first step in this direction.

To conclude this work we cannot resist comparing our result for $\alpha_s(m_Z)$ with the results of a selection of analyses using other techniques and observables, as shown in Fig. 3-11. We include a $\mathrm{N^3LO}$ analysis of data from deep inelastic scattering in the nonsinglet channel [42][10], the recent HPQCD lattice determination based on fitting Wilson loops and the Υ-Υ' mass difference [63], the result from fits to electroweak precision observables based on the Gfitter package [78], analyses of τ-decay data using fixed-order [35] and contour-improved perturbation theory [62], together with an average of τ results from Ref. [40]. Finally we also show a collection of α_s-averages from Refs. [40, 39, 149]. The DIS result is consistent with our fit result, whereas the deviation from HPQCD is 3.5σ. It is interesting to note that the high energy extractions from thrust and DIS appear to be smaller than the low energy extractions from Lattice and τ decays.

[10]Analyses studying α_s with data that depends also on the gluon PDF have been carried out in Refs. [118, 17, 65, 108].

Chapter 4

Determination of $\alpha_s(m_Z)$ from Thrust Moments

4.1 Introduction

We will use the full τ range results to analyze moments M_n of the thrust distribution in $e^+e^- \to$ jets,

$$M_n = \frac{1}{\sigma} \int_0^{\tau_{\max}=1/2} \mathrm{d}\tau \; \tau^n \, \frac{\mathrm{d}\sigma}{\mathrm{d}\tau} \,. \tag{4.1}$$

Unlike for tail fits, the entire physical τ range contributes, providing sensitivity to a different region of the spectrum. Experimental results are available for many values of Q, and the analysis of systematic uncertainties is to a large extent independent from that for the binned distributions. Thus the outcome for a fit of data for the first moment M_1 to $\alpha_s(m_Z)$ and Ω_1 serves as an important cross check of the results obtained in Ref. [1]. The M_n moments are also not sensitive to large logarithms, and hence provide a non-trivial check on whether the $\mathrm{N^3LL} + \mathcal{O}(\alpha_s^3)$ full spectrum results, which contain a summation of logarithms of τ with a substantial numerical effects for small τ values, can reproduce this property. We explore this issue both for central values and for theory uncertainty estimates.

The second purpose of this work is to discuss the structure of higher order power

corrections in thrust moments. We find that cumulant moments M_n' (cumulants) are very useful, since they allow for a cleaner separation of the subleading nonperturbative matrix elements compared to the M_n moments of Eq. (4.1). Cumulants include the variance M_2' and skewness M_3', and we will consider the first five:

$$\begin{aligned} M_1' &= M_1\,, \\ M_2' &= M_2 - M_1^2\,, \\ M_3' &= M_3 - 3\,M_2\,M_1 + 2\,M_1^3\,, \\ M_4' &= M_4 - 4\,M_3\,M_1 - 3\,M_2^2 + 12\,M_2\,M_1^2 - 6\,M_1^4\,, \\ M_5' &= M_5 - 5\,M_4\,M_1 - 10\,M_3\,M_2 + 20\,M_3\,M_1^2 \\ &\quad + 30\,M_2^2 M_1 - 60\,M_1^3\,M_2 + 24\,M_1^5\,. \end{aligned} \tag{4.2}$$

In the leading order thrust factorization theorem the power correction matrix elements for the moments M_n are called Ω_m while for the cumulants M_n' they are called Ω_m'. [The Ω_m' are also related to the Ω_m by Eq. (4.2) with $M_n \to \Omega_n$.] In particular, the invariance of the cumulants to shifts in τ implies that the $M_{n\geq 2}'$ moments are completely insensitive to the leading thrust power correction parameter Ω_1, and hence can provide non-trivial information on the higher order power corrections which enter as Ω_n'/Q^n and as $1/Q^2$ power corrections from terms beyond the leading factorization theorem. In contrast, for each $M_{n\geq 2}$ there is a term $\sim \alpha_s\Omega_1/Q$ that for larger Qs dominates over the Ω_m/Q^m terms.[1] This work has been presented in [2].

4.1.1 Review of Experiments and Earlier Literature

Dedicated experimental analyses of thrust moments have been reported by various experiments: JADE [124] measured the first moment at $Q = 35$, 44 GeV, and in [131] reported measurements of the first five moments at $Q = 14$, 22, 34.6, 35, 38.3, 43.8 GeV; OPAL [5] measured the first five moments at $Q = 91$, 133, 177, 197 GeV, and

[1] The cumulant moments begin to differ for $n \geq 4$ from the so-called central moments, $\langle(\tau - M_1)^n\rangle$. Both cumulant and central moments are shift independent, but the cumulants are slightly preferred because they are only sensitive to a single moment of the leading order soft function in the thrust factorization theorem.

there is an additional measurement of the first moment at $Q = 161$ GeV [13]; ALEPH [91] measured the first moment at $Q = 91.2$, 133, 161, 172, 183, 189, 196, 200, 206 GeV; DELPHI [6] has measurements of the first moment at $Q = 45.2$, 66, 76.3 GeV, measurements of the first three moments at $Q = 183$, 189, 192, 196, 200, 202, 205, 207 GeV [7], and at $Q = 91.2$, 133, 161, 172, 183 GeV [9]; and L3 [11] measured the first two moments at $Q = 91.2$ GeV and other center of mass energies which are superseded by the ones in [12] at $Q = 41.4$, 55.3, 65.4, 75.7, 82.3, 85.1, 130.1, 136.1, 161.3, 172.3, 182.8, 188.6, 194.4, 200.2, 206.2 GeV. Finally, the variance and skewness have been explicitly measured by DELPHI [9] at $Q = 133$, 161, 172, 183 GeV; and OPAL [13] at $Q = 161$ GeV. All of these experimental moments will be used in our fits, with the exception of the results in Ref. [131].

In principle the JADE results in Ref. [131] supersede the earlier analysis of this data reported in Ref. [124]. In the more recent analysis the contribution of primary $b\bar{b}$ events has been subtracted using Monte Carlo generators.[2] Since the theoretical precision of these generators is significantly worse than our $\mathrm{N^3LL} + \mathcal{O}(\alpha_s^3)$ treatment of massless quark effects and our $\mathrm{NNLL} + \mathcal{O}(\alpha_s)$ treatment of m_b-dependent corrections, it is not clear how our code should be modified consistently to account for these subtractions. The effect may be significant. For example, comparing the old versus new JADE data at $Q = 44\,\mathrm{GeV}$ one finds $M_1 = 0.0860 \pm 0.0014$ versus $M_1 = 0.0807 \pm 0.0016$. This corresponds to a $3.4\,\sigma$ change assuming 100% correlated uncertainties (or a $2.6\,\sigma$ change with uncorrelated uncertainties). For this reason our default dataset incorporates only the older JADE moment data. We will report on the change that would be induced by using the new JADE data if we simply ignore the fact that the $b\bar{b}$ events were removed. Overall in our analysis we find that the older JADE data provides consistent results when employed in a combined fit with data from the other experiments (related to smaller χ^2 values).

Event shape moments have also been extensively studied in the theoretical literature. The $\mathcal{O}(\alpha_s^3)$ QCD corrections for event shape moments have been calculated in Ref. [87, 145]. The leading Λ/Q power correction to the first moment of event shape

[2]We thank C. Pahl for clarifying precisely how this was done.

distributions were first studied in [74, 15, 16, 126] often with the study of renormalons (see [33] for a review). Hadronization effects have also been frequently considered in the framework of the dispersive model for the strong coupling [74, 73, 71]. In this approach an IR cutoff μ_I is introduced and the strong coupling constant below the scale μ_I is replaced by an effective coupling α_{eff} such that perturbative infrared effects coming from scales below μ_I are subtracted. In the dispersive model the term $\mu_I \alpha_0$ is the analog of the QCD matrix element Ω_1 that is derived from the operator product expansion (OPE). Since in the dispersive model there is only one nonperturbative parameter, it does not contain analogs of the independent nonperturbative QCD matrix elements $\Omega_{n\geq 2}$ of the operator product expansion. Thus measurements of $\Omega'_{n\geq 2}$ can be used as a test for additional nonperturbative physics that go beyond this framework.

The dispersive model has been used in Refs. [41, 5, 129] together with $\mathcal{O}(\alpha_s^2)$ fixed order results to analyze event shape moments, fitting simultaneously to $\alpha_s(m_Z)$ and α_0. Recently these analyses have been extended to $\mathcal{O}(\alpha_s^3)$ in Ref. [84], based on code for $n_f = 5$ massless quark flavors, using data from [5, 131] and fitting to the first five moments for several event-shape variables. Our numerical analysis is only of thrust moments, but with a global dataset from all available experiments. A detailed comparison with Ref. [84] will be made at appropriate points in the paper. Theoretically our analysis goes beyond their work by using a formalism that has no large logarithms in the renormalon subtraction, includes the analog of the "Milan factor" [72, 71] in our framework at $\mathcal{O}(\alpha_s^3)$ (one higher order than [84]), and incorporates higher order power corrections beyond the leading shift from Ω_1. We also test the effect of including resummation.

4.1.2 Outline

This article is organized as follows: We start out by defining moments and cumulants of distributions, and their respective generating functions in Sec. 4.2, where we also discuss the leading and subleading power corrections of thrust moments in an OPE framework. In Sec. 4.3 we present and discuss our main results for $\alpha_s(m_Z)$ from fits to the first thrust moment M_1. In Sec. 4.6 we analyze higher moments $M_{n\geq 2}$. Sec. 4.7

contains an analysis of subleading power corrections from fits to cumulant moment data. Our conclusions are presented in Sec. 4.8.

4.2 Formalism

4.2.1 Various Moments of a Distribution

The moments of a probability distribution function $p(k)$ are given by

$$M_n = \langle k^n \rangle = \int \mathrm{d}k\, p(k)\, k^n. \tag{4.3}$$

The characteristic function is the generator of these moments and is defined as the Fourier transform

$$\tilde{p}(y) = \langle e^{-iky} \rangle = \int \mathrm{d}k\, p(k)\, e^{-iky} = \sum_{n=0}^{\infty} \frac{(-iy)^n}{n!} M_n, \tag{4.4}$$

with $M_0 = 1$. The logarithm of $\tilde{p}(y)$ generates the cumulants (or connected moments) M'_n of the distribution

$$\ln \tilde{p}(y) = \sum_{n=1}^{\infty} \frac{(-iy)^n}{n!} M'_n, \tag{4.5}$$

and is called the cumulant generating function. For $n \geq 2$ the cumulants have the property of being invariant under shifts of the distribution. Replacing $p(k) \to p(k-k_0)$ takes $\tilde{p}(y) \to e^{-iyk_0}\, \tilde{p}(y)$, which shifts $M'_1 \to M'_1 + k_0$ while leaving all $M'_{n\geq 2}$ unchanged. Writing

$$\sum_{N=0}^{\infty} \frac{(-iy)^N}{N!} M_N = \exp\left[\sum_{j=1}^{\infty} \frac{(-iy)^j}{j!} M'_j\right] = \prod_{n=j}^{\infty} \sum_{R=0}^{\infty} \frac{(-iy)^{jR}}{R!} \left(\frac{M'_j}{j!}\right)^R, \tag{4.6}$$

one can derive an all-n relation between moments and cumulants of a distribution:

$$M_N = N! \sum_{i=1}^{p(N)} \prod_{j=1}^{N} \frac{(M'_j)^{\kappa_{ij}}}{\kappa_{ij}! \, (j!)^{\kappa_{ij}}} \,. \tag{4.7}$$

Here the κ_{ij} are non-negative integers which determine a partition of the integer N through $\sum_{j=1}^{N} j \, \kappa_{ij} = N$, and $p(N)$ is the the number of unique partitions of N. [A partition of N is a set of integers which sum to N. Here κ_{ij} is the number of times the value j appears as a part in the i'th partition, and corresponds to R in Eq. (4.6).] As an example we quote the relation for $N = 4$ which has five partitions, $p(4) = 5$, giving

$$M_4 = M'_4 + 4\, M'_3\, M'_1 + 3\, M'^2_2 + 6\, M'_2\, M'^2_1 + M'^4_1 \,. \tag{4.8}$$

In the fourth partition, $i = 4$, we have $\kappa_{41} = 2$, $\kappa_{42} = 1$, and $\kappa_{43} = \kappa_{44} = 0$, and the factorials give the prefactor of 6. Eq. (4.7) gives the moments M_i in terms of the cumulants M'_i, and these relations can be inverted to yield the formulas quoted for the cumulants in Eq. (4.2). $M'_2 \geq 0$ is the well known variance of the distribution. Higher order cumulants can be positive or negative. The skewness of the distribution M'_3 provides a measure of its asymmetry, and we expect $M'_3 > 0$ for thrust with its long tail to the right of the peak. The kurtosis M'_4 provides a measure of the "peakedness" of the distribution, where $M'_4 > 0$ for a sharper peak than a Gaussian.[3]

The shift independence of the cumulants M'_n make them an ideal basis for studying event shape moments. In particular, since the leading $\mathcal{O}(\Lambda_{\rm QCD}/Q)$ power correction acts similar to a shift to the event shape distribution [74, 73, 75, 110, 111], we can anticipate that $M'_{n\geq 2}$ will be more sensitive to higher order power corrections. We will quantify this statement in the next section by using factorization for the thrust distribution to derive factorization formulae for the thrust cumulants in the form of an operator product expansion.

[3]The cumulants of a Gaussian are all zero for $n > 2$, and the cumulants of a delta function are all zero for $n > 1$.

4.2.2 Thrust moments

We will first make use of the leading order factorization theorem, $\mathrm{d}\sigma/\mathrm{d}\tau = \int \mathrm{d}p\,(\mathrm{d}\hat{\sigma}/\mathrm{d}\tau)(\tau - p/Q)F_\tau(p)$, which is valid for all τ. It separates perturbative $\mathrm{d}\hat{\sigma}/\mathrm{d}\tau$ and nonperturbative $F_\tau(p)$ contributions to all orders in α_s and $\Lambda_{\rm QCD}/(Q\,\tau)$, but is only valid at leading order in $\Lambda_{\rm QCD}/Q$. For this factorization theorem we follow Ref. [1] (except that here we denote the nonperturbative soft function by F_τ).[4] We will then extend our analysis to parameterize corrections to all orders in $\Lambda_{\rm QCD}/Q$.

Taking moments of the leading order $\mathrm{d}\sigma/\mathrm{d}\tau$ gives[5]

$$\begin{aligned} M_n &= \int_0^{\tau_{\rm m}} \mathrm{d}\tau\,\tau^n \int_0^{Q\tau} \mathrm{d}p\,\frac{1}{\hat{\sigma}}\frac{\mathrm{d}\hat{\sigma}}{\mathrm{d}\tau}\Big(\tau - \frac{p}{Q}\Big)\,F_\tau(p) \\ &= \int_0^\infty \mathrm{d}\tau\,\mathrm{d}p\,\theta\Big(\tau_m - \tau - \frac{p}{Q}\Big)\Big(\tau + \frac{p}{Q}\Big)^n \frac{1}{\hat{\sigma}}\frac{\mathrm{d}\hat{\sigma}}{\mathrm{d}\tau}(\tau)\,F_\tau(p) \\ &= \Big[\sum_{\ell=0}^n \binom{n}{\ell}\Big(\frac{2}{Q}\Big)^{n-\ell}\hat{M}_\ell\,\Omega_{n-\ell}\Big] - E_n^{(A)} - E_n^{(B)}\,, \end{aligned} \tag{4.9}$$

where $\hat{\sigma}$ is the perturbative total hadronic cross section and all hatted quantities are perturbative. In the last line of Eq. (4.9) we used $\theta(\tau_m - \tau - p/Q) = \theta(\tau_m - \tau)[1 - \theta(p/Q - \tau_m) - \theta(\tau_m - p/Q)\,\theta(p/Q + \tau - \tau_m)]$ to obtain the three terms. In Eq. (4.9) the term in square brackets is our desired result containing the perturbative $\hat{M}_n$ and nonperturbative Ω_n moments

$$\begin{aligned} \hat{M}_n &= \int_0^{\tau_{\rm m}} \mathrm{d}\tau\,\tau^n\,\frac{1}{\sigma}\frac{\mathrm{d}\hat{\sigma}}{\mathrm{d}\tau}\,(\tau)\,, & \hat{M}_0 &= 1\,, \\ \Omega_n &= \int_0^\infty \mathrm{d}p\,\Big(\frac{p}{2}\Big)^n F_\tau(p)\,, & \Omega_0 &= 1\,. \end{aligned} \tag{4.10}$$

[4]Earlier discussions of shape functions for thrust can be found in Refs. [107, 106].

[5]This manipulation is valid when the renormalization scales of the jet and soft function which implement resummation are $\mu_i = \mu_i(\tau - p/Q)$, rather than the more standard $\mu_i(\tau)$ used in [1]. Both choices are perturbatively valid, and we have checked that the difference is 0.4 % for M_1, rising to 0.8 % for M_5, and hence is always well within the perturbative uncertainty.

The small "error" terms in Eq. (4.9) are given by

$$E_n^{(A)} = \sum_{\ell=0}^{n} \binom{n}{\ell} \Big(\frac{2}{Q}\Big)^{n-\ell} \hat{M}_\ell \int_{Q\,\tau_m}^{\infty} \mathrm{d}p \, \Big(\frac{p}{2}\Big)^{n-\ell} F_\tau(p), \tag{4.11}$$

$$E_n^{(B)} = \int_0^{\tau_m} \mathrm{d}\tau \int_{Q(\tau_m-\tau)}^{Q\tau_m} \mathrm{d}p \, \Big(\tau + \frac{p}{Q}\Big)^n \frac{1}{\hat{\sigma}} \frac{\mathrm{d}\hat{\sigma}}{\mathrm{d}\tau}(\tau) F_\tau(p)\,.$$

For the contribution $E_n^{(A)}$ the p-integral is smaller than 10^{-30} for any Q for the first five moments, and hence $E_n^{(A)} \simeq 0$. This occurs because $F_\tau(p)$ falls off exponentially for $p \gtrsim 2\,\Omega_1 \sim 2\,\Lambda_{\rm QCD}$, and hence values $p \geq Q\,\tau_m = Q/2$ are already far out on the exponential tail. The $E_n^{(B)}$ term gives a small contribution because the integral is suppressed by either F_τ or $\mathrm{d}\hat{\sigma}/\mathrm{d}\tau$: near the endpoint $\tau \sim \tau_m - 2\,\Lambda_{\rm QCD}/Q$ the p-integration is not restricted and $F_\tau(p) \sim 1$, but $\mathrm{d}\hat{\sigma}/\mathrm{d}\tau$ is highly suppressed. For smaller τ the p-integration is restricted and the exponential tail of $F_\tau(p)$ suppresses the contribution. We have checked numerically that at $Q = 91.2\,\mathrm{GeV}$ [$Q = 35\,\mathrm{GeV}$], for the first moment the relative contribution of $E_1^{(B)}$ compared to the term in square brackets in Eq. (4.9) is $\mathcal{O}(10^{-7})\,[\mathcal{O}(10^{-6})]$, while for the fifth moment $E_5^{(B)}$ it is $\mathcal{O}(10^{-6})\,[\mathcal{O}(10^{-4})]$. This suppression does not rely on the model used for $F_\tau(p)$. Thus $E_n^{(B)}$ can also be safely neglected.

Within the theoretical precision we conclude that the leading factorization theorem for the distribution yields an operator product expansion that separates perturbative and nonperturbative corrections in the moments

$$M_n = \sum_{\ell=0}^{n} \binom{n}{\ell} \Big(\frac{2}{Q}\Big)^{n-\ell} \hat{M}_\ell\, \Omega_{n-\ell}\,. \tag{4.12}$$

For M_n the terms that numerically dominate are $\hat{M}_n$ and $\hat{M}_{n-1}\Omega_1/Q$. However for the cumulants M_n' there are cancellations, and Eq. (4.12) does not suffice due to our neglect so far of $(\Lambda_{\rm QCD}/Q)^j$ suppressed terms in the factorization expression for the thrust distribution.

To rectify this we parameterize the $(\Lambda_{\rm QCD}/Q)^j$ power corrections by a series of power suppressed nonperturbative soft functions, $\Lambda^{j-1} F_{\tau,j}(p/\Lambda) \sim \Lambda_{\rm QCD}^{j-1}$. Here

$\Lambda^{-1}F_{\tau,0}(p/\Lambda) = F_\tau(p)$ is the leading soft function from Eq. (4.9). We introduced the parameter $\Lambda = 400\,\mathrm{MeV} \sim \Lambda_{\mathrm{QCD}}$ to track the dimension of these subleading soft functions. This parameterization is motivated by the fact that subleading factorization results can in principle be derived with SCET [112], and at each order in the power expansion will yield new soft function matrix elements.

Both the factorization analysis and calculation of cumulants is simpler in Fourier space, so we let

$$\begin{aligned} \sigma(y) &\equiv \int \mathrm{d}\tau\, e^{-iy\tau}\, \frac{\mathrm{d}\sigma}{\mathrm{d}\tau}(\tau)\,, \\ F_{\tau,j}(z\,\Lambda) &\equiv \int \frac{\mathrm{d}p}{\Lambda}\, e^{-izp}\, F_{\tau,j}\left(\frac{p}{\Lambda}\right)\,, \end{aligned} \tag{4.13}$$

and likewise for the leading power partonic cross section $\mathrm{d}\hat{\sigma}/\mathrm{d}\tau(\tau) \to \hat{\sigma}_0(y)$. The factorization-based formula for thrust is then

$$\frac{1}{\sigma}\,\sigma(y) = \frac{1}{\hat{\sigma}} \sum_{j=0}^{\infty} \left(\frac{\Lambda}{Q}\right)^j \hat{\sigma}_j(y)\, F_{\tau,j}\Big(\frac{y\,\Lambda}{Q}\Big)\,, \tag{4.14}$$

where $\hat{\sigma}_{j>0}(y)$ accounts for perturbative corrections in the $(\Lambda_{\mathrm{QCD}}/Q)^j$ power correction. The $j = 0$ term is equivalent to the result used in Eq. (4.9), $F_\tau(p) = \Lambda F_{\tau,0}(p/\Lambda)$, and the normalization condition for the leading nonperturbative soft function is $F_{\tau,0}(z = 0) = 1$. The terms in Eq. (4.14) beyond $j = 0$ are schematic since in reality they may involve convolutions in more variables in the nonperturbative soft functions (as observed in the subleading $b \to s\,\gamma$ factorization theorem results [24, 23, 114, 112, 45, 34]). Nevertheless the scaling is correct, and Eq. (4.14) will suffice for our analysis where we only seek to classify how various power corrections could enter higher moments.

The identities $\sigma(y = 0)/\sigma = 1$ and $\hat{\sigma}_0(y = 0)/\hat{\sigma} = 1$ together with Eq. (4.14) imply

$$F_{\tau,j}(y = 0) = 0\,, \qquad \text{for } j \geq 1\,. \tag{4.15}$$

Using the Fourier-space cross section the moments are

$$\begin{aligned} M_n &= i^n \frac{\mathrm{d}^n}{\mathrm{d}y^n}\biggl[\frac{1}{\sigma}\,\sigma(y)\biggr]_{y=0} \\ &= i^n \frac{\mathrm{d}^n}{\mathrm{d}y^n}\biggl[\frac{1}{\sigma}\sum_{j=0}^{\infty}\hat{\sigma}_j(y)\left(\frac{\Lambda}{Q}\right)^j F_{\tau,j}\Bigl(\frac{y\,\Lambda}{Q}\Bigr)\biggr]_{y=0} \\ &= \sum_{j=0}^{\infty}\left(\frac{1}{Q}\right)^j \sum_{\ell=0}^{n}\binom{n}{\ell}\hat{M}_{n-\ell,j}\left(\frac{2}{Q}\right)^{\ell}\Omega_{\ell,j}\,, \end{aligned} \tag{4.16}$$

which extends the OPE in Eq. (4.12) to parameterize the $(\Lambda_{\rm QCD}/Q)^j$ power corrections. Here the perturbative and nonperturbative moments are defined as

$$\begin{aligned} \hat{M}_{n,j} &= i^n \frac{\mathrm{d}^n}{\mathrm{d}y^n}\biggl[\frac{1}{\hat{\sigma}}\,\hat{\sigma}_j(y)\biggr]_{y=0}\,, \\ \Omega_{n,j} &= \frac{i^n}{2^n}\frac{\mathrm{d}^n}{\mathrm{d}z^n}\Bigl[\Lambda^j F_{\tau,j}(z\,\Lambda)\Bigr]_{z=0}\,, \end{aligned} \tag{4.17}$$

where $\hat{M}_{n,j}$ is a dimensionless series in $\alpha_s(\mu)$ and $\Omega_{n,j} \sim \Lambda_{\rm QCD}^{n+j}$. In order for $\hat{M}_{n,j}$ to exist it is crucial that our $\hat{\sigma}_j(y)$ and its derivatives do not contain $\ln(y)$ dependence in the $y \to 0$ limit at any order in α_s. In τ-space the perturbative coefficients have support over a finite range, $\tau \in [0, 1/2]$, and

$$\hat{\sigma}_j(y) = \int_0^{1/2} \mathrm{d}\tau\, e^{-i\tau y}\,\hat{\sigma}_j(\tau)\,. \tag{4.18}$$

Therefore the existence of $\int_0^{1/2}\mathrm{d}\tau\,\hat{\sigma}_j(\tau)$, which is the total perturbative cross section for $j = 0$, implies a well defined Taylor series under the integrand in Eq. (4.18), and hence the existence of $\hat{M}_{n,j}$. From Eq. (4.15) we have $\Omega_{0,j>0} = 0$, and furthermore $\Omega_{n,0} = \Omega_n$ and $\hat{M}_{n,0} = \hat{M}_n$.

For the first moment, Eq. (4.16) yields

$$M_1 = \hat{M}_1 + \frac{2\,\Omega_1}{Q} + \sum_{j=0}^{\infty}\hat{M}_{0,1+j}\frac{2\,\Omega_{1,1+j}}{Q^{2+j}}\,, \tag{4.19}$$

where the first two terms are determined by the leading order factorization theorem,

while the last term identifies the scaling of contributions from $(\Lambda_{\rm QCD}/Q)^{2+j}$ power corrections. Two properties of Eq. (4.19) will be relevant for our analysis: first, there is no perturbative Wilson coefficient for the leading $2\,\Omega_1/Q$ power correction; and second, terms from beyond the leading factorization theorem only enter at $\mathcal{O}(\Lambda^2_{\rm QCD}/Q^2)$ and beyond. For higher order moments, $n \geq 2$, we have

$$\begin{aligned} M_n = \hat{M}_n + \frac{2\,n\,\Omega_1}{Q}\,\hat{M}_{n-1} + \frac{n(n-1)\Omega_2}{Q^2}\,\hat{M}_{n-2} \\ + \frac{2\,n\,\Omega_{1,1}}{Q^2}\hat{M}_{n-1,1} + \mathcal{O}\Big(\frac{1}{Q^3}\Big)\,. \end{aligned} \tag{4.20}$$

Next we derive an analogous expression for the n-th order cumulants for $n \geq 2$, which are generated from Fourier space by

$$M'_n = i^n \frac{\mathrm{d}^n}{\mathrm{d}y^n}\bigg[\ln\frac{\sigma(y)}{\sigma}\bigg]_{y=0}. \tag{4.21}$$

Eq. (4.14) can be conveniently written as the product of three terms

$$\frac{1}{\sigma}\,\sigma(y) = \frac{1}{\hat{\sigma}}\,\hat{\sigma}_0(y)\,F_{\tau,0}\Big(\frac{y\,\Lambda}{Q}\Big)\bigg[1 + \sum_{j=1}^{\infty}\overline{\sigma}_j(y)\,\Big(\frac{\Lambda}{Q}\Big)^j\,\overline{F}_{\tau,j}\Big(\frac{y\,\Lambda}{Q}\Big)\bigg], \tag{4.22}$$

where bars indicate the ratios

$$\overline{\sigma}_j(y) = \frac{\hat{\sigma}_j(y)}{\hat{\sigma}_0(y)}, \qquad \overline{F}_{\tau,j}(x) = \frac{F_{\tau,j}(x)}{F_{\tau,0}(x)}. \tag{4.23}$$

From Eq. (4.15) we have $\overline{F}_{\tau,j}(x=0) = 0$ for all $j \geq 1$. Taking the logarithm of Eq. (4.22) expresses the thrust cumulants by the sum of three terms

$$\begin{aligned} M'_n = \hat{M}'_n + \Big(\frac{2}{Q}\Big)^n\,\Omega'_n + i^n\,\frac{\mathrm{d}^n}{\mathrm{d}y^n}\sum_{k=1}^{\infty}\frac{(-1)^{k+1}}{k} \\ \times\bigg[\sum_{j=1}^{\infty}\overline{\sigma}_j(y)\,\Big(\frac{\Lambda}{Q}\Big)^j\,\overline{F}_{\tau,j}\Big(\frac{y\,\Lambda}{Q}\Big)\bigg]^k\bigg|_{y=0}. \end{aligned} \tag{4.24}$$

The first two terms involve the perturbative cumulants $\hat{M}'_n$ and the cumulants of the

leading nonperturbative soft functions Ω'_n,

$$\hat{M}'_n = i^n \frac{\mathrm{d}^n}{\mathrm{d}y^n}\left[\ln\frac{1}{\sigma}\,\hat{\sigma}_0(y)\right]_{y=0}, \qquad (4.25)$$
$$\Omega'_n = \frac{i^n}{2^n}\frac{\mathrm{d}^n}{\mathrm{d}z^n}\left[\ln F_{\tau,0}(z\Lambda)\right]_{z=0}.$$

The third term in Eq. (4.24) represents contributions from power-suppressed terms that are not contained in the leading thrust factorization theorem. These terms start at $\mathcal{O}(\Lambda^2_{\rm QCD}/Q^2)$. At this order only $\overline{F}_{\tau,1}$ has to be considered. The terms $\overline{F}_{\tau,i>2}$ do not contribute due to explicit powers of $\Lambda_{\rm QCD}/Q$. Concerning $\overline{F}_{\tau,2}$, it must be hit by at least one derivative because $\overline{F}_{\tau,2}(0) = 0$, and hence does not contribute as well. Performing the n-th derivative at $y = 0$ and keeping only the dominant term from the power corrections gives the OPE

$$M'_n = \hat{M}'_n + \frac{2^n\Omega'_n}{Q^n} + n\,\overline{M}_{n-1,1}\frac{2\,\Omega_{1,1}}{Q^2} + \mathcal{O}\Big(\frac{\Lambda^3_{\rm QCD}}{Q^3}\Big). \qquad (4.26)$$

Here $\Omega_{1,1}$ is defined in Eq. (4.17). The perturbative coefficient is

$$\overline{M}_{j,1} = \left[i^j\frac{\mathrm{d}^j}{\mathrm{d}y^j}\,\overline{\sigma}_1(y)\right]_{y=0} \qquad (4.27)$$

and so far unknown.

The majority of our analysis will focus on M_1 where terms beyond the leading order factorization theorem are power suppressed. For our analysis of $M_{n\geq 2}$ we consider the impact of both $\alpha_s\Omega_1/Q$ corrections, and power corrections suppressed by more powers of $1/Q$. When we analyze $M'_{n\geq 2}$ we will consider both $1/Q^n$ and $1/Q^2$ power corrections in the fits.

4.3 Results for $\mathbf{M_1}$

In this section we present the main results of our analysis, the fits to the first moment of the thrust distribution and the determination of $\alpha_s(m_Z)$ and Ω_1. Prior to

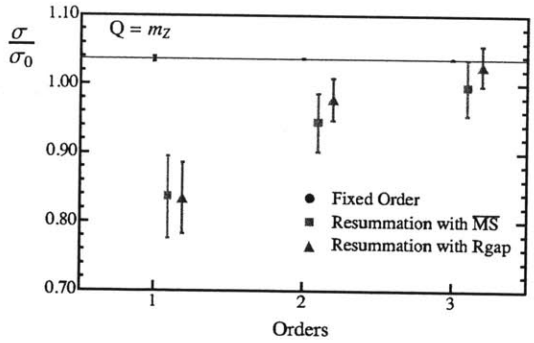

Figure 4-1: Theoretical computations at various orders in perturbation theory for the total hadronic cross section at the Z-pole normalized to the Born-level cross section σ_0. Here the small blue points correspond to fixed order perturbation theory, green squares to resummation without renormalon subtractions, and red triangles to resummation with renormalon subtractions.

presenting our final numbers in Sec. 4.3.4 we discuss various aspects important for their interpretation. In Sec. 4.3.1 we discuss the role of the log-resummation contained in our fit code, the perturbative convergence for different kinds of expansion methods, and we illustrate the numerical impact of power corrections and the renormalon subtraction. We also briefly discuss the degeneracy between $\alpha_s(m_Z)$ and Ω_1 that motivates carrying out global fits to data covering a large range of Q values. In Sec. 4.3.2 we present the outcome of the theory parameter scans, on which the estimate of theory uncertainties in our fits are based, and show the final results. We also display results for the fits at various levels of accuracy. Sec. 2.2.8 briefly discusses the effects of QED and bottom mass corrections. Sec. 4.4 shows the results of a fit in which renormalon subtractions and power corrections are included, but resummation of logs in the thrust distribution is turned off.

For our moment analysis we use the code developed in Ref. [1], where a detailed description of the various ingredients may be found. We are able to perform fits with different level of accuracy: fixed order at $\mathcal{O}(\alpha_s^3)$, resummation of large logarithms to N^{3}LL accuracy[6], power corrections, and subtraction of the leading renormalon ambiguity. Recently the complete calculation of the $\mathcal{O}(\alpha_s^2)$ hemisphere soft function has become available [103, 97, 123], so the code is updated to use the fixed parameter

[6]Throughout this publication N^{n}LL corresponds to the same order counting as N^{n}LL$'$ in Ref. [1].

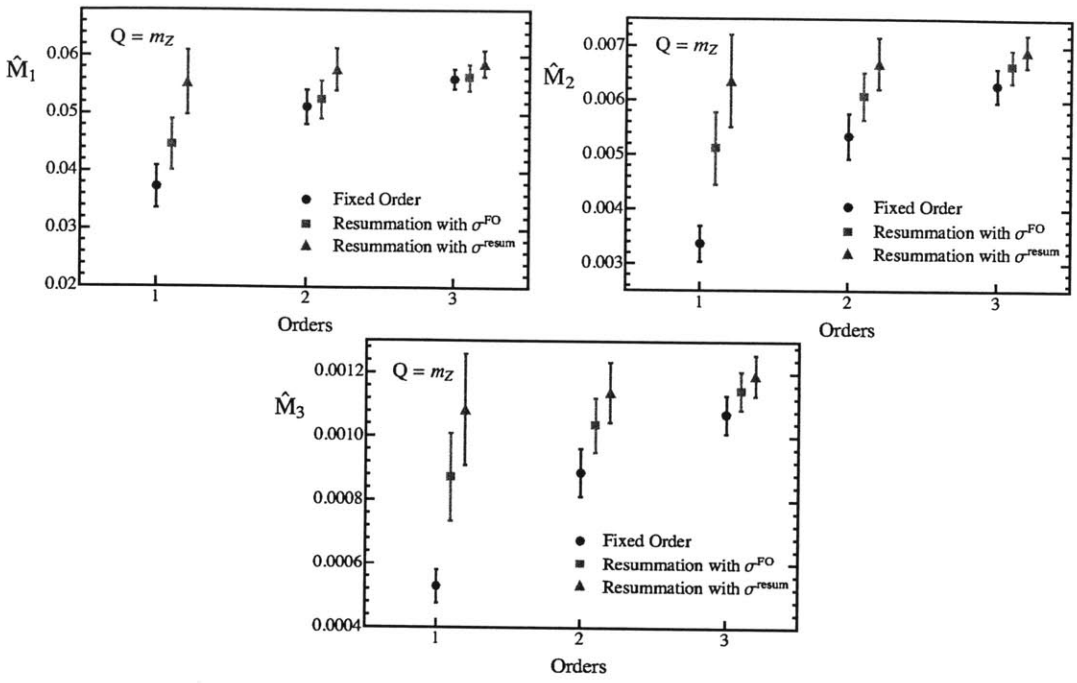

Figure 4-2: Theoretical prediction for the first three moments at the Z-pole at various orders in perturbation theory. The blue circles correspond to fixed order perturbation theory (normalized with the total hadronic cross section) at $\mathcal{O}(\alpha_s)$, $\mathcal{O}(\alpha_s^2)$ and $\mathcal{O}(\alpha_s^3)$, green squares correspond to resummed predictions at NLL, NNLL, and N^{3}LL normalized with the total hadronic cross section, and red triangles correspond to resummation normalized with the norm of the resummed distribution. For these plots we use $\alpha_s(m_Z) = 0.114$.

$s_2 = -40.6804$ from Refs. [103, 123]. A feature of our code is its ability to describe the thrust distribution in the whole range of thrust values. This is achieved with the introduction of what we call profile functions, which are τ-dependent factorization scales. In the $e^+ e^-$ annihilation process there are three relevant scales: hard, jet and soft, associated to the center of mass energy, the jet mass and the energy of soft radiation, respectively. The purpose of τ-dependent profile functions for these scales is to smoothly interpolate between the peak region where we must ensure that $\mu_i > \Lambda_{\rm QCD}$, the dijet region where the summation of large logs is crucial, and the multijet region where regular perturbation theory is appropriate to describe the partonic contribution [1]. The major part of the higher order perturbative uncertainties are directly related to the arbitrariness of the profile functions, and are estimated by scanning the

space of parameters that specify them. For details on the profile functions and the parameter scans we refer the reader to App. B. We note that our distribution code was designed for Q values above 22 GeV.

4.3.1 Ingredients

The theoretical fixed order expression for the thrust moments contain no large logarithms, so we might not expect that the resummation of logarithms in the thrust spectrum will play a role in the numerical analysis. We will show that there is nevertheless some benefit in accounting for the resummation of thrust logarithms. This is studied in Fig. 4-1 and 4-2, where for $Q = m_Z$ we compare the theoretical value of moments of the thrust distribution obtained in fixed order with those obtained including resummation. (The error bars for the fixed order expansion arise from varying the renormalization scale μ between $Q/2$ and $2\,Q$ and those for the resummed results arise from our theory parameter scan method.)

In Fig. 4-1 we show the total hadronic cross section σ from the fixed order α_s expansion (blue points with small uncertainties sitting on the horizontal line) and determined from the integral over the log-resummed distribution with/without renormalon subtractions (red triangles and green squares). Both expansions are displayed including fixed order corrections up to order $\alpha_s(m_Z)$, $\alpha_s^2(m_Z)$ and $\alpha_s^3(m_Z)$, as indicated by the orders 1, 2, 3, respectively. We immediately notice that the resummed result is not as effective in reproducing the total cross section as the fixed order expansion. Predictions that sum large logarithms have a substantial (perturbative) normalization uncertainty. On the other hand, as shown in Ref. [1], the resummation of logarithms combined with the profile function approach leads to a description of the thrust spectrum that converges nicely over the whole physical τ range when the norm of the spectrum is divided out, a property not present in the spectrum of the fixed order expansion.

In Fig. 4-2 the expansions of the partonic moments $\hat{M}_1$, $\hat{M}_2$, and $\hat{M}_3$ are displayed in the fixed order expansion (blue circles) and the log-resummed result with either the fixed order normalization (green squares) or a properly normalized spectrum (red

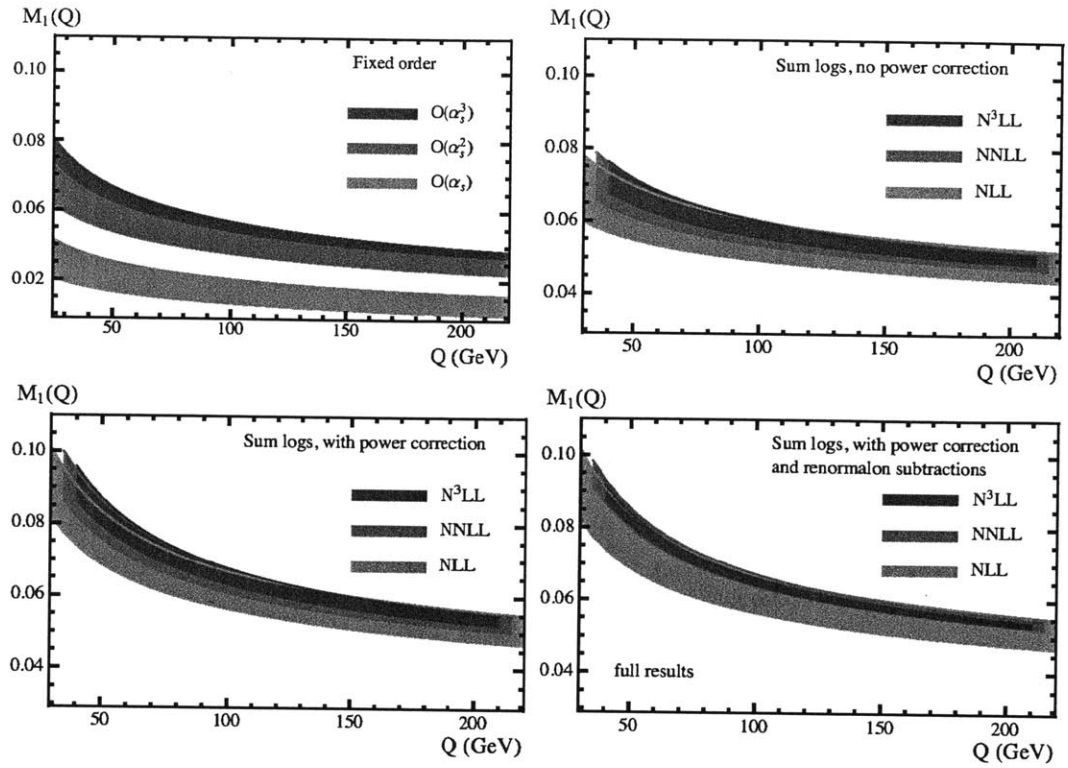

Figure 4-3: Theory scan for uncertainties in pure QCD with massless quarks. The panels are fixed order (top-left), resummation without the nonperturbative correction (top-right), resummation with a nonperturbative function using the $\overline{\text{MS}}$ scheme for $\overline{\Omega}_1$ (bottom-left), resummation with renormalon subtraction and a nonperturbative function in the Rgap scheme for Ω_1 (bottom-right).

triangles). We observe that the fixed order expansion has rather small variations from scale variation, but shows poor convergence indicating that its renormalization scale variation underestimates the perturbative uncertainty. For $\hat{M}_1$ the fixed order and log-resummed expressions with a common fixed-order normalization (blue circles and green squares) agree well at each order, indicating that, as expected, large logarithms do not play a significant role for this moment. On the other hand, the expansion based on the properly normalized log-resummed spectrum exhibits excellent convergence, and also has larger perturbative uncertainties at the lowest order. In particular, for the red triangles the higher order results are always within the 1-σ uncertainties of the previous order. The result shows that using the normalized log-resummed spectrum for thrust, which converges nicely for all τ, also leads to better convergence

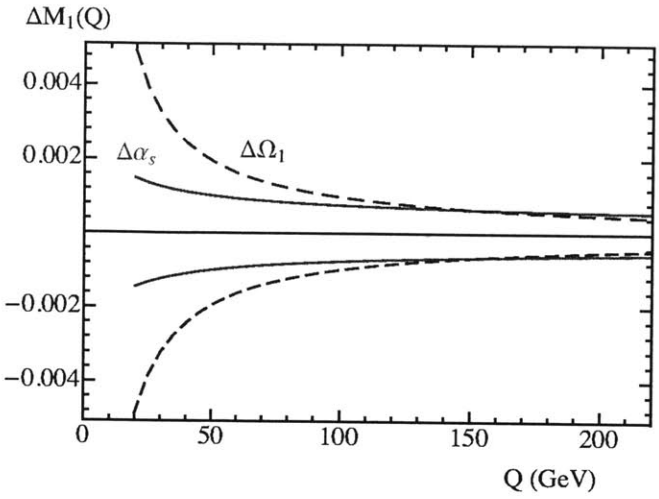

Figure 4-4: Difference between theoretical predictions with default parameters for the first moment as function of Q when varying one parameter at a time. The red solid line corresponds to varying $\Delta\alpha_s(m_Z) = \pm 0.001$ and the blue dashed lines to varying $\Delta\Omega_1 = \pm 0.1$, with respect to the pure QCD best-fit values. There is a strong degeneracy of the two parameters in the region $Q > 100$ GeV, which is obviously broken when considering values of Q below 70 GeV.

properties of the moments. At third order all the fixed order and resummed partonic moments are consistent with each other. Since the log-resummed moments exhibit more realistic estimates of perturbative uncertainties at each order, we will use the normalized resummed moments for our fit analysis.[7]

In Fig. 4-3 we show how the inclusion of various ingredients (fixed order contributions, log resummation, power corrections, renormalon subtraction) affects the convergence and uncertainty of our theoretical prediction for the first moment of the thrust distribution as a function of Q. From these plots we can observe four points: i) Fixed order perturbation theory does not converge very well. ii) Resummation of large logarithms in the distribution, when normalized with the integral of the resummed distribution, improves convergence for every center of mass energy. iii) The inclusion of power corrections has the effect of a $1/Q$-modulated vertical shift on the value of the first moment. iv) The subtraction of the renormalon ambiguity reduces

[7]For our most complete theory set up, following Ref. [1] we normalize the distribution with the fixed-order total hadronic cross section since it is faster and in this case the norm of the distribution and total hadronic cross section are fully compatible.

the theoretical uncertainty. This picture for the first moment is consistent with the results of Ref. [1] for the thrust distribution.

Another important element of our analysis is that we perform global fits, simultaneously using data at a wide range of center of mass energies Q. This is motivated by the fact that for each Q there is a complete degeneracy between changing $\alpha_s(m_Z)$ and changing Ω_1, which can be lifted only through a global analysis. Fig. 4-4 shows the difference between the theoretical prediction of M_1 as a function of Q, when $\alpha_s(m_Z)$ or Ω_1 are varied by ± 0.001 and ± 0.1 GeV, respectively. We see that the effect of a variation in $\alpha_s(m_Z)$ can be compensated with an appropriate variation in Ω_1 at a given center of mass energy (or in a small Q range). This degeneracy is broken if we perform a global fit including the wide range of Q values shown in the figure.

Finally, in Fig. 4-5 we show $\alpha_s(m_Z)$ extracted from fits to the first moment of the thrust distribution at three-loop accuracy including sequentially the different effects our code has implemented: $O(\alpha_s^3)$ fixed order, N^3LL resummation, power corrections, renormalon subtraction, b-quark mass and QED. The error bars of the first two points at the left hand side do not contain an estimate of uncertainties associated with the power correction. Though smaller, the resummed result is compatible at the 1-σ level with the fixed order result. The inclusion of the power correction is the element which has the greatest impact on $\alpha_s(m_Z)$; for the $\overline{\rm MS}$ definition of Ω_1 it reduces the central value by 7%. The subtraction of the renormalon ambiguity in the Rgap scheme reduces the theoretical uncertainty by a factor of 3, while b-quark mass and QED effects give negligible contributions with current uncertainties.

4.3.2 Uncertainty Analysis

In Fig. 4-6 we show the result of our theory scan to determine the perturbative uncertainties. At each order we carried out 500 fits, with theory parameters randomly chosen in the ranges given in Table 3.1 of App. B (where further details may be found). The left panel of Fig. 4-6 shows results with renormalon subtractions using the Rgap scheme for Ω_1, and the right-panel shows results in the $\overline{\rm MS}$ scheme without renormalon subtractions. Each point in the plot represents the result of a single fit.

As described in App. B, in order to estimate perturbative uncertainties, we fit an ellipse to the contour of best-fit points in the α_s-$2\Omega_1$ plane, and we interpret this as 1-σ theoretical error ellipse. This is represented by the dashed lines in Fig. 4-6. The solid lines represent the combined (theoretical and experimental) standard error ellipses. These are obtained by adding the theoretical and experimental error matrices which determined the individual ellipses. The central values of the fits, collected in Tables 4.1 and 4.2, are determined from the average of the maximal and minimal values of the theory scan, and are very close to the central values obtained when running with our default parameters. The minimal χ^2 values for these fits are quoted in Table 4.3 as well. The best fit based on our full code has $\chi^2/\text{dof} = 1.325 \pm 0.002$ where the range incorporates the variation from the displayed scan points at N^{3}LL. The fit results show a substantial reduction of the theoretical uncertainties with increasing perturbative order. Removal of the $\mathcal{O}(\Lambda_{\rm QCD})$ renormalon improves the perturbative convergence and leads to a reduction of the theoretical uncertainties at the highest order by a factor of 2 in Ω_1, and factor of 3 in $\alpha_s(m_Z)$

To analyze in detail the experimental and the total uncertainties of our results,

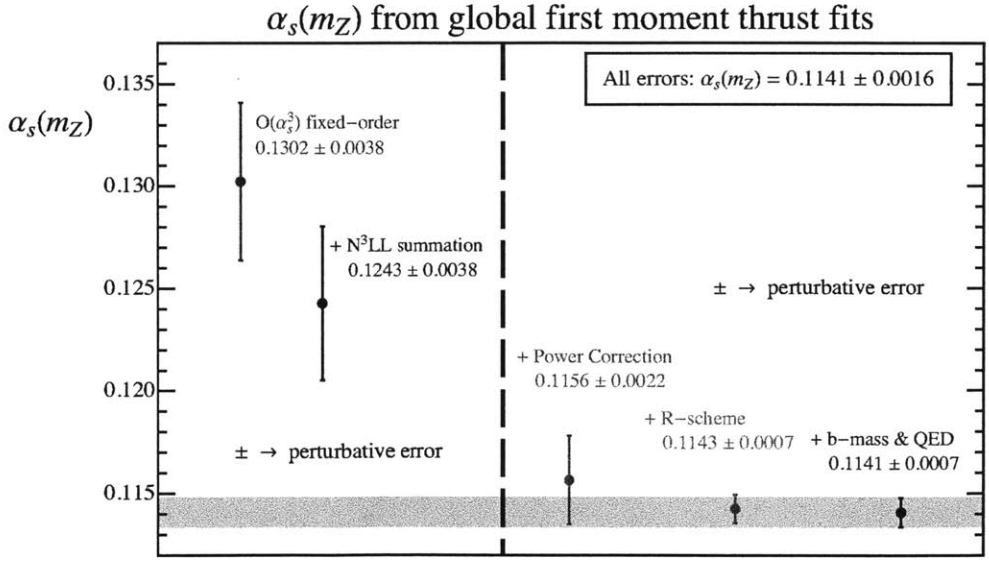

Figure 4-5: Evolution of the best-fit values for $\alpha_s(m_Z)$ from thrust first moment fits when including various levels of improvement with respect to fixed order QCD. Only points at the right of the vertical dashed line include nonperturbative effects.

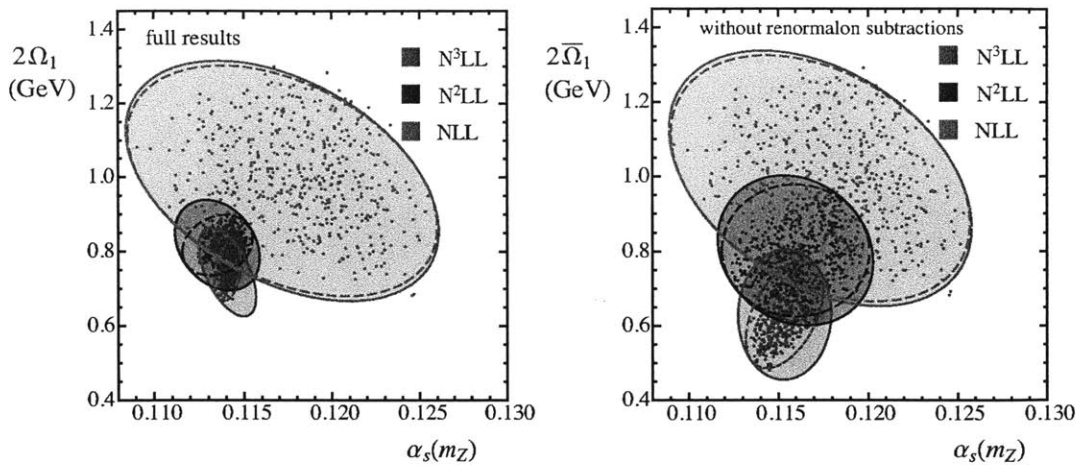

Figure 4-6: Distribution of best-fit points in the $\alpha_s(m_Z)$-$2\,\Omega_1$ and $\alpha_s(m_Z)$-$2\,\overline{\Omega}_1$ planes. The left panel shows results including perturbation theory, resummation of the logs, the soft nonperturbative function, and Ω_1 defined in the Rgap scheme with renormalon subtractions. The right panel shows the same results, but with $\overline{\Omega}_1$ defined in the $\overline{\rm MS}$ scheme, and without renormalon subtractions. In both panels the dashed lines corresponds to an ellipse fit to the contour of the best-fit points to determine the theoretical uncertainty. The respective total (experimental + theoretical) 39% CL standard error ellipses are displayed (solid lines), which correspond to 1-σ (68% CL) for either one-dimensional projection.

order	$\alpha_s(m_Z)$ (with $\overline{\Omega}_1^{\overline{\rm MS}}$)	$\alpha_s(m_Z)$ (with $\Omega_1^{\rm Rgap}$)
NLL	0.1174(82)(13)	0.1173(82)(13)
NNLL	0.1160(41)(14)	0.1135(19)(13)
N^{3}LL (full)	0.1153(21)(15)	**0.1141(07)(14)**
N^{3}LL$_{(\rm QCD+m_b)}$	0.1160(21)(15)	0.1146(07)(14)
N^{3}LL$_{(\rm pure\ QCD)}$	0.1156(22)(15)	0.1143(07)(14)

Table 4.1: Central values for $\alpha_s(m_Z)$ at various orders with theory uncertainties from the parameter scan (first value in parentheses), and experimental and hadronic error added in quadrature (second value in parentheses). The bold N^{3}LL value above the line is our final result, while values below the line show the effect of leaving out the QED and b-mass corrections.

we refer now to Fig. 4-7. Here we show the error ellipses for our highest order fit, which includes resummation, power corrections, renormalon subtraction, QED and b-quark mass contributions. The green dotted, blue dashed, and the solid red lines represent the standard error ellipses for, respectively, experimental, theoretical, and combined theoretical and experimental uncertainties. The experimental and theory

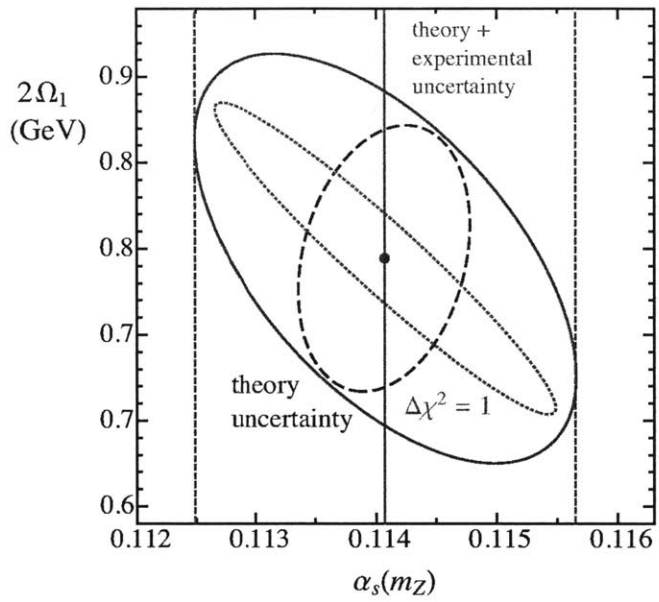

Figure 4-7: Experimental $\Delta\chi^2 = 1$ standard error ellipse (dotted green) at N^{3}LL accuracy with renormalon subtractions, in the α_s-$2\,\Omega_1$ plane. The dashed blue ellipse represents the theory uncertainty which is obtained by fitting an ellipse to the contour of the distribution of the best-fit points. This ellipse should be interpreted as the 1-σ theory uncertainty for 1-parameter (39% confidence for 2-parameters). The solid red ellipse represents the total (combined experimental and perturbative) uncertainty ellipse.

order	$\overline{\Omega}_1$ ($\overline{\text{MS}}$) [GeV]	Ω_1 (Rgap) [GeV]
NLL	0.498(156)(47)	0.495(154)(47)
NNLL	0.401(82)(49)	0.408(42)(46)
N^{3}LL (full)	0.315(75)(51)	**0.372(39)(46)**
N^{3}LL$_{(\text{QCD}+m_b)}$	0.306(74)(51)	0.364(38)(46)
N^{3}LL$_{(\text{pure QCD})}$	0.344(67)(51)	0.397(35)(46)

Table 4.2: Central values for Ω_1 at the reference scales $R_\Delta = \mu_\Delta = 2$ GeV and for $\overline{\Omega}_1$ and at various orders. The parentheses show theory uncertainties from the parameter scan, and experimental and hadronic uncertainty added in quadrature, respectively. The bold value above the line is our final result, while the N^{3}LL values below the horizontal line show the effect of leaving out the QED and b-mass corrections.

error ellipses are defined by $\Delta\chi^2 = 1$ since we are most interested in the 1-dimensional projection onto α_s. The correlation matrix of the experimental, theory, and total error

	$\alpha_s(m_Z)$	χ^2/(dof)
N^{3}LL with $\Omega_1^{\rm Rgap}$	0.1141(07)(14)	1.33
N^{3}LL with $\overline{\Omega}_1^{\overline{\rm MS}}$	0.1153(21)(15)	1.33
N^{3}LL no power corr.	0.1234(38)(03)	1.99
$\mathcal{O}(\alpha_s^3)$ fixed order no power corr.	0.1302(38)(04)	2.47

Table 4.3: Comparison of first moment fit results for analyses with full results and $\Omega_1 = \Omega_1^{\rm Rgap}$, with $\overline{\Omega}_1$ and no renormalon subtractions, without power corrections, and at fixed order without power corrections or log resummation. The first number in parentheses corresponds to the theory uncertainty, whereas the second corresponds to the experimental and hadronic uncertainty added in quadrature for the first two rows, and experimental uncertainty for the last two rows.

ellipses are $(i, j = \alpha_s, 2\,\Omega_1)$

$$V_{ij} = \begin{pmatrix} \sigma_{\alpha_s}^2 & 2\sigma_{\alpha_s}\sigma_{\Omega_1}\rho_{\alpha\Omega} \\ 2\sigma_{\alpha_s}\sigma_{\Omega_1}\rho_{\alpha\Omega} & 4\sigma_{\Omega_1}^2 \end{pmatrix}, \tag{4.28}$$

$$V_{ij}^{\rm exp} = \begin{pmatrix} 2.02(16)\cdot 10^{-6} & -1.25(12)\cdot 10^{-4}\,\text{GeV} \\ -1.25(12)\cdot 10^{-4}\,\text{GeV} & 0.85(12)\cdot 10^{-2}\,\text{GeV}^2 \end{pmatrix},$$

$$V_{ij}^{\rm theo} = \begin{pmatrix} 5.06\cdot 10^{-7} & 1.39\cdot 10^{-5}\ \text{GeV} \\ 1.39\cdot 10^{-5}\ \text{GeV} & 5.99\cdot 10^{-3}\ \text{GeV}^2 \end{pmatrix},$$

$$V_{ij}^{\rm tot} = \begin{pmatrix} 2.53(16)\cdot 10^{-6} & -1.11(12)\cdot 10^{-4}\,\text{GeV} \\ -1.11(12)\cdot 10^{-4}\,\text{GeV} & 1.45(12)\cdot 10^{-2}\,\text{GeV}^2 \end{pmatrix},$$

where the experimental correlation coefficient is significant and reads

$$\rho_{\alpha\Omega}^{\rm exp} = -0.95(12)\,. \tag{4.29}$$

Adding the theory scan uncertainties reduces the correlation coefficient in Eq. (3.2) to

$$\rho_{\alpha\Omega}^{\rm total} = -0.58(7). \tag{4.30}$$

In both Eqs. (3.2) and (4.30) the numbers in parentheses capture the range of values

obtained from the theory scan. From $V_{ij}^{\rm exp}$ in Eq. (4.28) it is possible to extract the experimental uncertainty for α_s and Ω_1 and the uncertainty due to variations of Ω_1 and α_s, respectively:

$$\begin{aligned}
\sigma_{\alpha_s}^{\rm exp} &= \sigma_{\alpha_s}\sqrt{1-\rho_{\alpha\Omega}^2} = 0.0004\,, \\
\sigma_{\Omega_1}^{\rm exp} &= \sigma_{\Omega_1}\sqrt{1-\rho_{\alpha\Omega}^2} = 0.013\ {\rm GeV}\,, \\
\sigma_{\alpha_s}^{\Omega_1} &= \sigma_{\alpha_s}\,|\rho_{\alpha\Omega}| = 0.0014\,, \\
\sigma_{\Omega_1}^{\alpha_s} &= \sigma_{\Omega_1}\,|\rho_{\alpha\Omega}| = 0.044\ {\rm GeV}\,.
\end{aligned} \tag{4.31}$$

Fig. 4-7 shows the total uncertainty in our final result quoted in Eq. (3.5) below.

The correlation exhibited by the green dotted experimental error ellipse in Fig. 4-7 is given by the line describing the semimajor axis

$$\frac{\Omega_1}{34.03\,{\rm GeV}} = 0.1250 - \alpha_s(m_Z)\,. \tag{4.32}$$

Note that extrapolating this correlation to the extreme case where we neglect the nonperturbative corrections ($\Omega_1 = 0$) gives $\alpha_s(m_Z) \to 0.1250$.

4.3.3 Effects of QED and the b-mass

The experimental correction procedures applied to the AMY, JADE, SLC, DELPHI and OPAL data sets were typically designed to eliminate initial state photon radiation, while those of the TASSO, L3 and ALEPH collaborations eliminated initial and final state photon radiation. It is straightforward to test for the effect of these differences in the fits by using our theory code with QED effects turned on or off depending on the data set. Using our N^{3}LL order code in the Rgap scheme we obtain the central values $\alpha_s(m_Z) = 0.1143$ and $\Omega_1 = 0.371$ GeV. Comparing to our default results given in Tabs. 4.1 and 4.2, which are based on the theory code were QED effects are included for all data sets, we see that the central value for α_s is larger by 0.0002 and the one for Ω_1 is smaller by 0.001 GeV. This shift is substantially smaller than our perturbative uncertainty. Hence our choice to use the theory code with QED effects

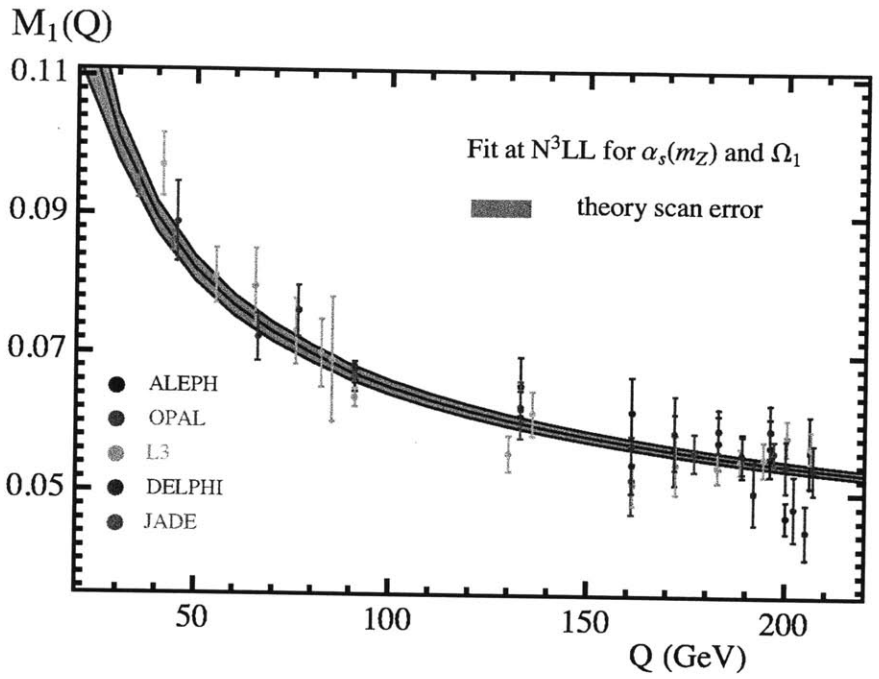

Figure 4-8: First moment of the thrust distribution as a function of the center of mass energy Q, using the best-fit values for $\alpha_s(m_Z)$ and Ω_1 in the Rgap scheme as given in Eq. (4.33). The blue band represents the perturbative uncertainty determined by our theory scan. Data is from ALEPH, OPAL, L3, DELPHI and JADE.

included everywhere as the default for our analysis does not cause an observable bias regarding experiments which remove final state photons.

By comparing the N^{3}LL (pure massless QCD) and N^{3}LL (QCD $+m_b$) entries in Tabs. 4.1 and 4.2 we see that including finite b-mass corrections causes a very mild shift of $\simeq +0.0003$ to $\alpha_s(m_Z)$, and a somewhat larger shift of $\simeq -0.033\,\text{GeV}$ to Ω_1. In both cases these shifts are within the 1-σ theory uncertainties. In the N^{3}LL (pure massless QCD) analysis the b-quark is treated as a massless flavor, hence this analysis differs from that done by JADE [131] where primary b quarks were removed using MC generators.

4.3.4 Final Results

As our final result for $\alpha_s(m_Z)$ and Ω_1, obtained at N^{3}LL order in the Rgap scheme for $\Omega_1(R_\Delta, \mu_\Delta)$, including bottom quark mass and QED corrections we obtain

$$\alpha_s(m_Z) = 0.1141 \pm (0.0004)_{\rm exp} \pm (0.0014)_{\rm hadr} \pm (0.0007)_{\rm pert}, \tag{4.33}$$

$$\Omega_1(R_\Delta, \mu_\Delta) = 0.372 \pm (0.013)_{\rm exp} \pm (0.044)_{\alpha_s(m_Z)} \pm (0.039)_{\rm pert}\ {\rm GeV},$$

where $R_\Delta = \mu_\Delta = 2$ GeV and we quote individual 1-σ uncertainties for each parameter. Here $\chi^2/{\rm dof} = 1.33$. Eq. (4.33) is the main result of this work.

In Fig. 4-8 we show the first moment of the thrust distribution as a function of the center of mass energy Q, including QED and m_b corrections. We use here the best-fit values given in Eq. (4.33). The band displays the theoretical uncertainty and has been determined with a scan on the parameters included in our theory, as explained in App. B. The fit result is shown in comparison with data from ALEPH, OPAL, L3, DELPHI and JADE. Good agreement is observed for all Q values. It is interesting to compare the result of this analysis with the result of our earlier fit of thrust tail distributions in Ref. [1]. This is shown in Fig. 4-9. Here the red upper shaded area and corresponding ellipses show the results from fits to the first moment of the thrust distribution, while the blue lower shaded area and ellipses show the result from fits of its tail region. Both analyses show the theory (dashed lines) and combined theoretical and experimental (solid lines) standard error ellipses, as well as the ellipses which correspond to $\Delta\chi^2 = 2.3$ (68% CL for a two-parameter fit, wide-dashed lines). We see that the two analyses are compatible.

4.4 Fixed Order Analysis of M_1

It is interesting to compare the result of our best fit with an analysis where we do not perform resummation in the thrust distribution, but where power corrections and renormalon subtractions are still considered. This is achieved by setting the scales μ_H, μ_S, μ_J, $\mu_{\rm ns}$ in our theoretical prediction all to a common scale $\mu \sim Q$. We use R

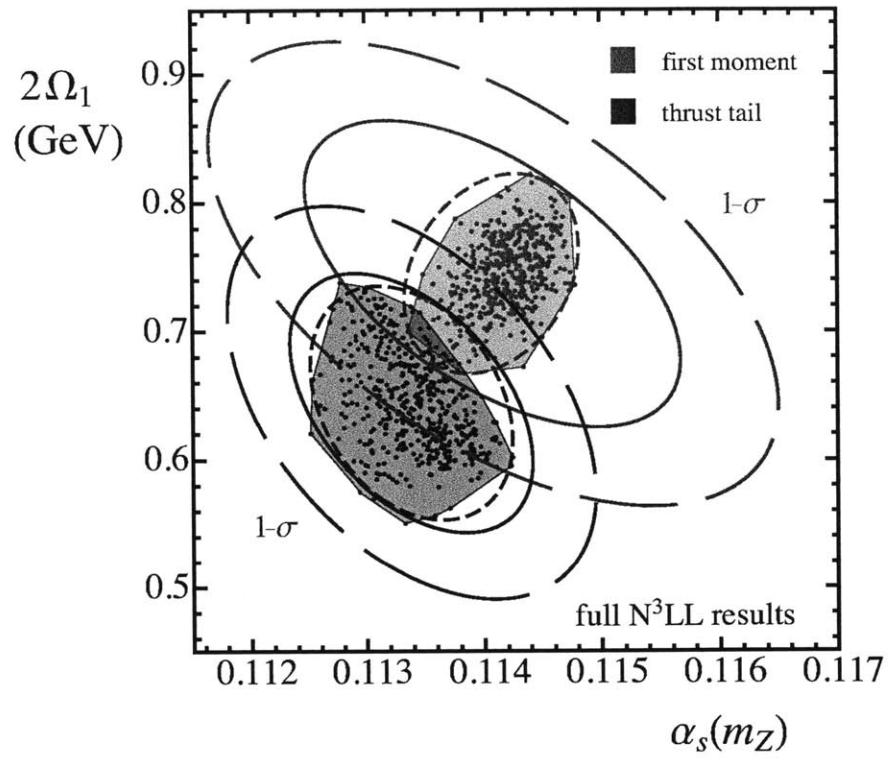

Figure 4-9: Comparison of $\alpha_s(m_Z)$ and Ω_1 determinations from thrust first moment data (red) and thrust tail data (blue). The plot corresponds to fits with N^{3}LL accuracy and in the Rgap scheme. The tail fits are performed with our improved code which uses a new nonsingular two-loop function, and the now known two-loop soft function. Dashed lines correspond to theory uncertainties, solid lines correspond to $\Delta\chi^2 = 1$ combined theoretical and experimental error ellipses, and wide-dashed lines correspond to $\Delta\chi^2 = 2.3$ combined error ellipses (corresponding to 1-σ uncertainty in two dimensions).

for the scale of the renormalon subtractions and renormalization group evolved power correction. Finally we will neglect QED and b-mass corrections in this subsection. Up to the treatment of power corrections and perturbative subtractions, the fixed order results used for this analysis are thus equivalent to those used in Ref. [84].

The OPE formula for the first moment in the Rgap scheme for this situation is given by

$$M_1 = \hat{M}_1^{\text{Rgap}}(R,\mu) + \frac{2\,\Omega_1(R,\mu)}{Q}\,, \tag{4.34}$$
$$\Omega_1(R,\mu) = \Omega_1 + \bar{\Delta}(R,\mu) - \bar{\Delta}(R_\Delta,\mu_\Delta)\,,$$

In Eq. (4.34), the Ω_1 with no arguments is the value determined by the fits, which is in the Rgap scheme at the reference scale $\mu_\Delta = R_\Delta = 2\,\mathrm{GeV}$. Here $\bar{\Delta}(R,\mu)$ is the running gap parameter, and $\bar{\Delta}(R,\mu) - \bar{\Delta}(R_\Delta,\mu_\Delta)$ is used to sum logarithms from (R_Δ,μ_Δ) to (R,μ) in Eq. (4.34). The analytic expression for $\bar{\Delta}(R,\mu) - \bar{\Delta}(R_\Delta,\mu_\Delta)$ can be found in Eq. (41) of Ref. [94, 1]. The perturbative $\hat{M}_1^{\mathrm{Rgap}}$ is related to the perturbative $\overline{\mathrm{MS}}$ result by

$$\begin{aligned} \hat{M}_1^{\mathrm{Rgap}}(R,\mu) &= \hat{M}_1^{\overline{\mathrm{MS}}}(\mu) + \frac{2\,\delta(R,\mu)}{Q}\,, \\ \delta(R,\mu) &= e^{\gamma_E} R \sum_{i=1}^{3} \alpha_s(\mu)^i \delta_i(R,\mu)\,, \end{aligned} \tag{4.35}$$

where the subtractions terms are [94, 1]

$$\begin{aligned} \delta_1(R,\mu) &= -0.848826 L_R\,, \\ \delta_2(R,\mu) &= -0.156279 - 0.46663 L_R - 0.517864 L_R^2\,, \\ \delta_3(R,\mu) &= -0.552986 - 0.622467 L_R - 0.777219 L_R^2 - 0.421261 L_R^3\,, \end{aligned} \tag{4.36}$$

with $L_R = \ln(\mu/R)$. In Eq. (4.35) $\delta(R,\mu)$ cancels the $\mathcal{O}(\Lambda_{\mathrm{QCD}})$ renormalon in $\hat{M}_1^{\overline{\mathrm{MS}}}(\mu)$, and it is crucial that the coupling expansions in both these objects are done at the same scale, $\alpha_s(\mu)$, for this cancellation to take place. The relation to the $\overline{\mathrm{MS}}$ scheme power correction is $\overline{\Omega}_1 = \Omega_1 + \delta(R_\Delta,\mu_\Delta)$, and the OPE in the $\overline{\mathrm{MS}}$ scheme at this level is

$$M_1 = \hat{M}_1^{\overline{\mathrm{MS}}}(\mu) + \frac{2\,\overline{\Omega}_1}{Q}\,. \tag{4.37}$$

In the $\overline{\mathrm{MS}}$ result there are no perturbative renormalon subtractions (and thus no log resummation related to the renormalon subtractions) and the parameter $\overline{\Omega}_1$ has a Λ_{QCD} renormalon ambiguity.

We will perform fits to the experimental data following the same procedure discussed in the previous section. Using Eq. (4.34) we consider two cases, i) $R \sim Q$ where Ω_1 is renormalization group evolved to R and there are no large logarithms in

order	$\mathcal{O}(\alpha_s^2)$	$\mathcal{O}(\alpha_s^3)$
(i) Rgap R-RGE	0.1160(27)(15)	0.1146(06)(14)
(ii) Rgap FO Subt.	0.1185(63)(15)	0.1138(20)(14)
(iii) $\overline{\rm MS}$ for $\overline{\Omega}_1$	0.1279(124)(19)	0.1186(38)(15)

Table 4.4: $\overline{\rm MS}$ scheme values for $\alpha_s(m_Z)$ obtained from various fixed order analyses. The first value in parentheses is the uncertainty from higher order perturbative corrections (obtained by the method described in the text), while the second value is the combined experimental and hadronization uncertainty.

order	$\mathcal{O}(\alpha_s^2)$	$\mathcal{O}(\alpha_s^3)$
(i) Rgap R-RGE	0.403(13)(47)	0.395(13)(47)
(ii) Rgap FO Subt.	0.204(126)(62)	0.337(76)(62)
(iii) $\overline{\rm MS}$ for $\overline{\Omega}_1$	0.383(62)(47)	0.355(54)(46)

Table 4.5: Ω_1 or $\overline{\Omega}_1$ values obtained from fixed order analyses at various orders. The first value in parentheses is the uncertainty from higher order perturbative corrections (obtained by the method described in the text), while the second value is the combined experimental and hadronization uncertainty.

the renormalon subtractions, and ii) fixing R at the reference scale, $R = 2\,\text{GeV}$, in which case large logarithms are present in the renormalon subtractions. We will also consider a third case, iii), using the $\overline{\rm MS}$-OPE of Eq. (4.37). Results for these fits are shown in Tabs. 4.4 and 4.5. For all cases $\chi^2/\text{dof} \simeq 1.32$.

For case i) we take $R \sim \mu \sim Q$, so there are no large logarithms in the $\delta(R,\mu)$ of Eq. (4.34), and all large logarithms associated with renormalon subtractions are summed in $\bar{\Delta}(R,\mu) - \bar{\Delta}(R_\Delta,\mu_\Delta)$. Here we estimate the perturbative uncertainty in $\alpha_s(m_Z)$ and Ω_1 by varying the renormalization scale μ and the scale R independently in the range $\{2Q, Q/2\}$. We use one-half the maximum minus minimum variation as the uncertainty, and the average for the central value. The results for both $\alpha_s(m_Z)$ and Ω_1 are fully compatible at 1-σ to our final results shown in Eq. (3.5). The agreement is even closer to the central values for the fits without QED or b-mass corrections in Tabs. 4.1 and 4.2, namely $\alpha_s(m_Z) = 0.1143(07)(14)$ and $\Omega_1 = 0.397(35)(46)$. The one difference is that the perturbative uncertainty for Ω_1 in Tab. 4.5 is a factor of three smaller. The case i) results in the table also exhibit nice order-by-order convergence, and if one plots M_1 versus Q (analogous to Fig. 4-2) the uncertainty bands are entirely contained within one another. In order to be conservative, we take our

resummation analysis in Eq. (3.5) as our final results (with its larger perturbative uncertainty and inclusion of QED and b-mass corrections).

For case ii) we take $R \sim 2\,\text{GeV}$ and $\mu \sim Q$ as typical values, so there are large logarithms, $\ln(R/Q)$, in the $\delta(R,\mu)$ renormalon subtractions. The central value for $\alpha_s(m_Z)$ at $\mathcal{O}(\alpha_s^3)$ is again fully compatible with that in Eq. (3.5). Here we estimate the perturbative uncertainty in $\alpha_s(m_Z)$ by varying $\mu \in \{2\,Q, Q/2\}$ and $R = 2 \pm 1\,\text{GeV}$. Due to the large logarithms the perturbative uncertainty in $\alpha_s(m_Z)$ for case ii), shown in Tab. 4.4, is three times larger than for case i). It is also compatible with the difference between central values at $\mathcal{O}(\alpha_s^2)$ and $\mathcal{O}(\alpha_s^3)$. To estimate the uncertainty for Ω_1 we only vary μ, which leads to the rather large error estimate for Ω_1 shown in Tab. 4.5. The contrast between the precision of the results in case i), to the results in case ii), illustrates the importance of summing large logarithms in the renormalon subtractions.

For case iii), where the $\overline{\Omega}_1$ power correction is defined in $\overline{\text{MS}}$ we do not have renormalon subtractions (and hence no large logs in subtractions). Due to the poor convergence of the fixed order prediction for the first moment, seen from the blue fixed order points in Fig. 4-2, it is not clear whether varying μ in the range $\{2\,Q, Q/2\}$ gives a realistic perturbative uncertainty estimate. Hence we determine the perturbative uncertainty for case iii) in Tabs. 4.4 and 4.5 by varying μ in the range $\{2\,Q, Q/2\}$ and multiply the result by a factor of two. The perturbative uncertainties for $\alpha_s(m_Z)$ are a factor of two larger than in case ii). The central values for $\alpha_s(m_Z)$ in case iii) are also larger, but are compatible with those in case ii) and Eq. (3.5) within 1-σ.

It is interesting to compare our results to those of Ref. [84], which also performs a fixed order analysis at $\mathcal{O}(\alpha_s^3)$, and incorporates subtractions based on the dispersive model.[8] Here the subtractions contain logarithms, $\ln(\mu_I/\mu)$, where $\mu_I \sim 2\,\text{GeV}$ and $\mu \sim Q$, that are not resummed. From a fit to M_1 in thrust they obtained $\alpha_s(m_Z) = 0.1166 \pm 0.0015_{\text{exp}} \pm 0.0032_{\text{th}}$ where the first uncertainty is experimental

[8]On the experimental side, Ref. [84] uses only the new JADE data from [131] and OPAL data. In our analysis the new JADE was excluded, but we utilized a larger dataset that includes ALEPH, OPAL, L3, DELPHI, and older JADE data. This may have a non-negligible impact on the outcome of the comparison.

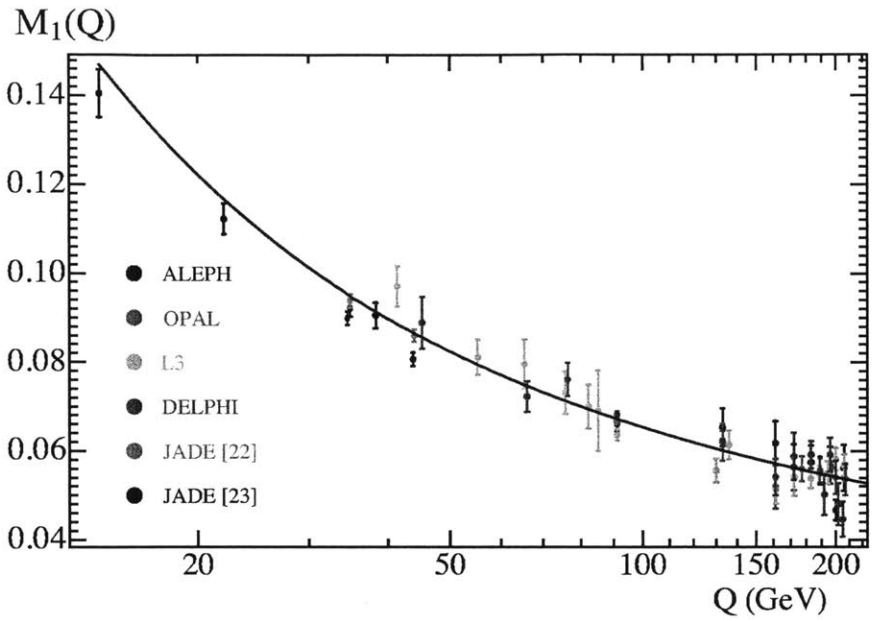

Figure 4-10: Experimental data for the first moment of thrust. The solid line corresponds to the result from Eq. (3.5).

and the second is theoretical. Our corresponding result is the one in case ii), and the central values and uncertainties for $\alpha_s(m_Z)$ are fully compatible. The perturbative uncertainty they obtain is a factor of 1.6 larger than ours. It arises from varying the renormalization scale $\mu \in \{2Q, Q/2\}$, the $\mathcal{O}(\alpha_s^2)$ Milan factor $\mathcal{M}$ by 20%, and the infrared scale $\mu_I = 2 \pm 1\,\text{GeV}$ in the dispersive model. In our analysis there is no precise analog of the Milan factor because our subtractions and Rgap scheme for Ω_1 fully account for two and three gluon infrared effects up to $\mathcal{O}(\alpha_s^3)$ that are associated to thrust. Other that this, the difference can be simply attributed to the differences in subtraction schemes which have an impact on the μ scale uncertainty. Finally, note that we have implemented the analytic results of Ref. [84] and confirmed their μ and μ_I uncertainties.

4.5 JADE Datasets

As discussed in Sec. 4.1 our global dataset includes thrust moment results from ALEPH, OPAL, L3, DELPHI, and the JADE data from Ref. [124]. In this sec-

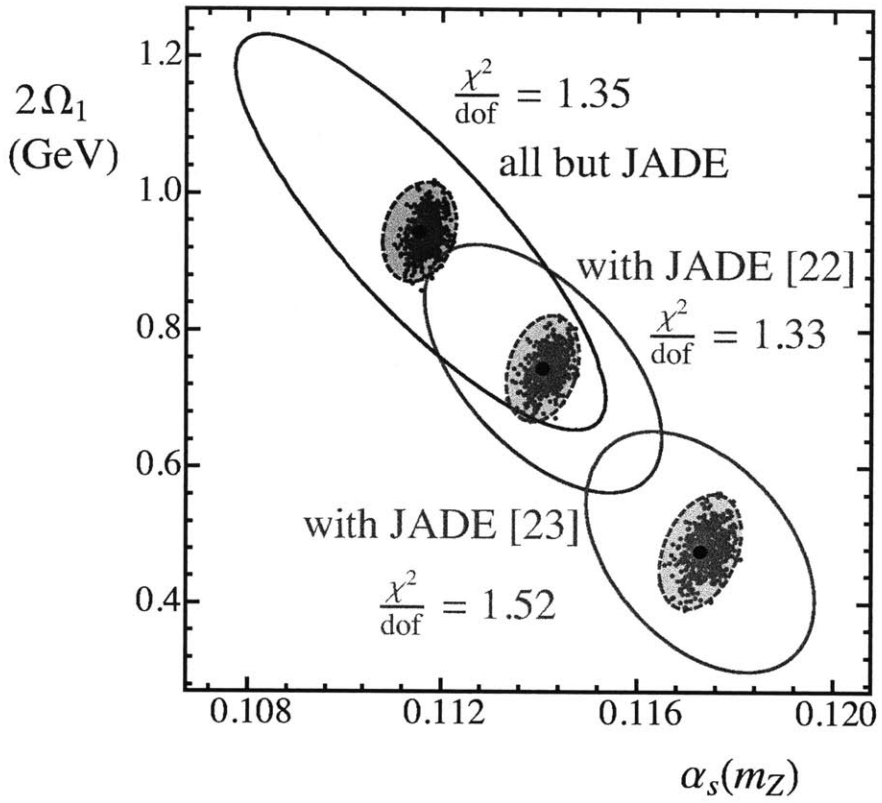

Figure 4-11: Fit results when using ALEPH, DELPHI, OPAL and L3, but no JADE data (upper blue ellipse), when also including JADE data from Ref. [124] (red central ellipse) [our default data set], and when instead including the JADE data from Ref. [131] (green lower ellipse).

tion we discuss the impact on the results in Secs. 4.3 and 4.4 of replacing the JADE data from Ref. [124] with moment results from an updated analysis carried out in Ref. [131], which removes the contributions from primary $b\bar{b}$ pair production and provides in addition measurements at $Q = 14$ and 22 GeV. In Fig. 4-10 we show the data for M_1, including the JADE results from Refs. [124] and [131]. The most significant difference occurs at $Q = 44\,\text{GeV}$. Our analysis will treat these datasets on the same footing without attempting to account for the effect of removing the $b\bar{b}$'s.

For our analysis in Sec. 4.3 with theory results at $\text{N}^3\text{LL} + \mathcal{O}(\alpha_s^3)$ we continue to exclude center of mass energies $Q \leq 22$ GeV. The dependence of the global fit result on the data set for M_1 is shown in Fig. 4-11. Theoretical uncertainties are analyzed again by the scan method giving the central dots and three inner ellipses, while the

outer three ellipses show the respective combined 1-σ total experimental and theoretical uncertainties. Using all experimental data but excluding JADE measurements entirely gives the fit result shown by the upper blue ellipse. This result is compatible at 1-σ with the central red ellipse which shows our default analysis, using the Ref. [124] JADE M_1 measurements. Replacing these two JADE data points by the four $Q > 22\,\mathrm{GeV}$ JADE M_1 results from Ref. [131] yields the lower green ellipse (whose center is $\simeq$ 1.5-σ from the central ellipse). For this fit the χ^2/dof increases from 1.33 to 1.52 demonstrating that there is less compatibility between the data. For this reason, together with the concern about the impact of removing primary $b\bar{b}$ events with MC simulations, we have used only JADE data from Ref. [124] in our main analysis.

A similar pattern is observed using the fixed order fits of M_1 discussed in Sec. 4.4. In this case it is also straightforward to include the $Q = 14, 22\,\mathrm{GeV}$ JADE data from Ref. [131]. If these two points are added to our default dataset (which contains $Q = 35$ and 45 GeV as the lowest Q results for M_1) then we find $\alpha_s(m_Z) = 0.1156 \pm 0.0013$ and $\Omega_1 = 0.353 \pm 0.038\,\mathrm{GeV}$ with $\chi^2/\mathrm{dof} = 1.3$. This is compatible at 1-σ with our final pure QCD result in Tab. 4.1. If we include the entire set of JADE data from Ref. [131] instead of those from Ref. [124] then we find $\alpha_s(m_Z) = 0.1170 \pm 0.0012$ and $\Omega_1 = 0.287 \pm 0.035\,\mathrm{GeV}$ with $\chi^2/\mathrm{dof} = 1.5$, very similar to the values observed for the green lower ellipse in Fig. 4-11. Hence, overall the fixed order analysis does not change the comparison of fits with the two different JADE datasets.

4.6 Higher Moment Analysis

In this section we consider higher moments, $M_{n\geq 2}$, which have been measured experimentally up to $n = 5$. From Eq. (4.20) we see that these moments have power corrections $\propto 1/Q^k$ for $k \geq 1$. Since for the perturbative moments we have $\hat{M}_n/\hat{M}_{n+1} \simeq 4$–9, we estimate that the $1/Q^2$ power corrections are suppressed by $9\Lambda_{\mathrm{QCD}}/Q$ which varies from 1/8 to 1/44 for the Q-values in our dataset, $Q \geq 35\,\mathrm{GeV}$. Hence, for the analysis in this section we can safely drop the $1/Q^2$ and higher power corrections and use the

form

$$M_n = \hat{M}_n + \frac{2\,n\,\Omega_1}{Q}\,\hat{M}_{n-1}\,. \tag{4.38}$$

By using our fit results for $\alpha_s(m_Z)$ and Ω_1 from Eq. (3.5) we can directly make predictions for the moments $M_{2,3,4,5}$. This tests how well the theory does at calculating the perturbative contributions $\hat{M}_{2,3,4,5}$. The results for these moments are shown in Fig. 4-12 and correspond to $\chi^2/\text{dof} = 1.3, 2.6, 0.8, 1.2$ for $n = 2, 3, 4, 5$ respectively, indicating that our formalism does quite well at reproducing these moments. The larger χ^2/dof for $n = 3$ is related to a quite significant spread in the experimental data for this moment at $Q \gtrsim 190\,\text{GeV}$. Note that we also see that the relation $M_n/M_{n+1} \simeq 4$–9 is satisfied by the experimental moments.

An alternate way to test the higher moments is to perform a fit to this data. Since we have excluded the new JADE data in Ref. [131], we do not have a significant dataset at smaller Q values for the higher moments. With our higher moment dataset the degeneracy between $\alpha_s(m_Z)$ and Ω_1 is not broken for $n \geq 2$, and one finds very large experimental errors for a two-parameter fit already at $n = 2$. However we can still fit for $\alpha_s(m_Z)$ from data for each individual $M_{n\geq 2}$ by fixing the value of Ω_1 to the best fit value in Eq. (3.5) from our fit to M_1. For this exercise we use our full $\text{N}^3\text{LL} + \mathcal{O}(\alpha_s^3)$ code, but with QED and mass effects turned off. The outcome is shown in Fig. 4-13 and Tab. 4.6. We find only a little dependence of α_s on n, and all values are compatible with the fit to the first moment within less than 1-σ. This again confirms that our value for Ω_1 and perturbative predictions for $\hat{M}_{n\geq 2}$ are consistent with the higher moment data. In Ref. [84] a two-parameter fit to higher thrust moments was carried out using OPAL data and the latest low energy JADE data. For $n = 2$ to $n = 5$ the results increase linearly from $\alpha_s(m_Z) = 0.1202 \pm (0.0018)_{\text{exp}} \pm (0.0046)_{\text{th}}$ to $\alpha_s(m_Z) = 0.1294 \pm (0.0027)_{\text{exp}} \pm (0.0070)_{\text{th}}$ respectively, and the weighted average for the first five moments of thrust is $\alpha_s(m_Z) = 0.1208 \pm 0.0018_{\text{exp}} \pm 0.0045_{\text{th}}$. The results are fully compatible within the uncertainties, and there is an indication of a trend towards larger $\alpha_s(m_Z)$ extracted from higher moments. In our analysis

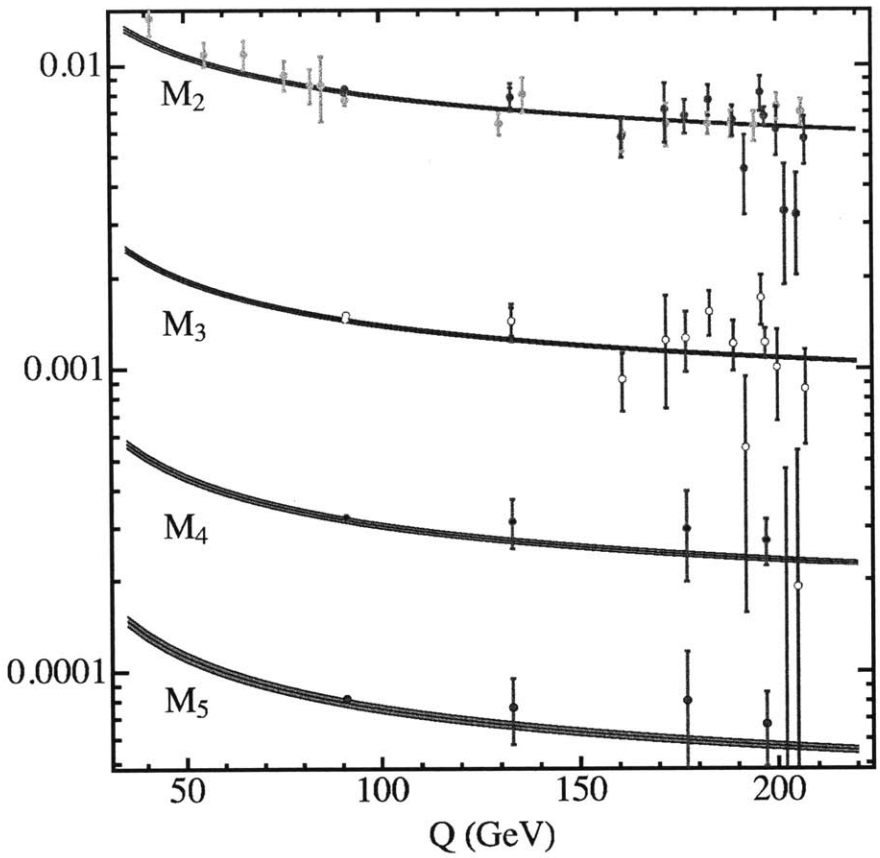

Figure 4-12: Predictions for the higher moments M_2, M_3, M_4, M_5 using the best fit values from Eq. (3.5), and our full $\mathrm{N^3LL} + \mathcal{O}(\alpha_s^3)$ code in the Rgap scheme, but with QED and mass effects turned off. The central points use different symbols for different moments.

n	$\alpha_s(m_Z)$	$\Delta_{\rm th}[\alpha_s]$	$\Delta_{\rm exp}[\alpha_s]$	χ^2/dof
2	0.1150	0.0009	0.0005	1.24
3	0.1158	0.0009	0.0005	1.87
4	0.1152	0.0011	0.0010	0.39
5	0.1157	0.0015	0.0010	0.23

Table 4.6: Numerical results for α_s from one-parameter fits to the M_n moments. The second column gives the central values for $\alpha_s(m_Z)$, the third and fourth show the theoretical and experimental errors, respectively. Since Ω_1 was fixed for this analysis we do not quote a hadronization error.

we do not observe this trend, but our results should not be directly compared since we have only performed a one parameter fit. After further averaging over results obtained from event shapes other than thrust Ref. [84] obtained as their final result

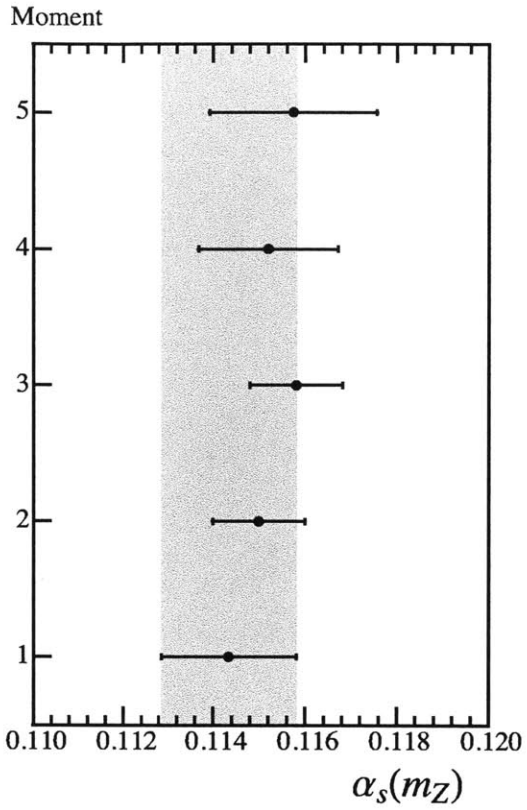

Figure 4-13: One-parameter fits for $\alpha_s(m_Z)$ to the first five moments. We use our full set up with power corrections and renormalon subtractions, with QED and mass corrections turned off. The value of Ω_1 is fixed from Eq. (3.5). The error bars include theoretical and experimental errors added in quadrature (not including uncertainty in Ω_1).

$\alpha_s(m_Z) = 0.1153 \pm 0.0017_{\rm exp} \pm 0.0023_{\rm th}$. This is again perfectly compatible with our result in Eq. (3.5).

4.7 Higher power corrections from Cumulant Moments

In this section we use cumulant moments as defined in Eq. (4.26) to discuss the presence of higher power corrections and their constraints from experimental data. There are two types of power corrections that are relevant for the cumulants, those defined rigorously by QCD matrix elements which come from the leading thrust factorization

theorem, Ω'_n, and those from our simple parameterization of higher order power corrections in Eq. (4.14), $\Omega_{n,j\geq 1}$. For the latter a systematic matching onto QCD matrix elements has not been carried out and the corresponding perturbative coefficients have not been determined.

For the second cumulant M'_2 both types of power correction contribute to the leading $1/Q^2$ term in the combination

$$\tilde{\Omega}'_2 = \Omega'_2 + \overline{M}_{1,1}\,\Omega_{1,1}\,. \tag{4.39}$$

Without a calculation of the perturbative coefficient $\overline{M}_{1,1}$ we cannot argue that either one dominates, and hence we keep both of them. In terms of this parameter the OPE with its leading power correction for the second cumulant becomes simply

$$M'_2 = \hat{M}'_2 + \frac{4\,\tilde{\Omega}'_2}{Q^2}\,, \tag{4.40}$$

where $\hat{M}'_2$ is computed from our leading order factorization theorem, see Eq. (4.10). For the third cumulant M'_3 the power correction from the leading thrust factorization theorem is $1/Q^3$, while that from the subleading factorization theorem is $1/Q^2$, so

$$M'_3 = \hat{M}'_3 + \frac{6\,\overline{M}_{2,1}\,\Omega_{1,1}}{Q^2} + \frac{8\,\Omega'_3}{Q^3}\,. \tag{4.41}$$

We will keep both of these power corrections. For our analysis we will assume that the perturbative coefficients $\overline{M}_{1,1}$ and $\overline{M}_{2,1}$ get contributions at tree-level, and hence that their logarithmic dependence on Q is α_s-suppressed. Thus for fits to $M'_{2,3}$ we will consider the three parameters $\tilde{\Omega}'_2$, $\overline{M}_{2,1}\,\Omega_{1,1}$, and Ω'_3. Our theoretical expectations are that $(\Omega'_n)^{1/n} \sim \Lambda_{\rm QCD}$ and $(\Omega_{1,1})^{1/2} \sim (\Omega'_n)^{1/n}$.

Since most of the experimental collaborations provide measurements only for moments we computed the cumulants using Eq. (4.2). To propagate the errors to the n-th cumulant one needs the correlations between the first n moments, both statistical and systematical. Following experimental procedures we will estimate the statistical correlation matrix from Monte Carlo simulations. These matrices are provided in

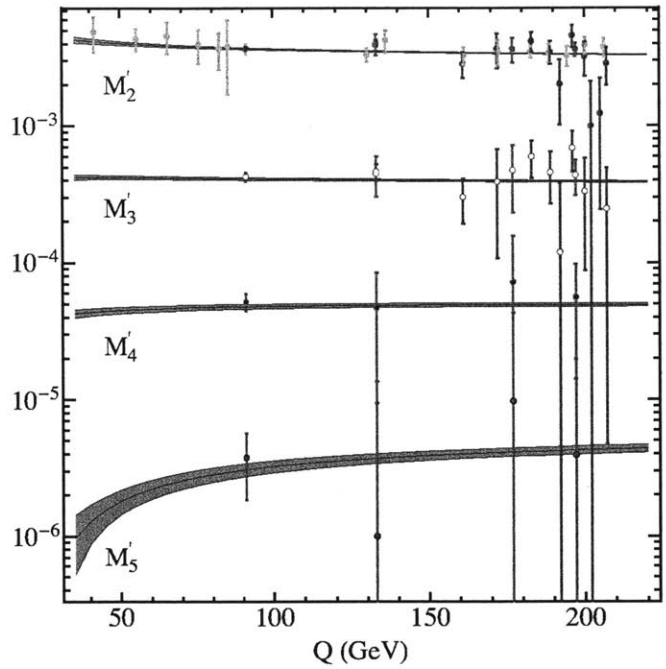

Figure 4-14: Prediction of cumulants using our best-fit values for $\alpha_s(m_Z)$ and Ω_1 from the fit to the first thrust moment. The band includes only the theoretical uncertainty from the random scan. The theory prediction includes QED and mass corrections, and uses our default model, which translates into the following values for higher nonperturbative power corrections: $\Omega_2' = \Omega_1^2/4$, $\Omega_3' = \Omega_1^3/8$, $\Omega_4' = 3\,\Omega_1^4/32$, $\Omega_5' = 3\,\Omega_1^5/32$.

Ref. [130] for $Q = 14$, 91.3, 206.6 GeV.[9] The computation of these matrices does not depend on the simulation of the detector and hence can be a priory employed on the data provided by any experimental collaboration. It was found that statistical correlation matrices depend very mildly on the center of mass energy, and our approach is to use the matrix computed at 14 GeV for $Q < 60$ GeV, the one computed at 91.3 for 60 GeV $\leq Q < 120$ GeV and the one at 206.6 GeV for $Q \geq 120$ GeV. The systematic correlation matrix for the moments is estimated using the minimal overlap model based on the systematic uncertainties, and then converted to uncertainties for the cumulants. We use this method even for the few cases in which experimental collaborations provide uncertainties for the cumulants directly, since we want to treat all data on the same footing. In these cases we have checked that the results are very

[9]We thank Christoph Pahl for providing details on the use of correlation matrices for moments.

	central	$\Delta_{\rm th}$	$\Delta_{\rm exp}$	$\frac{\chi^2}{\rm dof}$
$(\tilde{\Omega}_2')^{1/2}$	0.74	0.09	0.11	0.72
$(\Theta_2)^{1/2}$	1.21	0.10	0.22	0.93
$(\Theta_3)^{1/3}$	-2.61	0.15	1.51	

Table 4.7: Determination of power corrections from fits to M_2' and M_3'. All values in the table are in GeV. Columns two to four correspond to central value, theoretical uncertainty, and experimental uncertainty, respectively (the latter includes both statistical and systematic errors added in quadrature). The values displayed correspond to the linear combinations in Eq. (4.42), which for M_3' diagonalize the experimental error matrix.

similar.

To some extent the prescription we employ lies in between two extreme situations: a) moments are completely uncorrelated, and b) cumulants are completely uncorrelated. Situation a) corresponds to the naive assumption that the moments are independent. Situation b) is motivated by considering that properties like the location of the peak of the distribution ($\sim M_1$), the width of the peak ($\sim M_2'$), etc are independent. By assuming moments are uncorrelated one overestimates the errors of the cumulants. This would translate into larger experimental errors for our fit results and very small χ^2/dof. Assuming that cumulants are uncorrelated induces very strong positive correlations between moments, which then leads to small uncertainties for the cumulants, especially for the variance, and larger χ^2/dof values. With the adopted prescription we use one finds a weaker positive correlation among moments, which translates into a situation between these two extremes.[10] For our analysis we use our highest order code as described in Sec. 4.3, but without QED and b-mass effects, and take the value $\alpha_s(m_Z) = 0.1143$ obtained in our fit to the first moment data with this code (see Tab. 4.1). Since we are analyzing cumulant moments $M_{n\geq 2}'$ the value of Ω_1 is not required, and there is no distinction between having this parameter in $\overline{\rm MS}$ or the Rgap scheme. Hence in order to fit for higher power corrections we use our purely perturbative code in the $\overline{\rm MS}$ scheme. Thus all of the power correction

[10]One might also construct the correlation matrices using the statistical and systematic errors from the thrust distributions themselves. Bins in distributions are statistically independent and systematic correlations are estimated using the minimal overlap model. Unfortunately this often introduces strong biases, and we thank Christoph Pahl for clarifying this point.

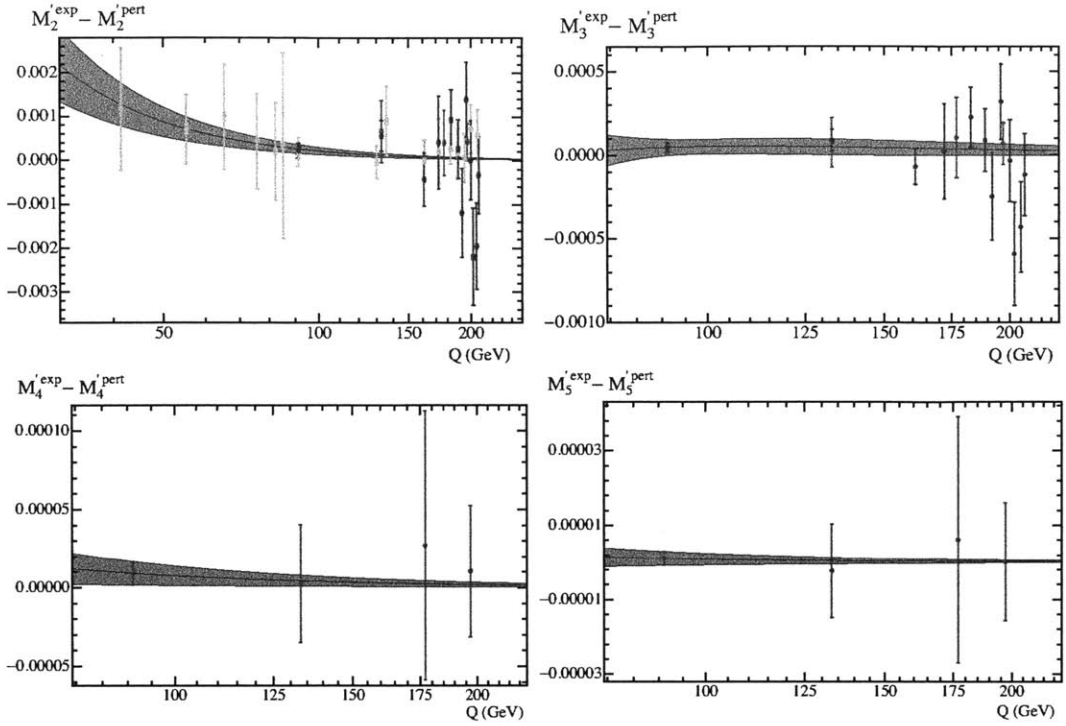

Figure 4-15: Determination of power corrections from fits to data. On the vertical axes we display the n-th experimental cumulant with the perturbative part subtracted $M'_n - \hat{M}'_n$. The error bars shown are experimental (statistical and systematic combined) added in quadrature with perturbative errors from the random scan over the profile parameters. The top-left panel shows the fit to $\tilde{\Omega}'_2/Q^2$, and the top-right panel shows the fit to $\overline{M}_{2,1}\,\Omega_{1,1}/Q^2$ and Ω'_3/Q^3 through the linear combinations in $\Theta_{2,3}$. The bottom two panels for $n = 4, 5$ show a simple fit to $\overline{M}_{3,1}\Omega_{1,1}$ and $\overline{M}_{4,1}\Omega_{1,1}$ taking $\Omega'_4 = \Omega'_5 = 0$.

parameters extracted in this section are in the $\overline{\text{MS}}$ scheme, and in particular we do not carry out renormalon subtractions beyond $\mathcal{O}(\Lambda_{\text{QCD}})$. The perturbative error is estimated as in Sec. 4.3, by a 500 point scan of theory parameters (see App. B).

Before we fit for the higher power corrections, we will check how well our factorization theorem predicts the experimental cumulants using a simple exponential model for the nonperturbative soft function (the model with only one coefficient $c_0 = 1$ from Refs. [1, 116]). This model has higher power corrections that are determined by its one parameter Ω_1: $\Omega'_2 = \Omega_1^2/4$, $\Omega'_3 = \Omega_1^3/8$, $\Omega'_4 = 3\,\Omega_1^4/32$, $\Omega'_5 = 3\,\Omega_1^5/32$. Results are shown in Fig. 4-14, where good agreement between theory and data is observed.

For the M'_n in Fig. 4-14 we also observe that $M'_{n+1}/M'_n \sim 1/10$, so the $(n+1)$-th

order cumulant is generically one order of magnitude smaller than the n-th order cumulant.

Next we will fit for the power correction parameters $\tilde{\Omega}_2'$, $\overline{M}_{2,1}\,\Omega_{1,1}$, and Ω_3'. To facilitate this we consider the difference between the experimental cumulants M_n' and the perturbative theoretical cumulants $\hat{M}_n'$, namely $M_2' - \hat{M}_2'$ and $M_3' - \hat{M}_3'$. From Eqs. (4.40) and (4.41) these differences are determined entirely by the power correction parameters we wish to fit. The results are shown in Tab. 4.7 and the upper two panels of Fig. 4-15. From the $M_2' - \hat{M}_2'$ fit a fairly precise result is obtained for $(\tilde{\Omega}_2')^{1/2}$. Its central value of 740 MeV is compatible with $\sim 2\Lambda_{\rm QCD}$, and hence agrees with naive dimensional analysis. Interestingly, we have checked that including a constant and $1/Q$ term in the second cumulant fit one finds that their coefficients are compatible with zero, in support of the theoretically expected $1/Q^2$-dependence.

For the fit to $M_3' - \hat{M}_3'$ there is a strong correlation between Ω_3' and $\overline{M}_{2,1}\,\Omega_{1,1}$ even though they occur at different orders in $1/Q$. Since the χ^2 is quadratic in these two parameters we can determine the linear combinations that exactly diagonalize their correlation matrix:

$$\Theta_2 \equiv \left[\frac{6\,\overline{M}_{2,1}}{0.07}\right]\frac{\Omega_{1,1}}{4} + (0.3105\,\mathrm{GeV}^{-1})\,\Omega_3'\,, \tag{4.42}$$

$$\Theta_3 \equiv \Omega_3' - (0.3105\,\mathrm{GeV})\left[\frac{6\,\overline{M}_{2,1}}{0.07}\right]\frac{\Omega_{1,1}}{4}\,.$$

Note that these combinations arise solely from experimental data. We have presented the coefficients of these combinations grouping together a factor of $[6\overline{M}_{2,1}/0.07]$, which is close to unity if $6\overline{M}_{2,1} \simeq \hat{M}_1$. The results in Tab. 4.7 exhibit a reasonable uncertainty for Θ_2, but a large uncertainty for Θ_3. Hence, at this time it is not possible to determine the original parameters Ω_3' and $\overline{M}_{2,1}\,\Omega_{1,1}$ independently. As in the previous case, the fit does not exhibit any evidence for a $1/Q$ correction, confirming the theoretical prediction for this cumulant.

In Fig. 4-15 we also show results for cumulant differences $M_n' - \hat{M}_n'$ versus Q for $n = 4$ and $n = 5$. In all cases $n = 2, 3, 4, 5$ the perturbative cumulants $\hat{M}_n'$ are the largest component of the cumulant moments M_n', as can be verified by the

reduction of the values by a factor of 2–3 in Fig. 4-15 compared to the values in Fig. 4-14. We also observe an order of magnitude suppression between the $(n+1)$'th and n'th terms, $(M'_{n+1} - \hat{M}'_{n+1})/(M'_n - \hat{M}'_n) \sim 1/10$. For $n = 4, 5$ the OPE formula in Eq. (4.26) involves both $2^n\Omega'_n/Q^n$ terms and terms with non-trivial perturbative coefficients: $(2\,n\,\overline{M}_{n-1,1}\Omega_{1,1})/Q^2 + \ldots$ (where here the ellipses are terms at $1/Q^3$ and beyond). If the former dominated we would expect a suppression by $2\,\Lambda_{\rm QCD}/Q$ for the $(n+1)$'th versus n'th term, which is not observed. The observed suppression by $1/10$ is consistent with domination by the $1/Q^2$ power correction terms in the $n = 4, 5$ cumulant differences. This would imply $[(n+1)\overline{M}_{n,1}]/[n\overline{M}_{n-1,1}] \sim 1/10$ and could in principle be verified by an explicit computation of these coefficients. In Fig. 4-15 we show fits to a $1/Q^2$ power correction, which are essentially dominated by the lowest energy point at the Z-pole. The results are $\sqrt{8\,\overline{M}_{3,1}\,\Omega_{1,1}} = 0.20 \pm 0.08$ from fits to M'_4 and $\sqrt{10\,\overline{M}_{4,1}\,\Omega_{1,1}} = 0.07 \pm 0.06$ from fits to M'_5. These findings nicely confirm our expectation of the $\sim 1/10$ suppression for the $\overline{M}_{n,1}$ matrix elements.

In this section we have determined the $1/Q^2$ power correction parameter $\tilde{\Omega}'_2$ with 25% accuracy, and find it is $3.8\,\sigma$ different from zero. For the higher moments there are important contributions from a $\Omega_{1,1}/Q^2$ power correction, which appears to even dominate for $n \geq 4$. Clearly experimental data supports the pattern expected from the OPE relation in Eq. (4.26).

4.8 Conclusions

In this work we have used a full τ-distribution factorization formula developed by the authors in a previous publication [1] to study moments and cumulant moments of the thrust distribution. Perturbatively it incorporates $\mathcal{O}(\alpha_s^3)$ matrix elements and nonsingular terms, a resummation of large logarithms, $\ln^k \tau$, to N^{3}LL accuracy, and the leading QED and bottom mass corrections. It also describes the dominant non-perturbative corrections, is free of the leading renormalon ambiguity, and sums up large logs appearing in perturbative renormalon subtractions.

Theoretically there are no large logs in the perturbative expression of the thrust

moments, and when normalized in the same way the perturbative result from the full τ code with resummation agrees very well with the fixed order results. Nevertheless, when the code is properly self normalized it significantly improves the order-by-order perturbative convergence towards the $\mathcal{O}(\alpha_s^3)$ result. In particular, the results remain within the perturbative error band of the previous order, in contrast to what is observed using fixed order expressions. This lends support to the theoretical uncertainty analysis from the code with resummation.

From fits to the first moment of the thrust distribution, M_1, we find the results for $\alpha_s(m_Z)$ and the leading power correction parameter Ω_1 given in Eq. (3.5). They are in nice agreement with values from the fit to the tail of the thrust distribution in Ref. [1]. The moment results have larger experimental uncertainties, and these dominate over theoretical uncertainties, in contrast with the situation in the tail region analysis of Ref. [1]. Repeating the M_1 fit using a fixed order code with no $\ln\tau$ resummation, but still retaining the summation of large logs in the perturbative renormalon subtractions, yields fully compatible results for $\alpha_s(m_Z)$ and Ω_1.

Using a Fourier space operator product expansion we have parameterized higher order power corrections which are beyond the leading factorization formula, and analyzed the OPE both for regular moments M_n and cumulant moments M'_n. In the regular moments the Ω_1/Q power correction from the leading factorization theorem enters with a perturbative suppression in its coefficient, and dominates numerically over higher $1/Q$ corrections. In contrast, the cumulant moments $M'_{n\geq 2}$ depend on higher order cumulant power corrections Ω'_n/Q^n from the leading factorization theorem, and are independent of $\Omega_1/Q, \ldots, \Omega'_{n-1}/Q^{n-1}$. Data on these cumulant moments appear to indicate that they receive important contributions from a $1/Q^2$ power correction that enters at a level beyond the leading thrust factorization theorem. Thus the OPE reveals that cumulant moments are appealing quantities for exploring subleading power corrections. We performed a fit to the second cumulant moment and determined a non-vanishing $\tilde{\Omega}'_2/Q^2$ power correction with a precision of 25%.

It would be interesting to extend the analysis performed here, based on OPE formulas related to factorization theorems, to other event shape moments and cu-

mulant moments. Examples of interest include the heavy jet mass event shape [59, 54, 60, 52, 56], angularities [36, 96], as well as more exclusive event shapes like jet broadening [53, 70, 57, 28, 58].

Chapter 5

Calculation of ISR Logarithms in Drell-Yan processes

5.1 Introduction

In [138] the hadronic event shapes variable beam thrust τ_B has been introduced to allow a simple theoretical description of the isolated Drell-Yan process with 0-jets. It allows for a calculation of thrust in a hadron collider when the thrust axis is taken to be the beam axis, and is an effective means to veto jets in the central region of the detector. In [138], the authors derived a factorization theorem for beam thrust and calculated the coefficient functions at NLO for the isolated Drell-Yan process.

In this Chapter we will first review the Drell-Yan process in section 5.2, we will define the beam thrust and state its factorization theorem in section 5.3. We will then discuss the original part of this work, which is the calculation of the logarithms of the NNLO beam function, section 5.4 and 5.5, and the calculation of the full set of logarithms of τ in the singular part of the NNLO coefficient functions for the isolated Drell-Yan cross section in sections 5.6 and 5.7. It is important to notice that most of the known NNLO cross-section results are given in the form of a numerical code. We present a fully analytic calculation which can be used to test the impact of higher order logarithms on central values and uncertainties. This calculation is required for the calculation of the nonsingular terms in resummed predictions, as we did in

Chapter 2.2.5 for thrust.

5.2 Drell-Yan process and factorization

The Drell-Yan process describes the process $pp \to X\ell^+\ell^-$ or $p\bar{p} \to X\ell^+\ell^-$. The kinematics of the process is parameterized as follows

$$P_a^\mu + P_b^\mu = p_X^\mu + q^\mu, \tag{5.1}$$

where $P_{a,b}^\mu$ are the incoming (anti)proton momenta, $E_{cm} = \sqrt{(P_a + P_b)^2}$ is the total center-of-mass energy, and q^μ is the total momentum of the lepton pair. It is common to define

$$\tau = \frac{q^2}{E_{\rm cm}^2}, \qquad Y = \frac{1}{2}\log\frac{P_b \cdot q}{P_a \cdot q}, \qquad x_a = \sqrt{\tau}\, e^Y, \qquad x_b = \sqrt{\tau}\, e^{-Y}, \tag{5.2}$$

where Y is the total rapidity of the leptons with respect to the beam axis, and $x_{a,b}$ are in one-to-one correspondence with τ and Y. The kinematic limits are

$$0 \le \tau \le 1, \qquad 2|Y| \le -\log\tau, \qquad \tau \le x_a \le 1, \qquad \tau \le x_b \le 1. \tag{5.3}$$

The invariant mass of the hadronic final state is bounded by

$$m_X^2 = p_X^2 \le E_{\rm cm}^2\,(1 - \sqrt{\tau})^2. \tag{5.4}$$

In the case of inclusive Drell-Yan, one sums over all hadronic final states X without imposing any cuts. The measurement is therefore infrared safe and insensitive to the details of the hadronic final state itself. In this situation there is a rigorous derivation of the classic factorization theorem

$$\frac{1}{\sigma_0}\frac{{\rm d}\sigma}{{\rm d}q^2{\rm d}Y} = \sum_{i,j}\int \frac{{\rm d}\xi_a}{\xi_a}\frac{{\rm d}\xi_b}{\xi_b}\, H_{ij}^{\rm incl}\left(\frac{x_a}{\xi_a}, \frac{x_b}{\xi_b}, q^2, \mu\right) f_i(\xi_a,\mu) f_j(\xi_b,\mu)\left[1 + \mathcal{O}\left(\frac{\Lambda_{\rm QCD}}{Q}\right)\right] \tag{5.5}$$

where $\sigma_0 = 4\pi\alpha_{\rm em}^2/(3N_C E_{\rm cm}^2 q^2)$, and the integration limits are $x_a \leq \xi_a \leq 1$ and $x_a \leq \xi_a \leq 1$. The sum is over partons $i,j = \{g,u,\overline{u},d,\dots\}$, and $f_i(\xi_a)$ is the parton distribution function for finding parton i inside the proton with light-cone momentum fractions ξ_a along the proton direction. The inclusive hard function $H_{ij}^{\rm incl}$ can be computed in fixed-order perturbative QCD as the partonic cross section to scatter parton i and j, and is known up to two loops.

5.3 Factorization theorem for Beam Thrust

The Beam Thrust is an event shape observable introduced in [138] to allow a simple theoretical description of isolated Drell-Yan processes. Here the hadronic final state is allowed to contain forward energetic radiation in jets about the beam axis, but only soft wide-angle radiation in the central region, *i.e.* no central jets. The beam thrust is defined as

$$\tau_B = \frac{e^{-Y}B_a^+(Y) + e^{Y}B_b^+(Y)}{Q^2} \tag{5.6}$$

where q^2 and Y are the total invariant mass and rapidity of the leptons, $Q = \sqrt{q^2}$. The hadronic momenta $B_a^\mu(Y)$ and $B_b^\mu(Y)$ measure the total momentum of all hadrons in the final state at rapidities $y > Y$ and $y < Y$, respectively(where the momenta are measured in the hadronic center-of-mass frame of the collision and the rapidities are with respect to the beam axis). Their plus components are defined as $B_i^+(Y) = n_i \cdot B_i(Y)$, where $n_a^\mu = (1,0,0,1)$ and $n_b = (1,0,0,-1)$ are light-cone vectors corresponding to the directions of the incoming protons (with the beam axis taken along the z direction). For $\tau_B \sim 1$ the hadronic final state contains radiation with momentum perpendicular to the beam axis of order of Q, while $\tau_B \ll 1$ corresponds to two-jets like events with radiation with momentum of order Q only near the direction of the beams. Requiring $\tau_B < \exp(-2y_B^{\rm cut})$ essentially vetoes hard radiation in the rapidity region $|y - Y| < y_B^{\rm cut} - 1$.

In Ref. [138] a rigorous factorization theorem for the Drell-Yan beam thrust cross

section for small τ_B has been derived and reads

$$\begin{aligned}\frac{\mathrm{d}\sigma}{\mathrm{d}q^2\mathrm{d}Y\mathrm{d}\tau_B} =&\sigma_0 \sum_{i,j} H_{i,j}(q^2,\mu_H)\, U_H(q^2,\mu_H,\mu_S) \int \mathrm{d}t_a\, \mathrm{d}t_b\, \mathrm{d}t'_a\, \mathrm{d}t'_b \\ &\times Q\, S_B\Big(Q\tau_B - \frac{t_a+t_b}{Q},\mu_S\Big) B_i(t_a-t'_a,x_a,\mu_B)\, U_B(t'_a,\mu_B,\mu_S) \\ &\times B_j(t_b-t'_b,x_b,\mu_B)\, U_B(t'_b,\mu_B,\mu_S)\Big[1+\mathcal{O}\big(\frac{\Lambda_{\mathrm{QCD}}}{Q},\tau_B\big)\Big]. \end{aligned} \tag{5.7}$$

The sum runs over partons $i,j = \{u\bar{u},\bar{u}u,d\bar{d},\dots\}$. The hard function $H_{ij}(q^2,\mu)$ contains virtual radiation at the hard scale $\mu_H \simeq Q$. The beam function $B_i(t_a,x_a,\mu)$ describes the formation of incoming jets prior to the hard collision due to collinear radiation form the incoming partons. The soft function $S_B(k,\mu)$ describes the effect of soft radiation form the incoming partons on the measurement of τ_B. When working at a fixed order in perturbation theory (without resummation), it is useful to express the cross section as

$$\begin{aligned}\frac{\mathrm{d}\sigma}{\mathrm{d}q^2\,\mathrm{d}Y\,\mathrm{d}\tau_B} = \sigma_0 \sum_{i,j}\Big[Q_i^2 + \frac{(v_i^2+a_i^2)(v_\ell^2+a_\ell^2) - 2Q_i v_i v_\ell (1-m_Z^2/q^2)}{(1-m_Z^2/q^2)^2 + m_Z^2\Gamma_Z^2/q^4}\Big] \\ \times \int \frac{\mathrm{d}\xi_a}{\xi_a}\frac{\mathrm{d}\xi_b}{\xi_b}\, C_{ij}\Big(\frac{x_a}{\xi_a},\frac{x_b}{\xi_b},q^2,\tau_B,\mu\Big)\, f_{i/a}(\xi_a,\mu)\, f_{j/b}(\xi_b,\mu), \end{aligned} \tag{5.8}$$

where, $f_{i/a}(\xi_a,\mu)$ and $f_{j/b}(\xi_b,\mu)$ are the PDFs for parton i in proton a and parton j in (anti-)proton b. In [138], the 1-loop fixed order cross section have been calculated, producing the following results. We decompose the coefficient functions C_{ij} as

$$C_{ij}(z_a,z_b,\tau,\mu) = C_{ij}^{\mathrm{s}}(z_a,z_b,\tau,\mu) + C_{ij}^{\mathrm{ns}}(z_a,z_b,\tau,\mu)\,, \tag{5.9}$$

into singular C_{ij}^{s} and nonsingular C_{ij}^{ns} terms. At tree level, the nonzero singular coefficients are

$$C_{q\bar{q}}^{\mathrm{s}(0)}(z_a,z_b,q^2,\tau_B,\mu) = C_{\bar{q}q}^{\mathrm{s}(0)}(z_a,z_b,q^2,\tau_B,\mu) = \delta(\tau_B)\,\delta(1-z_a)\,\delta(1-z_b)\,. \tag{5.10}$$

At one loop,

$$
\begin{aligned}
C_{q\bar{q}}^{\mathrm{s}(1)}(z_a, z_b, q^2, \tau_B, \mu) =& \frac{\alpha_s(\mu)\, C_F}{2\pi}\, \delta(1-z_a)\, \theta(z_b) \Bigg\{ \Bigg[-2 \left[\frac{\theta(\tau_B) \ln \tau_B}{\tau_B} \right]_+ - \frac{3}{2} \left[\frac{\theta(\tau_B)}{\tau_B} \right]_+ \\
& - \delta(\tau_B) \Big(4 - \frac{\pi^2}{2} \Big) \Bigg] \delta(1-z_b) \\
& + \left[\left[\frac{\theta(\tau_B)}{\tau_B} \right]_+ + \delta(\tau_B) \ln \frac{q^2}{\mu^2} \right] \left[\theta(1-z_b) \frac{1+z_b^2}{1-z_b} \right]_+ \\
& + \delta(\tau_B) \left[\left[\frac{\theta(1-z_b) \ln(1-z_b)}{1-z_b} \right]_+ (1+z_b^2) \right. \\
& \left. + \theta(1-z_b) \Big(1 - z_b - \frac{1+z_b^2}{1-z_b} \ln z_b \Big) \right] \Bigg\} + (z_a \leftrightarrow z_b)\,, \\
C_{\bar{q}q}^{\mathrm{s}(1)}(z_a, z_b, q^2, \tau_B, \mu) =& C^{\mathrm{s}}(1)_{q\bar{q}}(z_a, z_b, q^2, \tau_B, \mu)\,,
\end{aligned}
$$

$$
\begin{aligned}
C_{qg}^{\mathrm{s}(1)}(z_a, z_b, q^2, \tau_B, \mu) =& \frac{\alpha_s(\mu)\, T_F}{2\pi}\, \delta(1-z_a)\, \theta(z_b)\, \theta(1-z_b) \Bigg\{ \\
& \left[\left[\frac{\theta(\tau_B)}{\tau_B} \right]_+ + \delta(\tau_B) \ln \frac{q^2}{\mu^2} \right] \left[z_b^2 + (1-z_b)^2 \right] \\
& + \delta(\tau_B) \left[\ln \frac{1-z_b}{z_b} \left[z_b^2 + (1-z_b)^2 \right] + 2 z_b (1-z_b) \right] \Bigg\}\,, \\
C_{\bar{q}g}^{\mathrm{s}(1)}(z_a, z_b, q^2, \tau_B, \mu) =& C_{qg}^{\mathrm{s}(1)}(z_a, z_b, q^2, \tau_B, \mu)\,, \\
C_{gq}^{\mathrm{s}(1)}(z_a, z_b, q^2, \tau_B, \mu) =& C_{g\bar{q}}^{\mathrm{s}(1)}(z_a, z_b, q^2, \tau_B, \mu) = C_{qg}^{\mathrm{s}(1)}(z_b, z_a, q^2, \tau_B, \mu)\,. \qquad (5.11)
\end{aligned}
$$

The coefficient C_{gg} only starts to contribute at two loops. The single logarithms of q^2/μ^2 are multiplied by the QCD splitting kernels and the terms that correspond to renomalization group evolution of the PDFs. Thus, in fixed-order perturbation theory the PDFs should be evaluated at the hard scale $\mu = Q$, such that there are no large logarithms when integrating over $0 \leq \tau_B \lesssim 1$. However, if the integration is restricted to $\tau_B \leq \tau_B^{\mathrm{cut}} \ll 1$, the plus distributions in τ_B produce large logarithms $\ln^2 \tau_B^{\mathrm{cut}}$ and $\ln \tau_B^{\mathrm{cut}}$, which make a fixed-order expansion unreliable. These are precisely the logarithms that are resummed by the combined RGE of hard, jet, and soft functions in Eq. 5.7.

In this work we calculate the full set of logarithms in τ at NNLO, where τ is the

beam thrust defined in the hadronic center-of-mass frame

$$\tau = \frac{\mathcal{T}_{\rm cm}}{Q}, \qquad \mathcal{T}_{\rm cm} = \sum_k |\vec{p}_{k,T}| e^{-|\eta_k|} = \sum_k (E_k - |p_k^z|), \tag{5.12}$$

where the sum over k runs over all particles in the final state. Here $\vec{p}_{k,T}$ and η_k are the measured transverse momentum and rapidity of particle k with respect of the beam axis (taken to be the z axis). All particles are assumed massless for simplicity. The factorization theorem for this variable is

$$\begin{aligned}\frac{\mathrm{d}\sigma}{\mathrm{d}q^2 \mathrm{d}Y \mathrm{d}\tau} =& \sigma_0 \sum_{i,j} H_{i,j}(q^2, \mu_H)\, U_H(q^2, \mu_H, \mu_S) \int \mathrm{d}t_a\, \mathrm{d}t_b\, \mathrm{d}t'_a\, \mathrm{d}t'_b \\ & \times Q\, S_B\!\left(Q\tau - \frac{e^{-Y} t_a + e^{Y} t_b}{Q}, \mu_S\right) B_i(t_a - t'_a, x_a, \mu_B)\, U_B(t'_a, \mu_B, \mu_S) \\ & \times\; B_j(t_b - t'_b, x_b, \mu_B)\, U_B(t'_b, \mu_B, \mu_S) \left[1 + \mathcal{O}\Big(\frac{\Lambda_{\rm QCD}}{Q}, \tau\Big)\right]. \end{aligned} \tag{5.13}$$

Notice that now the soft function depends explicitly on the dilepton rapidity Y, and Eq. 5.7 is recovered setting the explicit Y dependence to zero. The one loop coefficients $C_{ij}^{\mathrm{s}(x)}(z_a, z_b, q^2, \tau_B, \mu)$ in Eq. 5.11, are then modified to

$$C_{ij}^{\mathrm{s}(x)}(z_a, z_b, q^2, \tau_B, \mu) \to C_{ij}^{\mathrm{s}(x)}(z_a, z_b, \tau, Y, q^2, \mu) \tag{5.14}$$

where

$$C_{ij}^{\mathrm{s}(x)}(z_a, z_b, \tau, Y, q^2, \mu) = C_{ij}^{\mathrm{s}(x)}(z_a, z_b, q^2, \tau_B, \mu) + \delta C_{ij}^{\mathrm{s}(x)}(z_a, z_b, \tau, Y, q^2, \mu). \tag{5.15}$$

The additional rapidity-dependent terms δC are

$$\begin{aligned}\delta C_{q\bar{q}}^{\mathrm{s}(1)}(z_a, z_b, \tau, Y, q^2, \mu) =& \delta(\tau)\, C_F\, \delta(1 - z_a) \Big[- P_{qq}(z_b) Y + \delta(1 - z_b) Y^2 \Big] \\ & + (z_a \leftrightarrow z_b, Y \to -Y) \\ \delta C_{qg}^{\mathrm{s}(1)}(z_a, z_b, \tau, Y, q^2, \mu) =& -\delta(\tau)\, T_F\, P_{qg}(z_b) \delta(1 - z_a) Y. \end{aligned} \tag{5.16}$$

In Eq. 5.41, the only factor for which we don't know the two loop contribution

is the beam function B. However, using the evolution factor of the beam functions, the evolution factors of the parton distribution functions, and the one loop beam function, it is possible to obtain all the singular contributions of the form $\mathcal{L}_k(\tau)$, with $k \geq 0$. We will now discuss the evolution of the pdfs, present the calculation of the logarithms of the two loop beam function and the results for the two loop coefficient functions.

5.4 Expansion of Parton Distribution Functions

We want to expand the pdfs at a generic scale μ, so we need to find an evolution factor U^f such that

$$f_i(\xi,\mu) = \int_\xi^1 \frac{d\xi'}{\xi'} U_{ij}^f\left(\frac{\xi}{\xi'},\mu,\mu_0\right) f_j(\xi',\mu_0). \tag{5.17}$$

In order to find such a factor, we recall that the scale dependence of the pdfs is given by the Altarelli-Parisi equations

$$\mu\frac{d}{d\mu} f_i(\xi,\mu) = \int_\xi^1 \frac{d\xi'}{\xi'} \gamma_{ij}^f\left(\frac{\xi}{\xi'},\mu\right) f_j(\xi',\mu) \tag{5.18}$$

where

$$\begin{aligned}
\gamma_{ij}^f(z,\mu) =& \sum_k P_{ij}^{(k)}(z,\alpha_S(\mu)),\\
P_{ij}^{(0)}(z,\alpha_S(\mu)) =& \frac{\alpha_S(\mu)}{\pi}\hat{P}_{ij}^{(0)}(z),\\
P_{ij}^{(1)}(z,\alpha_S(\mu)) =& \frac{\alpha_S^2(\mu)}{2\pi^2}\hat{P}_{ij}^{(1)}(z),
\end{aligned} \tag{5.19}$$

and the $\hat{P}$ are defined in Appendix C. Combining Eq 5.17 and Eq. 5.18, it follows that the evolution factor $U_{i,j}^f$ obeys the following differential equation

$$\mu\frac{d}{d\mu} U_{ij}^f(z,\mu,\mu_0) = \int_z^1 \frac{dz'}{z'} \gamma_{il}^f\left(\frac{z}{z'},\mu\right) U_{lj}^f(z',\mu,\mu_0) \tag{5.20}$$

with the boundary condition

$$U_{ij}^{f}(z,\mu_0,\mu_0) = \delta_{ij}\,\delta(1-z). \tag{5.21}$$

This equation can be solved iteratively, and its solution is given by

$$U_{ij}^{f}(z,\mu,\mu_0) = U_{ij}^{f}(z,\mu_0,\mu_0) + \int_{\mu_0}^{\mu} d\log\mu' \int_z^1 \frac{dz'}{z'}\,\gamma_{il}^{f}\left(\frac{z}{z'},\mu'\right) U_{lj}^{f}(z',\mu',\mu_0). \tag{5.22}$$

If we are interested in the solution up to the order α_S^2, we can write

$$U_{ij}^{f}(z,\mu,\mu_0) = \delta_{ij}\,\delta(1-z) + U_{ij}^{f(1)}(z,\mu,\mu_0) + U_{ij}^{f(2)}(z,\mu,\mu_0), \tag{5.23}$$

where $U_{ij}^{f(1)}$ and $U_{ij}^{f(2)}$ are the contributions at order $\mathcal{O}(\alpha_s)$ and $\mathcal{O}(\alpha_s^2)$, respectively. At order α_S we have

$$U_{ij}^{f(1)}(z,\mu,\mu_0) = \frac{\hat{P}_{ij}^{(0)}(z)}{\pi}\int_{\mu_0}^{\mu} d\log\mu'\,\alpha_S(\mu') = \frac{\hat{P}_{ij}^{(0)}(z)}{\pi}\alpha_S(\mu_0)\,\log\frac{\mu}{\mu_0}, \tag{5.24}$$

having used

$$\alpha_S(\mu) = \alpha_S(\mu_0) - \frac{\beta_0\,\alpha_S^2(\mu_0)}{2\pi}\,\log\frac{\mu}{\mu_0} + \frac{\alpha_S^3(\mu_0)}{8\pi^2}\left(2\beta_0^2\,\log^2\frac{\mu}{\mu_0} - \beta_1\,\log\frac{\mu}{\mu_0}\right). \tag{5.25}$$

At order α_S^2 we have

$$U_{ij}^{f(2)}(z,\mu,\mu_0) = \frac{\alpha_S^2(\mu_0)}{2\pi^2}\left[-\beta_0\,\hat{P}_{ij}^{(0)}(z)\frac{\log^2\frac{\mu}{\mu_0}}{2} + \hat{P}_{ij}^{(1)}(z)\log\frac{\mu}{\mu_0} + \log^2\frac{\mu}{\mu_0}\hat{P}_{il}^{(0)}\otimes\hat{P}_{lj}^{(0)}(z)\right] \tag{5.26}$$

where

$$\hat{P}_{il}^{(0)}\otimes\hat{P}_{lj}^{(0)}(z) = \int_z^1 \frac{dz'}{z'}\hat{P}_{il}^{(0)}\left(\frac{z}{z'}\right)\hat{P}_{lj}^{(0)}(z'). \tag{5.27}$$

All the necessary integrals have been computed and the results are listed in Appendix C.

5.5 Beam Function at NNLO

The beam functions can be expanded as

$$B_i(t,x,\mu_B) = \int_x^1 \frac{\mathrm{d}\xi}{\xi} \mathcal{I}_{ij}\left(t,\frac{x}{\xi},\mu_B\right) f_j(\xi,\mu_B) \tag{5.28}$$

where

$$\begin{aligned}\mathcal{I}_{ij}\left(t,z,\mu_B\right) &= \frac{1}{\mu_B^2}\sum_{m=-1}^{\infty} \mathcal{I}_{ij}^m\left[\alpha_S(\mu_B),z\right]\mathcal{L}_m\left(\frac{t}{\mu_B^2}\right) \\ &= \frac{1}{\xi}\sum_{m=-1}^{\infty} \mathcal{I}_{ij}^m\left[\alpha_S(\mu_B),z,\frac{\xi}{\mu_B^2}\right]\mathcal{L}_m\left(\frac{t}{\xi}\right),\end{aligned} \tag{5.29}$$

where ξ is arbitrary. Combining the RGE evolution of the beam function and of the pdfs, we have

$$\begin{aligned}\int dt' U_B(t',\mu,\mu_B)\, B_i(t-t',x,\mu) = \int dt' U_B(t',\mu,\mu_B)\frac{1}{\mu^2}\mathcal{L}_m\left(\frac{t-t'}{\mu^2}\right)\int_\xi^1 \frac{d\xi'}{\xi'} f_k(\xi',\mu_B) \\ \times \mathcal{J}_{ik}^m\left(\frac{x}{\xi'},\mu,\mu_B\right)\end{aligned} \tag{5.30}$$

where we have defined

$$\mathcal{J}_{ik}^m\left(\frac{x}{\xi'},\mu,\mu_B\right) = \sum_j \int_x^{\xi'} \frac{d\xi}{\xi}\mathcal{I}_{ij}^m\left(\alpha_S(\mu),\frac{x}{\xi}\right) U_{jk}^f\left(\frac{\xi}{\xi'},\mu,\mu_B\right). \tag{5.31}$$

In order to extract the logarithms at the two loop order, we evaluate this expression in the Fourier space conjugate of t, and we choose the scale $\mu = \mu_y = (ise^{-\gamma_E})^{-1/2}$ (s being the Fourier variable conjugate to t). This ensures that all the logs come from the evolution factors and not from $\mathcal{I}$. We obtain

$$\begin{aligned}&FT\left[\int dt' B_i(t-t',x,\mu_y)\, U_B(t',\mu_y,\mu_B)\right] = \\ &= \int_x^\xi \frac{\mathrm{d}\xi'}{\xi'}\left\{f_q(\xi',\mu_B)\tilde{\mathcal{I}}_{qq}\left(\frac{x}{\xi'},\mu_y,\mu_B\right) + f_g(\xi',\mu_B)\tilde{\mathcal{I}}_{qg}\left(\frac{x}{\xi'},\mu_y,\mu_B\right)\right. \\ &\quad \left. + f_{q'}(\xi',\mu_B)\tilde{\mathcal{I}}_{qq'}\left(\frac{x}{\xi'},\mu_y,\mu_B\right)\right\}\end{aligned} \tag{5.32}$$

with

$$\begin{aligned}
\tilde{\mathcal{I}}_{qq}\left(\frac{x}{\xi'},\mu_y,\mu_B\right) &= e^{2K(\Gamma,\gamma,\mu_B,\mu_y)-\frac{1}{2}\omega(\gamma,\mu_B,\mu_y)}\left[\mathcal{J}_{qq}^{-1}\left(\frac{x}{\xi'},\mu_y,\mu_B\right)+\frac{\pi^2}{12}\mathcal{J}_{qq}^{1}\left(\frac{x}{\xi'},\mu_y,\mu_B\right)\right]\\
\tilde{\mathcal{I}}_{qg}\left(\frac{x}{\xi'},\mu_y,\mu_B\right) &= e^{2K(\Gamma,\gamma,\mu_B,\mu_y)-\frac{1}{2}\omega(\gamma,\mu_B,\mu_y)}\left[\mathcal{J}_{qg}^{-1}\left(\frac{x}{\xi'},\mu_y,\mu_B\right)+\frac{\pi^2}{12}\mathcal{J}_{qg}^{1}\left(\frac{x}{\xi'},\mu_y,\mu_B\right)\right]\\
\tilde{\mathcal{I}}_{qq'}\left(\frac{x}{\xi'},\mu_y,\mu_B\right) &= e^{2K(\Gamma,\gamma,\mu_B,\mu_y)-\frac{1}{2}\omega(\gamma,\mu_B,\mu_y)}\left[\mathcal{J}_{qq'}^{-1}\left(\frac{x}{\xi'},\mu_y,\mu_B\right)+\frac{\pi^2}{12}\mathcal{J}_{qq'}^{1}\left(\frac{x}{\xi'},\mu_y,\mu_B\right)\right],
\end{aligned} \tag{5.33}$$

where the factors K and ω are defined in Eq.A.28 and Eq.A.29. Expanding out these functions at $\mathcal{O}(\alpha_S^2)$ and Fourier-transforming to the original momentum space, we obtain the beam functions up to two loops.

$$\begin{aligned}
\mathcal{I}_{qq'}(t,z,\mu_B) &= \sum_{m=-1}^{3}\mathcal{I}_{qq'}^{m}[\alpha_S(\mu_B),z]\frac{1}{\mu_B^2}\mathcal{L}_m\left(\frac{t}{\mu_B^2}\right)\\
\mathcal{I}_{qg}(t,z,\mu_B) &= \sum_{m=-1}^{3}\mathcal{I}_{qg}^{m}[\alpha_S(\mu_B),z]\frac{1}{\mu_B^2}\mathcal{L}_m\left(\frac{t}{\mu_B^2}\right).
\end{aligned} \tag{5.34}$$

Note that this procedure allows us to calculate all the logarithmic terms at two loops, but not the coefficient of the $\delta(t/\mu^2)$ term, for which an explicit two-loop calculation would be necessary.

5.6 Drell-Yan coefficient functions at NNLO

We will now manipulate the factorization theorem in Eq. 5.13 to obtain an explicit expression for the singular coefficient functions. First, we write it as

$$\begin{aligned}
\frac{1}{\sigma_0}\frac{\mathrm{d}\sigma_{\mathrm{s}}}{\mathrm{d}q^2\mathrm{d}Y\,\mathrm{d}\tau} = &\sum_{i,j}H_{i,j}(q^2,\mu_H)\,U_H(q^2,\mu_H,\mu_S)\int \mathrm{d}t_S\,\mathrm{d}t_b\,\mathrm{d}t'_S\,\mathrm{d}t'_b\,Q\,S_B\left(Q\tau-\frac{t_S}{Q},\mu_S\right)\\
&\times B_i(e^Y(t_S-t_b-t'_S),x_a,\mu_B)\,U_B(t'_S-t'_b,\mu_B,\mu_S)\\
&\times B_j(e^{-Y}t_b,x_b,\mu_B)\,U_B(t'_b,\mu_B,\mu_S).
\end{aligned} \tag{5.35}$$

Then we use the fact that

$$\int dt_b' U_B(t_a', \mu_B, \mu_S)\, U_B(t_b', \mu_B, \mu_S) = E_{BB}(\xi, \mu_B, \mu_S) \left[\frac{1}{\xi}\,\delta\left(\frac{t_S'}{\xi}\right) + \frac{2\eta_B}{\xi}\mathcal{L}^{2\eta_B}\left(\frac{t_S'}{\xi}\right)\right] \tag{5.36}$$

with

$$E_{BB}(\xi, \mu_B, \mu_S) = \frac{e^{2k_B - \gamma_E\, 2\eta_B}}{\Gamma(1+2\eta_b)}\left(\frac{\xi}{\mu_B^2}\right)^{2\eta_B}, \tag{5.37}$$

and ξ arbitrary. Here and in the following

$$\begin{aligned} k_B = K_B(\mu_B, \mu_S) &= \int_{\alpha_S(\mu_B)}^{\alpha_S(\mu_S)} \frac{\mathrm{d}\alpha_s}{\beta(\alpha_s)}\left[4\Gamma_{\text{cusp}}(\alpha_S)\int_{\alpha_S(\mu_B)}^{\alpha_S(\mu_S)}\frac{\mathrm{d}\alpha_s'}{\beta(\alpha_S')} + \gamma_B(\alpha_S)\right] \\ \eta_B = \eta_B(\mu_B, \mu_S) &= \int_{\alpha_S(\mu_B)}^{\alpha_S(\mu_S)} \frac{\mathrm{d}\alpha_s}{\beta(\alpha_S)}\Gamma_{\text{cusp}}(\alpha_S). \end{aligned} \tag{5.38}$$

Expanding the soft function as

$$QS_B\left(Q\tau - \frac{t_S}{Q}, \mu_S\right) = \frac{Q^2}{\xi}\sum_{h=-1}^{\infty} S_B^h\left[\alpha_S(\mu_S), \frac{Q\mu_S}{\xi}\right]\mathcal{L}_h\left(\frac{Q^2\tau - t_S}{\xi}\right) \tag{5.39}$$

with ξ arbitrary, and combining it with the beam functions, we have

$$\begin{aligned} &\int \mathrm{d}t_S \mathrm{d}t'\, B_i(e^Y(t_S - t'), x_a, \mu_B)\, B_j(e^{-Y}t, x_b, \mu_B)\, Q\, S_B\left(Q\tau - \frac{t_S}{Q}, \mu_S\right) \\ &= \frac{Q^2}{\xi}\sum_{m,n,h=-1}^{\infty}\sum_{k=-1}^{m+n+1}\sum_{g=-1}^{k+h+1}\int\frac{\mathrm{d}\xi_a}{\xi_a}\frac{\mathrm{d}\xi_b}{\xi_b}\, f_{i'}(\xi_a, \mu_B)\, f_\ell(\xi_b, \mu_B)\, \mathcal{I}_{ii'}^m\left[\alpha_S(\mu_B), \frac{x_a}{\xi_a}, \frac{e^Y\xi}{\mu_B^2}\right] \\ &\quad \times \mathcal{I}_{i\ell}^n\left[\alpha_S(\mu_B), \frac{x_b}{\xi_b}, \frac{e^{-Y}\xi}{\mu_B^2}\right] V_k^{mn}\, S_B^h\left[\alpha_S(\mu_S), \frac{Q\mu_S}{\xi}\right] V_g^{kh}\mathcal{L}_g\left(\frac{Q^2\tau}{\xi}\right), \end{aligned} \tag{5.40}$$

where the V's are defined in Eq. A.24 and Eq. A.25. The factorization theorem can then be written as

$$\begin{aligned}\frac{1}{\sigma_0}\frac{\mathrm{d}\sigma_{\mathrm{s}}}{\mathrm{d}q^2\mathrm{d}Y\,\mathrm{d}\tau} =& \sum_{i,j} H_{i,j}(q^2,\mu_H)\, U_H(q^2,\mu_H,\mu_S) \int \frac{\mathrm{d}\xi_a}{\xi_a}\frac{\mathrm{d}\xi_b}{\xi_b}\, f_{i'}(\xi_a,\mu_B)\, f_{\ell}(\xi_b,\mu_B) \\ &\times \frac{Q^2}{\xi} E_{BB}(\xi,\mu_B,\mu_S) \sum_{m,n,h=-1}^{\infty} \sum_{k=-1}^{m+n+1} \sum_{g=-1}^{k+h+1} S_B^h\left[\alpha_S(\mu_S), \frac{Q\mu_S}{\xi}\right] \\ &\times \mathcal{I}_{ii'}^m\left[\alpha_S(\mu_B), \frac{x_a}{\xi_a}, \frac{e^Y\xi}{\mu_B^2}\right] \mathcal{I}_{j\ell}^n\left[\alpha_S(\mu_B), \frac{x_b}{\xi_b}, \frac{e^{-Y}\xi}{\mu_B^2}\right] V_k^{mn} V_g^{kh} \\ &\times \sum_{l=-1}^{g+1} V_l^g(2\eta_B)\, \mathcal{L}_l^{2\eta_B}\left(\frac{Q^2\tau}{\xi}\right). \end{aligned} \tag{5.41}$$

Since we are looking for the fixed order terms, we fix $\mu_H = \mu_B = \mu_S = \mu$ and $\xi = Q^2$, so that we can write Eq. 5.35 as

$$\begin{aligned}\frac{1}{\sigma_0}\frac{\mathrm{d}\sigma_{\mathrm{s}}}{\mathrm{d}q^2\mathrm{d}Y\,\mathrm{d}\tau} =& \int_{x_a}^1 \frac{\mathrm{d}\xi_a}{\xi_a}\int_{x_b}^1 \frac{\mathrm{d}\xi_b}{\xi_b}\, f_r(\xi_a,\mu)\, f_t(\xi_b,\mu) \sum_{i,j} H_{i,j}(q^2,\mu) \\ &\times \sum_{m,n,h=-1}^{\infty} \sum_{k=-1}^{m+n+1} \sum_{g=-1}^{k+h+1} S_B^h\left[\alpha_S(\mu), \frac{Q}{\mu}\right] \mathcal{I}_{ir}^m\left[\alpha_S(\mu), \frac{x_a}{\xi_a}, \frac{e^Y Q^2}{\mu^2}\right] \\ &\times \mathcal{I}_{jt}^n\left[\alpha_S(\mu), \frac{x_b}{\xi_b}, \frac{e^{-Y}Q^2}{\mu^2}\right] V_k^{mn} V_g^{kh} \sum_{l=-1}^{g+1} V_l^g(0)\, \mathcal{L}_l(\tau) \\ =& \int_{x_a}^1 \frac{\mathrm{d}\xi_a}{\xi_a}\int_{x_b}^1 \frac{\mathrm{d}\xi_b}{\xi_b}\, f_r(\xi_a,\mu)\, f_t(\xi_b,\mu)\, C_{r,t}^{\mathrm{s}}\left(\frac{x_a}{\xi_a}, \frac{x_b}{\xi_b}, \tau, Y, \mu, Q\right), \end{aligned} \tag{5.42}$$

where the coefficient functions are calculated as

$$\begin{aligned} C_{r,t}^{\mathrm{s}}\left(\frac{x_a}{\xi_a}, \frac{x_b}{\xi_b}, \tau, Y, \mu, Q\right) =& \sum_{i,j} H_{i,j}(q^2,\mu) \sum_{m,n,h=-1}^{\infty} \sum_{k=-1}^{m+n+1} \sum_{g=-1}^{k+h+1} S_B^h\left[\alpha_S(\mu), \frac{Q}{\mu}\right] \\ &\times \mathcal{I}_{ir}^m\left[\alpha_S(\mu), \frac{x_a}{\xi_a}, \frac{e^Y Q^2}{\mu^2}\right] \mathcal{I}_{jt}^n\left[\alpha_S(\mu), \frac{x_b}{\xi_b}, \frac{e^{-Y}Q^2}{\mu^2}\right] \\ &\times V_k^{mn} V_g^{kh} \sum_{l=-1}^{g+1} V_l^g(0)\, \mathcal{L}_l(\tau). \end{aligned} \tag{5.43}$$

Given the results for $H_{i,j}$, S_B^h and $\mathcal{I}_{ir}^m$ up to $\mathcal{O}(\alpha_s^2)$, this expression allows us to calculate the $\mathcal{O}(\alpha_s^2)$ contribution to the singular coefficients $C_{r,s}^{\mathrm{s}}$ in the cross section.

5.7 Results

In this section we decompose the singular coefficient functions $C^{\rm s}_{i,j}$ as

$$C^{\rm s}_{ij}(z_a, z_b, \tau, Y, \mu) = C^{-1}_{ij}(z_a, z_b, Y, \mu)\,\delta(\tau) + \sum_{k\geq 0} C^{k}_{ij}(z_a, z_b, Y, \mu)\,\mathcal{L}_k(\tau). \tag{5.44}$$

As stated before, we will provide results for C^k_{ij} with $k \geq 0$.

Symmetries

The DY process involves the annihilation of a quark and an antiquark and in general we must specify whether the quark comes from beam a or b. We can write the coefficient as

$$C^k_{ij}\Big(\frac{x_a}{\xi_a}, \frac{x_b}{\xi_b}, Y, \mu\Big) = C^{q\bar{q},k}_{ij}\Big(\frac{x_a}{\xi_a}, \frac{x_b}{\xi_b}, Y, \mu\Big) + C^{\bar{q}q,k}_{ij}\Big(\frac{x_a}{\xi_a}, \frac{x_b}{\xi_b}, Y, \mu\Big), \tag{5.45}$$

where in $C^{q\bar{q},k}_{ij}$ the quark q came from beam a and the antiquark $\bar{q}$ from beam b. Each of the coefficients has an expansion in α_S which we write as

$$C^x_{ij} = C^{x(0)}_{ij} + \frac{\alpha_s(\mu)}{2\pi} C^{x(1)}_{ij} + \frac{\alpha_s^2(\mu)}{(2\pi)^2} C^{x(2)}_{ij} + \cdots, \qquad x = -1, 0, 1, \cdots \tag{5.46}$$

corresponding to the LO, NLO, NNLO contributions. In order to understand the symmetries of C_{ij}, we can write schematically (ignoring the complication of convoluting plus distributions), from Eq 5.43,

$$C^{q\bar{q}}_{ij}\Big(z_a, z_b, Y, \mu\Big) \sim I^q_i\Big(z_a, \frac{e^Y Q^2}{\mu^2}\Big) I^{\bar{q}}_j\Big(z_b, \frac{e^{-Y} Q^2}{\mu^2}\Big). \tag{5.47}$$

In all the cases, we take $\bar{q}$ as the charge conjugate of q, which can be a quark or an antiquark. For two quark PDF's, only one of the quarks can change flavor or be charge conjugated. Otherwise the lowest order in the cross section would consist of multiplying a two-loop contribution from both beam functions and give an $\mathcal{O}(\alpha_s^4)$

result,

$$C_{q'q}^{q\bar{q}}\Big(z_a, z_b, Y, \mu\Big) = C_{qq'}^{\bar{q}q}\Big(z_b, z_a, -Y, \mu\Big) = \mathcal{O}(\alpha_s^4). \tag{5.48}$$

For one quark changing flavors we have one independent nonzero coefficient

$$C_{qq'}^{q\bar{q}}\Big(z_a, z_b, Y, \mu\Big) = C_{q'q}^{\bar{q}q}\Big(z_b, z_a, -Y, \mu\Big). \tag{5.49}$$

If neither of the quarks changes flavor nor is charge conjugated, we have two independent nonzero coefficients

$$\begin{aligned} C_{q\bar{q}}^{q\bar{q}}\Big(z_a, z_b, Y, \mu\Big) &= C_{\bar{q}q}^{\bar{q}q}\Big(z_a, z_b, Y, \mu\Big) \\ C_{qq}^{q\bar{q}}\Big(z_a, z_b, Y, \mu\Big) &= C_{qq}^{\bar{q}q}\Big(z_b, z_a, -Y, \mu\Big) \\ C_{\bar{q}q}^{q\bar{q}}\Big(z_a, z_b, Y, \mu\Big) &= C_{q\bar{q}}^{\bar{q}q}\Big(z_a, z_b, Y, \mu\Big) = \mathcal{O}(\alpha_s^4). \end{aligned} \tag{5.50}$$

For one quark and one gluon PDF, the incoming quark must be of the same kind as the DY quark, otherwise the cross sections starts at $\mathcal{O}(\alpha_s^3)$. Now we have one independent nonzero coefficient

$$\begin{aligned} C_{qg}^{q\bar{q}}\Big(z_a, z_b, Y, \mu\Big) &= C_{gq}^{\bar{q}q}\Big(z_b, z_a, -Y, \mu\Big) \\ C_{qg}^{\bar{q}q}\Big(z_a, z_b, Y, \mu\Big) &= C_{gq}^{q\bar{q}}\Big(z_b, z_a, -Y, \mu\Big) = \mathcal{O}(\alpha_s^3). \end{aligned} \tag{5.51}$$

For two gluon PDF's we have one coefficient:

$$C_{gg}^{q\bar{q}}\Big(z_a, z_b, Y, \mu\Big) = C_{gg}^{\bar{q}q}\Big(z_a, z_b, Y, \mu\Big). \tag{5.52}$$

Quark-quark

When neither of the quark changes flavor or complex conjugates, we get

$$
\begin{aligned}
C_{q\bar{q}}^{q\bar{q},3(2)}(z_a,z_b,Y,\mu) &= 8C_F^2\,\delta(1-z_a)\delta(1-z_b)\,,\\
C_{q\bar{q}}^{q\bar{q},2(2)}(z_a,z_b,Y,\mu) &= \delta(1-z_a)\Big\{-6C_F^2P_{qq}(z_b)+\Big[\frac{3}{2}C_F\beta_0+9C_F^2\Big]\delta(1-z_b)\Big\}+(z_a\leftrightarrow z_b)\,,\\
C_{q\bar{q}}^{q\bar{q},1(2)}(z_a,z_b,Y,\mu) &= \delta(1-z_a)\Big\{C_F^2\Big[\Big(\frac{9}{2}-\frac{5}{3}\pi^2-12L_\mu-8L_\mu^2-4Y^2\Big)\delta(1-z_b)\\
&\quad+4\Big(Y+2L_\mu-\frac{3}{2}\Big)P_{qq}(z_b)+(P_{qq}\otimes P_{qq})(z_b)-4\mathcal{I}_{qq}^{(1,\delta)}(z_b)\Big]\\
&\quad-2C_FH^{(1)}\delta(1-z_b)-C_F\beta_0\Big[\Big(\frac{31}{12}+2L_\mu\Big)\delta(1-z_b)+\frac{1}{2}P_{qq}(z_b)\Big]\\
&\quad+C_FT_F(P_{qg}\otimes P_{gq})(z_b)\\
&\quad+\Big[C_FC_A\Big(\frac{43}{9}+\frac{1}{3}\pi^2\Big)+\frac{20}{9}C_FT_Fn_f\Big]\delta(1-z_b)\Big\}\\
&\quad+C_F^2P_{qq}(z_a)P_{qq}(z_b)+(z_a\leftrightarrow z_b,Y\to-Y)\,,\\
C_{q\bar{q}}^{q\bar{q},0(2)}(z_a,z_b,Y,\mu) &= \delta(1-z_a)\Big\{P_{q_iq_i}^{(1)}(z_b)\\
&\quad+C_F^2\Big[\Big(-\frac{3}{8}-\frac{3}{4}\pi^2-9L_\mu-6L_\mu^2-3Y^2+2\zeta_3\Big)\delta(1-z_b)\\
&\quad+\Big(\frac{2}{3}\pi^2+12L_\mu+4L_\mu^2+3Y+2Y^2\Big)P_{qq}(z_b)\\
&\quad-(Y+2L_\mu)(P_{qq}\otimes P_{qq})(z_b)+\frac{\pi^2}{12}(\mathcal{I}_{qq}^{(1,1)}\otimes P_{qq})(z_b)\\
&\quad+(\mathcal{I}_{qq}^{(1,\delta)}\otimes P_{qq})(z_b)-3\mathcal{I}_{qq}^{(1,\delta)}(z_b)\Big]+C_FT_F(\mathcal{I}_{qg}^{(1,\delta)}\otimes P_{gq})(z_b)\\
&\quad-C_FT_F(Y+2L_\mu)(P_{qg}\otimes P_{gq})(z_b)\\
&\quad+C_F\Big(\frac{1}{2}\beta_0(Y+2L_\mu)+H^{(1)}\Big)P_{qq}(z_b)-\frac{1}{2}C_F\beta_0\mathcal{I}_{qq}^{(1,\delta)}(z_b)\\
&\quad+\Big[C_F\beta_0\Big(-\frac{1}{8}-\frac{\pi^2}{4}+\frac{11}{6}L_\mu-\frac{Y^2}{2}\Big)+C_FC_A\Big(-\frac{1}{4}-\frac{110}{9}L_\mu+3\zeta_3\Big)\\
&\quad+\frac{40}{9}C_FT_Fn_fL_\mu-\frac{3}{2}C_FH^{(1)}\Big]\delta(1-z_b)\Big\}\\
&\quad-2C_F^2L_\mu P_{qq}(z_a)P_{qq}(z_b)+C_F^2P_{qq}(z_b)\mathcal{I}_{qq}^{(1,\delta)}(z_a)\\
&\quad+(z_a\leftrightarrow z_b,Y\to-Y)\,. \qquad (5.53)
\end{aligned}
$$

where $\mathcal{I}_{ij}^{(k,\ell)}(z)$, $\mathcal{I}_{ij}^{(k,\ell)}\otimes P_{jm}(z)$ and $P_{ij}\otimes P_{jk}(z)$ are discussed in Appendix C and $H^{(1)}$ is the one-loop piece of the hard function without $\alpha_s/2\pi$, which can be extracted

from Eq. A.7. Here and in the following $L_\mu = \log(\mu/Q)$. We also note that in the convolutions one can change the order of the convoluted functions without changing the result. For the case of one quark changing from quark to antiquark we get

$$
\begin{aligned}
C_{qq}^{q\bar{q},3(2)}(z_a,z_b,Y,\mu) &= 0\,,\\
C_{qq}^{q\bar{q},2(2)}(z_a,z_b,Y,\mu) &= 0\,,\\
C_{qq}^{q\bar{q},1(2)}(z_a,z_b,Y,\mu) &= C_F T_F \delta(1-z_a)(P_{qg}\otimes P_{gq})(z_b)\,,\\
C_{qq}^{q\bar{q},0(2)}(z_a,z_b,Y,\mu) &= \delta(1-z_a)\Big\{P_{q_i\bar{q}_i}^{(1)}(z_b) + C_F T_F\Big[(\mathcal{I}_{qg}^{(1,\delta)}\otimes P_{gq})(z_b)\\
&\qquad - (Y+2L_\mu)(P_{qg}\otimes P_{gq})(z_b)\Big]\Big\}\,. \qquad (5.54)
\end{aligned}
$$

We get exactly the same result for $C_{qq'}^{q\bar{q}}$ except that $P_{q_i\bar{q}_i}^{(1)}(z_b)$ is replaced by $P_{q_iq_j}^{(1)}(z_b)$.

Quark-gluon

For the quark-gluon case we have

$$
\begin{aligned}
C_{qg}^{q\bar{q},3(2)}(z_a,z_b,Y,\mu) &= 0\,,\\
C_{qg}^{q\bar{q},2(2)}(z_a,z_b,Y,\mu) &= -6C_F T_F \delta(1-z_a)P_{qq}(z_b)\,,\\
C_{qg}^{q\bar{q},1(2)}(z_a,z_b,Y,\mu) &= \delta(1-z_a)\Big\{C_F T_F\Big[(P_{qq}\otimes P_{qg})(z_b) - 6P_{qg}(z_b) + 4(Y+2L_\mu)P_{qg}(z_b)\\
&\qquad - 4\mathcal{I}_{qg}^{(1,\delta)}(z_b)\Big] + C_A T_F (P_{qg}\otimes P_{gg})(z_b)\Big\} + 2C_F T_F P_{qq}(z_a)P_{qg}(z_b)\,,\\
C_{qg}^{q\bar{q},0(2)}(z_a,z_b,Y,\mu) &= \delta(1-z_a)\Big\{P_{qg}^{(1)}(z_b) + C_A T_F\Big[(\mathcal{I}_{qg}^{(1,\delta)}\otimes P_{gg})(z_b)\\
&\qquad - (Y+2L_\mu)(P_{qg}\otimes P_{gg})(z_b)\Big]\\
&\qquad + C_F T_F\Big[\frac{\pi^2}{12}(\mathcal{I}_{qq}^{(1,1)}\otimes P_{qg})(z_b) + (\mathcal{I}_{qq}^{(1,\delta)}\otimes P_{qg})(z_b)\\
&\qquad - (Y+2L_\mu)(P_{qq}\otimes P_{qg})(z_b)\\
&\qquad + \Big(12L_\mu + 4L_\mu^2 + \frac{2\pi^2}{3} + 3Y + 2Y^2\Big)P_{qg}(z_b) - 3\mathcal{I}_{qg}^{(1,\delta)}(z_b)\Big]\\
&\qquad + T_F F^{(1)} P_{qg}(z_b)\Big\} + C_F T_F\Big[-4L_\mu P_{qg}(z_b)P_{qq}(z_a) + P_{qg}(z_b)\mathcal{I}_{qq}^{(1,\delta)}(z_a)\\
&\qquad + P_{qq}(z_a)\mathcal{I}_{qg}^{(1,\delta)}(z_b)\Big]\,. \qquad (5.55)
\end{aligned}
$$

Gluon-gluon

$$
\begin{aligned}
&C_{gg}^{q\bar{q},3(2)}(z_a, z_b, Y, \mu) = 0\,,\\
&C_{qg}^{q\bar{q},2(2)}(z_a, z_b, Y, \mu) = 0\,,\\
&C_{qg}^{q\bar{q},1(2)}(z_a, z_b, Y, \mu) = 2T_F^2 P_{qg}(z_a) P_{qg}(z_b)\,,\\
&C_{qg}^{q\bar{q},0(2)}(z_a, z_b, Y, \mu) = T_F^2\Big[-4L_\mu P_{qg}(z_a) P_{qg}(z_b) + P_{qg}(z_b)\mathcal{I}_{qg}^{(1,\delta)}(z_a) + P_{qg}(z_a)\mathcal{I}_{qg}^{(1,\delta)}(z_b)\Big]\,.
\end{aligned}
\tag{5.56}
$$

5.8 Conclusion

In this Chapter we studied the beam functions and we calculated at NNLO the full set of logarithms of beam thrust defined in the hadronic center-of-mass frame, τ. Using this result, we have then analytically calculated the full set of logarithms of τ in the singular part of the NNLO coefficient functions for the isolated Drell-Yan cross section. This result is useful for the calculation of the nonsigular terms in resummed predictions, as we did in Chapter 2.2.5 in the case of thrust in e^+e^- annihilation.

Chapter 6

Conclusions

In this thesis we have studied the thrust distribution in electron positron annihilation. We have extended the event shapes formalism in the SCET framework, where we have given a factorization theorem for the thrust event shape valid at the N^{3}LL+$\mathcal{O}(\alpha_s^3)$ level in all regions of the thrust distribution. This is achieved with the introduction of what we call profile functions, which are thrust dependent factorization scales. In the e^+e^- anihilation process there are three relevant scales: hard, jet, and soft, associated to the center-of-mass energy, the jet mass and the energy of the soft radiation, respectively. The purpose of τ-dependent profile functions for these scales is to smoothly interpolate between the peak region where we must ensure $\mu_i > \Lambda_{\rm QCD}$, the dijet region where the summation of large logarithms is crucial, and multijet region, where regular perturbation theory is appropriate to describe the partonic contribution. Our factorization theorem includes a field theoretical definition of renormalon-free power corrections. We have applied this factorization theorem to perform a global fit to all the available experimental data of the thrust distribution to obtain one of the most precise determination of $\alpha_s(m_Z)$, and to obtain the first power correction Ω_1 from data. At a given center-of-mass energy, these two parameters are strongly degenerate, but the degeneracy is lifted when data at different center-of-mass energies are combined in a global dataset, which is therefore a crucial part of our analysis. The

result of these fits is

$$\alpha_s(m_Z) = 0.1135 \pm (0.0002)_{\rm exp} \pm (0.0005)_{\rm hadr} \pm (0.0009)_{\rm pert}, \tag{6.1}$$

$$\Omega_1(R_\Delta, \mu_\Delta) = 0.323 \pm (0.009)_{\rm exp} \pm (0.013)_{\Omega_2} \pm (0.020)_{\alpha_s(m_Z)} \pm (0.045)_{\rm pert}\ {\rm GeV},$$

where $R_\Delta = \mu_\Delta = 2$ GeV and we quote individual 1-sigma errors for each parameter. This fit has a $\chi^2/{\rm dof} = 0.91$ with dof$= 487 - 2$.

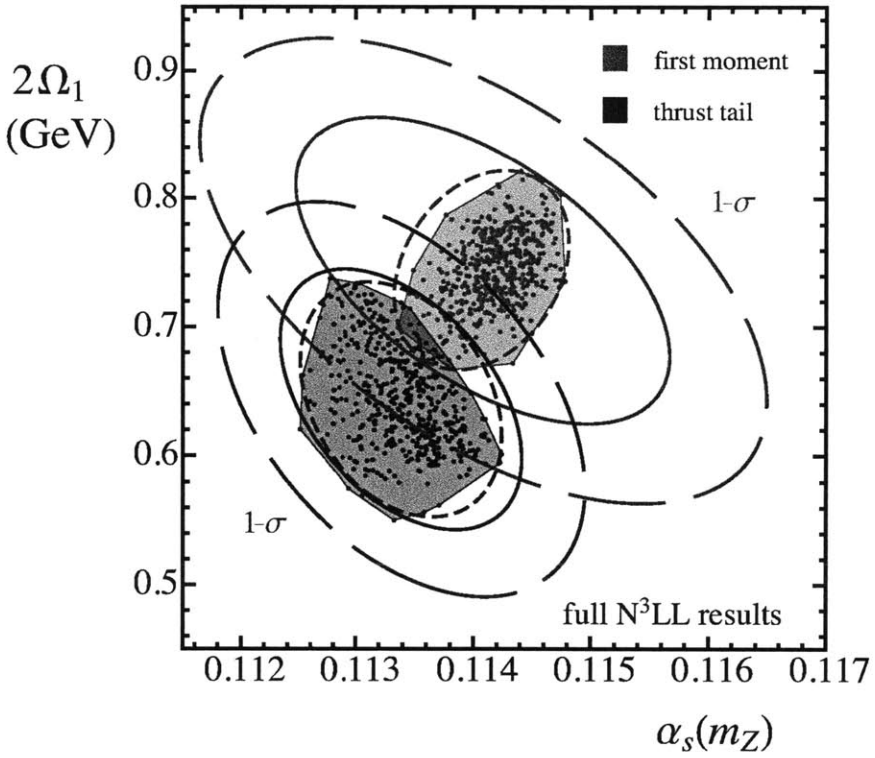

Figure 6-1: Comparison of $\alpha_s(m_Z)$ and Ω_1 determinations from thrust first moment data (red) and thrust tail data (magenta). The plot corresponds to fits with N^{3}LL accuracy and in the Rgap scheme. The tail fits are performed with our improved code which uses a new nonsingular two-loop function, and the now known two-loop soft function. Solid lines correspond to theory uncertainties, dashed lines correspond to $\Delta\chi^2 = 1$ combined theoretical and experimental error ellipses, and dotted lines correspond to $\Delta\chi^2 = 2.3$ combined error ellipses.

We also performed a fit for $\alpha_s(m_Z)$ and Ω_1 to all existing data on the first moment of the thrust distribution. In this case, we again found it necessary to build a global dataset using data at different center-of-mass energies in order to lift the degeneracy

between these two parameters. In this case we obtained

$$\alpha_s(m_Z) = 0.1141 \pm (0.0004)_{\rm exp} \pm (0.0014)_{\rm hadr} \pm (0.0007)_{\rm pert}, \qquad (6.2)$$

$$\Omega_1(R_\Delta, \mu_\Delta) = 0.372 \pm (0.013)_{\rm exp} \pm (0.044)_{\alpha_s(m_Z)} \pm (0.039)_{\rm pert}\ {\rm GeV},$$

where $R_\Delta = \mu_\Delta = 2$ GeV and we quote individual 1-sigma uncertainties for each parameter. Here $\chi^2/{\rm dof} = 1.33$, with dof$= 47 - 2$. In figure 6-1, we summarize and compare the results of these two analyses, showing their full compatibility.

In Chapter 5, we analyzed the initial state radiation in Drell-Yan process in pp collisions. We studied the beam functions and we calculated at NNLO the full set of logarithms of beam thrust defined in the hadronic center-of-mass frame, τ. Using this result, we have then analytically calculated the full set of logarithms of τ in the singular part of the NNLO coefficient functions for the isolated Drell-Yan cross section. This result is necessary for the calculation of the nonsingular terms in resummed predictions.

Appendix A

Formulae

In this appendix we collect all the remaining formulas used in our analysis for the case of massless quarks. The total hadronic cross section at tree level at the energies we are considering is

$$\sigma_0(Q) = \sum_{q \neq \text{top}} \left[\sigma^q_{ax}(Q) + \sigma^q_{vec}(Q) \right], \tag{A.1}$$

where Q is the c.m. energy. For a quark of flavor q the tree level axial-vector and vector cross sections are

$$\begin{aligned} \sigma_0^{qa} &= N_c \frac{4\pi\alpha^2}{3Q^2} \frac{Q^4(v_e^2 + a_e^2)a_q^2}{(m_Z^2 - Q^2)^2 + \frac{Q^4}{m_Z^2}\Gamma_Z^2}, \\ \sigma_0^{qv} &= N_c \frac{4\pi\alpha^2}{3Q^2} \left[e_q^2 - \frac{2\, e_q v_q v_e\, Q^2(Q^2 - m_Z^2) + Q^4(v_e^2 + a_e^2)v_q^2}{(m_Z^2 - Q^2)^2 + \frac{Q^4}{m_Z^2}\Gamma_Z^2} \right], \end{aligned} \tag{A.2}$$

where e_q is the electric charge of the quark, and

$$v_q = \frac{T_3^q - 2\, e_q \sin^2\theta_W}{\sin(2\,\theta_W)}, \quad a_q = \frac{T_3^q}{\sin(2\,\theta_W)}. \tag{A.3}$$

Here T_3^q is the third component of the weak isospin, and θ_W is the weak mixing angle. For our numerics we use the following values:

$$\begin{aligned} \sin^2\theta_W &= 0.23119, & m_Z &= 91.187\,\text{GeV}, \\ \Gamma_Z &= 2.4952\,\text{GeV}, & m_t &= 172\,\text{GeV}, \\ m_b &= 4.2\,\text{GeV}, & \alpha(m_Z) &= 1/127.925. \end{aligned} \tag{A.4}$$

Singular Cross Section Formula

To simplify the numerical evaluation of the singular part of the differential cross section given in Eq. (2.8) we take $\mu = \mu_J$ so that $U_J^\tau(s - s', \mu_J, \mu_J) = \delta(s - s')$ and express the result in the following form

$$\int \mathrm{d}k \frac{\mathrm{d}\hat{\sigma}_s}{\mathrm{d}\tau}\Big(\tau - \frac{k}{Q}\Big) S_\tau^{\mathrm{mod}}\Big(k - 2\bar{\Delta}(R,\mu_S)\Big) = Q \sum_I \sigma_0^I \, H_Q^I(Q,\mu_H)\, U_H\big(Q,\mu_H,\mu_J\big) \\ \times \int \mathrm{d}k \, P\big(Q, Q\tau - k, \mu_J\big)\, e^{-2\delta(R,\mu_S)\frac{\mathrm{d}}{\mathrm{d}k}}\, S_\tau^{\mathrm{mod}}\Big(k - 2\bar{\Delta}(R,\mu_S)\Big), \qquad \text{(A.5)}$$

where the perturbative corrections from the partonic soft function, jet function, and soft evolution factor are contained in

$$P(Q,k,\mu_J) = \int \mathrm{d}s \int \mathrm{d}k' \, J_\tau(s,\mu_J) U_S^\tau(k',\mu_J,\mu_S) S_\tau^{\mathrm{part}}(k - k' - s/Q, \mu_S). \qquad \text{(A.6)}$$

The integrals in P can be carried out explicitly so that it is given by a simple set of functions. The soft nonperturbative function $S_\tau^{\mathrm{mod}}(k - 2\bar{\Delta})$ is discussed in Sec. 2.4, and in Eq. (A.5) we have integrated by parts so the derivative in the exponential with the $\delta(R,\mu_S)$ acts on this nonperturbative function. H_Q^I, J_τ, S_τ^{part} and $\exp(-2\delta(R,\mu_S)\mathrm{d}/\mathrm{d}k)$ (cf. Eq. (2.34)) involve series in $\alpha_s(\mu_h)$, $\alpha_s(\mu_J)$, and $\alpha_s(\mu_S)$ with no large logs, and in our numerical analysis we expand the product of these series out, order-by-order in α_s. This expansion is crucial for $S_\tau^{\mathrm{part}}(k,\mu_S)$ and $\exp(-2\delta(R,\mu_S)\mathrm{d}/\mathrm{d}k)$ since it is needed to allow the renormalon in the two series to cancel. For simplicity where possible we give ingredients in a numerical form for SU(3) color with $n_f = 5$ active flavors. The vector hard function to $\mathcal{O}(\alpha_s^3)$

is [120, 119, 83, 122, 113, 18]

$$
\begin{aligned}
H_Q^v(Q,\mu) =& 1 + \frac{\alpha_s(\mu)\,C_F}{\pi}\Big[-2\log^2\frac{\mu}{Q} - 3\log\frac{\mu}{Q} - 4 + \frac{7\,\pi^2}{12}\Big] \\
&+ \frac{\alpha_s^2(\mu)}{16\pi^2}\Bigg[C_F^2\bigg(2L^4 - 12L^3 + (50 - \frac{14\pi^2}{3})L^2 + (-93 + 10\pi^2 + 48\zeta_3)L + \frac{511}{4} \\
&- \frac{83\pi^2}{3} + \frac{67\pi^4}{30} - 60\zeta_3\bigg) \\
&+ C_A C_F\bigg(L^2\Big(-\frac{8}{3} + \frac{2\pi^2}{3}\Big) + L\Big(\frac{82}{9} - 52\zeta_3\Big) - \frac{1037}{54} + \frac{10\pi^2}{9} - \frac{8\pi^4}{45} + 72\zeta_3\bigg) \\
&+ C_F\beta_0\bigg(\frac{2}{3}L^3 - \frac{19}{3}L^2 + L\Big(\frac{209}{9} - \frac{4\pi^2}{3}\Big) - \frac{4085}{108} + \frac{91\pi^2}{18} - \frac{2\zeta_3}{3}\bigg)\Bigg] \\
&+ \Big(\frac{\alpha_s(\mu)}{4\pi}\Big)^3\Bigg[64h_3 + C_F^3\bigg(\frac{1495}{2}L - \frac{1051}{2}L^2 + 222L^3 - 68L^4 + 12L^5 - \frac{4}{3}L^6 \\
&- 89L\pi^2 + \frac{220\pi^2}{3}L^2 - 20L^3\pi^2 + \frac{14\pi^2}{3}L^4 + \frac{109\pi^4}{15}L - \frac{67\pi^4}{15} - 992\zeta_3 L \\
&+ 408L^2\zeta_3 - 96\zeta_3 L^3 + \frac{304\pi^2\zeta_3}{3}L - 480\zeta_5 L\bigg) \\
&+ C_F^2\bigg(\beta_0\Big(-\frac{6947}{18}L + \frac{7474}{27}L^2 - \frac{838}{9}L^3 + \frac{50}{3}L^4 - \frac{4}{3}L^5 + \frac{2030\pi^2}{27}L \\
&- \frac{260\pi^2}{9}L^2 + \frac{38\pi^2}{9}L^3 - \frac{166\pi^4}{45}L + \frac{604\zeta_3}{3}L - \frac{68\zeta_3}{3}L^2\Big) \\
&+ C_A\Big(-\frac{26002}{27}L + \frac{14557}{54}L^2 - \frac{374}{9}L^3 + \frac{16}{3}L^4 + \frac{646\pi^2}{27}L - \frac{172\pi^2}{9}L^2 \\
&+ 4\pi^2L^3 - \frac{4\pi^2}{3}L^4 + \frac{44\pi^4}{45}L + \frac{86\pi^4}{45} \\
&+ \frac{13624\zeta_3}{9}L - 544\zeta_3L^2 + 104\zeta_3L^3 - 116L\zeta_3\pi^2 + 240L\zeta_5\Big)\bigg) \\
&+ C_F\bigg(\beta_0^2\Big(\frac{4919}{81}L - \frac{203}{9}L^2 + \frac{38}{9}L^3 - \frac{L^4}{3} - \frac{76\pi^2}{9}L + \frac{4\pi^2}{3}L^2 + \frac{8\zeta_3}{3}L\Big) \\
&+ C_A\beta_0\Big(\frac{5189}{27}L - \frac{470}{9}L^2 + \frac{46}{9}L^3 - \frac{818\pi^2}{81}L + \frac{20\pi^2}{9}L^2 - \frac{4\pi^2}{9}L^3 \\
&+ \frac{49\pi^4}{45}L - \frac{2348\zeta_3}{9}L + 24\zeta_3L^2\Big) \\
&+ C_A^2\Big(-\frac{6995}{81}L + \frac{301}{9}L^2 - \frac{14}{3}L^3 + \frac{770\pi^2}{81}L + \frac{16\pi^2}{9}L^2 - \frac{38\pi^4}{45}L \\
&- \frac{22\pi^4}{45}L^2 - \frac{3356\zeta_3}{9}L + 88\zeta_3L^2 + \frac{88\pi^2\zeta_3}{9}L + 272\zeta_5L\Big)\bigg)\Bigg], \qquad \text{(A.7)}
\end{aligned}
$$

with $L = \log(Q^2/\mu^2)$. Numerically,

$$\begin{aligned} H_Q^v(Q,\mu) =& 1 + \alpha_s(\mu_h)\Big(0.745808 - 1.27324 L_Q - 0.848826 L_Q^2\Big) \\ &+ \alpha_s^2(\mu_h)\Big(2.27587 - 0.0251035\, L_Q - 1.06592\, L_Q^2 \\ &+ 0.735517 L_Q^3 + 0.360253 L_Q^4\Big) \\ &+ \alpha_s^3(\mu_h)\Big(0.00050393\, h_3 + 2.78092 L_Q - 2.85654 L_Q^2 \\ &- 0.147051 L_Q^3 + 0.865045 L_Q^4 - 0.165638 L_Q^5 \\ &- 0.101931\, L_Q^6\Big)\,, \end{aligned} \tag{A.8}$$

where $L_Q = \ln \frac{\mu_h}{Q}$ and from Eq. (2.9) we have $h_3 = 8998.080$. Our axial-vector hard function for b quarks has an extra two-loop singlet piece from the large top-bottom mass splitting, $H_Q^{ba} = H_Q^v + H_Q^{\rm singlet}$. $H_Q^{\rm singlet}$ was given in Eq. (2.10) and involves the real function [104]

$$\begin{aligned} I_2(r_t) =& 10\,\Phi(r_t)^2 + 6\gamma(r_t) + \frac{\pi^2}{3} - \frac{1}{r_t^2}\Big\{ {\rm Cl}_2[2\,\Phi(r_t)]\Phi(r_t) \\ &+ {\rm Cl}_3[2\,\Phi(r_t)] - \Phi(r_t)^2 - \zeta(3)\Big\} - \frac{2}{r_t}\Big\{ 2\,\Phi(r_t)\,{\rm Cl}_2[4\,\Phi(r_t)] \\ &- 2{\rm Cl}_3[2\Phi(r_t)] + {\rm Cl}_3[4\Phi(r_t)] + [4\gamma(r_t) + 3]\Phi(r_t)^2 + \zeta(3)\Big\} \\ &+ \sqrt{\frac{1}{r_t} - 1}\Big\{ 4(4h(r_t) + \gamma(r_t))\Phi(r_t) + 4{\rm Cl}_2[4\,\Phi(r_t)] \\ &- 6\Phi(r_t) - 6{\rm Cl}_2[2\Phi(r_t)] - \frac{{\rm Cl}_2[2\Phi(r_t)] + 2\gamma(r_t)\Phi(r_t)}{r_t}\Big\}\,, \end{aligned} \tag{A.9}$$

where $r_t = Q^2/(4m_t^2)$ and

$$\begin{aligned} \Phi(r_t) &= \arcsin(\sqrt{r_t})\,, \qquad \gamma(r_t) = \ln(2) + \frac{1}{2}\ln(r_t)\,, \\ {\rm Cl}_2(x) &= {\rm Im}[{\rm Li}_2(e^{ix})]\,, \qquad {\rm Cl}_3(x) = {\rm Re}[{\rm Li}_3(e^{ix})]\,, \\ h(r_t) &= \ln(2) + \frac{1}{2}\ln(1 - r_t)\,. \end{aligned} \tag{A.10}$$

The resummation of large logs from μ_H to μ_J is given by $U_H(Q,\mu_H,\mu_J)$ in Eq. (A.5) which is the solution of the RGE for the square of the SCET Wilson coefficient [22]

$$U_H(Q,\mu_H,\mu) = e^{2K(\Gamma_H,\gamma_H,\mu,\mu_H)}\left(\frac{\mu_H^2}{Q^2}\right)^{\omega(\Gamma_H,\mu,\mu_H)}, \tag{A.11}$$

and the functions ω and K are given in Eqs. (A.28) and (A.29) below. Finally using results for the convolution of plus-functions from Ref. [116] we have the momentum space formula

$$\begin{aligned} P(Q,k,\mu_J) =& \frac{1}{\xi}\, E_S^{(\tau)}(\xi,\mu_J,\mu_S) \sum_{\substack{n,m,k,l=-1\\ m+n+1\geq k\\ k+1\geq l}}^{\infty} V_k^{mn}\, J_m\Big[\alpha_s(\mu_J),\frac{\xi Q}{\mu_J^2}\Big]\, S_n\Big[\alpha_s(\mu_S),\frac{\xi}{\mu_S}\Big] \\ & \times V_l^k\big[-2\omega(\Gamma_S,\mu_J,\mu_S)\big]\, \mathcal{L}_l^{-2\omega(\Gamma_S,\mu_J,\mu_S)}\Big(\frac{k}{\xi}\Big). \end{aligned} \tag{A.12}$$

This result is independent of the dummy variable ξ.[1] Here $E_S^{(\tau)}(\xi,\mu_J,\mu_S)$ encodes part of the running between the jet and the soft scale [19, 127],

$$E_S^{(\tau)}(\xi,\mu_J,\mu_S) = \exp\big[2K(\Gamma_S,\gamma_S,\mu_J,\mu_S)\big]\Big(\frac{\xi}{\mu_S}\Big)^{-2\omega(\Gamma_S,\mu_J,\mu_S)} \frac{\exp\big[2\gamma_E\,\omega(\Gamma_S,\mu_J,\mu_S)\big]}{\Gamma\big[1-2\,\omega(\Gamma_S,\mu_J,\mu_S)\big]}.$$

The sum in Eq. (A.12) contains coefficients of the momentum space soft and jet functions. Shifting the plus-functions so that they have common arguments gives

$$\begin{aligned} J(p^-k,\mu_J) &= \frac{1}{p^-\xi}\sum_{m=-1}^{\infty} J_m\Big[\alpha_s(\mu_J),\frac{p^-\xi}{\mu_J^2}\Big]\mathcal{L}_m\Big(\frac{k}{\xi}\Big), \\ S(k,\mu_S) &= \frac{1}{\xi}\sum_{n=-1}^{\infty} S_n\Big[\alpha_s(\mu_S),\frac{\xi}{\mu_S}\Big]\mathcal{L}_n\Big(\frac{k}{\xi}\Big). \end{aligned} \tag{A.13}$$

[1] When convoluted with $S_\tau^{\rm mod}$ we evaluate the right-hand side of Eq. (A.12) for $\xi = Q\tau - 2\bar{\Delta}(R,\mu_S)$ which simplifies the final numerical integration.

Here the thrust soft function coefficients are

$$S_{-1}[\alpha_s, x] = S_{-1}(\alpha_s) + \sum_{n=0}^{\infty} S_n(\alpha_s) \frac{\ln^{n+1} x}{n+1},$$
$$S_n[\alpha_s, x] = \sum_{k=0}^{\infty} \frac{(n+k)!}{n!\,k!} S_{n+k}(\alpha_s) \ln^k x\,. \tag{A.14}$$

The soft function is known to $\mathcal{O}(\alpha_s^3)$ except for the constant s_3 term [136, 79, 31, 94]

$$\begin{aligned}
S_{-1}(\alpha_s) &= 1 + \frac{1}{12}\pi C_F \alpha_s + \alpha_s^2 \bigg[\bigg(\frac{67}{108} - \frac{\pi^2}{36} \bigg) C_A C_F - \frac{3}{160}\pi^2 C_F^2 + \frac{s_1}{8\pi^2} - \frac{5}{27} C_F n_f T_F \\
&\quad + \frac{2 C_F \beta_0 \zeta(3)}{3\pi^2} \bigg] \\
&\quad + \alpha_s^3 \bigg[\frac{C_F s_1}{96\pi} + \frac{s_3}{\pi^3} - \frac{C_F n_f^2 T_F^2}{81\pi} + \frac{13\pi C_F \beta_0^2}{1440} + \frac{C_F \beta_1 \zeta(3)}{6\pi^3} + C_A C_F n_f T_F \bigg(- \frac{209}{648\pi} + \frac{5\pi}{162} \\
&\quad - \frac{7\zeta(3)}{18\pi} \bigg) \\
&\quad + C_F^2 n_f T_F \bigg(- \frac{55}{144\pi} + \frac{\pi}{108} + \frac{112\zeta(3)}{27\pi^3} + \frac{\zeta(3)}{9\pi} \bigg) + C_A^2 C_F \bigg(\frac{245}{288\pi} - \frac{67\pi}{648} + \frac{11\pi^3}{2160} + \frac{11\zeta(3)}{72\pi} \bigg) \\
&\quad + C_F^3 \bigg(\frac{1579\pi^3}{40320} - \frac{160\zeta(3)^2}{3\pi^3} \bigg) + C_A C_F^2 \bigg(- \frac{67\pi}{2160} + \frac{\pi^3}{720} - \frac{404\zeta(3)}{27\pi^3} + \frac{11\zeta(3)}{18\pi} + \frac{14\zeta(3)^2}{\pi^3} \bigg) \\
&\quad + \beta_0 \bigg(C_F n_f T_F \bigg(- \frac{7}{81\pi} + \frac{\pi}{216} - \frac{20\zeta(3)}{27\pi^3} \bigg) + C_A C_F \bigg(\frac{101}{324\pi} - \frac{11\pi}{864} + \frac{67\zeta(3)}{27\pi^3} - \frac{29\zeta(3)}{72\pi} \bigg) \\
&\quad + C_F^2 \bigg(\frac{14\zeta(3)}{9\pi} - \frac{16\zeta(5)}{\pi^3} \bigg) \bigg) \bigg] \\
S_0(\alpha_s) &= \alpha_s^2 \bigg[\bigg(\frac{1}{18} - \frac{28}{27\pi^2} \bigg) C_F n_f T_F - \frac{C_F \beta_0}{24} + \frac{16 C_F^2 \zeta(3)}{\pi^2} + C_A C_F \bigg(- \frac{11}{72} + \frac{101}{27\pi^2} - \frac{7\zeta(3)}{2\pi^2} \bigg) \bigg] \\
&\quad + \alpha_s^3 \bigg[\bigg(\bigg(- \frac{67}{108\pi} + \frac{\pi}{36} \bigg) C_A C_F + \frac{23\pi C_F^2}{288} - \frac{s_1}{8\pi^3} + \frac{5 C_F n_f T_F}{27\pi} \bigg) \beta_0 - \frac{C_F \beta_1}{96\pi} - \frac{2 C_F \beta_0^2 \zeta(3)}{3\pi^3} \\
&\quad + C_F^2 n_f T_F \bigg(- \frac{1711}{432\pi^3} - \frac{53}{72\pi} + \frac{19\pi}{360} - \frac{47\zeta(3)}{3\pi^3} \bigg) + C_F n_f^2 T_F^2 \bigg(- \frac{260}{729\pi^3} - \frac{5}{162\pi} + \frac{14\zeta(3)}{27\pi^3} \bigg) \\
&\quad + C_A C_F n_f T_F \bigg(- \frac{5921}{5832\pi^3} + \frac{707}{1944\pi} - \frac{\pi}{30} + \frac{91\zeta(3)}{54\pi^3} \bigg) \\
&\quad + C_A C_F^2 \bigg(\frac{101}{36\pi} - \frac{11\pi}{96} + \frac{536\zeta(3)}{9\pi^3} - \frac{127\zeta(3)}{24\pi} \bigg) + C_F^3 \bigg(\frac{68\zeta(3)}{3\pi} - \frac{192\zeta(5)}{\pi^3} \bigg) \\
&\quad + C_A^2 C_F \bigg(\frac{136781}{23328\pi^3} - \frac{6325}{7776\pi} + \frac{11\pi}{180} - \frac{329\zeta(3)}{24\pi^3} + \frac{11\zeta(3)}{36\pi} + \frac{6\zeta(5)}{\pi^3} \bigg) \bigg]
\end{aligned}$$

$$
\begin{aligned}
S_1(\alpha_s) &= -\frac{4C_F\alpha_s}{\pi} + \left(\left(\frac{1}{3} - \frac{67}{9\pi^2}\right)C_AC_F - 3C_F^2 + \frac{20C_Fn_fT_F}{9\pi^2}\right)\alpha_s^2 \\
&\quad + \alpha_s^3\left(\left(-\frac{469}{36\pi} + \frac{7\pi}{12}\right)C_AC_F^2 + \frac{5\pi C_F^3}{24} - \frac{C_Fs_1}{2\pi^3} + \frac{4C_Fn_f^2T_F^2}{27\pi^3} + \frac{C_F\beta_0^2}{24\pi}\right. \\
&\quad + C_F^2n_fT_F\left(\frac{55}{12\pi^3} + \frac{35}{9\pi} - \frac{4\zeta(3)}{\pi^3}\right) + C_A^2C_F\left(-\frac{245}{24\pi^3} + \frac{67}{54\pi} - \frac{11\pi}{180} - \frac{11\zeta(3)}{6\pi^3}\right) \\
&\quad + \beta_0\left(\left(\frac{28}{27\pi^3} - \frac{1}{18\pi}\right)C_Fn_fT_F - \frac{80C_F^2\zeta(3)}{3\pi^3} + C_AC_F\left(-\frac{101}{27\pi^3} + \frac{11}{72\pi} + \frac{7\zeta(3)}{2\pi^3}\right)\right) \\
&\quad \left. + C_AC_Fn_fT_F\left(\frac{209}{54\pi^3} - \frac{10}{27\pi} + \frac{14\zeta(3)}{3\pi^3}\right)\right) \\
S_2(\alpha_s) &= \frac{C_F\alpha_s^2\beta_0}{\pi^2} + \alpha_s^3\left(\left(\frac{56}{9\pi^3} - \frac{1}{3\pi}\right)C_F^2n_fT_F + \left(\left(\frac{67}{18\pi^3} - \frac{1}{6\pi}\right)C_AC_F + \frac{7C_F^2}{3\pi} - \frac{10C_Fn_fT_F}{9\pi^3}\right)\beta_0\right. \\
&\quad \left. + \frac{C_F\beta_1}{4\pi^3} - \frac{160C_F^3\zeta(3)}{\pi^3} + C_AC_F^2\left(-\frac{202}{9\pi^3} + \frac{11}{12\pi} + \frac{21\zeta(3)}{\pi^3}\right)\right) \\
S_3(\alpha_s) &= \frac{8C_F^2\alpha_s^2}{\pi^2} + \alpha_s^3\left(\left(\frac{268}{9\pi^3} - \frac{4}{3\pi}\right)C_AC_F^2 + \frac{34C_F^3}{3\pi} - \frac{80C_F^2n_fT_F}{9\pi^3} - \frac{C_F\beta_0^2}{3\pi^3}\right) \\
S_4(\alpha_s) &= -\frac{10C_F^2\alpha_s^3\beta_0}{3\pi^3} \\
S_5(\alpha_s) &= -\frac{8C_F^3\alpha_s^3}{\pi^3}.
\end{aligned}
\tag{A.15}
$$

Numerically,

$$
\begin{aligned}
S_{-1}(\alpha_s) &= 1 + 0.349066\alpha_s + (1.26859 + 0.0126651\,s_2)\alpha_s^2 \\
&\quad + (1.54284 + 0.00442097\,s_2 + 0.00100786\,s_3)\,\alpha_s^3\,, \\
S_0(\alpha_s) &= 2.07321\alpha_s^2 + (4.80020 - 0.0309077\,s_2)\alpha_s^3\,, \\
S_1(\alpha_s) &= -1.69765\,\alpha_s - 6.26659\,\alpha_s^2 - (16.4676 + 0.021501\,s_2)\,\alpha_s^3\,, \\
S_2(\alpha_s) &= 1.03573\,\alpha_s^2 - 0.567799\,\alpha_s^3\,, \\
S_3(\alpha_s) &= 1.44101\,\alpha_s^2 + 9.29297\,\alpha_s^3\,, \\
S_4(\alpha_s) &= -1.46525\,\alpha_s^3\,, \\
S_5(\alpha_s) &= -0.611585\,\alpha_s^3\,.
\end{aligned}
\tag{A.16}
$$

Note that s_2 and s_3 are the $\mathcal{O}(\alpha_s^{2,3})$ coefficients of the non-logarithmic terms in the series expansion of the logarithm of the position space thrust soft function. The

coefficients appearing in the shifted thrust jet function are

$$J_{-1}[\alpha_s, x] = J_{-1}(\alpha_s) + \sum_{n=0}^{\infty} J_n(\alpha_s) \frac{\ln^{n+1} x}{n+1},$$
$$J_n[\alpha_s, x] = \sum_{k=0}^{\infty} \frac{(n+k)!}{n!\,k!} J_{n+k}(\alpha_s) \ln^k x, \tag{A.17}$$

and are known up to $\mathcal{O}(\alpha_s^3)$ except for the constant j_3 term [117, 25, 44, 29, 121, 31]

$$\begin{aligned}
J_{-1}(\alpha_s) =& 1 + \alpha_s C_F \left(\frac{7}{2\pi} - \frac{\pi}{2}\right) + \alpha_s^2 \Bigg[C_F^2 \Big(-2.57469 + \frac{401}{64\pi^2} + \frac{43\pi^2}{240} - \frac{9\zeta_3}{4\pi^2} \Big) \\
&+ C_A C_F \Big(-\frac{7}{72} + \frac{1417}{864\pi^2} - \frac{17\pi^2}{1440} - \frac{9\zeta_3}{4\pi^2} \Big) \\
&+ C_F \beta_0 \Big(-\frac{17}{72} + \frac{4057}{1728\pi^2} - \frac{\zeta_3}{6\pi^2} \Big) \Bigg] \\
&+ \alpha_s^3 \Bigg[\frac{J_3}{\pi^3} + C_F^3 \Bigg(0.208958 + \frac{1435}{256\pi^3} - \frac{355}{96\pi} + \frac{401\pi}{576} - \frac{577\pi^3}{15120} - \frac{225\zeta_3}{32\pi^3} + \frac{11\zeta_3}{8\pi} \\
&- \frac{4\zeta_3^2}{3\pi^3} - \frac{9\zeta_5}{2\pi^3} \Bigg) + C_F^2 \Bigg(C_A \Big(0.429483 + \frac{9919}{3456\pi^3} - \frac{1709}{5184\pi} + \frac{751\pi}{17280} + \frac{\pi^3}{480} - \frac{719\zeta_3}{144\pi^3} \\
&+ \frac{25\zeta_3}{24\pi} + \frac{5\zeta_3^2}{\pi^3} \Big) + \beta_0 \Big(-0.130462 + \frac{28399}{6912\pi^3} - \frac{18257}{10368\pi} + \frac{47\pi}{432} - \frac{959\zeta_3}{288\pi^3} + \frac{\zeta_3}{4\pi} - \frac{\zeta_5}{\pi^3} \Big) \Bigg) \\
&+ C_F \Bigg(C_A^2 \Big(\frac{413}{3456\pi} + \frac{\pi}{108} - \frac{11\pi^3}{4320} + \frac{7\zeta_3}{24\pi^3} + \frac{11\zeta_3}{24\pi} \Big) \\
&+ C_A \beta_0 \Big(-\frac{787}{3456\pi} + \frac{5\pi}{432} - \frac{23\zeta_3}{72\pi^3} + \frac{13\zeta_3}{144\pi} \Big) + \beta_0^2 \Big(-\frac{235}{3456\pi} + \frac{11\pi}{5760} - \frac{29\zeta_3}{144\pi^3} \Big) \Bigg) \Bigg]
\end{aligned} \tag{A.18}$$

$$
\begin{aligned}
J_0(\alpha_s) = &-\frac{3\,C_F}{2\pi}\,\alpha_s + \alpha_s^2\left[\left(1.74359 - \frac{87}{16\pi^2} - \frac{\zeta_3}{\pi^2}\right)C_F^2 + \left(-\frac{73}{72\pi^2} + \frac{5\,\zeta_3}{\pi^2}\right)C_A\,C_F\right.\\
&\left. + \left(\frac{1}{12} - \frac{247}{144\pi^2}\right)C_F\,\beta_0\right]\\
&+ \alpha_s^3\left[\left(0.0361087 - \frac{1345}{128\pi^3} + \frac{83}{16\pi} + \frac{289\pi}{480} - \frac{9\zeta_3}{8\pi^3} + \frac{\zeta_3}{4\pi} + \frac{27\zeta_5}{2\pi^3}\right)C_F^3\right.\\
&+ C_F^2\left(C_A\left(-0.379842 + \frac{34777}{3456\pi^3} + \frac{209}{216\pi} - \frac{29\pi}{576} + \frac{1109\zeta_3}{72\pi^3}\right.\right.\\
&\left. - \frac{15\zeta_3}{4\pi} - \frac{15\zeta_5}{4\pi^3}\right) + \beta_0\left(0.225488 - \frac{8237}{576\pi^3} + \frac{1007}{432\pi} - \frac{7\pi}{144} + \frac{23\zeta_3}{8\pi^3}\right)\Big)\\
&+ C_F\left(C_A^2\left(\frac{4891}{5184\pi^3} - \frac{115}{1296\pi} + \frac{41\pi}{1440} + \frac{605\zeta_3}{72\pi^3} - \frac{11\zeta_3}{36\pi} - \frac{29\zeta_5}{4\pi^3}\right)\right.\\
&\left.\left. + C_A\,\beta_0\left(-\frac{1807}{423\pi^3} + \frac{283}{1296\pi} - \frac{13\pi}{720} + \frac{335\zeta_3}{72\pi^3}\right) + \beta_0^2\left(-\frac{4357}{5184\pi^3} + \frac{29}{288\pi} - \frac{\zeta_3}{12\pi^3}\right)\right)\right]
\end{aligned}
$$

$$
\begin{aligned}
J_1(\alpha_s) = &\frac{2\,C_F}{\pi}\,\alpha_s + \alpha_s^2\left[\left(\frac{2}{3\pi^2} - \frac{1}{6}\right)C_A\,C_F + \left(\frac{65}{8\pi^2} - 1.55268\right)C_F^2 + \frac{29}{24\pi^2}\,C_F\,\beta_0\right]\\
&+ \alpha_s^3\left[C_F^3\left(-1.18975 + \frac{67}{4\pi^3} - \frac{337}{48\pi} + \frac{37\pi}{72}\right)\right.\\
&+ C_F^2\left(\left(-0.137915 - \frac{43}{216\pi^3} - \frac{4}{3\pi} + \frac{84\pi}{720} - \frac{13\,\zeta_3}{2\pi^3}\right)C_A\right.\\
&\left. + \left(-0.163063 + \frac{11743}{864\pi^3} - \frac{43}{24\pi} - \frac{11\,\zeta_3}{6\pi^3}\right)\beta_0\right)\\
&+ C_F\left(\left(-\frac{413}{288\pi^3} - \frac{1}{9\pi} + \frac{11\pi}{360} - \frac{11\,\zeta_3}{2\pi^3}\right)C_A^2\right.\\
&\left.\left. + \left(\frac{787\,\beta_0}{288\pi^3} - \frac{5}{36\pi} - \frac{3\zeta_3}{4\pi^3}\right)C_A\,\beta_0 + \left(\frac{235}{288\pi^3} - \frac{1}{24\pi}\right)\beta_0^2\right)\right]
\end{aligned}
$$

$$
\begin{aligned}
J_2(\alpha_s) =& \alpha_s^2 \left[\left(-0.227973 - \frac{9}{4\pi^2} \right) C_F^2 - \frac{C_F \beta_0}{4\pi^2} \right] \\
&+ \alpha_s^3 \left[C_F^3 \left(1.29686 - \frac{549}{64\pi^3} + \frac{9}{4\pi} \right) + C_F^2 \left(0.277207 C_A - \frac{19}{12\pi^3} C_A \right. \right. \\
&+ \left(-0.047245 - \frac{959}{192\,\pi^3} + \frac{3}{8\pi} \right) \beta_0 \\
&\left. \left. + \frac{15}{2\pi^3} C_A \zeta_3 \right) + C_F \left(\frac{7}{16\pi^3} C_A^2 + \left(-\frac{23}{48\pi^3} + \frac{1}{24\pi} \right) C_A \beta_0 - \frac{29}{96\pi^3} \beta_0^2 \right) \right]
\end{aligned}
\tag{A.19}
$$

$$
\begin{aligned}
J_3(\alpha_s) =& \alpha_s^2 \left[0.101321 C_F^2 + \frac{C_F^2}{\pi^2} \right] + \alpha_s^3 \left[C_A C_F^2 \left(-0.0315506 + \frac{2}{3\pi^3} + \frac{1}{6\pi} \right) \right. \\
&\left. + C_F^3 \left(-0.255736 + \frac{37}{8\pi^3} - \frac{5}{6\pi} \right) + C_F^2 \beta_0 \left(0.0470335 + \frac{35}{24\pi^3} \right) + \frac{C_F \beta_0^2}{24\pi^3} \right] \\
J_4(\alpha_s) =& \alpha_s^3 \left[-0.0907074\, C_F^3 - \frac{15}{16\pi^3} C_F^3 - 0.00671907 C_F^2 \beta_0 - \frac{5}{24\pi^3} C_F^2 \beta_0 \right] \\
J_5(\alpha_s) =& \frac{\alpha_s^3 C_F^3}{\pi^3}.
\end{aligned}
\tag{A.20}
$$

Numerically,

$$
\begin{aligned}
J_{-1}(\alpha_s) &= 1 - 0.608949\alpha_s - 2.26795\alpha_s^2 + (2.21087 + 0.00100786\, j_3)\, \alpha_s^3 , \\
J_0(\alpha_s) &= -0.63662\alpha_s + 3.00401\alpha_s^2 + 4.45566\alpha_s^3 , \\
J_1(\alpha_s) &= 0.848826\alpha_s - 0.441765\alpha_s^2 - 11.905\alpha_s^3 , \\
J_2(\alpha_s) &= -1.0695\alpha_s^2 + 5.36297\alpha_s^3 , \\
J_3(\alpha_s) &= 0.360253\alpha_s^2 + 0.169497\alpha_s^3 , \\
J_4(\alpha_s) &= -0.469837\alpha_s^3 , \\
J_5(\alpha_s) &= 0.0764481\alpha_s^3 .
\end{aligned}
\tag{A.21}
$$

The $\mathcal{L}$ distributions are defined as $[n \geq 0]$

$$\mathcal{L}_n^a(x) = \left[\frac{\theta(x)\ln^n x}{x^{1-a}}\right]_+ = \frac{\mathrm{d}^n}{\mathrm{d}a^n}\,\mathcal{L}^a(x)\,, \tag{A.22}$$

$\mathcal{L}_{-1}^a(x) = \mathcal{L}_{-1}(x) = \delta(x)$, and for $a > -1$

$$\mathcal{L}^a(x) = \left[\frac{\theta(x)}{x^{1-a}}\right]_+ = \lim_{\epsilon\to 0}\frac{\mathrm{d}}{\mathrm{d}x}\left[\theta(x-\epsilon)\,\frac{x^a-1}{a}\right]. \tag{A.23}$$

In Eq. (A.12) we use the coefficients [116]

$$V_k^n(a) = \begin{cases} a\,\dfrac{\mathrm{d}^n}{\mathrm{d}b^n}\,\dfrac{V(a,b)}{a+b}\Big|_{b=0}\,, & k=-1\,,\\ a\binom{n}{k}\dfrac{\mathrm{d}^{n-k}}{\mathrm{d}b^{n-k}}\,V(a,b)\Big|_{b=0} + \delta_{kn}\,, & 0\leq k\leq n\,,\\ \dfrac{a}{n+1}\,, & k=n+1\,, \end{cases} \tag{A.24}$$

and the coefficients

$$V_k^{mn} = \begin{cases} \dfrac{\mathrm{d}^m}{\mathrm{d}a^m}\,\dfrac{\mathrm{d}^n}{\mathrm{d}b^n}\,\dfrac{V(a,b)}{a+b}\Big|_{a=b=0}\,, & k=-1\,,\\ \displaystyle\sum_{p=0}^{m}\sum_{q=0}^{n}\delta_{p+q,k}\binom{m}{p}\binom{n}{q}\frac{\mathrm{d}^{m-p}}{\mathrm{d}a^{m-p}}\,\frac{\mathrm{d}^{n-q}}{\mathrm{d}b^{n-q}}\,V(a,b)\Big|_{a=b=0}\,, & 0\leq k\leq m+n\,,\\ \dfrac{1}{m+1}+\dfrac{1}{n+1}\,, & k=m+n+1\,, \end{cases} \tag{A.25}$$

where

$$V(a,b) = \frac{\Gamma(a)\,\Gamma(b)}{\Gamma(a+b)} - \frac{1}{a} - \frac{1}{b}\,. \tag{A.26}$$

Special cases not covered by the general formulae in Eqs. (A.24) and (A.25) include

$$V_{-1}^{-1}(a) = 1\,, \quad V_0^{-1}(a) = a\,, \quad V_{k\geq 1}^{-1}(a) = 0\,, \qquad V_k^{-1,n} = V_k^{n,-1} = \delta_{nk}\,. \tag{A.27}$$

Evolution factors and Anomalous Dimensions

The evolution factors appearing in Eqs. (A.11), (A.12), and (A.13) are

$$\begin{aligned}\omega(\Gamma,\mu,\mu_0) =& 2\int_{\alpha_s(\mu_0)}^{\alpha_s(\mu)}\frac{\mathrm{d}\,\alpha}{\beta(\alpha)}\,\Gamma(\alpha)\\ =& -\frac{\Gamma_0}{\beta_0}\Big\{\ln r+\frac{\alpha_s(\mu_0)}{4\pi}\Big(\frac{\Gamma_1}{\Gamma_0}-\frac{\beta_1}{\beta_0}\Big)(r-1)+\frac{1}{2}\frac{\alpha_s^2(\mu_0)}{(4\pi)^2}\Big(\frac{\beta_1^2}{\beta_0^2}-\frac{\beta_2}{\beta_0}+\frac{\Gamma_2}{\Gamma_0}-\frac{\Gamma_1\beta_1}{\Gamma_0\beta_0}\Big)(r^2-1)\\ &+\frac{1}{3}\frac{\alpha_s^3(\mu_0)}{(4\pi)^3}\Big[\frac{\Gamma_3}{\Gamma_0}-\frac{\beta_3}{\beta_0}+\frac{\Gamma_1}{\Gamma_0}\Big(\frac{\beta_1^2}{\beta_0^2}-\frac{\beta_2}{\beta_0}\Big)-\frac{\beta_1}{\beta_0}\Big(\frac{\beta_1^2}{\beta_0^2}-2\frac{\beta_2}{\beta_0}+\frac{\Gamma_2}{\Gamma_0}\Big)\Big](r^3-1)\Big\},\end{aligned} \tag{A.28}$$

and

$$\begin{aligned}K(\Gamma,\gamma,\mu,\mu_0)-\omega\Big(\frac{\gamma}{2},\mu,\mu_0\Big) &= 2\int_{\alpha_s(\mu_0)}^{\alpha_s(\mu)}\frac{\mathrm{d}\,\alpha}{\beta(\alpha)}\,\Gamma(\alpha)\int_{\alpha_s(\mu_0)}^{\alpha}\frac{\mathrm{d}\alpha'}{\beta(\alpha')}\\ =&\frac{\Gamma_0}{2\beta_0^2}\Big\{\frac{4\pi}{\alpha_s(\mu_0)}\Big(\ln r+\frac{1}{r}-1\Big)+\Big(\frac{\Gamma_1}{\Gamma_0}-\frac{\beta_1}{\beta_0}\Big)(r-1-\ln r)-\frac{\beta_1}{2\beta_0}\ln^2 r\\ &+\frac{\alpha_s(\mu_0)}{4\pi}\Big[\Big(\frac{\Gamma_1\beta_1}{\Gamma_0\beta_0}-\frac{\beta_1^2}{\beta_0^2}\Big)(r-1-r\ln r)-B_2\ln r+\Big(\frac{\Gamma_2}{\Gamma_0}-\frac{\Gamma_1\beta_1}{\Gamma_0\beta_0}+B_2\Big)\frac{(r^2-1)}{2}\\ &+\Big(\frac{\Gamma_2}{\Gamma_0}-\frac{\Gamma_1\beta_1}{\Gamma_0\beta_0}\Big)(1-r)\Big]+\frac{\alpha_s^2(\mu_0)}{(4\pi)^2}\Big[\Big[\Big(\frac{\Gamma_1}{\Gamma_0}-\frac{\beta_1}{\beta_0}\Big)B_2+\frac{B_3}{2}\Big]\frac{(r^2-1)}{2}\\ &+\Big(\frac{\Gamma_3}{\Gamma_0}-\frac{\Gamma_2\beta_1}{\Gamma_0\beta_0}+\frac{B_2\Gamma_1}{\Gamma_0}+B_3\Big)\Big(\frac{r^3-1}{3}-\frac{r^2-1}{2}\Big)\\ &-\frac{\beta_1}{2\beta_0}\Big(\frac{\Gamma_2}{\Gamma_0}-\frac{\Gamma_1\beta_1}{\Gamma_0\beta_0}+B_2\Big)\Big(r^2\ln r-\frac{r^2-1}{2}\Big)-\frac{B_3}{2}\ln r-B_2\Big(\frac{\Gamma_1}{\Gamma_0}-\frac{\beta_1}{\beta_0}\Big)(r-1)\Big]\Big\},\end{aligned} \tag{A.29}$$

where $r=\alpha_s(\mu)/\alpha_s(\mu_0)$ depends on 4-loop running couplings, and the coefficients are $B_2=\beta_1^2/\beta_0^2-\beta_2/\beta_0$ and $B_3=-\beta_1^3/\beta_0^3+2\beta_1\beta_2/\beta_0^2-\beta_3/\beta_0$. These results are expressed in terms of series expansion coefficients of the QCD β function $\beta[\alpha_s]$, of $\Gamma[\alpha_s]$ which is given by a constant of proportionality times the QCD cusp anomalous dimension, and of a non-cusp anomalous dimension $\gamma[\alpha_s]$,

$$\begin{aligned}\beta(\alpha_s) &= -2\,\alpha_s\sum_{n=0}^{\infty}\beta_n\Big(\frac{\alpha_s}{4\pi}\Big)^{n+1},\\ \Gamma(\alpha_s) &= \sum_{n=0}^{\infty}\Gamma_n\Big(\frac{\alpha_s}{4\pi}\Big)^{n+1},\ \gamma(\alpha_s)=\sum_{n=0}^{\infty}\gamma_n\Big(\frac{\alpha_s}{4\pi}\Big)^{n+1}.\end{aligned} \tag{A.30}$$

The coefficients are [139, 109, 141, 105, 121, 61]

$$
\begin{aligned}
\beta_0 &= \frac{11C_A}{3} - \frac{4n_fT_F}{3} \\
\beta_1 &= \frac{34C_A^2}{3} - \frac{20C_An_fT_F}{3} - 4C_Fn_fT_F \\
\beta_2 &= \frac{2857}{54}C_A^3 + 2C_F^2T_Fn_f - \frac{205}{9}C_FC_AT_Fn_f - \frac{1415}{27}C_A^2T_Fn_f + \frac{44}{9}C_FT_F^2n_f^2 + \frac{158}{27}C_AT_F^2n_f^2 \\
\beta_3 &= C_A^4\left(\frac{150653}{486} - \frac{44}{9}\zeta_3\right) + C_A^3T_Fn_f\left(-\frac{39143}{81} + \frac{136}{3}\zeta_3\right) + C_A^2C_FT_Fn_f\left(\frac{7073}{243} - \frac{656}{9}\zeta_3\right) \\
&\quad + C_AC_F^2T_Fn_f\left(-\frac{4204}{27} + \frac{352}{9}\zeta_3\right) + 46C_F^3T_Fn_f + C_A^2T_F^2n_f^2\left(\frac{7930}{81} + \frac{224}{9}\zeta_3\right) \\
&\quad + C_F^2T_F^2n_f^2\left(\frac{1352}{27} - \frac{704}{9}\zeta_3\right) + C_AC_FT_F^2n_f^2\left(\frac{17152}{243} + \frac{448}{9}\zeta_3\right) + \frac{424}{243}C_AT_F^3n_f^3 \\
&\quad + \frac{1232}{243}C_FT_F^3n_f^3 + \frac{d_A^{abcd}d_A^{abcd}}{N_A}\left(-\frac{80}{9} + \frac{704}{3}\zeta_3\right) + n_f\frac{d_F^{abcd}d_A^{abcd}}{N_A}\left(\frac{512}{9} - \frac{1664}{3}\zeta_3\right) \\
&\quad + n_f^2\frac{d_F^{abcd}d_F^{abcd}}{N_A}\left(-\frac{704}{9} + \frac{512}{3}\zeta_3\right)
\end{aligned}
\tag{A.31}
$$

with

$$
\frac{d_A^{abcd}d_A^{abcd}}{N_A} = \frac{N_C^2\left(N_C^2+36\right)}{24} \tag{A.32}
$$

$$
\frac{d_F^{abcd}d_A^{abcd}}{N_A} = \frac{N_C\left(N_C^2+6\right)}{48} \tag{A.33}
$$

$$
\frac{d_F^{abcd}d_F^{abcd}}{N_A} = \frac{N_C^4 - 6N_C^2 + 18}{96N_C^2} \tag{A.34}
$$

$$
\begin{aligned}
\Gamma_0^{\text{cusp}} &= 4C_F \\
\Gamma_1^{\text{cusp}} &= -C_AC_F\left(-\frac{268}{9} + \frac{4\pi^2}{3}\right) - \frac{80C_Fn_fT_F}{9} \\
\Gamma_2^{\text{cusp}} &= -\frac{64}{27}C_Fn_f^2T_F^2 - C_A^2C_F\left(-\frac{490}{3} + \frac{536\pi^2}{27} - \frac{44\pi^4}{45} - \frac{88\zeta_3}{3}\right) \\
&\quad - n_fT_FC_F^2\left(\frac{220}{3} - 64\zeta_3\right) - n_fT_FC_AC_F\left(\frac{1672}{27} - \frac{160\pi^2}{27} + \frac{224\zeta_3}{3}\right)
\end{aligned}
\tag{A.35}
$$

Numerically, for $n_f = 5$,

$$\begin{aligned} &\beta_0 = 23/3\,, \quad \beta_1 = 116/3\,, \quad \beta_2 = 180.907, \\ &\beta_3 = 4826.16, \\ &\Gamma_0^{\rm cusp} = 16/3, \quad \Gamma_1^{\rm cusp} = 36.8436, \quad \Gamma_2^{\rm cusp} = 239.208\,. \end{aligned} \tag{A.36}$$

For the unknown four-loop cusp anomalous dimension we use the Padè approximation assigning 200% uncertainty:

$$\Gamma_3^{\rm cusp} = (1 \pm 2)\frac{(\Gamma_2^{\rm cusp})^2}{\Gamma_1^{\rm cusp}}. \tag{A.37}$$

The anomalous dimensions for the hard, jet, and soft functions are [51, 142, 121, 127, 122, 98, 30]

$$\Gamma_n^H = -\Gamma_n^{\rm cusp}, \quad \Gamma_n^J = 2\Gamma_n^{\rm cusp}, \quad \Gamma_n^S = -\Gamma_n^{\rm cusp}, \tag{A.38}$$

$$\begin{aligned} \gamma_0^H &= -6C_F \\ \gamma_1^H &= C_F n_f \left(\frac{260}{27} + \frac{4\pi^2}{3}\right) T_F + C_F^2\left(-3 + 4\pi^2 - 48\zeta_3\right) + C_A C_F \left(-\frac{961}{27} - \frac{11\pi^2}{3} + 52\zeta_3\right) \\ \gamma_2^H &= C_F n_f^2 T_F^2 \left(\frac{19336}{729} - \frac{80\pi^2}{27} - \frac{64\zeta_3}{27}\right) + n_f T_F C_A C_F \left(-\frac{34636}{729} + \frac{5188\pi^2}{243} + \frac{44\pi^4}{45} - \frac{3856\zeta_3}{27}\right) \\ &\quad + n_f T_F C_F^2 \left(\frac{5906}{27} - \frac{52\pi^2}{9} - \frac{56\pi^4}{27} + \frac{1024\zeta_3}{9}\right) \\ &\quad + C_A^2 C_F \left(-\frac{139345}{1458} - \frac{7163\pi^2}{243} - \frac{83\pi^4}{45} + \frac{7052\zeta_3}{9} - \frac{88\pi^2\zeta_3}{9} - 272\zeta_5\right) \\ &\quad + C_F^3 \left(-29 - 6\pi^2 - \frac{16\pi^4}{5} - 136\zeta_3 + \frac{32\pi^2\zeta_3}{3} + 480\zeta_5\right) \\ &\quad + C_F^2 C_A \left(-\frac{151}{2} + \frac{410\pi^2}{9} + \frac{494\pi^4}{135} - \frac{1688\zeta_3}{3} - \frac{16}{3}\pi^2\zeta_3 - 240\zeta_5\right) \end{aligned} \tag{A.39}$$

$$\gamma_0^J = 6C_F$$

$$\gamma_1^J = C_F n_f \left(-\frac{484}{27} - \frac{8\pi^2}{9}\right) T_F + C_A C_F \left(\frac{1769}{27} + \frac{22\pi^2}{9} - 80\zeta_3\right) + C_F^2 \left(3 - 4\pi^2 + 48\zeta_3\right)$$

$$\begin{aligned}\gamma_2^J = {} & C_F^2 n_f T_F \left(-\frac{9328}{27} + \frac{64\pi^2}{9} + \frac{328\pi^4}{135} - \frac{416\zeta_3}{9}\right) + C_F n_f^2 T_F^2 \left(-\frac{27656}{729} + \frac{160\pi^2}{81} + \frac{512\zeta_3}{27}\right) \\ & + C_A C_F n_f T_F \left(\frac{10952}{729} - \frac{2360\pi^2}{243} - \frac{92\pi^4}{45} + \frac{5312\zeta_3}{27}\right) \\ & + C_F^3 \left(29 + 6\pi^2 + \frac{16\pi^4}{5} + 136\zeta_3 - \frac{32\pi^2\zeta_3}{3} - 480\zeta_5\right) \\ & + C_A C_F^2 \left(\frac{151}{2} - \frac{410\pi^2}{9} - \frac{494\pi^4}{135} + \frac{1688\zeta_3}{3} + \frac{16\pi^2\zeta_3}{3} + 240\zeta_5\right) \\ & + C_A^2 C_F \left(\frac{412907}{1458} + \frac{838\pi^2}{243} + \frac{19\pi^4}{5} - \frac{11000\zeta_3}{9} + \frac{176\pi^2\zeta_3}{9} + 464\zeta_5\right) \end{aligned} \tag{A.40}$$

Numerically,

$$\begin{aligned} &\gamma_0^H = -8, \quad \gamma_1^H = 1.14194, \quad \gamma_2^H = -249.388, \\ &\gamma_0^J = 8, \quad \gamma_1^J = -77.3527, \quad \gamma_2^J = -409.631, \\ &\gamma_n^S = -\gamma_n^H - \gamma_n^J. \end{aligned} \tag{A.41}$$

To determine the strong coupling $\alpha_s(\mu)$ in terms of $\alpha_s(m_Z)$ at 4-loops with 5 light flavors we use

$$\frac{\alpha_S(m_Z)}{\alpha_S(\mu)} = X + B_1 \alpha_S(m_Z) \log X + \frac{\alpha_S^2(m_Z)}{X}\left[(B_1^2 - B_2)(1-X) + B_1^2 \log X\right] \tag{A.42}$$

$$+ \frac{\alpha_S^3(m_Z)}{X^2}\left[\frac{B_1^3}{2}((1-X)^2 - \log^2 X) + B_1 B_2 (X - X^2 + \log X) + \frac{B_3}{2}(X^2 - 1)\right] \tag{A.43}$$

with

$$X = 1 + \frac{\beta_0}{2\pi}\alpha_S(m_Z) \log\frac{\mu}{m_Z} \qquad\qquad B_i = \frac{\beta_i}{(4\pi)^i \beta_0}. \tag{A.44}$$

Numerically,

$$\frac{1}{\alpha_s(\mu)} = \frac{X}{\alpha_s(m_Z)} + 0.401347248\,\ln X \qquad \text{(A.45)}$$
$$+ \frac{\alpha_s(m_Z)}{X}\left[0.01165228\,(1-X) + 0.16107961\ln X\right]$$
$$+ \frac{\alpha_s^2(m_Z)}{X^2}\left[0.1586117\,(X^2-1) + 0.0599722\,(X\right.$$
$$\left. + \ln X - X^2) + 0.0323244\,\{(1-X)^2 - \ln^2 X\}\right].$$

The form in Eq. (A.45) agrees very well with the numerical solution of the beta function equation.

Nonsingular Cross Section Formula

At $\mathcal{O}(\alpha_s^2)$ there is an axial singlet contribution to the nonsingular terms through the three-parton cut of Fig. 2-1, which is given by the function $f_{\rm singlet}$ appearing in Eq. (2.24) for $f_{\rm qcd}^{ba}$. The result for this function can be extracted from results in Ref. [89] and reads: $[r_t = Q^2/(4m_t^2)]$

$$f_{\rm singlet}(\tau, r_t) = -\frac{64}{3}\,\theta\left(\frac{1}{3}-\tau\right)\left[\int_{1+\tau}^{2(1-\tau)} dy\, y\, g(y-1, r_t) + (1-3\,\tau)\,\frac{(1+\tau)}{2}\,g(\tau, r_t)\right], \qquad \text{(A.46)}$$

$$g(\tau, r_t) = \frac{2\,r_t\left[\sqrt{\frac{1-r_t\,\tau}{r_t\,\tau}}\sin^{-1}\left(\sqrt{r_t\,\tau}\right) - \sqrt{\frac{1-r_t}{r_t}}\sin^{-1}\left(\sqrt{r_t}\right)\right] + \left[\sin^{-1}\left(\sqrt{r_t\,\tau}\right)\right]^2}{4\,r_t\,(1-\tau)^2}$$
$$+ \frac{\left[\sin^{-1}\left(\sqrt{r_t}\right)\right]^2 + r_t\log(\tau)}{4\,r_t\,(1-\tau)^2}.$$

R-evolution

Finally we display here the function $D^{(k)}$ [92] which appears in the solution in

Eq. (2.38) of the R-RGE equation for $\bar{\Delta}(R,R)$:

$$D^{(k)}(\alpha_1,\alpha_2) = e^{i\pi\hat{b}_1}\sum_{j=0}^{k}(-1)^j S_j \times \\ \left[\Gamma(-\hat{b}_1-j,t_1)-\Gamma(-\hat{b}_1-j,t_2)\right], \tag{A.47}$$

which is real since the complex phase $e^{i\pi\hat{b}_1}$ cancels the imaginary part coming from the incomplete Gamma functions, defined as

$$\Gamma(c,t) = \int_t^\infty \mathrm{d}x\, x^{c-1}e^{-x}. \tag{A.48}$$

Here k is the order of the matrix elements (that is $k=0$ for NLL′ and NNLL, $k=1$ for NNLL′ and N^{3}LL, and $k=2$ for N^{3}LL′. For lower orders $D^{(k)}=0$). In Eq. (A.47) we have defined

$$t_i = -\frac{2\pi}{\beta_0\alpha_i}, \quad \hat{b}_1 = \frac{\beta_1}{2\beta_0^2}, \quad S_0 = 0, \quad S_1 = \frac{\gamma_1^R}{(2\beta_0)^2}, \\ S_2 = \frac{\gamma_2^R}{(2\beta_0)^3} - \frac{2\beta_0^2\beta_1+\beta_1^2-\beta_0\beta_2}{16\beta_0^6}\gamma_1^R, \tag{A.49}$$

where the R-anomalous dimensions γ_i^R were given in Eq. (2.37).

Total Hadronic Cross Section

The total hadronic QCD cross section, can be evaluated in fixed-order perturbation theory with $\mu \simeq Q$, and was given in Eq. (2.55) with the vector QCD results given in Eq. (2.56). The function appearing in the singlet contribution in Eq. (2.55) at $\mathcal{O}(\alpha_s^2)$

is [104]

$$I(r_t) = \frac{-\Phi(r_t)\,\mathrm{Cl}_2[2\,\Phi(r_t)] - \mathrm{Cl}_3[2\,\Phi(r_t)] + \zeta_3}{r_t^2} + \sqrt{\frac{1}{r_t} - 1}\left(\frac{2\,[1-\gamma(r_t)\,]\Phi(r_t) - \mathrm{Cl}_2[2\,\Phi(r_t)]}{r_t} + 2\,\mathrm{Cl}_2[2\,\Phi(r_t)] + 2\,[\,2\gamma(r_t) - 3\,]\Phi(r_t)\right) + 6\,\gamma(r_t) + 2\,\Phi(r_t)^2 - \frac{4\,\Phi(r_t)^2 + 1}{r_t} - \frac{\pi^2}{3}, \tag{A.50}$$

where the necessary functions appear in Eq. (A.10). Note that we have dropped the four particle cut contribution $I_4 = \pi^2/3 - 15/4$ since we have not accounted for it in the $\mathcal{O}(\alpha_s^2)$ nonsingular distribution.

A.1 Soft Function OPE Matching

To derive Eq. (2.18) we must demonstrate uniqueness of the power correction Ω_1 and derive its perturbative Wilson coefficient to all orders in α_s. We carry out these two parts of the proof in turn. Since the operator appearing in the matrix element Ω_1 is non-local, the proof of uniqueness is more involved than for a typical OPE where we could just enumerate all local operators of the appropriate dimension. Here we are integrating out perturbative soft gluons in $S_\tau(k,\mu)$, while retaining nonperturbative soft gluons. The hierarchy between these soft gluons is in their invariant masses, $k^2 \gg \Lambda_{\rm QCD}^2$. This process can not introduce Wilson lines in new light-like directions, nor additional Wilson lines following paths in n and $\bar{n}$. Thus the Wilson lines will be the same as those in the full theory operator, Eq. (2.14). Additional Wilson lines could only be induced by integrating out collinear or hard gluons, which would yield power corrections suppressed by the hard or jet scales. The second point to demonstrate is that dimension one combinations of derivatives other than $i\widehat{\partial}$ do not lead to new nonperturbative matrix elements at this order. The key is that for derivative operators inside our vacuum matrix element involving Wilson lines, boost invariance along the thrust axis relates all matrix elements to Ω_1 [110]. The proof

relies on boost invariance along the thrust axis of derivative operators inside the vacuum matrix element. To see this one defines the transverse energy flow operator $\mathcal{E}_T(\eta)$ by its action on states [107, 32]

$$\mathcal{E}_T(\eta)|X\rangle = \sum_{i\in X} |\vec{k}_i^{\perp}|\,\delta(\eta-\eta_i)\,|X\rangle\,. \tag{A.51}$$

Any dimension one derivative operator we might wish to consider, such as $n\cdot\partial$, $\bar{n}\cdot\partial$, ∂_t, ∂_z, ..., or combinations thereof, are given by an integral $\int \mathrm{d}\eta\, h(\eta)\,\mathcal{E}_T(\eta)$ for an appropriate rapidity function $h(\eta)$. For example, for the thrust derivative $i\widehat{\partial}$ we have $h(\eta) = e^{-|\eta|}$. Boost invariance implies [110]

$$\begin{aligned}
\bar{\Omega}_1 &= \frac{1}{2N_c}\langle 0|\mathrm{tr}\;\overline{Y}_{\bar{n}}^T(0)Y_n(0)\,i\widehat{\partial}\,Y_n^\dagger(0)\overline{Y}_{\bar{n}}^*(0)|0\rangle \\
&= \int \mathrm{d}\eta\,\frac{h(\eta)}{2N_c}\langle 0|\mathrm{tr}\;\overline{Y}_{\bar{n}}^T(0)Y_n(0)\,\mathcal{E}_T(\eta+\eta')Y_n^\dagger(0)\overline{Y}_{\bar{n}}^*(0)|0\rangle \\
&= \frac{1}{N_c}\langle 0|\mathrm{tr}\;\overline{Y}_{\bar{n}}^T(0)Y_n(0)\,\mathcal{E}_T(\eta')Y_n^\dagger(0)\overline{Y}_{\bar{n}}^*(0)|0\rangle,
\end{aligned} \tag{A.52}$$

for arbitrary η'. The same steps hold for any other derivative operator and function $h(\eta)$, and different choices only affects the constant calculable prefactor. This suffices to show the second point. To derive an all orders expression for the Wilson coefficient of Ω_1 we construct an analog of the OPE matching done for the soft function in $B\to X_s\gamma$ [25]. The proof is considerably simpler for $B\to X_s\gamma$ because the OPE in that case yields local HQET operators. Nevertheless the thrust soft function can be manipulated such that a similar strategy can be used. Using the thrust axis we define hemisphere a where $p^+ < p^-$ and hemisphere b where $p^- < p^+$. Consider the soft function written as a matrix element squared

$$\begin{aligned}
S_\tau(k,\mu) = \frac{1}{N_c}\sum_X \delta(k-k_s^{a+}-k_s^{b-})\;\mathrm{tr}\,\langle 0|\overline{Y}_{\bar{n}}^T(0)Y_n(0)|X\rangle \\
\times\,\langle X|Y_n^\dagger(0)\overline{Y}_{\bar{n}}^*(0)|0\rangle\,,
\end{aligned} \tag{A.53}$$

where the trace is over color, $k_s^{a+} = n \cdot p_X^a$ is the total plus-momentum of the particles in state X in hemisphere a and $k_s^{b-} = \bar{n} \cdot p_X^b$ is the minus-momenta of particles in X in hemisphere b. To carry out the OPE we need to consider a state that has overlap with the operator in Eq. (2.17). Thus we could replace the vacuum by very soft nonperturbative gluons with momenta of $\mathcal{O}(\Lambda_{\rm QCD})$ and then consider matrix elements with perturbative gluons having momenta $\sim k \gg \Lambda_{\rm QCD}$. Since the OPE is independent of the particular states we choose, we will instead consider a simpler alternative in the following. First we write the matrix element in Eq. (A.53) as

$$\begin{aligned} &\mathrm{tr}\,\langle 0|\overline{Y}_{\bar{n}}^T Y_n|X\rangle\langle X|Y_n^\dagger \overline{Y}_{\bar{n}}^*|0\rangle \\ &= \langle 0|\bar{\zeta}_{\bar{n}} \overline{Y}_{\bar{n}}^T Y_n \zeta_n|X u_n v_{\bar{n}}\rangle\langle X u_n v_{\bar{n}}|\bar{\zeta}_n Y_n^\dagger \overline{Y}_{\bar{n}}^* \zeta_{\bar{n}}|0\rangle\,, \end{aligned} \tag{A.54}$$

where ζ_n and $\zeta_{\bar{n}}$ are non-interacting collinear fields whose contractions with the sterile quark u_n and anti-quark $v_{\bar{n}}$ are chosen with a normalization to reproduce the original matrix element (and a sum over their color correctly reproduces the trace). Here u_n should be thought of as a very energetic collinear quark in hemisphere a with large label momentum p_n^-, and zero residual momentum. The large momentum is conserved by soft interactions from the Wilson lines due to the SCET multipole expansion. Here the plus-momentum of u_n is included into k_s^{a+}, but is zero and does not contribute to the δ-function. The same is true for $v_{\bar{n}}$ which has zero minus-momentum, large label $p_{\bar{n}}^+$ momentum, and is always in hemisphere b. We introduced u_n and $v_{\bar{n}}$ so that we can use them to systematically add a very soft momentum to the end of the Wilson lines (at ∞). They provide a convenient state with which to carry out the OPE, because there is nonzero overlap taking only the 1 out of the Wilson lines, Y. In particular they allow us to perform the OPE and pick out the $i\widehat{\partial}$ present in $\bar{\Omega}_1$ at tree level, without the necessity to add explicit soft gluons with momenta $\ll k$. To carry out the OPE we now give u_n a very small soft momentum ℓ^+ and $v_{\bar{n}}$ a very small soft momentum ℓ^-, and denote them by u_n^ℓ and $v_{\bar{n}}^\ell$ respectively. These particles are kept on-shell by adjusting their large label $\perp$-momenta so that $\ell^+ = p_{n\perp}^2/p_n^-$ and $\ell^- = p_{\bar{n}\perp}^2/p_{\bar{n}}^+$. Due to the multipole expansion these $\perp$-momenta have no influence

on diagrams with perturbative soft gluons having momenta $k \ll p_{n\perp} = -p_{\bar{n}\perp}$. The Wilson line propagators reduce to the same as before, such as

$$\frac{p_n^-}{k^+ p_n^- + \ell^+ p_n^- + p_{n\perp}^2} = \frac{1}{k^+}\,. \tag{A.55}$$

This property is familiar in SCET where soft couplings to energetic collinear quarks in SCET remain eikonal for any values of the quark's large momenta by using the equations of motion, as long as the final particles are on-shell. Thus at any order in perturbation theory, with any number of soft gluons and soft quarks of momenta $\sim k$ in the matrix elements, the only change caused by $\ell^\pm$ is on the $\delta(k - k_s^{a+} - k_s^{b-})$ in Eq. (A.53) which is shifted to $\delta(k - \ell - k_s^{a+} - k_s^{b-})$, where $\ell \equiv \ell^+ + \ell^-$. Expanding with $\ell \ll k$ the matrix element with this choice of state evaluates to

$$S_\tau^{\rm part}(k - \ell, \mu) = S_\tau^{\rm part}(k) - \frac{\mathrm{d}S_\tau^{\rm part}(k)}{\mathrm{d}k}\,\ell + \dots\,. \tag{A.56}$$

At lowest order in emission of very soft gluons $\sim \Lambda_{\rm QCD}$ the corresponding matrix element in the lower energy theory is

$$\frac{1}{N_c}\langle 0|\bar{\zeta}_{\bar{n}}\overline{Y}_{\bar{n}}^T Y_n \zeta_n i\widehat{\partial}\big|u_n^\ell v_{\bar{n}}^\ell\big\rangle\big\langle u_n^\ell v_{\bar{n}}^\ell\big|\bar{\zeta}_n Y_n^\dagger \overline{Y}_{\bar{n}}^* \zeta_{\bar{n}}\big|0\big\rangle = \ell\,. \tag{A.57}$$

Virtual radiative corrections do not correct this result since they are scaleless and vanish in pure dimensional regularization. Thus we can identify $\ell \to 2\bar{\Omega}_1$ in Eq. (A.56), and this then yields the stated result for the OPE in Eq. (2.18).

A.1.1 Operator Expansion for the First Thrust Moment

For moment integrals of the thrust distribution over $\tau \in [0, 1/2]$ there is not a hierarchy of scales that induces large logs, and one may formulate the theoretical result in terms of an expansion in α_s and $\Lambda_{\rm QCD}/Q$. The zero'th moment of thrust is just the total cross section for $e^+e^- \to$ hadrons, and the power corrections are formulated in terms of the well known OPE [137]. For higher moments the fact that thrust constrains a non-trivial combination of final state momenta makes carrying out an OPE

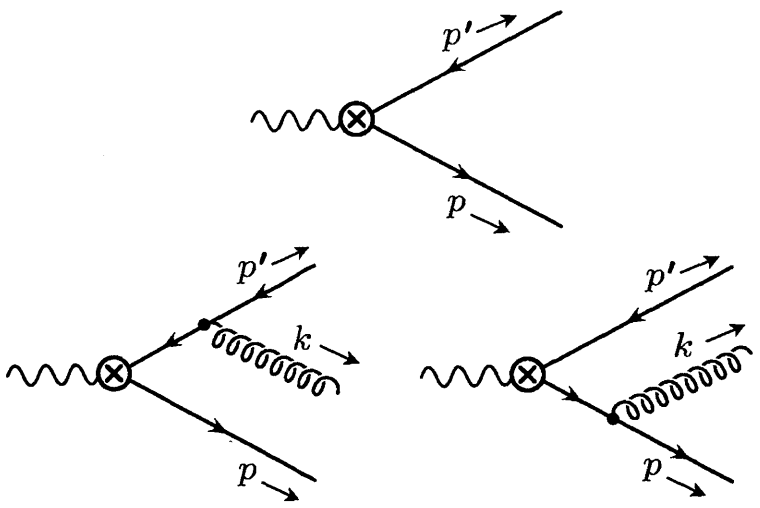

Figure A-1: Amplitudes for zero and one soft gluon.

more difficult. For example, when we weigh the integral by a power of thrust it is not possible to collapse all propagators to a point, so the nonperturbative parameters are no longer constrained to be given by a basis of local operators. In the effective coupling model [73] the same nonperturbative parameter α_0 that appears for the thrust distribution, also occurs in the first moment. However it is not clear to what level of accuracy this carries over to a field theoretical description of power corrections derived from QCD. In this appendix we show how one can carry out an OPE for the 1st moment of the thrust distribution, and demonstrate that at leading order it only involves the same nonperturbative matrix element Ω_1 from Eq. (2.3). To carry out an OPE for the thrust moment we can work order by order in the hard $\alpha_s(Q)$ expansion, and analyze direct computations where we couple soft nonperturbative gluons to hard partons in Feynman diagrams. The appropriate non-local operator(s) appearing in the expansion will be identified by the structure of the amplitudes in this computation. In the following discussion the soft gluons will *not* be treated as final state particles for which there is a phase space integral, but rather as a means of probing the structure of the nonperturbative operator. The lowest order graphs with zero or one soft gluon and a virtual photon current (for simplicity) are shown in Fig. A-1. Here $k^\mu \sim \Lambda_{\rm QCD}$ is soft, and $p^\mu \sim Q$, $p'^\mu \sim Q$ are hard momenta. To carry out the OPE we calculate and square the on-shell amplitude, $\mathcal{M}_h^\mu \mathcal{M}_h^\nu$, where μ, ν

are the virtual photon current indices. We sum over the final quark/antiquark spins since these particles are hard and are being integrated out. On the other hand the gluon vector indices α, α' are left uncontracted and are used to help in identifying the operator for the nonperturbative matrix element. For simplicity, the indices α and α' are suppressed in writing down the amplitudes below. We start out without making restrictions on the number of gluons coming from $\mathcal{M}_h^\mu$ and $\mathcal{M}_h^{\nu *}$, which corresponds to directly matching onto the nonperturbative operator, without considering the final vacuum matrix element which gives a nonperturbative parameter. Since $p^2 = p'^2 = k^2 = 0$ the denominators of the propagators in the one gluon graphs reduce to $2p \cdot k$ and $2p' \cdot k$. In the numerators we can drop $\not{k}$'s relative to the large $\not{p}$ and $\not{p}'$. The interference between the zero and one gluon amplitudes gives

$$\mathcal{M}_h^\mu \mathcal{M}_h^{\nu *} = N_c \mathrm{tr}[\not{p}\gamma^\mu \not{p}'\gamma^\nu] \, \frac{2gT^A}{N_c} \left[\frac{p'^\alpha}{p' \cdot k} - \frac{p^\alpha}{p \cdot k} \right]. \tag{A.58}$$

The interference with one gluon from each of $\mathcal{M}_h^\mu$ and $\mathcal{M}_h^{\nu *}$ is

$$\mathcal{M}_h^\mu \mathcal{M}_h^{\nu *} = N_c \, \mathrm{tr}[\not{p}\gamma^\mu \not{p}'\gamma^\nu] \frac{g^2 T^A T^B}{N_c} \left[\frac{p^\alpha p^{\alpha'}}{(p \cdot k)^2} + \frac{p'^\alpha p'^{\alpha'}}{(p' \cdot k)^2} - \frac{(p^\alpha p'^{\alpha'} + p'^\alpha p^{\alpha'})}{(p \cdot k)(p' \cdot k)} \right]. \tag{A.59}$$

Continuing in this fashion with any number of gluons from $\mathcal{M}_h^\mu$ and any number from $\mathcal{M}_h^{\nu *}$ we always find the tree level amplitude squared with no soft gluons, $N_c \, \mathrm{tr}[\not{p}\gamma^\mu \not{p}'\gamma^\nu]$, times an amplitude from the soft gluons. Since the hard quarks are on-shell and back-to-back their four-momenta are given by light-like vectors along the thrust axis,

$$p^\mu = n^\mu \frac{\bar{n} \cdot p}{2}, \qquad\qquad p'^\mu = \bar{n}^\mu \frac{n \cdot p}{2}, \tag{A.60}$$

up to power corrections beyond those considered here. Here $n^\mu = (1, \hat{\mathbf{t}})$ and $\bar{n}^\mu = (1, -\hat{\mathbf{t}})$ are identical to the n and $\bar{n}$ appearing in Eq. (2.3). Using Eq. (A.60) the soft gluon amplitudes in Eqs. (A.58) and (A.59) are eikonal with precisely the right factors to come from the $\overline{Y}_{\bar{n}}^T(0)$, $Y_n(0)$, $Y_n^\dagger(0)$, $\overline{Y}_{\bar{n}}^*(0)$ in the Ω_1 matrix element in Eq. (2.3). For the first moment observable we can focus on amplitudes that have the

same number of gluons in $\mathcal{M}_h^\mu$ and $\mathcal{M}_h^{\nu *}$, and at least one gluon for the $i\widehat{\partial}$ operation in Eq. (2.3) to act on. Since the gluon is soft, the factor of τ in $\int \mathrm{d}\tau(\tau/\sigma)(\mathrm{d}\sigma/\mathrm{d}\tau)$ is given by

$$\begin{aligned}\tau &= \min\Big[\frac{2p\cdot k}{q^2}, \frac{2p'\cdot k}{q^2}\Big] = \frac{1}{Q}\min\Big[n\cdot k, \bar{n}\cdot k\Big] \\ &= \frac{1}{Q}\Big\{n\cdot k\,\theta(\bar{n}\cdot k - n\cdot k) + \bar{n}\cdot k\,\theta(n\cdot k - \bar{n}\cdot k)\Big\}\,,\end{aligned} \tag{A.61}$$

and is exactly equal to $i\widehat{\partial}$ given in Eq. (2.4) acting on the soft gluon in Fig. A-1. Hence in the first moment of thrust we find that τ together with the soft gluon amplitude give precisely $2\Omega_1/Q$, with the vacuum matrix in Eq. (2.3) (where the trace comes from the sum over color for the final state quarks). The remaining $N_c\,\mathrm{tr}[\not{p}\gamma^\mu\not{p}'\gamma^\nu]$ amplitude goes together with the two-body phase space to yield the tree level cross section σ_0^I. Together these results yield Eq. (2.22) for the lowest order OPE for the first moment of thrust.

Appendix B

Theory parameter scan for fit to first moment

In this Appendix we describe the method we use to estimate uncertainties in our analysis. We will briefly review the profile functions and the theoretical parameters which determine the theory uncertainty. We will also describe the scan over those parameters and the effects they have on the fit results.

The profile functions used in Ref. [1], to which we refer for a more extensive description, are τ-dependent factorization scales which allow us to smoothly interpolate between the theoretical constraints the hard, jet and soft scale must obey in different regions of the thrust distribution:

$$\begin{aligned}
&\text{1) peak:} && \mu_H \sim Q\,, \;\; \mu_J \sim \sqrt{\Lambda_{\rm QCD}\, Q}\,, && \mu_S \gtrsim \Lambda_{\rm QCD}\,,\\
&\text{2) tail:} && \mu_H \sim Q\,, \;\; \mu_J \sim Q\sqrt{\tau}\,, && \mu_S \sim Q\,\tau\,,\\
&\text{3) far-tail:} && \mu_H = \mu_J = \mu_S \sim Q\,. &&
\end{aligned} \tag{B.1}$$

The factorization theorem derived for thrust in Ref. [1] is formally invariant under $\mathcal{O}(1)$ changes of the profile function scales. The residual dependence on the choice of profile functions constitutes one part of the theoretical uncertainties and provides a method to estimate higher order perturbative corrections. We adopt a set of six parameters that can be varied in our theory error analysis which encode this residual

parameter	default value	range of values
μ_0	2 GeV	1.5 to 2.5 GeV
n_1	5	2 to 8
t_2	0.25	0.20 to 0.30
e_J	0	-1, 0, 1
e_H	1	0.5 to 2.0
n_s	0	-1, 0, 1
$\Gamma_3^{\rm cusp}$	1553.06	-1553.06 to $+4659.18$
j_3	0	-3000 to $+3000$
s_3	0	-500 to $+500$
ϵ_2	0	-1, 0, 1
ϵ_3	0	-1, 0, 1

Table B.1: Theory parameters relevant for estimating the theory uncertainty, their default values and range of values used for the theory scan during the fit procedure.

freedom while still satisfying the constraints in Eq. (B.1).

For the profile function at the hard scale, we adopt

$$\mu_H = e_H\, Q, \tag{B.2}$$

where e_H is a free parameter which we vary from 1/2 to 2 in our theory error analysis.

For the soft profile function we use the form

$$\mu_S(\tau) = \begin{cases} \mu_0 + \frac{b}{2t_1}\tau^2, & 0 \le \tau \le t_1, \\ b\,\tau + d, & t_1 \le \tau \le t_2, \\ \mu_H - \frac{b}{1-2t_2}(\frac{1}{2} - \tau)^2, & t_2 \le \tau \le \frac{1}{2}. \end{cases} \tag{B.3}$$

Here, t_1 and t_2 represent the borders between the peak, tail and far-tail regions. μ_0 is the value of μ_S at $\tau = 0$. Since the thrust value where the peak region ends and the tail region begins is Q dependent, $t_1 \simeq 1/Q$, we define the Q-independent parameter n_1 by $t_1 = n_1/(Q/1\,\text{GeV})$. To ensure that $\mu_S(\tau)$ is a smooth function, the quadratic and linear forms are joined by demanding continuity of the function and its first derivative at $\tau = t_1$ and $\tau = t_2$, which fixes $b = 2\,(\mu_H - \mu_0)/(t_2 - t_1 + \frac{1}{2})$ and $d = [\mu_0(t_2 + \frac{1}{2}) - \mu_H\, t_1]/(t_2 - t_1 + \frac{1}{2})$. In our theory error analysis we vary the free parameters n_1, t_2 and μ_0.

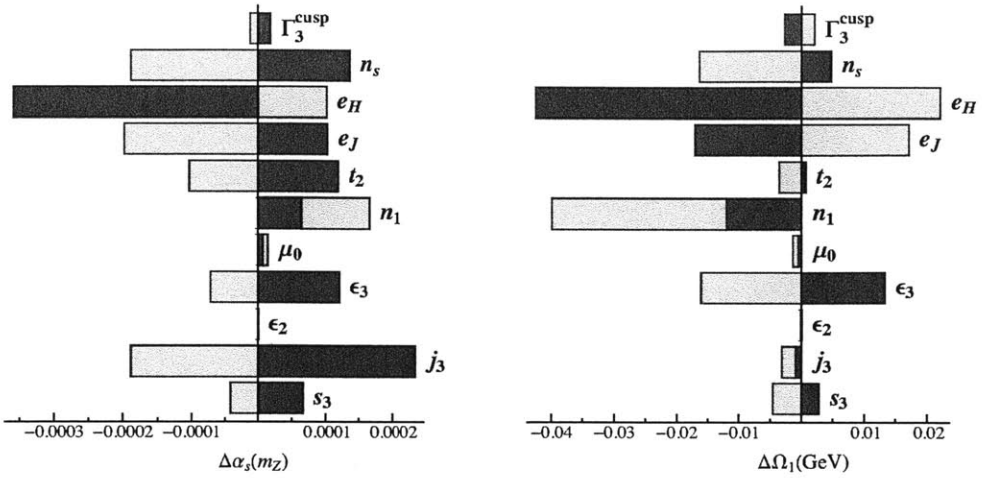

Figure B-1: Impact on parameters of the M_1 fit from variations of the best-fit values for $\alpha_s(m_Z)$ and Ω_1 values in the ranges given in Table B.1. The dark shaded blue regions represent values of the parameters larger than their default values, the light shaded green regions where the parameters are smaller than their default values.

The profile function for the jet scale is determined by the natural relation between the hard, jet, and soft scales

$$\mu_J(\tau) = \left(1 + e_J\Big(\frac{1}{2} - \tau\Big)^2\right)\sqrt{\mu_H\,\mu_S(\tau)}\,. \tag{B.4}$$

The term involving the free $\mathcal{O}(1)$-parameter e_J implements a modification to this relation and vanishes in the multijet region where $\tau = 1/2$. We use a variation of e_J to include the effect of such modifications in our estimation of the theoretical uncertainties.

In our theory error analysis we vary $\mu_{\rm ns}$ to account for our ignorance on the resummation of logarithms of τ in the nonsingular corrections. We consider three possibilities

$$\mu_{\rm ns}(\tau) = \begin{cases} \mu_H, & n_s = 1, \\ \mu_J(\tau), & n_s = 0, \\ \frac{1}{2}[\,\mu_J(\tau) + \mu_S(\tau)\,], & n_s = -1. \end{cases} \tag{B.5}$$

The complete set of theoretical parameters and the their ranges of variation are summarized in Table B.1.

Besides the parameters associated with the profile functions, the other theory parameters are $\Gamma_3^{\rm cusp}$, j_3, s_3, and $\epsilon_{1,2}$. The cusp anomalous dimension at $\mathcal{O}(\alpha_s^4)$, $\Gamma_3^{\rm cusp}$ is estimated via Padé approximants and we assign a 200% uncertainty to this approximation. j_3 and s_3 represent the nonlogarithmic 3-loop term in the position-space hemisphere jet and soft functions, respectively. These two parameters and their variations are estimated via Padé approximations. The last two parameters ϵ_2 and ϵ_3 allow us to include the statistical errors in the numerical determination of the nonsingular distribution at two (from EVENT2 [49, 50]) and three (from EERAD3 [86]) loops, respectively.

At each order we randomly scan the parameter space summarized in Table B.1 with a uniform measure, extracting 500 points. Each of the points in Fig. 3-2 is the result of the fit performed with a single choice of a point in the parameter space. The contour of the area in the α_s-$2\,\Omega_1$ plane covered by the fit results at each given order is fit to an ellipse, which is interpreted as a 1-σ theoretical uncertainty. The ellipse is determined as follows: in a first step we determine the outermost points on the α_s-$2\,\Omega_1$ plane (defined by the outermost convex polygon). We then perform a fit to these points using a χ^2 which is the square of the formula for an ellipse:

$$\begin{aligned}\chi^2_{\rm ellipse} = \sum_i \big[a\,(\alpha_i-\alpha_0)^2 + 4\,b\,(\Omega_i-\Omega_0)^2 \\ + \,2\,c\,(\alpha_i-\alpha_0)(\Omega_i-\Omega_0)\,-\,1\big]^2 .\end{aligned} \tag{B.6}$$

Here the sum is over the outermost points, and coordinates for the center of the ellipse, α_0 and Ω_0, are fixed ahead of time to the average of the maximum and minimum values of $\alpha_s(m_Z)$ and Ω_1 in the scan. We then minimize $\chi^2_{\rm ellipse}$ to determine the parameters a, b, c of the ellipse.

One could further constrain the coefficients a and b by writing

$$\begin{aligned} a &= \frac{1+\sqrt{1+4\,c^2\,\Delta\alpha^2\,\Delta\Omega^2}}{2\,\Delta\alpha^2}, \\ b &= \frac{1+\sqrt{1+4\,c^2\,\Delta\alpha^2\,\Delta\Omega^2}}{8\,\Delta\Omega^2}, \end{aligned} \tag{B.7}$$

where $\Delta\alpha$ and $\Delta\Omega$ correspond to the half the difference of the maximum and minimum values of $\alpha_s(m_Z)$ and Ω_1, respectively (the perturbative errors). The minimization of χ^2_{ellipse} in Eq. (B.6) gives almost identical results regardless of whether or not Eq. (B.7) is imposed.

In Fig. B-1 we vary a single parameter of Table B.1 keeping all the others fixed at their respective default values, and we plot the change of $\alpha_s(m_Z)$ and Ω_1 as compared to the values obtained from the first moment thrust fit with the default setup. In the figure, the dark shaded blue area represents a variation where the parameter is larger than the default value, and the light shaded green one where the parameter is smaller. The largest uncertainty is associated with the variation of the hard scale, e_H. The value of $\alpha_s(m_Z)$ is similarly affected by the uncertainty of the profile function parameters, the statistical error from the numerical determination of the 3-loop nonsingular distribution from EERAD3 [86], and by the parameter j_3. It is rather insensitive to the variation of the 4-loop cusp anomalous dimension and the statistical error from the determination of the 2-loop nonsingular. The value of Ω_1 is mainly sensitive to the profile function parameters and ϵ_3, but is quite insensitive to j_3.

Appendix C

One loop beam function

In this appendix we summarize the results of the one loop beam function.

$$\begin{aligned}
\mathcal{I}_{qq}(t,z,\mu) =&\delta(t)\delta(1-z) \\
&+\frac{\alpha_S(\mu)C_F}{2\pi}\theta(z)\left\{\frac{1}{\mu^2}\mathcal{L}_1\left(\frac{t}{\mu^2}\right)\mathcal{I}_{qq}^{(1,1)}(z)+\frac{1}{\mu^2}\mathcal{L}_0\left(\frac{t}{\mu^2}\right)\mathcal{I}_{qq}^{(1,0)}(z)+\delta(t)\,\mathcal{I}_{qq}^{(1,\delta)}(z)\right\} \\
\mathcal{I}_{qg}(t,z,\mu) =&\frac{\alpha_S(\mu)T_F}{2\pi}\theta(z)\left\{\frac{1}{\mu^2}\mathcal{L}_0\left(\frac{t}{\mu^2}\right)\mathcal{I}_{qg}^{(1,0)}(z)+\delta(t)\,\mathcal{I}_{qg}^{(1,\delta)}(z)\right\}
\end{aligned} \tag{C.1}$$

$$\begin{aligned}
\mathcal{I}_{qq}^{(1,\delta)}(z) =&\mathcal{L}_1(1-z)(1+z^2)-\frac{\pi^2}{6}\delta(1-z)+\theta(1-z)\left(1-z-\frac{1+z^2}{1-z}\log z\right) \\
\mathcal{I}_{qq}^{(1,0)}(z) =&P_{qq}(z)-\frac{3}{2}\delta(1-z) \\
\mathcal{I}_{qq}^{(1,1)}(z) =&2\delta(1-z) \\
\mathcal{I}_{qg}^{(1,\delta)}(z) =&P_{qg}(z)\left(\log\left(\frac{1-z}{z}\right)-1\right)+\theta(1-z) \\
\mathcal{I}_{qg}^{(1,0)}(z) =&P_{qg}(z)
\end{aligned} \tag{C.2}$$

The beam function can be expanded on a basis given by the $\mathcal{L}_i$, whose arguments can be arbitrarily rescaled as follows.

$$\begin{aligned}\mathcal{I}_{ij}(t,z,\mu) &= \sum \mathcal{I}_{ij}^{m}\left[\alpha_S(\mu),z\right]\frac{1}{\mu^2}\mathcal{L}_m\left(\frac{t}{\mu^2}\right)\\ &= \sum \mathcal{I}_{ij}^{m}\left[\alpha_S(\mu),z,\frac{\xi}{\mu^2}\right]\frac{1}{\xi}\mathcal{L}_m\left(\frac{t}{\xi}\right)\end{aligned} \tag{C.3}$$

The rescaled coefficients are related to the non rescaled ones by the following equations,

$$\begin{aligned}\mathcal{I}_{ij}^{-1}\left[\alpha_S(\mu),z,x\right] =& \mathcal{I}_{ij}^{-1}\left[\alpha_S(\mu),z\right] + \sum_{n=0}^{\infty}\mathcal{I}_{ij}^{n}\left[\alpha_S(\mu),z\right]\frac{\log^{n+1}x}{n+1}\\ \mathcal{I}_{ij}^{k}\left[\alpha_S(\mu),z,x\right] =& \sum_{n=0}^{\infty}\frac{(n+k)!}{n!k!}\mathcal{I}_{ij}^{n+k}\left[\alpha_S(\mu),z\right]\log^n x.\end{aligned} \tag{C.4}$$

Explicitly, at one loop,

$$\begin{aligned}\mathcal{I}_{qq}^{-1}\left[\alpha_S(\mu),z\right] =& \delta(1-z) + \frac{\alpha_S(\mu)C_F}{2\pi}\theta(z)\,\mathcal{I}_{qq}^{(1,\delta)}(z)\\ \mathcal{I}_{qq}^{0}\left[\alpha_S(\mu),z\right] =& \frac{\alpha_S(\mu)C_F}{2\pi}\theta(z)\,\mathcal{I}_{qq}^{(1,0)}(z)\\ \mathcal{I}_{qq}^{1}\left[\alpha_S(\mu),z\right] =& \frac{\alpha_S(\mu)C_F}{2\pi}\theta(z)\,\mathcal{I}_{qq}^{(1,1)}(z)\\ \mathcal{I}_{qg}^{-1}\left[\alpha_S(\mu),z\right] =& \frac{\alpha_S(\mu)T_F}{2\pi}\theta(z)\,\mathcal{I}_{qg}^{(1,\delta)}(z)\\ \mathcal{I}_{qg}^{0}\left[\alpha_S(\mu),z\right] =& \frac{\alpha_S(\mu)T_F}{2\pi}\theta(z)\,\mathcal{I}_{qg}^{(1,0)}(z)\end{aligned} \tag{C.5}$$

and therefore the rescaled coefficients are

$$\begin{aligned}
\mathcal{I}_{qq}^{-1}\left[\alpha_S(\mu), z, x\right] =& \delta(1-z) + \frac{\alpha_S(\mu) C_F}{2\pi}\theta(z)\left[\mathcal{I}_{qq}^{(1,\delta)}(z) + \mathcal{I}_{qq}^{(1,0)}(z)\,\log x + \mathcal{I}_{qq}^{(1,1)}(z)\,\frac{\log^2 x}{2}\right] \\
\mathcal{I}_{qq}^{0}\left[\alpha_S(\mu), z, x\right] =& \frac{\alpha_S(\mu) C_F}{2\pi}\theta(z)\left[\mathcal{I}_{qq}^{(1,0)}(z) + \mathcal{I}_{qq}^{(1,1)}(z)\,\log x\right] \\
\mathcal{I}_{qq}^{1}\left[\alpha_S(\mu), z\, x\right] =& \frac{\alpha_S(\mu) C_F}{2\pi}\theta(z)\,\mathcal{I}_{qq}^{(1,1)}(z) \\
\mathcal{I}_{qg}^{-1}\left[\alpha_S(\mu), z, x\right] =& \frac{\alpha_S(\mu) T_F}{2\pi}\theta(z)\left[\mathcal{I}_{qg}^{(1,\delta)}(z) + \mathcal{I}_{qg}^{(1,0)}(z)\,\log x\right] \\
\mathcal{I}_{qg}^{0}\left[\alpha_S(\mu), z, x\right] =& \frac{\alpha_S(\mu) T_F}{2\pi}\theta(z)\,\mathcal{I}_{qg}^{(1,0)}(z)
\end{aligned} \tag{C.6}$$

The Altarelli-Parisi splitting functions are

$$\begin{aligned}
\hat{P}_{qq}^{(0)}(z) =& \theta(z)\, C_F\, P_{qq}(z) \\
\hat{P}_{qg}^{(0)}(z) =& \theta(z)\, T_F\, P_{qg}(z) \\
\hat{P}_{gq}^{(0)}(z) =& \theta(z)\, C_F\, P_{gq}(z) \\
\hat{P}_{gg}^{(0)}(z) =& \theta(z)\left[C_A\, P_{gg}(z) + \frac{\beta_0}{2}\delta(1-z)\right]
\end{aligned} \tag{C.7}$$

with

$$\begin{aligned}
P_{qq}^{(0)}(z) =& \left[\frac{\theta(1-z)(1+z^2)}{1-z}\right]_+ = 2\mathcal{L}_0(1-z) - \theta(1-z)\,(1+z) + \frac{3}{2}\mathcal{L}_{-1}(1-z) \\
P_{qg}^{(0)}(z) =& \theta(1-z)\left[z^2 + (1-z)^2\right] \\
P_{gq}^{(0)}(z) =& \theta(1-z)\,\frac{1+(1-z)^2}{z} \\
P_{gg}^{(0)}(z) =& 2\left[z\mathcal{L}_0(1-z) + \theta(1-z)\left(\frac{1-z}{z} + z(1-z)\right)\right].
\end{aligned} \tag{C.8}$$

For the two loop splitting functions, we used

$$\begin{aligned}
\hat{P}_{qq}^{(1)}(z) =& 2P_{qq}^{V(1)}(z) + 2P_{qq}^{(1)}(z) \\
\hat{P}_{qq'}^{(1)}(z) =& 2P_{qq}^{(1)}(z) \\
\hat{P}_{q\bar{q}}^{(1)}(z) =& 2P_{q\bar{q}}^{V(1)}(z) + 2P_{qq}^{(1)}(z) \\
\hat{P}_{qg}^{(1)}(z) =& P_{qg}^{(1)}(z) \\
\hat{P}_{gq}^{(1)}(z) =& 2P_{gq}^{(1)}(z) \\
\hat{P}_{gg}^{(1)}(z) =& P_{gg}^{(1)}(z),
\end{aligned} \tag{C.9}$$

where the functions on the right hand side of Eq. C.9 are defined in Eq. 4.107-4.112 of [133].

Convolutions

Here are listed the convolutions which have been used to calculate the Drell-Yan coefficients in Chapter 5

$$
\begin{aligned}
P_{qq}\otimes P_{qq}(z) &= \int_z^1 \frac{dz'}{z'} P_{qq}\left(\frac{z}{z'}\right) P_{qq}(z') \\
&= -5 - z - 4(1+z)\log(1-z) + 3(1+z)\log z + \left(\frac{9}{4} - \frac{2\pi^2}{3}\right)\mathcal{L}_{-1}(1-z) \\
&\quad + (6 - 4\log z)\mathcal{L}_0(1-z) + 8\mathcal{L}_1(1-z) \\
P_{qg}\otimes P_{gq}(z) &= \int_z^1 \frac{dz'}{z'} P_{qg}\left(\frac{z}{z'}\right) P_{gq}(z') = 1 + \frac{4}{3z} - z - \frac{4z^2}{3} + 2(1+z)\log z \\
P_{qq}\otimes P_{qg}(z) &= \int_z^1 \frac{dz'}{z'} P_{qq}\left(\frac{z}{z'}\right) P_{qg}(z') = \\
&= -\frac{1}{2} + 2z + 2(1 - 2z + 2z^2)\log(1-z) + (-1 + 2z - 4z^2)\log z \\
P_{qg}\otimes P_{gg}(z) &= \int_z^1 \frac{dz'}{z'} P_{qg}\left(\frac{z}{z'}\right) P_{gg}(z') = \\
&= 1 + \frac{4}{3z} + 8z - \frac{31z^2}{3} + 2(1 - 2z + 2z^2)\log(1-z) + 2(1+4z)\log z \\
\mathcal{I}_{qq}^{(1,\delta)}\otimes P_{qq}(z) &= \int_z^1 \frac{dz'}{z'} P_{qq}^{(0)}\left(\frac{z}{z'}\right) \mathcal{I}_{qq}^{1,\delta}(z') \\
&= \frac{9}{2} + \frac{2\pi^2}{3} - \frac{9z}{2} + \frac{2\pi^2 z}{3} - \frac{4 - 8z + 4z^2}{1-z} - 3(1+z)\log^2(1-z) \\
&\quad + \left(-\frac{3}{2} - z + \frac{z^2}{2}\right)\frac{\log z}{1-z} - 2(1+z^2)\frac{\log(1-z)\log z}{1-z} + (1-z)^2\frac{\log^2 z}{1-z} \\
&\quad - \frac{1}{2}(1+z)\log^2(z) \\
&\quad + \left(4\zeta_3 - \frac{\pi^2}{4}\right)\delta(1-z) - \pi^2\mathcal{L}_0(1-z) + \frac{3}{2}\mathcal{L}_1(1-z) + 6\mathcal{L}_2(1-z) \\
&\quad + 2(1-2z^2)\frac{\mathrm{Li}_2(1-z)}{1-z} - (1+z)\mathrm{Li}_2(z) - 2(1+z)\mathrm{Li}_2(1-z) \\
\mathcal{I}_{qq}^{(1,1)}\otimes P_{qq}(z) &= \int_z^1 \frac{dz'}{z'} P_{qq}\left(\frac{z}{z'}\right) \mathcal{I}_{qq}^{(1,1)}(z') = 2\,P_{qq}(z) \\
\mathcal{I}_{qg}^{(1,\delta)}\otimes P_{gq}(z) &= \int_z^1 \frac{dz'}{z'} P_{gq}\left(\frac{z}{z'}\right) \mathcal{I}_{qg}^{(1,\delta)}(z') \\
&\quad - \frac{5}{3} + \frac{2}{3z} - \frac{z}{3} + \frac{4z^2}{3} - \left(1 + z + \frac{4z^2}{3}\right)\log\frac{1-z}{z} + \left(2 + \frac{4}{3z}\right)\log(1-z) \\
&\quad + 2(1+z)\log z\log\frac{1-z}{z} - 2(1+z)\mathrm{Li}_2\left(\frac{1-z}{z}\right)
\end{aligned}
$$

$$
\begin{aligned}
\mathcal{I}_{qg}^{(1,\delta)} \otimes P_{gg}(z) &= \int_z^1 \frac{dz'}{z'} P_{gg}\left(\frac{z}{z'}\right) \mathcal{I}_{qg}^{(1,\delta)}(z') \\
&= -\frac{13}{6} - \frac{\pi^2}{3} + \frac{2}{3z} - \frac{37z}{3} + \frac{2\pi^2 z}{3} + \frac{83z^2}{6} - \frac{2\pi^2 z^2}{3} \\
&\quad + \left(1 + \frac{4}{3z} + 12z - \frac{43z^2}{3}\right) \log(1-z) + 2(1 - 2z + 2z^2) \log^2(1-z) \\
&\quad + \left(1 - 8z + \frac{31z^2}{3}\right) \log z + 4z(3-z) \log z \log(1-z) \\
&\quad - 2(1 + 3z + z^2) \log^2 z - 2(1 + 2z + 2z^2) \mathrm{Li}_2\left(\frac{z-1}{z}\right) \\
&\quad + 4z(1-z) \mathrm{Li}_2(1-z) \\
\mathcal{I}_{qq}^{(1,\delta)} \otimes P_{qg}(z) &= \int_z^1 \frac{dz'}{z'} P_{qg}\left(\frac{z}{z'}\right) \mathcal{I}_{qq}^{(1,\delta)}(z') \\
&= -\frac{1}{2} - \frac{\pi^2}{3} - 4z + \frac{2\pi^2 z}{3} + \frac{9z^2}{2} - \pi^2 z^2 - 6z^2 \mathrm{atanh}(1-2z) \\
&\quad + (-2 + 5z) \log(1-z) + (1 - 2z + 2z^2) \log^2(1-z) - 7z \log z \\
&\quad + \left(\frac{1}{2} - z + 2z^2\right) \log^2 z + 2(1 - 2z + 2z^2) \mathrm{Li}_2(1-z) + (1 - 2z + 4z^2) \mathrm{Li}_2(z) \\
\mathcal{I}_{qq}^{(1,1)} \otimes P_{qg}(z) &= \int_z^1 \frac{dz'}{z'} P_{qg}^{(0)}\left(\frac{z}{z'}\right) \mathcal{I}_{qq}^{(1,1)}(z') = 2\, P_{qg}(z)
\end{aligned}
\tag{C.10}
$$

Fourier Transforms of plus functions

Fourier transforms of plus functions and their inverses.

$$
\begin{aligned}
FT\Big[\frac{1}{\mu^2}\mathcal{L}_{-1}\Big(\frac{t}{\mu^2}\Big)\Big] &= 1 \\
FT\Big[\frac{1}{\mu^2}\mathcal{L}_{0}\Big(\frac{t}{\mu^2}\Big)\Big] &= -\log\Big(is\mu^2 e^{\gamma}\Big) \\
FT\Big[\frac{1}{\mu^2}\mathcal{L}_{1}\Big(\frac{t}{\mu^2}\Big)\Big] &= \frac{\pi^2}{12} + \frac{1}{2}\log^2\Big(is\mu^2 e^{\gamma}\Big) \\
FT^{-1}\Big[\log^0\Big(is\mu^2 e^{\gamma}\Big)\Big] &= \frac{1}{\mu^2}\mathcal{L}_{-1}\Big(\frac{t}{\mu^2}\Big) \\
FT^{-1}\Big[\log^1\Big(is\mu^2 e^{\gamma}\Big)\Big] &= -\frac{1}{\mu^2}\mathcal{L}_{0}\Big(\frac{t}{\mu^2}\Big) \\
FT^{-1}\Big[\log^2\Big(is\mu^2 e^{\gamma}\Big)\Big] &= -\frac{\pi^2}{6}\frac{1}{\mu^2}\mathcal{L}_{-1}\Big(\frac{t}{\mu^2}\Big) + 2\frac{1}{\mu^2}\mathcal{L}_{1}\Big(\frac{t}{\mu^2}\Big) \\
FT^{-1}\Big[\log^3\Big(is\mu^2 e^{\gamma}\Big)\Big] &= -2\zeta_3\frac{1}{\mu^2}\mathcal{L}_{-1}\Big(\frac{t}{\mu^2}\Big) + \frac{\pi^2}{2}\frac{1}{\mu^2}\mathcal{L}_{0}\Big(\frac{t}{\mu^2}\Big) - 3\frac{1}{\mu^2}\mathcal{L}_{2}\Big(\frac{t}{\mu^2}\Big) \\
FT^{-1}\Big[\log^4\Big(is\mu^2 e^{\gamma}\Big)\Big] &= \frac{\pi^4}{60}\frac{1}{\mu^2}\mathcal{L}_{-1}\Big(\frac{t}{\mu^2}\Big) + 8\zeta_3\frac{1}{\mu^2}\mathcal{L}_{0}\Big(\frac{t}{\mu^2}\Big) - 2\pi^2\frac{1}{\mu^2}\mathcal{L}_{1}\Big(\frac{t}{\mu^2}\Big) \\
&\quad + 4\frac{1}{\mu^2}\mathcal{L}_{3}\Big(\frac{t}{\mu^2}\Big)
\end{aligned}
\tag{C.11}
$$

Bibliography

[1] Riccardo Abbate, Michael Fickinger, Andre H. Hoang, Vicent Mateu, and Iain W. Stewart. Thrust at N^3LL with Power Corrections and a Precision Global Fit for $\alpha_s(m_Z)$. *Phys. Rev.*, D83:074021, 2011.

[2] Riccardo Abbate, Michael Fickinger, Andre H. Hoang, Vicent Mateu, and Iain W. Stewart. Precision Thrust Cumulant Moments at N^3LL. 2012.

[3] G. Abbiendi et al. Test of the flavour independence of alpha(s) using next-to-leading order calculations for heavy quarks. *Eur. Phys. J.*, C11:643–659, 1999.

[4] G. Abbiendi et al. QCD studies with e+ e- annihilation data at 172-GeV to 189-GeV. *Eur. Phys. J.*, C16:185–210, 2000.

[5] G. Abbiendi et al. Measurement of event shape distributions and moments in e+ e- to hadrons at 91-GeV - 209-GeV and a determination of alpha(s). *Eur. Phys. J.*, C40:287–316, 2005.

[6] J. Abdallah et al. A study of the energy evolution of event shape distributions and their means with the DELPHI detector at LEP. *Eur. Phys. J.*, C29:285–312, 2003.

[7] J. Abdallah et al. The Measurement of alpha(s) from event shapes with the DELPHI detector at the highest LEP energies. *Eur.Phys.J.*, C37:1–23, 2004.

[8] K. Abe et al. Measurement of alpha-s (M(Z)**2) from hadronic event observables at the Z0 resonance. *Phys. Rev.*, D51:962–984, 1995.

[9] P. Abreu et al. Energy dependence of event shapes and of alpha(s) at LEP- 2. *Phys. Lett.*, B456:322–340, 1999.

[10] P. Abreu et al. Consistent measurements of alpha(s) from precise oriented event shape distributions. *Eur. Phys. J.*, C14:557–584, 2000.

[11] M. Acciarri et al. QCD studies in e^+e^- annihilation from 30-GeV to 189-GeV. *Phys.Lett.*, B489:65–80, 2000.

[12] P. Achard et al. Studies of hadronic event structure in e^+e^- annihilation from 30-GeV to 209-GeV with the L3 detector. *Phys. Rept.*, 399:71–174, 2004.

[13] K. Ackerstaff et al. QCD studies with e+ e- annihilation data at 161-GeV. *Z. Phys.*, C75:193–207, 1997.

[14] B. Adeva et al. Studies of hadronic event structure and comparisons with QCD models at the Z0 resonance. *Z. Phys.*, C55:39–62, 1992.

[15] R. Akhoury and Valentin I. Zakharov. On the universality of the leading, 1/Q power corrections in QCD. *Phys. Lett.*, B357:646–652, 1995.

[16] R. Akhoury and Valentin I. Zakharov. Leading power corrections in QCD: From renormalons to phenomenology. *Nucl.Phys.*, B465:295–314, 1996.

[17] S. Alekhin, J. Blumlein, S. Klein, and S. Moch. The 3-, 4-, and 5-flavor NNLO Parton from Deep-Inelastic- Scattering Data and at Hadron Colliders. *Phys. Rev.*, D81:014032, 2010.

[18] P. A. Baikov, K. G. Chetyrkin, A. V. Smirnov, V. A. Smirnov, and M. Steinhauser. Quark and gluon form factors to three loops. *Phys. Rev. Lett.*, 102:212002, 2009.

[19] Christopher Balzereit, Thomas Mannel, and Wolfgang Kilian. Evolution of the light-cone distribution function for a heavy quark. *Phys. Rev. D*, 58:114029, 1998.

[20] Christian W. Bauer, Sean Fleming, and Michael E. Luke. Summing sudakov logarithms in b to x/s gamma in effective field theory. *Phys. Rev. D*, 63:014006, 2001.

[21] Christian W. Bauer, Sean Fleming, Dan Pirjol, Ira Z. Rothstein, and Iain W. Stewart. Hard scattering factorization from effective field theory. *Phys. Rev. D*, 66:014017, 2002.

[22] Christian W. Bauer, Sean Fleming, Dan Pirjol, and Iain W. Stewart. An effective field theory for collinear and soft gluons: Heavy to light decays. *Phys. Rev. D*, 63:114020, 2001.

[23] Christian W. Bauer, Michael Luke, and Thomas Mannel. Subleading shape functions in b to x(u) lepton anti-nu and the determination of —v(ub)—. *Phys.Lett.*, B543:261–268, 2002.

[24] Christian W. Bauer, Michael E. Luke, and Thomas Mannel. Light cone distribution functions for B decays at subleading order in 1 / m(b). *Phys.Rev.*, D68:094001, 2003.

[25] Christian W. Bauer and Aneesh V. Manohar. Shape function effects in B to X/s gamma and B to X/u l nu decays. *Phys. Rev.*, D70:034024, 2004.

[26] Christian W. Bauer, Dan Pirjol, and Iain W. Stewart. Soft-Collinear Factorization in Effective Field Theory. *Phys. Rev.*, D65:054022, 2002.

[27] Christian W. Bauer and Iain W. Stewart. Invariant operators in collinear effective theory. *Phys. Lett. B*, 516:134–142, 2001.

[28] Thomas Becher, Guido Bell, and Matthias Neubert. Factorization and Resummation for Jet Broadening. *Phys.Lett.*, B704:276–283, 2011. 15 pages, 4 figures.

[29] Thomas Becher and Matthias Neubert. Toward a NNLO calculation of the anti-B to X/s+ gamma decay rate with a cut on photon energy. II: Two-loop result for the jet function. *Phys. Lett.*, B637:251–259, 2006.

[30] Thomas Becher, Matthias Neubert, and Ben D. Pecjak. Factorization and momentum-space resummation in deep-inelastic scattering. *JHEP*, 01:076, 2007.

[31] Thomas Becher and Matthew D. Schwartz. A Precise determination of α_s from LEP thrust data using effective field theory. *JHEP*, 07:034, 2008.

[32] Andrei V. Belitsky, G. P. Korchemsky, and G. Sterman. Energy flow in QCD and event shape functions. *Phys. Lett.*, B515:297–307, 2001.

[33] M. Beneke. Renormalons. *Phys. Rept.*, 317:1–142, 1999.

[34] M. Beneke, F. Campanario, T. Mannel, and B.D. Pecjak. Power corrections to anti-B to X(u) l anti-nu (X(s) gamma) decay spectra in the 'shape-function' region. *JHEP*, 0506:071, 2005.

[35] Martin Beneke and Matthias Jamin. α_s and the τ hadronic width: fixed-order, contour-improved and higher-order perturbation theory. *JHEP*, 09:044, 2008.

[36] Carola F. Berger, Tibor Kucs, and George Sterman. Event shape / energy flow correlations. *Phys. Rev. D*, 68:014012, 2003.

[37] Carola F. Berger and George Sterman. Scaling rule for nonperturbative radiation in a class of event shapes. *JHEP*, 09:058, 2003.

[38] S. Bethke, S. Kluth, C. Pahl, and J. Schieck. Determination of the Strong Coupling $\boldsymbol{\alpha_s}$ from hadronic Event Shapes and NNLO QCD predictions using JADE Data. *Eur. Phys. J.*, C64:351–360, 2009.

[39] Siegfried Bethke. Experimental tests of asymptotic freedom. *Prog. Part. Nucl. Phys.*, 58:351–386, 2007.

[40] Siegfried Bethke. The 2009 Wolrd Average of $\alpha_s(M_Z)$. *Eur. Phys. J.*, C64:689–703, 2009.

[41] O. Biebel. Experimental tests of the strong interaction and its energy dependence in electron positron annihilation. *Phys.Rept.*, 340:165–289, 2001.

[42] Johannes Blumlein, Helmut Bottcher, and Alberto Guffanti. Non-singlet QCD analysis of deep inelastic world data at O(alpha(s)**3). *Nucl. Phys.*, B774:182–207, 2007.

[43] H. Boos, Th. Feldmann, T. Mannel, and B. D. Pecjak. Can anti-b to x/c l anti-nu/l help us extract —v(ub)—? *JHEP*, 05:056, 2006.

[44] S. W. Bosch, B. O. Lange, M. Neubert, and Gil Paz. Factorization and shape-function effects in inclusive B- meson decays. *Nucl. Phys.*, B699:335–386, 2004.

[45] Stefan W. Bosch, Matthias Neubert, and Gil Paz. Subleading shape functions in inclusive B decays. *JHEP*, 0411:073, 2004.

[46] Arnd Brandenburg and Peter Uwer. Next-to-leading order QCD corrections and massive quarks in e+ e- to 3jets. *Nucl. Phys.*, B515:279–320, 1998.

[47] W. Braunschweig et al. GLOBAL JET PROPERTIES AT 14-GeV TO 44-GeV CENTER-OF-MASS ENERGY IN e+ e- ANNIHILATION. *Z. Phys.*, C47:187–198, 1990.

[48] D. Buskulic et al. Test of the flavor independence of alpha-s. *Phys. Lett.*, B355:381–393, 1995.

[49] S. Catani and M. H. Seymour. The Dipole Formalism for the Calculation of QCD Jet Cross Sections at Next-to-Leading Order. *Phys. Lett.*, B378:287–301, 1996.

[50] S. Catani and M. H. Seymour. A general algorithm for calculating jet cross sections in NLO QCD. *Nucl. Phys.*, B485:291–419, 1997.

[51] S. Catani, L. Trentadue, G. Turnock, and B. R. Webber. Resummation of large logarithms in e+ e- event shape distributions. *Nucl. Phys.*, B407:3–42, 1993.

[52] S. Catani, G. Turnock, and B.R. Webber. Heavy jet mass distribution in e+ e- annihilation. *Phys.Lett.*, B272:368–372, 1991.

[53] S. Catani, G. Turnock, and B.R. Webber. Jet broadening measures in e^+e^- annihilation. *Phys.Lett.*, B295:269–276, 1992.

[54] T. Chandramohan and L. Clavelli. CONSEQUENCES OF SECOND ORDER QCD FOR JET STRUCTURE IN e+ e- ANNIHILATION. *Nucl.Phys.*, B184:365, 1981.

[55] K. G. Chetyrkin, Johann H. Kuhn, and A. Kwiatkowski. QCD corrections to the e^+e^- cross-section and the Z boson decay rate: Concepts and results. *Phys. Rept.*, 277:189–281, 1996.

[56] Yang-Ting Chien and Matthew D. Schwartz. Resummation of heavy jet mass and comparison to LEP data. *JHEP*, 08:058, 2010.

[57] Jui-yu Chiu, Ambar Jain, Duff Neill, and Ira Z. Rothstein. The Rapidity Renormalization Group. 2011.

[58] Jui-yu Chiu, Ambar Jain, Duff Neill, and Ira Z. Rothstein. A Formalism for the Systematic Treatment of Rapidity Logarithms in Quantum Field Theory. 2012.

[59] L. Clavelli. JET INVARIANT MASS IN QUANTUM CHROMODYNAMICS. *Phys.Lett.*, B85:111, 1979.

[60] L. Clavelli and D. Wyler. KINEMATICAL BOUNDS ON JET VARIABLES AND THE HEAVY JET MASS DISTRIBUTION. *Phys.Lett.*, B103:383, 1981.

[61] M. Czakon. The four-loop QCD beta-function and anomalous dimensions. *Nucl. Phys.*, B710:485–498, 2005.

[62] M. Davier, S. Descotes-Genon, Andreas Hocker, B. Malaescu, and Z. Zhang. The Determination of α_s from τ Decays Revisited. *Eur. Phys. J.*, C56:305–322, 2008.

[63] C. T. H. Davies et al. Update: Accurate Determinations of α_s from Realistic Lattice QCD. *Phys. Rev.*, D78:114507, 2008.

[64] R. A. Davison and B. R. Webber. Non-Perturbative Contribution to the Thrust Distribution in e^+e^- Annihilation. *Eur. Phys. J.*, C59:13–25, 2009.

[65] Federico Demartin, Stefano Forte, Elisa Mariani, Juan Rojo, and Alessandro Vicini. The impact of PDF and alphas uncertainties on Higgs Production in gluon fusion at hadron colliders. 2010.

[66] Ansgar Denner, Stefan Dittmaier, Thomas Gehrmann, and Christian Kurz. Electroweak corrections to three-jet production in electron-positron annihilation. *Phys. Lett.*, B679:219–222, 2009.

[67] Ansgar Denner, Stefan Dittmaier, Thomas Gehrmann, and Christian Kurz. Electroweak corrections to hadronic event shapes and jet production in e+e- annihilation. *Nucl. Phys.*, B836:37–90, 2010.

[68] G. Dissertori et al. First determination of the strong coupling constant using NNLO predictions for hadronic event shapes in e^+e^- annihilations. *JHEP*, 02:040, 2008.

[69] G. Dissertori et al. Determination of the strong coupling constant using matched NNLO+NLLA predictions for hadronic event shapes in e+e- annihilations. *JHEP*, 08:036, 2009.

[70] Yuri L. Dokshitzer, A. Lucenti, G. Marchesini, and G.P. Salam. On the QCD analysis of jet broadening. *JHEP*, 9801:011, 1998.

[71] Yuri L. Dokshitzer, A. Lucenti, G. Marchesini, and G.P. Salam. On the universality of the Milan factor for 1 / Q power corrections to jet shapes. *JHEP*, 9805:003, 1998.

[72] Yuri L. Dokshitzer, A. Lucenti, G. Marchesini, and G.P. Salam. Universality of 1 / Q corrections to jet shape observables rescued. *Nucl.Phys.*, B511:396–418, 1998.

[73] Yuri L. Dokshitzer, G. Marchesini, and B. R. Webber. Dispersive Approach to Power-Behaved Contributions in QCD Hard Processes. *Nucl. Phys.*, B469:93–142, 1996.

[74] Yuri L. Dokshitzer and B. R. Webber. Calculation of power corrections to hadronic event shapes. *Phys. Lett.*, B352:451–455, 1995.

[75] Yuri L. Dokshitzer and B.R. Webber. Power corrections to event shape distributions. *Phys.Lett.*, B404:321–327, 1997.

[76] R. Keith Ellis, D. A. Ross, and A. E. Terrano. The Perturbative Calculation of Jet Structure in e+ e- Annihilation. *Nucl. Phys.*, B178:421, 1981.

[77] Edward Farhi. A QCD Test for Jets. *Phys. Rev. Lett.*, 39:1587–1588, 1977.

[78] Henning Flacher et al. Gfitter - Revisiting the Global Electroweak Fit of the Standard Model and Beyond. *Eur. Phys. J.*, C60:543–583, 2009.

[79] Sean Fleming, Andre H. Hoang, Sonny Mantry, and Iain W. Stewart. Jets from massive unstable particles: Top-mass determination. *Phys. Rev.*, D77:074010, 2008.

[80] Sean Fleming, Andre H. Hoang, Sonny Mantry, and Iain W. Stewart. Top Jets in the Peak Region: Factorization Analysis with NLL Resummation. *Phys. Rev.*, D77:114003, 2008.

[81] Einan Gardi and Johan Rathsman. The thrust and heavy-jet mass distributions in the two-jet region. *Nucl. Phys.*, B638:243–287, 2002.

[82] T. Gehrmann, E. W. N. Glover, T. Huber, N. Ikizlerli, and C. Studerus. Calculation of the quark and gluon form factors to three loops in QCD. 2010.

[83] T. Gehrmann, T. Huber, and D. Maitre. Two-loop quark and gluon form factors in dimensional regularisation. *Phys. Lett.*, B622:295–302, 2005.

[84] T. Gehrmann, M. Jaquier, and G. Luisoni. Hadronization effects in event shape moments. *Eur. Phys. J.*, C67:57–72, 2010.

[85] A. Gehrmann-De Ridder, T. Gehrmann, E. W. N. Glover, and G. Heinrich. NNLO corrections to event shapes in e^+e^- annihilation. *JHEP*, 12:094, 2007.

[86] A. Gehrmann-De Ridder, T. Gehrmann, E. W. N. Glover, and G. Heinrich. Second-order QCD corrections to the thrust distribution. *Phys. Rev. Lett.*, 99:132002, 2007.

[87] A. Gehrmann-De Ridder, T. Gehrmann, E.W.N. Glover, and G. Heinrich. NNLO moments of event shapes in e+e- annihilation. *JHEP*, 0905:106, 2009.

[88] H. Georgi. Effective field theory. *Annu. Rev. Nucl. Part. Sci.*, 43:209–252, 1993.

[89] Kaoru Hagiwara, T. Kuruma, and Y. Yamada. Three jet distributions from the one loop Z g g vertex at e+ e- colliders. *Nucl. Phys.*, B358:80–96, 1991.

[90] G. Heinrich, T. Huber, D. A. Kosower, and V. A. Smirnov. Nine-Propagator Master Integrals for Massless Three-Loop Form Factors. *Phys. Lett.*, B678:359–366, 2009.

[91] A. Heister et al. Studies of QCD at e+ e- centre-of-mass energies between 91-GeV and 209-GeV. *Eur. Phys. J.*, C35:457–486, 2004.

[92] Andre H. Hoang, Ambar Jain, Ignazio Scimemi, and Iain W. Stewart. Infrared Renormalization Group Flow for Heavy Quark Masses. *Phys. Rev. Lett.*, 101:151602, 2008.

[93] Andre H. Hoang, Ambar Jain, Ignazio Scimemi, and Iain W. Stewart. R-evolution: Improving perturbative QCD. 2009.

[94] Andre H. Hoang and Stefan Kluth. Hemisphere Soft Function at $O(alpha_s^2)$ for Dijet Production in e+e- Annihilation. 2008.

[95] Andre H. Hoang and Iain W. Stewart. Designing Gapped Soft Functions for Jet Production. *Phys. Lett.*, B660:483–493, 2008.

[96] Andrew Hornig, Christopher Lee, and Grigory Ovanesyan. Effective Predictions of Event Shapes: Factorized, Resummed, and Gapped Angularity Distributions. *JHEP*, 05:122, 2009.

[97] Andrew Hornig, Christopher Lee, Iain W. Stewart, Jonathan R. Walsh, and Saba Zuberi. Non-global Structure of the $O(\alpha_s^2)$ Dijet Soft Function. 2011.

[98] Ahmad Idilbi, Xiang dong Ji, and Feng Yuan. Resummation of Threshold Logarithms in Effective Field Theory For DIS, Drell-Yan and Higgs Production. *Nucl. Phys. B*, 753:42–68, 2006.

[99] B. L. Ioffe. ASSOCIATED PRODUCTION OF GLUONIC JETS AND HEAVY MESONS IN e+ e- ANNIHILATION. *Phys. Lett.*, B78:277, 1978.

[100] Ambar Jain, Ignazio Scimemi, and Iain W. Stewart. Two-loop Jet-Function and Jet-Mass for Top Quarks. *Phys. Rev.*, D77:094008, 2008.

[101] Peter Jenni, Marzio Nessi, Markus Nordberg, and Smith Kenway. Atlas-tdr-016; cern-lhcc-2003-022. Technical report, CERN, 2003.

[102] Roger W. L. Jones, Matthew Ford, Gavin P. Salam, Hasko Stenzel, and Daniel Wicke. Theoretical uncertainties on alpha(s) from event-shape variables in e+ e- annihilations. *JHEP*, 12:007, 2003.

[103] Randall Kelley, Robert M. Schabinger, Matthew D. Schwartz, and Hua Xing Zhu. The two-loop hemisphere soft function. 2011.

[104] Bernd A. Kniehl and Johann H. Kuhn. QCD Corrections to the Z Decay Rate. *Nucl. Phys.*, B329:547, 1990.

[105] G. P. Korchemsky and A. V. Radyushkin. Renormalization of the Wilson Loops Beyond the Leading Order. *Nucl. Phys. B*, 283:342–364, 1987.

[106] G. P. Korchemsky and S. Tafat. On power corrections to the event shape distributions in QCD. *JHEP*, 10:010, 2000.

[107] Gregory P. Korchemsky and George Sterman. Power corrections to event shapes and factorization. *Nucl. Phys.*, B555:335–351, 1999.

[108] Hung-Liang Lai et al. Uncertainty induced by QCD coupling in the CTEQ-TEA global analysis of parton distributions. 2010.

[109] S. A. Larin and J. A. M. Vermaseren. The three-loop QCD β function and anomalous dimensions. *Phys. Lett. B*, 303:334–336, 1993.

[110] Christopher Lee and George Sterman. Universality of nonperturbative effects in event shapes. 2006.

[111] Christopher Lee and George Sterman. Momentum flow correlations from event shapes: Factorized soft gluons and soft-collinear effective theory. *Phys. Rev.*, D75:014022, 2007.

[112] Keith S. M. Lee and Iain W. Stewart. Factorization for power corrections to B to X/s gamma and B to X/u l anti-nu. *Nucl. Phys.*, B721:325–406, 2005.

[113] R. N. Lee, A. V. Smirnov, and V. A. Smirnov. Analytic Results for Massless Three-Loop Form Factors. *JHEP*, 04:020, 2010.

[114] Adam K. Leibovich, Zoltan Ligeti, and Mark B. Wise. Enhanced subleading structure functions in semileptonic B decay. *Phys.Lett.*, B539:242–248, 2002.

[115] Y. K. Li et al. Multi - hadron event properties in e^+e^- annihilation at $\sqrt{s} = 52$ GeV to 57-GeV. *Phys. Rev.*, D41:2675, 1990.

[116] Zoltan Ligeti, Iain W. Stewart, and Frank J. Tackmann. Treating the b quark distribution function with reliable uncertainties. *Phys. Rev.*, D78:114014, 2008.

[117] Enrico Lunghi, Dan Pirjol, and Daniel Wyler. Factorization in leptonic radiative B to gamma e nu decays. ((U)). *Nucl. Phys.*, B649:349–364, 2003.

[118] A. D. Martin, W. J. Stirling, R. S. Thorne, and G. Watt. Uncertainties on $alpha_S$ in global PDF analyses and implications for predicted hadronic cross sections. *Eur. Phys. J.*, C64:653–680, 2009.

[119] T. Matsuura, S. C. van der Marck, and W. L. van Neerven. The Calculation of the Second Order Soft and Virtual Contributions to the Drell-Yan Cross-Section. *Nucl. Phys.*, B319:570, 1989.

[120] T. Matsuura and W. L. van Neerven. SECOND ORDER LOGARITHMIC CORRECTIONS TO THE DRELL-YAN CROSS-SECTION. *Z. Phys.*, C38:623, 1988.

[121] S. Moch, J. A. M. Vermaseren, and A. Vogt. The three-loop splitting functions in QCD: The non-singlet case. *Nucl. Phys.*, B688:101–134, 2004.

[122] S. Moch, J. A. M. Vermaseren, and A. Vogt. The quark form factor at higher orders. *JHEP*, 08:049, 2005.

[123] Pier Francesco Monni, Thomas Gehrmann, and Gionata Luisoni. Two-Loop Soft Corrections and Resummation of the Thrust Distribution in the Dijet Region. 2011.

[124] P. A. Movilla Fernandez, O. Biebel, S. Bethke, S. Kluth, and P. Pfeifenschneider. A study of event shapes and determinations of alpha(s) using data of e+ e- annihilations at s**(1/2) = 22-GeV to 44-GeV. *Eur. Phys. J.*, C1:461–478, 1998.

[125] Paolo Nason and Carlo Oleari. Next-to-leading-order corrections to the production of heavy-flavour jets in e+ e- collisions. *Nucl. Phys.*, B521:237–273, 1998.

[126] Paolo Nason and Michael H. Seymour. Infrared renormalons and power suppressed effects in e+ e- jet events. *Nucl. Phys.*, B454:291–312, 1995.

[127] Matthias Neubert. Renormalization-group improved calculation of the B to X/s+ gamma branching ratio. *Eur. Phys. J.*, C40:165–186, 2005.

[128] Hans Peter Nilles. ISOLATING GLUON JETS. *Phys. Rev. Lett.*, 45:319, 1980.

[129] C. Pahl, S. Bethke, O. Biebel, S. Kluth, and J. Schieck. Tests of analytical hadronisation models using event shape moments in e^+e^- annihilation. *Eur.Phys.J.*, C64:533–547, 2009.

[130] Christoph Pahl. . PhD thesis, TU Munich, 2007.

[131] Christoph Pahl, Siegfried Bethke, Stefan Kluth, Jochen Schieck, and the JADE collaboration. Study of moments of event shapes and a determination of $alpha_s$ using e^+e^- annihilation data from Jade. *Eur.Phys.J.*, C60:181–196, 2009.

[132] Gil Paz. Subleading Jet Functions in Inclusive B Decays. *JHEP*, 06:083, 2009.

[133] B.R.Webber R.K.Ellis, W.J.Stirling. *QCD and Collider Physics.* Cambridge University Press, Cambridge, United Kingdom, 1996.

[134] German Rodrigo, Mikhail S. Bilenky, and Arcadi Santamaria. Quark-mass effects for jet production in e+ e- collisions at the next-to-leading order: Results and applications. *Nucl. Phys.*, B554:257–297, 1999.

[135] G. P. Salam and D. Wicke. Hadron masses and power corrections to event shapes. *JHEP*, 05:061, 2001.

[136] Matthew D. Schwartz. Resummation and NLO Matching of Event Shapes with Effective Field Theory. *Phys. Rev.*, D77:014026, 2008.

[137] Mikhail A. Shifman, A. I. Vainshtein, and Valentin I. Zakharov. QCD and Resonance Physics. Sum Rules. *Nucl. Phys.*, B147:385–447, 1979.

[138] Iain W. Stewart, Frank J. Tackmann, and Wouter J. Waalewijn. Factorization at the LHC: From PDFs to Initial State Jets. 2009.

[139] O. V. Tarasov, A. A. Vladimirov, and A. Yu. Zharkov. The Gell-Mann-Low Function of QCD in the Three Loop Approximation. *Phys. Lett. B*, 93:429–432, 1980.

[140] W. L. van Neerven. DIMENSIONAL REGULARIZATION OF MASS AND INFRARED SINGULARITIES IN TWO LOOP ON-SHELL VERTEX FUNCTIONS. *Nucl. Phys.*, B268:453, 1986.

[141] T. van Ritbergen, J. A. M. Vermaseren, and S. A. Larin. The four-loop beta function in quantum chromodynamics. *Phys. Lett.*, B400:379–384, 1997.

[142] A. Vogt. Next-to-next-to-leading logarithmic threshold resummation for deep-inelastic scattering and the Drell-Yan process. *Phys. Lett.*, B497:228–234, 2001.

[143] Stefan Weinzierl. NNLO corrections to 3-jet observables in electron-positron annihilation. *Phys. Rev. Lett.*, 101:162001, 2008.

[144] Stefan Weinzierl. Event shapes and jet rates in electron-positron annihilation at NNLO. *JHEP*, 06:041, 2009.

[145] Stefan Weinzierl. Moments of event shapes in electron-positron annihilation at NNLO. *Phys. Rev.*, D80:094018, 2009.

[146] Daniel Wicke. Energy dependence of the event shape observables and the strong coupling. (In German). 1999. WU-B-DIS-1999-05.

[147] Inc Wolfram Research. *Mathematica Edition: Version 7.0.* Wolfram Research, Inc., Champaign, Illinois, 2008.

[148] H. Yamamoto. An efficient algorithm for calculating thrust in high multiplicity reactions. *Journal of Computational Physics*, 52:597–601, 1983.

[149] W. M. Yao et al. Review of particle physics. *J. Phys.*, G33:1–1232, 2006.